IN-SITU INVESTIGATIONS ON GROWTH AND STRUCTURAL CHANGES IN NANOSTRUCTURES BY TIME-RESOLVED EXAFS MEASUREMENT

By

CHANDRANI NAYAK

PHYS01201304033

Bhabha Atomic Research Centre

A thesis submitted to the
Board of Studies in Physical Sciences
In partial fulfillment of requirements
for the Degree of

DOCTOR OF PHILOSOPHY

of

HOMI BHABHA NATIONAL INSTITUTE

March, 2019

HOMI BHABHA NATIONAL INSTITUTE

Recommendations of the Viva Voce Committee

As members of the Viva Voce Committee, we certify that we have read the dissertation prepared by Ms. Chandrani Nayak entitled **"*In-situ* investigations on growth and structural changes in nanostructures by time-resolved EXAFS measurement"** and recommend that it may be accepted as fulfilling the thesis requirement for the award of Degree of Doctor of Philosophy.

Sr.No.	Name	Designation	Signature	Date
1.	**Dr. N.K. Sahoo**	Chairman		6/3/2019
2.	**Professor Subodh Kumar De**	Examiner		06.03.2019
3.	**Prof. S. S. Major**	Member		6/3/2019
4.	**Dr. A. K. Tripathi**	Member		06/03/2019
5.	**Dr. D. Bhattacharyya**	Guide & Convener		06/03/2019

Final approval and acceptance of this thesis is contingent upon the candidate's submission of the final copies of the thesis to HBNI.

I hereby certify that I have read this thesis prepared under my direction and recommend that it may be accepted as fulfilling the thesis requirement.

Date: 06/03/2019
Place: Mumbai

Dr. Dibyendu Bhattacharyya
(Guide)

STATEMENT BY AUTHOR

This dissertation has been submitted in partial fulfilment of requirements for an advanced degree at Homi Bhabha National Institute (HBNI) and is deposited in the Library to be made available to borrowers under rules of the HBNI.

Brief quotations from this dissertation are allowable without special permission, provided that accurate acknowledgement of source is made. Requests for permission for extended quotation from or reproduction of this manuscript in whole or in part may be granted by the Competent Authority of HBNI when in his or her judgment the proposed use of the material is in the interests of scholarship. In all other instances, however, permission must be obtained from the author.

CHANDRANI NAYAK

DECLARATION

I, hereby declare that the investigation presented in the thesis has been carried out by me. The work is original and has not been submitted earlier as a whole or in part for a degree / diploma at this or any other Institution / University.

CHANDRANI NAYAK

List of Publications arising from the thesis

Journals:

1. C. Nayak, D. Bhattacharyya, S. N. Jha and N. K. Sahoo, “Growth of Block Copolymer stabilized Metal Nanoparticles: Probed simultaneously by in-situ XAS and UV-Vis spectroscopy”, J. Synchrotron Radiation, 23 (2016) 293-303.

2. Chandrani Nayak, D. Bhattacharyya, K. Bhattacharyya, A. K. Tripathi, S. N. Jha and N. K. Sahoo, “Insight into growth of Au@Pt bimetallic nanoparticles: an in-situ XAS study”, J. Synchrotron Radiation, 24 (2017) 825-835.

3. Chandrani Nayak, S. N. Jha and Dibyendu Bhattacharyya, “In-Situ X ray Absorption Spectroscopy to Study Growth of Nanoparticles” , *In-situ* Characterization Techniques for Nanomaterials, Springer, ISBN 978-3-662-56322-9, Challa S. S. R. Kumar (Ed.), 2018, p. 189-222.

4. Chandrani Nayak, Dibyendu Bhattacharyya, Shambhu Nath Jha and Naba Kishore Sahoo, “*In-Situ* XAS Study on Growth of PVP-Stabilized Cu Nanoparticles”, Chem. Select, 3 (2018) 1-9.

5. Chandrani. Nayak, Preeti Jain, C. P. Vinod, S. N. Jha and D. Bhattacharyya, “*In-situ* X ray Absorption Spectroscopy Study of Fischer Tropsch Reaction with Co catalysts”, J. Synchrotron Radiation, 26 (2019) 137-144.

Conference publications

1. C. Nayak, K. Bhattacharyya, A. K. Tripathi, S. N. Jha, D. Bhattacharyya, and N. K. Sahoo, “Growth of Au@Pt coreshell nanoparticles: Probed by in-situ XANES and UV-visible spectroscopy”, AIP Conference Proceedings 1731 (2016) 060011.

2. C. Nayak, D. Bhattacharyya, S. N. Jha and N. K. Sahoo, “Flow-setup for in situ XAFS measurement to probe growth of PVP stabilized Cu nanoparticles”, AIP Conference Proceedings 1832 (2017) 060003.

CHANDRANI NAYAK

Dedicated

To

My Parents

ACKNOWLEDGEMENTS

I would like to gratefully and sincerely thank my supervisor Dr. Dibyendu Bhattacharyya, Head Synchrotron Science & Multilayer Physics Section, Atomic & Molecular Physics Division, BARC, for his guidance, understanding and patience during my doctoral studies. I am extremely grateful to Dr. N.K. Sahoo, Ex Associate Director, Physics Group and Ex Head, Atomic & Molecular Physics Division, BARC for his continuous encouragement throughout this thesis work. I would like to thank all of the members of my XAFS research group, Dr. Shambhu Nath Jha, Ashwini Kumar Poswal, Dr. Arup Biswas, Ashok Kumar Yadav, Nidhi Tiwari, Ankur Agrawal, Ashutosh Dwivedi and Nirmalendu Patra and other colleagues who have helped me in every possible way. A special mention for Dr. (Smt.) Sohini Basu (formerly at Atomic & Molecular Physics Division at BARC, Mumbai, and now at UOP-Honeywell, Gurugram, Haryana), Ashok Kumar Yadav and Nidhi Tiwari, who made my long working hours worthwhile and for the stimulating discussions on XAFS.

I would also like to thank members of my doctoral committee for their input and valuable discussions. I am also thankful to my principal collaborators, Dr. A. K. Tripathi and Dr. K. Bhattacharyya from Chemistry Division, BARC, Mumbai and Dr. C. P. Vinod and Ms. Preeti Jain from National Chemical Laboratory, Pune. Last but not the least; I acknowledge all my teachers, friends and family members for their inspiration and silent support during the course of this thesis work.

CONTENTS

Synopsis i

List of Figures ix

List of Tables xvi

Chapter 1: Introduction **1**

1.1 X-ray Absorption Spectroscopy 6

1.1.1 X-ray Absorption Near Edge Spectroscopy (XANES) 9

1.1.2 Extended X-ray Absorption Fine Structure Spectroscopy (EXAFS) 11

1.1.3 Theoretical formulation of EXAFS 12

1.2 Time Resolved X-ray Absorption Spectroscopy (TR-XAS) 19

1.2.1 Quick XAFS (QXAFS) 19

1.2.2 Dispersive XAFS (DXAFS) 20

1.3 Applications of TR-XAS 22

1.3.1 Growth of nanoparticles 23

1.3.2 Catalysis 27

1.4 Outline of the thesis 28

Chapter 2: Experimentation and Data Analysis **30**

2.1 TR-XAS Experiment 30

2.1.1 Energy Dispersive EXAFS Beamline (BL-08) 32

2.1.2 Energy Scanning EXAFS beamline (BL-09) 36

2.2 Analytical tools for TR-XANES 40

2.2.1 Linear Combination Fitting (LCF) 41

2.2.2 Principal Component Analysis (PCA) 42

2.2.3 Multivariate Curve Resolution with Alternating Least Squares (MCR-ALS) 44

2.3 EXAFS Data Analysis 45

2.3.1 Data Processing using Athena 46

2.3.2 Data fitting using Artemis 50

2.4 Complementary Techniques 52

2.4.1 UV-Visible Spectroscopy 53

2.4.2 Gas chromatography 56
2.5 *Ex-situ* techniques 58
2.5.1 X-ray Diffraction 58
2.5.2 X-ray Photoelectron Spectroscopy 59
2.5.3 Transmission Electron Microscopy 61
2.5.4 High Resolution Transmission Electron Microscopy 62
Chapter 3: In-situ XAS studies on growth of Au and Pt monometallic nanoparticle 64
3.1 Synthesis of Block copolymer stabilized Au and Pt nanoparticles 65
3.2 *In-situ* EXAFS measurement cell for one pot synthesis 66
3.3 Growth of Block Copolymer stabilized Au nanoparticles 69
3.3.1 *In-situ* XANES studies 69
3.3.2 *In-situ* EXAFS studies 71
3.3.3 *In-situ* UV-Visible spectroscopy studies 75
3.3.4 Growth Mechanism 77
3.4 Growth of Block Copolymer stabilized Pt nanoparticles 78
3.4.1 *In-situ* XANES studies 78
3.4.2 *In-situ* EXAFS studies 80
3.4.3 *In-situ* UV-Visible spectroscopy studies 84
3.4.4 Growth Mechanism 85
3.5 Comparison of growth of Au and Pt nanoparticles 86
3.6 Conclusion 87
Chapter 4: In-situ XAS studies on growth of Au-Pt bimetallic nanoparticle 89
4.1 Synthesis of Block copolymer stabilized Au-Pt bimetallic nanoparticle 91
4.2 *In-situ* studies during growth of Au-Pt bimetallic nanoparticles 91
4.2.1 *In-situ* XANES studies 92
4.2.2 *In-situ* EXAFS studies 96
4.2.3 *In-situ* UV-Visible spectroscopy studies 102
4.3 *Ex-situ* studies 103
4.3.1 Transmission Electron Microscopy 103
4.3.2 X-ray Photoelectron Spectroscopy 107
4.4 Growth of Au-Pt bimetallic nanoparticles 109

4.5 Comparison of growth of Au-Pt bimetallic nanoparticles with growth of Au and Pt monometallic nanoparticles 112

4.6 Conclusion 113

Chapter 5: In-situ XAS studies on growth of Cu nanoparticles 115

5.1 Synthesis of Cu nanoparticles 116

5.2 Flow setup for *in-situ* XAS studies 116

5.3 *In-situ* XANES study 119

5.3.1 Linear Combination Fitting 119

5.3.2 Principal Component Analysis 121

5.3.3 Multivariate Curve Resolution with Alternating Least Squares (MCR-ALS) 124

5.4 *In-situ* EXAFS study 127

5.5 *Ex-situ* XRD and TEM Measurements 129

5.6 Reduction Mechanism 131

5.7 Conclusion 131

Chapter 6: In-situ XAS studies on Fischer Tropsch reaction with Co catalysts 133

6.1 Synthesis of the catalyst 135

6.2 Fischer Tropsch Reaction 136

6.3 *In-situ* XAS-GC Setup for heterogenous catalysis 138

6.4 *In-situ* XAS studies during activation of the catalyst 140

6.5 *In-situ* XAS studies during Fischer Tropsch reaction 144

6.6 *In-situ* XAS studies during deactivation of the catalyst 145

6.7 Conclusion 151

Chapter 7: In-situ XAS studies during photocatalytic reduction of CO_2 using Cu doped TiO_2 catalyst 153

7.1 Synthesis of Cu doped TiO_2 photocatalyst 154

7.2 *In-situ* XAS-GC measurement setup for photocatalytic reactions 154

7.3 *In-situ* XAS studies during adsorption of CO_2 and water vapour 156

7.3.1 *In-situ* XAS studies at Ti K edge 156

7.3.2 *In-situ* XAS studies at Cu K edge 160

7.4 *In-situ* XAS studies during photocatalytic reduction of CO_2 164

7.4.1 *In-situ* XAS studies at Ti K edge 164

7.4.2 *In-situ* XAS studies at Cu K edge 168
7.5 Gas Chromatograph Measurements 173
7.6 Reaction Mechanism 173
7.7 Conclusion 175
Chapter 8: Conclusions and Future Work **177**
8.1 *In-situ* XAS studies during growth of nanoparticles 177
8.2 *In-situ* XAS studies during catalysis 179
8.3 Future work 181

SYNOPSIS

In-situ investigations on growth and structural changes in nanostructures by time-resolved EXAFS measurement

X-ray absorption spectroscopy (XAS), which comprises of both X-ray absorption near edge structure (XANES) and extended X-ray absorption fine structure (EXAFS) techniques is a powerful tool to determine the local structure of atoms in a material [1,2]. XANES gives information regarding valence state of an atom in a material, when measured alongwith some standard samples with unambiguous oxidation state of that particular element alongwith the test sample under the same experimental set-up, apart from some signature regarding the long range order in crystalline solids and coupling of valence levels in molecules. EXAFS, on the other hand gives quantitative information regarding bond distances, coordination number and disorder of the neighbouring shells of the absorbing atomic species which interact with the X-ray photons. It is an element specific technique which can be applied not only to crystals, but also to materials that possess little or no long-range translational order like amorphous systems, glasses, disordered films, membranes, solutions, liquids, metalloproteins and also for nanostructured materials and thin films. However, X-ray absorption measurements require an intense and energy-tuneable X-ray source like a synchrotron accelerator and also, by implementing specialised optical and mechanical design in the synchrotron beamline, it is possible to record an entire XAS spectrum with millisecond resolution. This establishes XAS or time–resolved XAS (TR-XAS) as a fast technique and one of the most suitable candidates to see the structural changes during a reaction as well as changes in the oxidation states of the metal cations *in-situ*.

"*In-situ*" is a Latin phrase which translates to the English meaning "On-Site". Therefore, these measurements focus on characterizing the system when some process is going on. Understanding the structural changes in materials during chemical processes remained a challenge for a long time. This is mainly because of the scarcity of suitable technique that can probe the system during evolution and provide necessary information to understand the evolution process. *In-situ* XAS studies are presently being carried out in various fields including nucleation and growth of nanoparticles [3], formation of thin films [4], catalytic reactions [5], photochemical processes [6], charging-discharging of batteries [7], etc. However, no technique is self sufficient and every technique helps us to understand only a part of the system. In case of complicated studies where many species are involved, the analysis and conclusion become very challenging. Therefore, it is always better to rely on more than one technique to have a broad and better understanding of the processes. With this point of view often several other techniques have been complemented with TR-XAS for simultaneous measurements to get a better insight into the reaction procedure. UV-Vis spectroscopy is often complemented with XAS measurement while studying the growth of nanoparticles [8]. This combination of techniques gives information not only about the local structure of different species in the solution but also about their optical properties. Similarly, Grunwaldt *et. al.* [9] have combined XRD and EXAFS with on line gas analysis and studied Cu based catalysts for methanol synthesis. The combination of XRD and EXAFS provided information regarding both long range and short range orders in the catalyst samples during the reaction. The online monitoring of the gaseous species during the *in-situ* XAS measurement of a catalytic process provides the exact information regarding the reaction which in turn decides the activity of the catalysts. Since TR-XAS gives information regarding structural changes in the catalyst, therefore, such a combined measurement can give insight into the structure-activity correlation of the catalyst system.

The present thesis work focuses on two areas of *in-situ* studies namely growth of nanoparticles and catalysis using synchrotron based XAS techniques along with the complementary experimental techniques. Nanoparticles have fascinated the scientific community over decades due to their interesting properties that is much different from their bulk counterpart. With the essence that shape and size of nanoparticles determines their properties comes the need to understand the mechanism of nucleation and growth of these particles. This envisages a new era of "*in-situ*" studies in the field of nanoscience. Recently several *in-situ* time-resolved XAS measurements have been carried out on nanoparticles synthesized by various routes [10,11]. Through these experiments the understanding of these processes have been improved which has ultimately helped to obtain a better yield and size distribution of the nanoparticles for various technological applications. Similarly, the structure-activity correlation has become an essence to understand the performance of catalysts. In recent years, lots of attempts have been made to use several experimental techniques or combination of techniques which would help to get an insight into this [5]. *In-situ* measurements have become inevitable in the field of catalysis as they provide the exact information during the catalysis process which gives a better outlook regarding the activity and selectivity of catalysts, and also addresses the problem of deactivation of the catalyst. Recently, several *in-situ* EXAFS measurements have been done on various catalyst system to understand their structure-activity correlation [12,13].

Chapter 1 of the thesis gives a brief introduction and motivation behind the work carried out under this PhD programme. This chapter begins with an introduction of X-ray absorption spectroscopy and time resolved X ray absorption spectroscopy. Subsequently works reported in the litertautes on the two areas of research where TR-XAS has been emploiyed in this thesis work viz., *in-situ* studies on growth of nanoparticles and *in-situ* studies on catalytic processes have been discussed in details. . Reports where other *in-situ* techniques have also been employed alongwith TR-XAS have also been covered in the above discussion. In summary the contents of this chapter provides the basis for the works presented in subsequent chapters.

Chapter 2 describes the details of different experimental techniques used in this thesis work. The conventional XAS measurement takes almost an hour to measure one complete spectrum with an acceptable signal to noise ratio and a reasonable energy range. Therefore, the conventional step-wise scanning measurement is not at all suitable for time resolved studies which needs second or millisecond resolution for data acquisition. With improvements in machine performance and fast data acquisition systems, the XAFS spectra could be measured in seconds [5].The two modes of measuring fast EXAFS spectra are: Quick EXAFS (QEXAFS) and Dispersive EXAFS (DEXAFS), which have been discussed briefly. The in-situ XAS experiments on growth of nanoparticles have been done in this thesis work at the energy dispersive EXAFS beamline (BL-08) at Indus 2, RRCAT, Indore [14], while the *in-situ* XAS experiment on catalytic processes have been carried out using the quick EXAFS facility at energy scanning EXAFS beamline (BL-09) at Indus 2, RRCAT, Indore [15]. The optical and mechanical layouts of both the beamlines have been discussed in this chapter. Other *in-situ* and *ex-situ* experimental techniques used in this thesis work viz., UV visible spectroscopy, Gas chromatography, X-ray photoelectron spectroscopy, Transmission electron microscopy, High Resolution Transmission electron microscopy are also briefly discussed. Finally the data reduction and data analysis procedure of EXAFS signal is described elaborately which involves extensive use of the IFEFFIT software package including ATHENA and ARTEMIS subroutines [16].

Chapter 3 discusses the *in -situ* study of growth of Au and Pt monometallic nanoparticles. A set-up has been developed at the energy dispersive EXAFS beamline (BL-08), mentioned above, for *in-situ* XAS measurements on chemical processes using a specially designed teflon cell with one optical path for X-ray in the direction of synchrotron beam and another in the perpendicular direction for visible radiation. Using the above set-up the growth of Au and Pt nanoparticles from their respective chloride precursors using block copolymer based reduce-cum-stabilizer have been studied by simultaneous *in-situ* measurement of XAS and UV-Vis spectroscopy. The growth kinetics of both types of nanoparticles are found to follow the three stages viz., (i) reduction of metal ions by block copolymer and formation of small cluster of typical 5 coordinations, (ii) absorption of block copolymer and reduction of metal ions on the surface of the cluster and increase in cluster size and (iii) growth of gold nanoparticles stabilized by block copolymer. The stages of the growth of Au and Pt nanoparticles as obtained by *in-situ* XAS measurements are also corroborated by simultaneous in-situ measurement of UV-Vis spectroscopy.

Chapter 4 focusses on the growth of Au@Pt core shell nanoparticles. Au-Pt bimetallic nanoparticles have been synthesized through a one-pot synthesis route from their respective chloride precursors using block copolymer as a stabilizer. Growth of the nanoparticles has been studied by simultaneous *in-situ* measurement of X-ray Absorption Spectroscopy (XAS) and UV-Vis spectroscopy at the energy dispersive EXAFS beamline (BL-08) mentioned above. *In-situ* XAS spectra have been measured simultaneously at Au and Pt L_3 edges. While the XANES spectra of the precursors give real time information on the reduction process, the EXAFS spectra reveal the structure of the clusters formed at the intermediate stages of growth. The insight into the formation process throws light on how the difference in the reduction potential of the two precursors could be used to get the core-shell type configuration of bimetallic alloy in an one–pot synthesis method. The core-shell type structure of the nanoparticles have also been confirmed by *ex-situ* Energy Dispersive Spectroscopy (EDS) line scan and X-ray photo-electron spectroscopy (XPS) measurements with *in-situ* ion etching on fully formed nanoparticles.

The growth of noble metal nanoparticles has been discussed in chapters 3 and 4 as mentioned above. However, studying the growth of transition metal nanoparticles are more challenging as the synthesis may require special environment. Chapter 5 discusses the growth of Cu nanoparticles using a flow setup. Cu nanoparticles have been synthesized from copper acetate using $NaBH_4$ as a reducing agent and PVP as a stabilizing agent under an inert ambience. *In-situ* time-resolved X-ray absorption spectroscopy measurements have been carried out in a specially designed measurement cell during the formation of Cu nanoparticles using a specialized computer controlled flow setup. Principal Component Analysis (PCA) and Multivariate Curve Resolution with Alternating Least Squares (MCR-ALS) analysis have been successfully applied to the time-resolved Cu K-edge XANES data recorded during the growth of Cu nanoparticles. PCA of the XANES spectra predicted three chemical species present in the reaction solution including an intermediate species apart from the initial and the product species. From MCR-ALS analysis of the Cu K-edge XANES spectra, the oxidation state of the reaction intermediate species and the concentration profile of the constituents during the reactions have been determined. Finally the EXAFS spectra of the intermediate species has been extracted and analyzed to predict the local structure of Cu cations in this species.

As has been mentioned above, one of the major applications of TR-EXAFS is in *in-situ* studies of catalytic processes. Chapter 6 deals with the *in-situ* EXAFS study of Fischer Tropsch (FT) reaction of methane (CH_4) generation from CO and H_2 using Co based catalyst. Simultaneous gas chromatograph (GC) measurements during the FT reaction facilitate the monitoring of the product gases, which in turn gives information regarding the activity of the catalyst. The combination of XAS and GC experimental techniques has been used to correlate the structural changes with activity of the catalyst at different reaction temperatures. Intially the reduction process of the catalyst at 400°C under H_2 ambient has been studied by *in-situ* XANES and EXAFS measurements. Subsequently, the deactivation of the Co catalyst has also been studied for 10 hours at 320 ºC and an attempt has been made to understand the process of deactivation. From the XANES and EXAFS analysis, it has been obvious that there is no formation of CoO phase in the catalyst which may be responsible for the deactivation of the catalyst. Therefore, there is a strong possibility that the deactivation of the catalyst is caused due to coke formation on the surface of the catalyst, which has subsequently been confirmed from ex-situ Raman spectroscopy measurement.

Similarly, Chapter 7 discusses the structural changes of Cu doped TiO_2 catalysts during the photocatalytic reduction of CO_2 and splitting of water and subsequent generation of methane (CH_4). The 5% and 10 % Cu doped TiO_2 catalyst samples are irradiated with UV-Vis source in a specially designed reaction cum measurement cell which consists of quartz and glass windows for UV-Visible radiation in addition to the Kapton windows for X ray transmission. CO_2 and water vapour have been inserted into the cell and the photocatalysis reaction has been monitored for 10-12 hours. From the XANES analysis, it has been seen that the effective charge of Cu cations decreases in both the catalyst samples during the photocatalysis reaction. *In-situ* EXAFS spectra also suggest structural changes in the catalyst samples during the photocatalysis reaction.

Finally in Chapter-8 the conclusions obtained from each study performed under this thesis work are summarized and future directions of the works have been mentioned.

References:

1. D. C. Konigsberger and R. Prins, *X ray Absorption: Principles, Applications, Techniques of EXAFS, SEXAFS and XANES*. (Wiley, New York, 1988).
2. Grant Bunker, *Introduction to XAFS: A practical guide to X ray Absorption Fine Structure Spectroscopy*. (Cambridge University Press, 2010).
3. Dorota Koziej, Chem. Mater. 28, (2016) 2478–2490.
4. R. Frahm, T. W. Barbee, Jr., W. Warburton, Physical Review B 44, (1991) 2822-2825.
5. Mark A. Newton, Andrew J. Dent, John Evans,Chem. Soc. Rev. 31, (2002) 83-95.
6. M. Harada, Y. Inada, Langmuir 25, (2009) 6049-6061.
7. Yoshinari Makimura, Tsuyoshi Sasaki, Hideaki Oka, Chikaaki Okuda, Takamasa Nonaka, Yusaku F. Nishimura, Shigehiro Kawauchi, Yoji Takeuchi, J. Electrochem. Soc. 163, (2016) A1450-A1456.
8. Jan Stötzel, Dirk Lutzenkirchen-Hecht, Ronald Frahm, Celso Valentim Santilli,Sandra Helena Pulcinelli, Renata Kaminski, Emiliano Fonda, Francoise Villain, Valerie Briois**,**.J. Phys Chem C 114, (2010) 6228-6236.
9. J.D. Grunwaldt, B. S. Clausen. Topics in Catalysis 18, (2002) 37-43.
10. J. Ohyama, K. Teramura, Y. Higuchi, T. Shishido, Y. Hitomi, K. Kato, H. Tanida, T. Uruga, T. Tanaka, Chem. Phys. Chem. 12, (2011) 127-131.
11. M. Harada, Y. Inada, M. Nomura, Journal of Colloid and Interface Science 337, (2009) 427–438.
12. Alexey Voronov, Nikolaos E. Tsakoumis, Nina Hammer, Wouter van Beek, Hermann Emerich, Magnus Rønning, Catalysis Today 229, (2014) 23-33.
13. Mark A. Newton, Carolina Belver-Coldeira, Arturo Martinez-Arias, Marcos Fernandez-Garcia, Nature materials 6, (2007) 528-532.
14. D. Bhattacharyya, A. K. Poswal, S. N. Jha, Sangeeta, S. C. Sabharwal, *Nucl. Instrum. Meth. Phys. Res.A* 609**,** (2009) 286-293.
15. S. Basu, C. Nayak, A. K. Yadav, A. Agrawal, A. K. Poswal, D. Bhattacharyya, S. N. Jha, N. K. Sahoo, J. Phys.: Conf. Ser. 493, (2014) 012032.
16. M. Newville, B.Ravel, D. Haskel, J.J. Rehr, E.A. Stern and Y. Yacoby. Physica B 154 (1995) 208.

List of Figures

Figure 1.1: Photo absorption cross section for different phenomenon of interaction of X-ray with matter. 7

Figure 1.2: A typical XAS spectrum 9

Figure 1.3: Cr K edge XANES spectra of standard Cr metal and oxides. 11

Figure 1.4: Schematic of scattering. 14

Figure 1.5: Typical characteristic of photoelectron mean free path vs. wave number. 17

Figure 1.6: Schematic of QEXAFS monochromator (Taken from Ref. 37) 22

Figure 1.7: Schematic optical lay-out of a typical Dispersive EXAFS set-up. 22

Figure 2.1: Indus-2 Synchrotron Source (2.5 GeV, 100 mA) at Raja Ramanna Centre for Advanced Technology (RRCAT), Indore, India 32

Figure 2.2: Working principle of the Energy Dispersive EXAFS beamline (BL-08) at Indus-2 SRS 33

Figure 2.3: Optical layout of BL-08. 33

Figure 2.4: Photograph of the Energy Dispersive EXAFS beamline (BL-08). 36

Figure 2.5: Schematic layout of Scanning EXAFS Beamline BL-09. 37

Figure 2.6: Photograph of (a) optics hutch and (b) experimental station of Scanning EXAFS 38

Figure 2.7: Experimental set-up for transmission mode of EXAFS measurement. 38

Figure 2.8: Experimental set-up for fluorescence mode of XAFS measurement. 39

Figure 2.9: The main window of ATHENA program. 47

Figure 2.10: Pre-edge, post-edge polynomial and background subtraction. 48

Figure 2.11: *k* space EXAFS spectrum with hanning window. 49

Figure 2.12: Fourier transformed EXAFS spectra alongwith real and imaginary contribution. 49

Figure 2.13: Main window of ARTEMIS program. 52

Figure 2.14: Schematics of UV Visible spectrophotometer. 54

Figure 2.15: Schematics of Fiber optics based UV Visible spectrometer 55

Figure 2.16: (a) Photograph of Avalight DHc light source (b) Photograph of AvaSpec-ULS2048L-USB2 Fiber optics based UV Visible spectrometer 56

Figure 2.17: Photograph of Gas Chromatograph (Make: Netel India Ltd.). 57

Figure 2.18: Schematics of autosampling valve working principal. 58

Figure 2.19: Photograph of X-ray diffractometer (Bruker D8 Advance diffractometer). 59

Figure 2.20: Block diagram of XPS instrument. 60

Figure 2.21: Photograph of XPS instrument. 61

Figure 2.22: Photograph of the Transmission Electron Microscope (CM200) used in this thesis work. 62

Figure 3.1: Changes in colour of (a) Au nanoparticle precursor solution and (b) Pt nanoparticle precursor solution with time after mixing the reducers. 65

Figure 3.2: (a) TEM micrograph of fully formed Au nanoparticles (b) TEM micrograph of fully formed Pt nanoparticles 66

Figure 3.3: Schematic diagram of the experimental setup for simultaneous time resolved EXAFS measurement and UV-Visible absorption measurement of one-pot synthesis processes. 68

Figure 3.4: Photograph of the experimental setup for simultaneous time resolved EXAFS measurement and UV-Visible absorption measurement of one-pot synthesis processes. 68

Figure 3.5: *In-situ* XANES spectra measured at Au L_3 edge at different time intervals during growth of Au nanoparticles 70

Figure 3.6: Linear combination fit results of *in-situ* XANES spectra at Au L_3 edge recorded during growth of Au nanoparticles. Inset: linear combination fitting of selected data. 70

Figure 3.7: *In-situ* EXAFS $\chi(k)$versus k spectra measured at Au L_3 edge at different time intervals during growth of Au nanoparticles 72

Figure 3.8: *In-situ* EXAFS $|\chi(r)|$ versus r spectra measured at Au L_3 edge at different time intervals during growth of Au nanoparticles 73

Figure 3.9: *In-situ* EXAFS Re[$\chi(r)$] versus r spectra measured at Au L_3 edge at different time intervals during growth of Au nanoparticles 73

Figure 3.10: Variation of Au and Cl co-ordinations around Au sites and particle size obtained from EXAFS measurements during growth of Au nanoparticles. 74

Figure 3.11: UV-Vis spectra recorded in the wavelength range of 400-800 nm at different time intervals during growth of Au nanoparticles. 76

Figure 3.12: Variation of intensity and position of the Au surface plasmon peak in the UV-Vis spectra measured during growth of Au nanoparticles. 76

Figure 3.13: *In-situ* XANES spectra measured at Pt L_3 edge at different time intervals during growth of Pt nanoparticles 79

Figure 3.14: Linear combination fit results of *in-situ* XANES spectra at Pt L_3 edge recorded during growth of Pt nanoparticles. Inset: linear combination fitting of selected data. 80

Figure 3.15: *In-situ* EXAFS $\chi(k)$versus k spectra measured at Pt L_3 edge at different time intervals during growth of Pt nanoparticles 81

Figure 3.16: *In-situ* EXAFS $|\chi(r)|$ versus r spectra measured at Pt L_3 edge at different time intervals during growth of Pt nanoparticles 82

Figure 3.17: EXAFS fitting of the experimental $|\chi(r)|$ versus r data at few selected time intervals during the growth of Pt nanoparticles. 83

Figure 3.18: Variation of Pt and Cl co-ordinations around Pt sites and particle size obtained from EXAFS measurements during growth of Pt nanoparticles. 83

Figure 3.19: UV-Vis spectra recorded in the wavelength range of 300-600 nm at different time intervals during growth of Pt nanoparticles. 84

Figure 3.20: Variation of intensity of absorption at 328, 394 and 450 nm in the UV-Vis spectra measured during growth of Pt nanoparticles. 85

Figure 4.1: Photographs showing colour of the solution at different stages during formation of Au@Pt core shell nanoparticles. 91

Figure 4.2: *In-situ* XANES spectra at (a) Au and (b) Pt L_3 edge recorded at different time intervals during the growth of Au@Pt nanoparticles. 94

Figure 4.3: Linear combination fit results of *in-situ* XANES spectra at (a) Au and (b) Pt L_3 edge recorded during growth of Au@Pt nanoparticles. 95

Figure 4.4: Linear combination fitting of *in-situ* XANES spectra at selected time interval at (a) Au and (b) Pt L_3 edge recorded during growth of Au@Pt nanoparticles. 96

Figure 4.5: *In-situ* X ray absorption spectra at Pt and Au L_3 edges recorded at different time intervals during growth of Au@Pt nanoparticles. 97

Figure 4.6: $\chi(r)$ versus r plot (FT-EXAFS spectra) measured at (a) Au and (b) Pt L_3 edge recorded at different time intervals during growth of Au@Pt nanoparticles. 99

Figure 4.7: Variation of co-ordination numbers of (a) Au-Cl, Au-Au, Au-Pt bonds and (b) Pt-Cl bonds as a function of reaction time during growth of Au@Pt nanoparticles. 100

Figure 4.8: *In-situ* UV-Vis spectra recorded at different time intervals during growth of Au@Pt nanoparticles. 104

Figure 4.9: TEM image of Au-Pt bimetallic particle 105

Figure 4.10: Particle size histogram of Au-Pt bimetallic particles 105

Figure 4.11: (a) HR-STEM micrograph and (b) EDS line scan on fully formed Au-Pt bi-metallic nanocrystal. 106

Figure 4.12: a) XPS Spectra of Au-4f with different sputtering time 0 min, 1 min, 15 min, 45 min and 105 min. (b)XPS Spectra of Pt-4f with different sputtering time 0 min, 1 min, 15 min, 45 min and 105 min. (c) Variation of intensity as a function of sputtering time of the Au-$4f_{7/2}$ XPS peak after background correction using a Shirley Background and normalisation w.r.t. the intensity after 105 min. etching and (d) Variation of intensity as a function of sputtering time of the Pt-4f $_{7/2}$ XPS peak after background correction using a Shirley Background and normalisation w.r.t. the intensity after 105 min. etching. 108

Figure 5.1: Schematics of Flow setup for *in-situ* XAS studies 117

Figure 5.2: Photograph of the Reaction Vessel and *in-situ* XAS measurement cell 118

Figure 5.3: *In-situ* XANES spectra of the reaction solution measured at Cu K edge at different time intervals after mixing reducer in the precursor solution. Inset (a): Derivative of XANES spectra recorded during synthesis of Cu nanoparticles Inset (b): 1 sec., 750 sec. and 1 hr. spectra shown separately. 120

Figure 5.4: XANES spectra of Cu Metal, Cu_2O and CuO standards. 120

Figure 5.5: Linear Combination Fitting of the 550 s experimental data using different combination of Cu Metal, Cu_2O and CuO standards. 122

Figure 5.6: First five components of PCA analysis of the TR-XANES spectra recorded during growth of Cu nanoparticles. 123

Figure 5.7: Fit residuals of the two, three and four Principal Component fitting of the TR-XANES spectra recorded during growth of Cu nanoparticles. 123

Figure 5.8: Constituent spectra predicted by MCR-ALS analysis of the TR-XANES spectra recorded during growth of Cu nanoparticles. 126

Figure 5.9: Concentration profiles of the constituents as determined by MCR-ALS analysis of the TR-XANES spectra recorded during growth of Cu nanoparticles. 126

Figure 5.10: LCF fitting of the experimental XANES spectra using the MCR-ALS predicted constituent spectra as standards. 127

Figure 5.11: The FT-EXAFS spectra of the three constituent species of the reaction solution as predicted by MCR-ALS analysis of the TR-XANES data. 128

Figure 5.12: *Ex-situ* XRD spectra of the Cu nanoparticles. 130

Figure 5.13: *Ex-situ* TEM micrograph of the Cu nanoparticles. 130

Figure 6.1: XRD data of the as prepared Co_3O_4/SBA-15 catalyst. 136

Figure 6.2: Schematic of the experimental setup for *in-situ* XAS-GC measurement during heterogenous catalysis along with the photograph of the reaction cum measurement cell. 140

Figure 6.3: (a) *In-situ* XANES spectra recorded at different temperatures during the reduction of the as-prepared oxide catalyst sample. Inset: XANES spectra of Co standards i.e., Co_3O_4, CoO and Co metal. (b) *In-situ* XANES spectra recorded at 400 ºC at different time intervals during the reduction of the as-prepared oxide catalyst sample. 142

Figure 6.4: (a) *In-situ* EXAFS spectra recorded at different temperatures during the reduction of the as-prepared oxide catalyst sample. Inset: EXAFS spectra of Co standards i.e., Co_3O_4, CoO and Co metal.(b) *In-situ* EXAFS spectra recorded at 400 ºC at different time intervals during the reduction of the as-prepared oxide catalyst sample. 143

Figure 6.5: Variation in the EXAFS radial distribution function of the catalyst sample undergoing FT reaction at different temperatures. 144

Figure 6.6: Variation in the $\chi(k)$versus k spectra of the catalyst sample undergoing FT reaction at different temperatures. 145

Figure 6.7: CO conversion percentage at 280ºC and at 320ºC with time. 146

Figure 6.8: Gas chromatograph data showing the variation in methane peak intensity. Inset: Gas chromatograph data showing the variation of CO peak intensity. 146

Figure 6.9: *In-situ* XANES spectra recorded during the deactivation of the catalyst at 320ºC. 147

Figure 6.10: Results of Linear combination fitting of the *in-situ*XANES spectra recorded during the deactivation of the catalyst at 320ºC with metallic Co and CoO as standards. 148

Figure 6.11: *In-situ* EXAFS spectra recorded during the deactivation of the catalyst at 320ºC. Inset: Enlarged view of the peak at 2 Å in the *in-situ* EXAFS spectra recorded during the deactivation of the catalyst at 320ºC 148

Figure 6.12: *Ex-situ* Raman spectrum of the deactivated catalyst 151

Figure 7.1: Schematic Diagram of the experimental setup for *in-situ* XAS measurement during photocatalytic reactions along with the photograph of the reaction cell. 155

Figure 7.2: Actual photograph of the experimental setup for *in-situ* XAS measurement during photocatalytic reactions. 156

Figure 7.3: (a) *In-situ* XANES spectra measured at Ti K edge during the adsorption of CO_2 and water vapour on Cu5 catalyst sample. Inset: Ti K edge XANES spectrum of anatase TiO_2 (b) *In-situ* XANES spectra measured at Ti K edge during the adsorption of CO_2 and water vapour on Cu10 catalyst sample. 158

Figure 7.4: (a)*In-situ* EXAFS spectra measured at Ti K edge during the adsorption of CO_2 and water vapour on Cu5 catalyst sample. (b) *In-situ* EXAFS spectra measured at Ti K edge during the adsorption of CO_2 and water vapour on Cu10 catalyst sample. Open circles: experimental data and solid lines: best theoretical fit. 159

Figure 7.5: (a) *In-situ* XANES spectra measured at Cu K edge during the adsorption of CO_2 and water vapour on Cu5 catalyst sample. Inset: enlarged view of the absorption edge (b) *In-situ* XANES spectra measured at Cu K edge during the adsorption of CO_2 and water vapour on Cu10 catalyst sample. Inset: enlarged view of the absorption edge. 162

Figure 7.6: *In-situ*EXAFS spectra measured at Cu K edge during the adsorption of CO_2 and water vapour on Cu5 catalyst sample. (b) *In-situ* EXAFS spectra measured at Cu K edge during the adsorption of CO_2 and water vapour on Cu10 catalyst sample. Open circles : experimental data and solid lines: best theoretical fit. 163

Figure 7.7: (a) *In-situ* XANES spectra measured at Ti K edge of Cu5 catalyst sample during the photocatalytic reduction of CO_2. Inset: enlarged view of pre-edge peaks (b) *In-situ* XANES spectra measured at Ti K edge of Cu10

catalyst sample during the photocatalytic reduction of CO_2. Inset: enlarged view of pre-edge peaks. 165

Figure 7.8: (a)*In-situ* EXAFS spectra measured at Ti K edge of Cu5 catalyst sample during the photocatalytic reduction of CO_2. (b) *In-situ*EXAFS spectra measured at Ti K edge of Cu5 catalyst sample during the photocatalytic reduction of CO_2. Rounds: experimental data and solid lines: best theoretical fit. 166

Figure 7.9: (a) *In-situ* XANES spectra measured at Cu K edge of Cu5 catalyst sample during the photocatalytic reduction of CO_2. (b) *In-situ* XANES spectra measured at Cu K edge of Cu10 catalyst sample during the photocatalytic reduction of CO_2. 169

Figure 7.10: *In-situ* XANES spectra measured at Cu K edge of Cu5 and Cu 10 catalyst sample at some selected time intervals during the photocatalytic reduction of CO_2. 170

Figure 7.11: (a)*In-situ*EXAFS spectra measured at Cu K edge of Cu5 catalyst sample during the photocatalytic reduction of CO_2. (b) *In-situ*EXAFS spectra measured at Cu K edge of Cu5 catalyst sample during the photocatalytic reduction of CO_2. Open circles : experimental data and solid lines: best theoretical fit. 171

Figure 7.12: Concentration of CH_4 produced during the photocatalytic reduction of CO_2. 173

List of Tables

Table 4.1: Au L_3 edge EXAFS Fitting Results 98

Table 4.2: Pt L_3 edge EXAFS Fitting Results 101

Table 6.1: Co K edge EXAFS fitting results during the deactivation of the catalyst at 320ºC. 149

Table 7.1: Ti K edge EXAFS fitting of Cu doped TiO_2 samples during adsorption of CO_2 and water vapour 160

Table 7.2: Cu K edge EXAFS fitting of Cu doped TiO_2 samples during adsorption of CO_2 and water vapour 164

Table 7.3: Ti K edge EXAFS fitting of Cu5 sample during the photocatalytic reduction of CO_2 167

Table 7.4: Ti K edge EXAFS fitting of Cu10 sample during the photocatalytic reduction of CO_2 167

Table 7.5: Cu K edge EXAFS fitting of Cu5 sample during the photocatalytic reduction of CO_2 172

Table 7.6: Cu K edge EXAFS fitting of Cu10 sample during the photocatalytic reduction of CO_2 172

Chapter 1

Introduction

In recent years X-ray absorption spectroscopy (XAS) or X-ray absorption fine structure (XAFS) has emerged as a popular structure determining technique for a wide range of materials. Though the fine structures in the X-ray absorption spectrum of an element residing within a material, above its X-ray absorption edge was first observed by Hugo Fricke in 1920, it was established as a practical tool in 1970 by Stern, Sayers, and Lytle who formulated the theory of X-ray absorption fine structure (XAFS)[1, 2].

However, this technique has become popular only with the advent and easy availability of modern Synchrotron sources. One of the pre requisite of EXAFS measurement is the availability of an intense and energy-tunable X-ray source. The background radiation from a laboratory based X-ray tube source offers a very weak tunable X-ray continuum and this had been a serious limitation in obtaining XAFS spectrum of reasonable quality till a long time. The availability of modern bright Synchrotron radiation sources since 1970's, has removed this experimental difficulty and since then XAFS has emerged out to be one of the most powerful tools for local structure determination. Presently many Synchrotron sources around the world are operational round the clock. Some examples are Spring 8 (8 GeV) in Japan, ESRF (6 Gev) in France, APS (7GeV) in USA, etc. Most of the Synchrotron facilities have several beamlines for XAFS measurements which are being used extensively by researchers from various fields.Another important advantage of XAS over other structure determining experimental techniques like X-Ray Diffraction, isthat it is an element specific technique which can be applied not only to crystals, but also to materials that possess little or no long-range translational order like amorphous systems, glasses, disordered films, membranes, solutions, liquids, metalloproteins and also for nanostructured materials and thin films.The XAS spectra comprises of both X-ray absorption near edge structure (XANES) and extended X-ray absorption fine structure (EXAFS)[3, 4]. XANES gives information regarding valence state of an atom in a material, when measured alongwith some standard samples with unambiguous oxidation state of that particular element alongwith the test sample under the same experimental set-up, apart from some signature regarding the long range order in crystalline solids and coupling of valence levels in molecules. EXAFS, on the other hand is the extended region of the absorption edge (above 50 eV) and gives quantitative information regarding bond distances, coordination number and disorder of the neighboring shells of the absorbing atomic species which interact with the X-ray photons.

Conventional X-ray absorption measurements require step-wise scanning of an energy range of 1000 eV using a monochromator and this takes approximate time of 20 minutesfor a single scan. Therefore, it is known as a slow technique, however, by implementing specialised optical and mechanical design in the synchrotron beamlines and with fast data acquisition systems, it is possible to record an entire XAS spectrum with millisecond resolution. This establishes XAS or time–resolved XAS (TR-XAS) as a fast technique and one of the most suitable candidates to see the structural changes during a reaction as well as changes in the oxidation states of the metal cations *in-situ*. "*In-situ*" is a Latin phrase which translates to the English meaning "On-Site". Therefore, these measurements focus on characterizing the system when some process is going on.

Understanding the structural changes in materials during chemical processes remained a challenge for a long time. This is mainly because of the scarcity of suitable technique that can probe the system during evolution and provide necessary information to understand the evolution process. UV-Vis spectroscopy is one of the most popular and oldest techniques to study the kinetics of growth. Many studies have been done where depending on the intensity of the Surface Plasma Resonance (SPR) peak of nanoparticles, the growth kinetics has been predicted. For example, Mizutani *et. al.* investigated the growth of gold nanoparticles synthesized by solution plasma sputtering method by *in-situ* UV-Vis measurement[5]. However, this technique is limited to systems which give absorption in this particular wavelength range. Also, this can only throw light on the kinetics of reaction and is insufficient to reveal the structural changes during the reaction. Transmission Electron Microscopy (TEM)is also another popular technique that can be used *in-situ*to study the changes in particle size during nucleation and growth[6, 7]. However, *in-situ* TEM has the limitation that the electron beam can interfere with the reacting species thus changing the whole redox reaction process to be studied. Similarly, Infrared and Raman spectroscopies have been widely used for *in situ* studies during homogenous and heterogenous catalysis[8, 9]. However, these techniques can only be used to probe systems which are IR or Raman active.

X-ray based techniques, on the other hand, generally are not system specific and in most of the cases, they do not alter the processes to be studied. With the advent of synchrotron based techniques, many X-ray based experiments are being carried out *in-situ* to investigate the growth of nanoparticles. Tay *et. al.*[10] observed the growth and nucleation of electrodeposited ZnO nanostructures using a Transmission X-ray Microscope (TXM). TXM has the same advantages and requirements as TEM. The only relaxation is the dimension of the liquid cell in TXM can be of the order of millimeters, while for TEM it is of the order of hundred nanometers. Small angle X-ray scattering (SAXS) is another important X-ray based technique which can act as a substitute of TEM measurements revealing the changes in particle size during growth and nucleation [11, 12]. The above techniques mostly yield information on real time changes in particle sizes only and cannot throw light on the structural evolution during a process. Also these techniques cannot find out the coordination of atoms in clusters which are formed in the initial phase of the growth and act as seeds for further growth of the nanoparticles. In this regard X-ray absorption spectroscopy (XAS) has played a crucial role in giving structural insight into reaction process from a very different aspect as compared to the other popular *in-situ* techniques since it can simultaneously give insight into the structural changes in the species during growth of nanoparticles as well as in the oxidation states of the metal cations. X ray Diffraction (XRD) is another popular structure determining technique for *in-situ* studies[13], however this can be used only for samples with long range order. On the other hand, XAS provides the local structure information and can be used for samples without any long range order. However, in some cases the high intensity of the synchrotron radiation, which is often used as a X ray source for different X-ray based experimental techniques, induces changes in the samples to be studied[14-16] and this aspect should be taken care of while using synchrotron based X-ray sources as a probe for *in situ* studies.

In-situ XAS studies are presently being carried out in various fields including nucleation and growth of nanoparticles[17], formation of thin films[18] , catalytic reactions[19] , photochemical processes[20], charging-discharging of batteries[21], etc. Despite the several advantages that has popularized *in-situ* XAS, some challenges are still there that need to be dealt with. One of the major disadvantages of all X-ray based techniques is that they give an ensemble average information. Therefore, if many species are present in the sample which is the case for most reactions to be studied *in-situ*, it is very difficult to identify them. Though analysis tools like

Principal Component Analysis (PCA) and Multivariate Curve Resolution- Alternate Least Square (MCR-ALS) help to identify reaction intermediates but they also have limitations. Therefore, several other techniques have also been complemented with time resolved XAS for simultaneous measurements to get a better insight into the reaction procedure. For example, UV-Vis spectroscopy is often complemented with XAS measurement while studying the growth of nanoparticles[22]. This combination of techniques gives information not only about the local structure of different species in the solution but also about their optical properties. Shannon *et. al.*[23] complemented XAS with XRD to study solid-liquid catalytic reactions to get information on short range and long range structural changes. Tromp *et. al.*[24] have carried out XAS and UV-Vis spectroscopy simultaneously. Raman, UV-Vis and XANES have been used simultaneously by Briois *et. al.*[25] while *in-situ* XAFS, IR and mass spectroscopy have been combined for heterogeneous catalysis studies by Newton *et. al.*[26]. Complementary techniques give a broader view of the system and focus on different aspects of it which in turn results in more consolidated conclusions.

The present thesis work focuses on two applications of *in-situ* studies namely growth of nanoparticles and catalysis using synchrotron based XAS techniques along with the complementary experimental techniques. Nanoparticles have fascinated the scientific community over decades due to their interesting properties that is much different from their bulk counterpart. With the essence that shape and size of nanoparticles determines their properties comes the need to understand the mechanism of nucleation and growth of these particles. This envisages a new era of "*in-situ*" studies in the field of nanoscience. Recently several *in-situ* time-resolved XAS measurements have been carried out on nanoparticles synthesized by various routes[27, 28]. Through these experiments the understanding of these processes have been improved which has ultimately helped to obtain a better yield and size distribution of the nanoparticles for various technological applications. Similarly, the structure-activity correlation has become an essence to understand the performance of catalysts. In recent years, lots of attempts have been made to use several experimental techniques or combination of techniques which would help to get an insight into this[19]. *In-situ* measurements have become inevitable in the field of catalysis as they provide the exact information during the catalysis process which gives a better outlook regarding the activity and selectivity of catalysts, and also addresses the problem of deactivation of the catalyst. Recently, several *in-situ* EXAFS measurements have been done on various catalyst system to understand their structure-activity correlation[29, 30]. A survey of recent literatures on this has been presented later in this chapter and also in Chapter-6 of this thesis.

1.1 X-ray Absorption Spectroscopy

X-ray can interact with material either by scattering or absorption phenomena. Interaction of X-ray with matter (Fig. 1.1) is primarily divided in three processes depending on energy of X-ray and the elemental composition: Thomson scattering, Compton scattering and Photoelectric effect.

Thomson scattering is an elastic scattering of photons by the free or bound charged particles (electrons) in the medium. For most of the materials Thomson scattering is dominant when the energy of the photon is less. According to classical theory, in the low-energy limit, the electric field of the incident wave (photon) accelerates the charged particle, causing it, in turn, to emit radiation at the same frequency as the incident wave. Thus, the particle is behaving like small radiating dipole, consequently emitting radiation. Compton scattering is the result of a high-energy photon colliding with a free electron or with an atom having loosely bound electrons. The scattered radiation experiences a wavelength or energy shift due to transfer of momentum to the electron. Compton scattering is purely quantum mechanical phenomena, which can be explained by assuming particle nature of light.

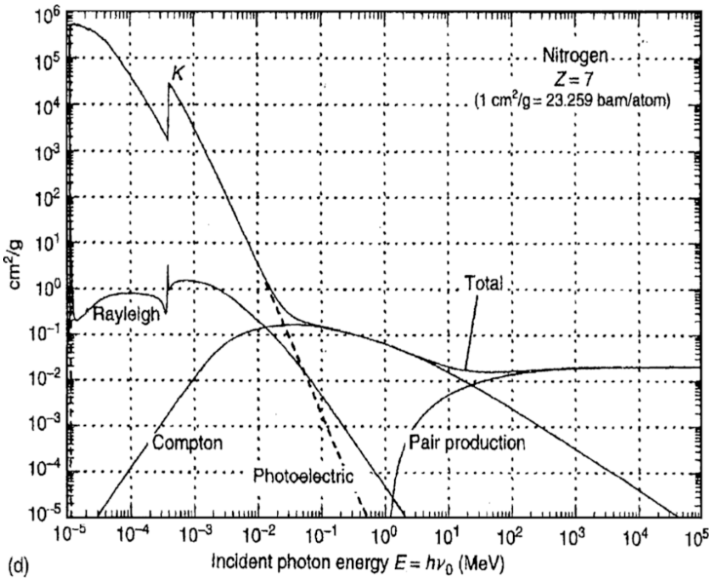

Figure 1.1: Photo absorption cross section for different phenomenon of interaction of X-ray with matter[31].

In photoelectric process an X-ray is absorbed by an atom ejecting a core level electron (K, L or M shell) out of the atom and into the continuum. This phenomenon occurs when energy of the incident photon matches with the binding energy of one of the core level electron. The atom is then left in an excited state with an empty electronic level (a core hole). The electron ejected from the atom is called the photo electron and this phenomenon is known as photo electric effect. Following the photoelectric effect, secondary processes such as emission of fluorescence or Auger electrons can also occur. The excited core hole will relax back to a ground state by another core level electron jumping into the ground level. This can be accompanied by either emission of X-ray in which excess energy of electron is emitted as X-ray called fluorescence or ejection of electron in which excess energy is transferred to another core level electron and prompting that electron to emit out of the material is called Auger emission. In the hard X-ray regime (> 2 keV), X-ray fluorescence is more likely to occur than Auger emission, but for lower energy X-ray absorption, Auger processes dominate[32].

In different energy regime of X-ray, the probabilities of occurrence of the above processes are different and it is defined by absorption cross section which represents the probability of a specific type of X-ray interaction with matter. Fig. 1.1 depicts the cross section of different processes while interaction of X-ray with matter. In general, the absorption cross section smoothly decreases as the energy increases as $\sim E^{-3}$, however at specific energies there are sharp increase in absorption cross section, defined as X-ray absorption edge. These absorption edges occur due to photoelectric effect i.e. when energy of incident X-ray photon matches with binding energy of one of the core level electron and it knocks out this electron by photoelectric process. These absorption edges are characteristics of element present in the material. A closer look near the absorption edge reveals fine oscillations near and above the absorption edge is called X-ray Absorption Fine Structure (XAFS) and it contains information related to the physical and chemical state of absorbing element. X-ray Absorption spectroscopy (XAS) thus deals with the study of these oscillations to obtain various information like formal oxidation state, coordination chemistry, near neighbour distances, coordination number and species of the atoms immediately surrounding the selected element.

For the energy range involved in XAS measurements, the pair production phenomenon is negligible and X-ray absorption, elastic scattering and inelastic scattering are the main interactions of X-rays with matter. In XAS, the X-ray absorption coefficient, μ of a sample is measured as a function of photon energy over a range of 1000 eV around the absorption edge of an element.

A typical XAS spectrum can be divided into two regimes: X-ray Absorption Near Edge Spectroscopy (XANES) and Extended X-ray Absorption Fine Structure Spectroscopy (EXAFS) as shown in Figure 1.2. These two regimes involve the same physical process i.e. photoelectric effect, but they differ in the energy range of the emitted photoelectron and hence provide different information regarding the system.

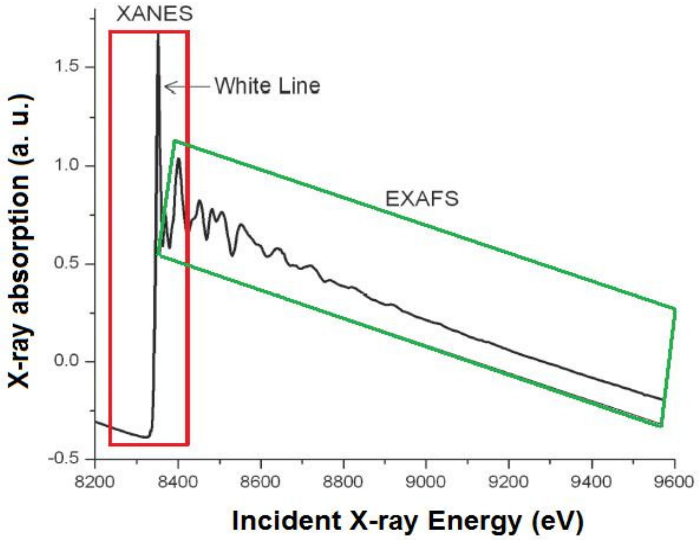

Figure 1.2: A typical XAS spectrum

1.1.1 X-ray Absorption Near Edge Spectroscopy (XANES)

XANES region extends upto 50 eV above the absorption edge and gives information about the external perturbations in the valence states to which electrons make transitions from core levels upon absorption of X-ray photons. Hence XANES can yield information regarding hybridization of orbitals in case of molecule or long range order existing in a crystalline sample apart from the oxidation states of the absorbing atom in the material. Moreover, the shape of the absorption edge is related to the density of states available for the excitation of the photoelectrons. The absorption edges often show features like isolated peaks, shoulders and strong peaks just above the absorption edge, popularly known as white line. These features are characteristic of the density of the unoccupied states to which excited photo electrons may make transitions. Since, the density of unoccupied states depends on the formal valence state, ligand type and coordination geometry, therefore, XANES spectroscopy can be used as a fingerprint to identify phases.

An important and common application of XANES spectroscopy is to use the shift of the absorption edge position to determine the oxidation state of the particular atomic species. Figure1.3 shows the XANES spectra of Cr metal foil, Cr_2O_3 and CrO_3 standards which contain Cr cations in 0, +3 and +6 oxidation states respectively. With increase in the oxidation state of the cation, the absorption edge shifts towards higher energy. Therefore, for an unknown sample, a comparison of the absorption edge position with that of standards gives the information about the oxidation state of the cation in the sample. In case of mixed oxidation state, a linear combination fitting of the absorption edge is used to predict the ratio of valence states present in the sample. In many cases, isolated peaks appear just before the absorption edge in the XANES spectra which are known as pre-edge peaks. Appearance of the pre-edge peaks depends on the centrosymmetry of the coordination environment and hybridization of orbitals of the cations. For example, in Figure 1.3, CrO_3 which contains Cr(VI) cation shows a strong pre-edge peak. This peak corresponds to electron transition from 1s to 3d orbital, which is not an allowed transition. However, the tetrahedral coordination of Cr(VI) facilitates the hybridization of the 3d and 4p orbitals, which makes the transition allowed. The octahedral Cr(III) cation in Cr_2O_3 having centrosymmetry does not allow the hybridization of the 3d orbitals, hence do not have the pre-edge peak. In case of Cr, the pre-edge peak can be used to determine the presence of Cr (VI) and Cr(III) species.

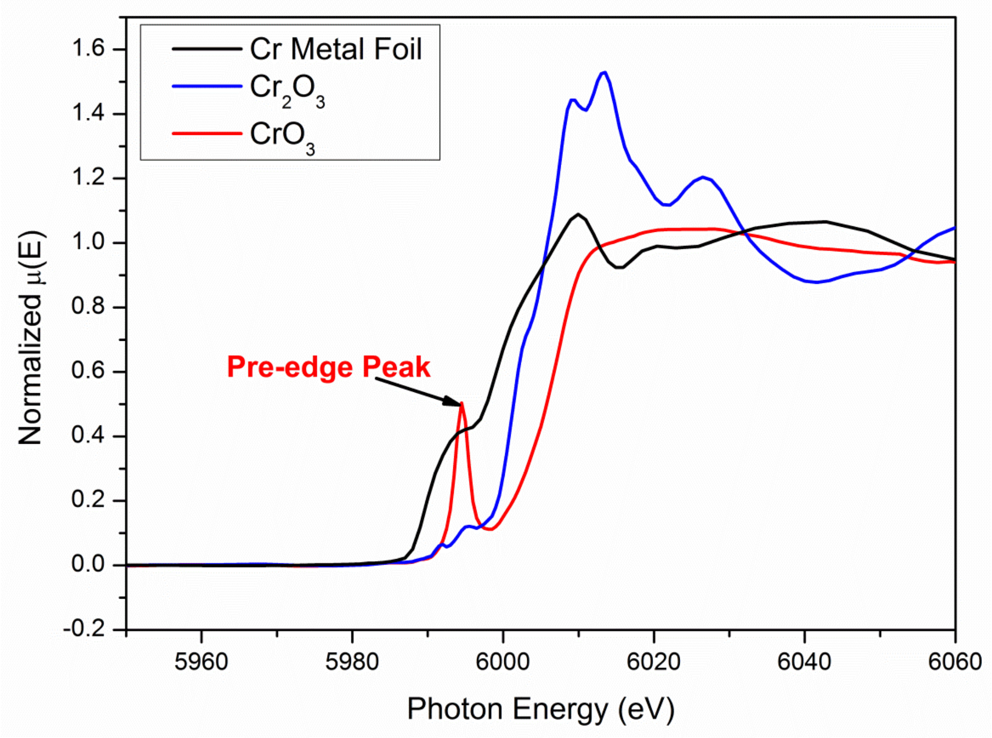

Figure 1.3: Cr K edge XANES spectra of standard Cr metal and oxides.

1.1.2 Extended X-ray Absorption Fine Structure Spectroscopy (EXAFS)

The EXAFS region which spans from 50 eV to 800 eV above the absorption edge, consists of fine structure oscillations arising due to back scattering of outgoing photo-electron by the electron cloud of neighboring atoms, and can give precise information regarding the short range order and local structure around the particular atomic species in the material. A quantum mechanical approach is needed to understand the origin of EXAFS oscillations, which has been discussed elaborately in sub-section 1.1.3. In photoelectric effect, an X-ray photon with sufficient energy is absorbed in the sample and an electron is emitted from the core shells of the atoms. The emitted electron, known as photoelectron, can be represented as an outgoing wave for an isolated atom. When the absorbing atom is surrounded by other atoms, the outgoing photoelectron wave is scattered by the electron cloud of the surrounding atoms. The interference between the outgoing and scattered photoelectron wave causes an energy dependent variation in the X-ray absorption co-efficient in accordance with the Fermi's Golden Rule which are generally referred to as EXAFS oscillations. Since the EXAFS oscillations arise due to the presence of neighboring atoms, they can be analyzed to extract information like bond distances, coordination numbers and disorder factor of neighboring atoms with respect to the absorbing atom[3, 4]. EXAFS is a local structure technique and element specific, therefore can be applied not only to crystals, but also to materials that possess little or no long-range translational order: amorphous systems, glasses, quasicrystals, disordered films, membranes, solutions, liquids, metalloproteins. This versatility allows it to be used in a wide variety of disciplines: physics, chemistry, biology, biophysics, medicine, engineering, environmental science, materials science, and geology[33-36].

1.1.3 Theoretical formulation of EXAFS

EXAFS is a quantum mechanical phenomenon that is based on X-ray photoelectric effect, in which X-ray photon incident on an atom within a sample is absorbed and liberates a photoelectron from an inner atomic orbital. The photoelectron wave scatters from the atoms around the X-ray absorbing atom, creating interferences between the outgoing and scattered parts of the photoelectron wave function. These quantum interference effects cause an energy-dependent variation in the X-ray absorption probability, which is proportional to the X-ray absorption coefficient, a measurable quantity. Since the EXAFS oscillations arise due to the presence of neighboring atoms, these oscillations can be analyzed to extract information like bond distances, coordination numbers and disorder factor of neighboring atoms with respect to the absorbing atom.

The observed oscillations can be described by EXAFS equation. The derivation of EXAFS equation is given in many books and reviews[32-34, 37-39]. X-ray absorption is a transition between two quantum states, absorption coefficient in this process is proportion to transition probability and can be written using Fermi Golden's rule as:-

$$\mu \propto \left|\langle i|H|f\rangle\right|^2 \tag{1.1}$$

Where $\langle i|$ represents the initial state with an X-ray, a core electron, and no photo-electron to a final state and $|f\rangle$ represents the final state with no X-ray, a core hole, and a photo-electron.

The photoelectron emitted from absorbing atom will travel in material and backscattered by electron cloud of nearby atoms (Fig. 1.4). This backscattered photoelectron wave will interfere with the outgoing wave and change the final state, however the initial state will be same since the core level electron is very tightly bound to the absorbing atom. The final state now can be written using two terms, "bare atom" portion $|f_0\rangle$ and one that is the effect of neighbouring atoms $|\Delta f\rangle$, i.e. $|f\rangle = |f_0\rangle + |\Delta f\rangle$. Thus,

$$\mu(E) \propto \left(\langle i|H|f_0\rangle + \langle i|H|\Delta f\rangle\right) \times \left(\langle i|H|f_0\rangle + \langle i|H|\Delta f\rangle\right)^*$$

$$\propto \left|\langle i|H|f_0\rangle\right|^2 + \left|\langle i|H|\Delta f\rangle\right|^2 + \langle i|H|f_0\rangle \times \langle i|H|\Delta f\rangle^* + \langle i|H|\Delta f\rangle \times \langle i|H|f_0\rangle^*$$

$$\propto \left|\langle i|H|f_0\rangle\right|^2 + 2\,\mathrm{Re}\left[\langle i|H|\Delta f\rangle \times \langle i|H|f_0\rangle^*\right]$$

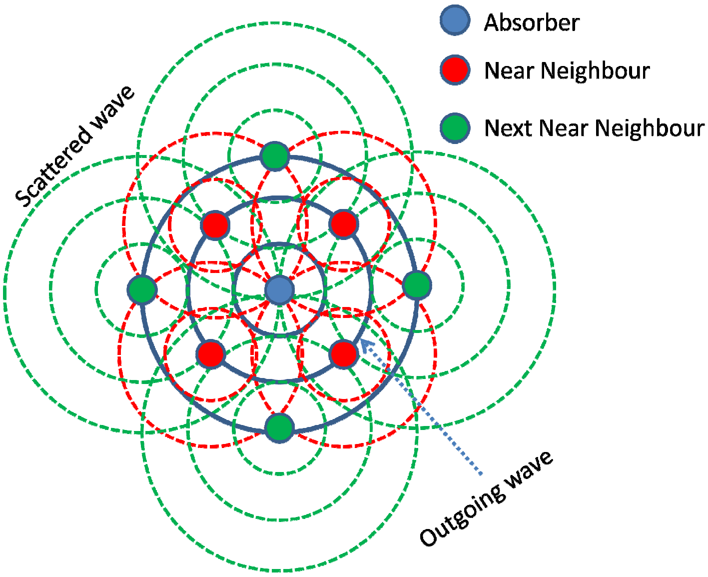

Figure 1.4: Schematic of scattering.

Neglecting the small contribution due to $\left|\langle i|H|\Delta f\rangle\right|^2$ term, one gets-

$$\mu(E) \propto \left|\langle i|H|f_0\rangle\right|^2 \left[1 + \frac{2\,\mathrm{Re}\left[\langle i|H|\Delta f\rangle \times \langle i|H|f_0\rangle^*\right]}{\left|\langle i|H|f_0\rangle\right|^2}\right] \tag{1.2}$$

By rearranging above equation,

$$\mu(E) = \mu_0(E)[1 + \chi(E)] \tag{1.3}$$

Comparing equation (1.3) with equation (1.2) we can write,

$$\chi(E) = \frac{\mu(E) - \mu_0(E)}{\Delta\mu_0(E)} \tag{1.4}$$

So, EXAFS oscillation can be written as,

$$\chi(E) \propto \langle i|H|\Delta f\rangle \tag{1.5}$$

As per quantum radiation theory, the interaction term H is proportional to e^{ikr} .The initial state is a tightly bound core level which can be approximated as a delta function. The change in final state is same as the wave function of scattered photo electron $\Psi_{scatt}(r)$ .Putting all these terms, one can write the expression for EXAFS as

$$\chi(E) \propto \int \delta r\, e^{ikr}\, \psi_{scatt}(r)\, dr = \psi_{scatt}(0) \tag{1.6}$$

To say it in words, the EXAFS function is proportional to the scatted photoelectron at the absorbing atom. Now if we consider the outgoing photo electron wave function $\psi(k,r)$ as spherical wave, we can write-

$$\psi(k,r) = \frac{e^{ikr}}{kr} \tag{1.7}$$

where$k$ is the photoelectron wave vector, defined as $k = \sqrt{\frac{2m(E-E_0)}{\hbar^2}}$, where E is the incident photon energy and E_0 is the binding energy of the core shell electron. This photoelectron travels a distance R to the neighbouring atom, gets scattered from neighbouring atoms and then traverses back to the absorbing atom. The amplitude of scattered photo electron at the position of absorbing atom then becomes

$$\psi_{scatt}(k, r=0) = \frac{e^{ikR}}{kR}\left[2kf(k)e^{i\delta(k)}\right]\frac{e^{ikR}}{kR} + C.C. \tag{1.8}$$

where, $f(k)$ and $\delta(k)$ are back scattering amplitude and scattering phase shift due to the scattering atom. The scattering factors $f(k)$ and $\delta(k)$ depends upon the atomic number, Z of the neighbouring atom. These scattering factors make EXAFS sensitive to the presence of neighbouring atoms. Combining equation 1.6 and 1.8 we get, after few more simplification

$$\chi(k) = \frac{f(k)}{kR^2}\sin\left[2kR + \delta(k)\right] \tag{1.9}$$

This represents EXAFS equation considering one pair of absorbing atom and scattering atoms. However, in real scenario, often there is large number of scattering atoms are present at approximately same distance, called coordination shells. However, the distance of each atom in coordination shell is not same due to the effect of thermal or static disorder in the bond distances and we need to average over their contribution. As a first approximation i.e. assuming one type of neighbouring atoms and Gaussian distributions of neighbouring atom's disorder, the EXAFS equation becomes:

$$\chi(k) = \frac{Ne^{-2k^2\sigma^2} f(k)}{kR^2} \sin\left[2kR + \delta(k)\right] \tag{1.10}$$

where, N is the coordination number in one coordination shell at a distance of R and σ^2 is the mean-square-displacement in the bond distance R .Summing over the contribution due to different coordination shells, EXAFS equation becomes

$$\chi(k) = \sum_j \frac{N_j f_j(k)}{kR_j^2} \sin\left[2kR_j + \delta_j(k)\right] e^{-2k^2\sigma_j^2} \tag{1.11}$$

where, j stands for the individual coordination shell of identical atoms at approximately the same distance from the central atom. In principle there could be many such shells, but as shells of similar Z become close enough (i.e., within a 0.05Å of each other), they become difficult to distinguish from one another and they are often represented by a single shell having equivalent multiple degeneracy.

Before applying the EXAFS equation (1.11) to any practical case, it needs an important correction. At the start of the derivation, we assumed that photoelectron wave traverses the distance between absorbing and neighbouring atom as spherical wave. In reality, these photoelectrons can undergo inelastic scattering with the conduction electrons; phonons etc. and its energy may get changed. The criteria for a photo electron to participate in the XAFS is that the photo-electron has to elastically scatter from the neighbouring atom and return to the absorbing atom and also, the photoelectron has to return back before the excited state decays. To take inelastic scattering and the core-hole lifetime into account one should rather use a damped spherical wave like:

$$\psi(k,r) = \frac{e^{ikr} e^{-2r/\lambda(k)}}{kr} \tag{1.12}$$

where, λ is the mean free path that represents the distance that a photoelectron can traverse without undergoing inelastic scattering and before the core hole is filled. The mean free path typically falls in the range of 5-30 Å and has a fairly universal functional relationship with photo electron wave number, k as shown in Fig. 1.5.

One more correction is added to the final equation is called passive electron effect. As a consequence of absorption of the incident photon, a core electron is knocked out from the excited atom. The atomic electrons of this excited atom perceive a modified potential, which can be approximated by that of an atom with its Z increased by 1. Thus the many body relaxation effect reduces the value of $\mu$by the factor S_0^2.This usually has a value between 0.7 and 1.0 and does not depend on k.

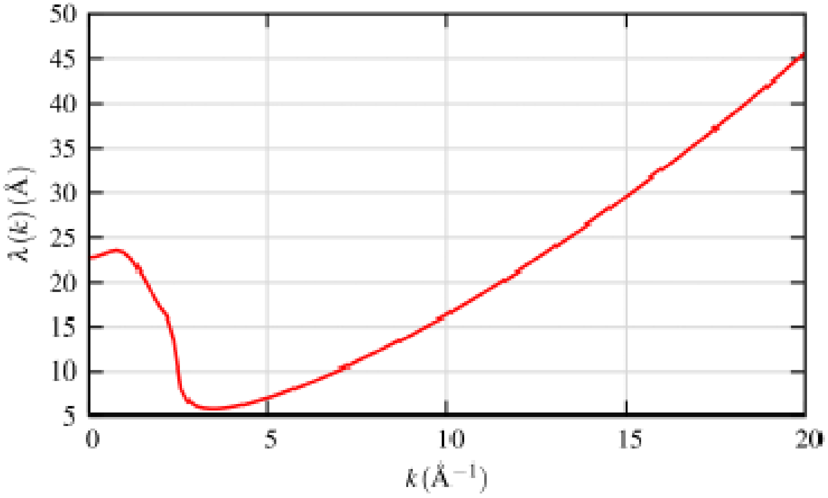

Figure 1.5: Typical characteristic of photoelectron mean free path vs. wave number.

Taking the mean free path correction into account, the EXAFS equation becomes-

$$\chi(k) = \sum_j \frac{N_j S_0^2 f_j(k)}{kR_j^{\,2}} \sin\left[2kR_j + \delta_j(k)\right] e^{-2k^2\sigma_j^2} e^{-2R_j/\lambda(k)} \tag{1.13}$$

This is the EXAFS equation which widely used for simulating theoretical EXAFS spectra of any species in order to carry out the analysis of experimental EXAFS data. Certainly, this requires apriori knowledge about scattering factors $f(k)$ and $\delta(k)$. These scattering factors are function of atomic number Z and are usually calculated theoretically with very high accuracy. One important corollary that can be drawn from EXAFS equation follows that because of $\lambda(k)$ term and R^{-2} term in the equation, EXAFS is inherently a local probe i.e. EXAFS cannot see much further than ~8 Å. The contribution of different terms in EXAFS oscillation is as follows:

(1) N_j : Coordination number N_j contributes in amplitude of EXAFS signal and does not have k dependence.

(2) S_0^2: This term basically contributes in amplitude of EXAFS oscillation. It is different for different elements, but the value is generally transferable between different species from the same element and the same edge.

(3) R_j: The term R_j is the half path length of the photoelectron (i.e., the distance between the absorber and a coordinating atom for a single-scattering event). The term $sin(2kR_j+\delta_j(k))$ defines the oscillation frequency of each coordination shell. The EXAFS oscillations are convolution from all the coordination shells. It is this sine term in the EXAFS equation that makes the Fourier transform (FT) of the XAFS signal such a powerful tool, because a FT results in peaks at distances related to R_j.

(4) σ^2: This term has contributions from dynamic (thermal) disorder as well as static disorder (structural heterogeneity) as stated above. A distribution of distances within a single shell

decreases the amplitude of the EXAFS signal because the phase differences between outgoing and scattered photoelectrons are shifted slightly for each atom in the coordination shell.

1.2 Time Resolved X-ray Absorption Spectroscopy (TR-XAS)

Conventional EXAFS measurement takes almost an hour to measure one complete spectrum with an acceptable S/N ratio of 10^3 or better and upto a reasonable k range of $12Å^{-1}$. This is done by step-wise scanning of the whole energy range of 1000 eV around the absorption edge. Therefore, the conventional step-wise scanning measurement is not at all suitable for time resolved studies of fast processes which needs second or millisecond resolution for data acquisition and two alternative modes of measuring fast and time-resolved EXAFS spectra are: Quick EXAFS (QEXAFS) and Dispersive EXAFS (DEXAFS). Both of these modes have their own advantages and disadvantages[19].

1.2.1 Quick XAFS (QXAFS)

QEXAFS[40, 41] is a modified version of the conventional EXAFS measurement mode which is optimized to reduce the measurement time of an EXAFS spectrum. In QEXAFS, XAFS spectrum is recorded during quick scanning of the monochromator. Therefore, this is limited by the speed of the monochromator movement achievable, the integration time required per point to achieve acceptable statistics and the reproducibility of the monochromator movements in both forward and reverse direction. QEXAFS uses a specialized monochromator that allows fast and repetitive energy scans by oscillating the monochromator crystal. In this monochromator, channel cut crystals are mounted on a stage which in turn is connected to a goniometer with fast movements that moves the crystal to the desired Bragg angle[42]. Fig. 1.6 shows the schematics of the QEXAFS monochromator. The smooth oscillation of the monochromator crystal results in a continuous change of the Bragg angle and the reflected energy which reduces the time of measurement to seconds. Recently, this technique has been improved to give millisecond time resolution[43, 44]. However, improved time resolution has led to new disadvantages such as loss of the fixed exit and a limited choice of energy range. One of the main advantages of QEXAFS technique is that it can measure very dilute sample or thin film samples using fluorescence mode of EXAFS measurement. Therefore it can be extensively used for quick surface EXAFS measurements to study the *in-situ* growth of thin films. Some examples of the QEXAFS measurement facilities are Super XAS beamline at Swiss Light Source[42], BM29 at ESRF[44], ROCK beamline at Soleil Synchrotron source[43] etc.

1.2.2 Dispersive XAFS (DXAFS)

In Dispersive EXAFS, on the other hand, a band of X-ray energies is dispersed as well as focused on the sample using a long bent crystal (polychromator) and the transmitted and spatially dispersed defocused beam is detected on a position sensitive detector (PSD) as shown in Figure 1.7[45]. This mode of measurement demands high temporal and spatial beam stability. Since, the focused band of energies will always be associated with some defocussing aberrations, therefore the uniformity of the sample is very crucial in this mode. The measurements are possible only in transmission mode, therefore very dilute samples or surface studies using fluorescence mode is not possible in this technique. Since the whole spectrum is recorded in a single shot using a PSD, therefore the time resolution of this mode is only limited by the integration time of the detector. Hence using this mode it is possible to reach microseconds resolution. One of the major advantages of the DEXAFS technique is that the data is not affected by the noise generated from mechanical movements since there is no moving mechanism during the course of data acquisition. Another tempting advantage of this technique is since it focuses and measures a band simultaneously, therefore for multi element system, different edges can be measured simultaneously at one shot. However, since the incident flux and the transmitted flux cannot be measured at the same instant of time and have to be measured with and without the sample separately, it is affected by the fluctuations in the synchrotron beam. Another major disadvantage of this technique is that for energies less than 5 KeV, the energy band available is not wide enough to record the full EXAFS spectrum and therefore only XANES information can be achieved for elements having edges at lower X-ray energies. Though DEXAFS gives a high time resolution, the measurable range energy and k range are intrinsically limited by the optics of the beamline, which ultimately affects resolution of the radial distribution function of the Fourier Transformed-EXAFS spectrum. Therefore data upto only two coordination shells can generally be extracted by DEXAFS whereas upto three coordination shells can be extracted using QEXAFS technique and due to the short analyzable range the error in the reported values increases. The resolution of EXAFS radial distribution function depends on the k range used for Fourier Transform. Higher the k range of the data, higher is the resolution in r space. The spatial resolution is given by $\Delta r=\pi/2\Delta k$. A higher energy band results in lager k range which in turn gives better spatial resolution. However, at high k the contribution from noise also becomes significant, therefore k range should be selected by optimization between spatial resolution and high k noise contribution. Thus to summarize, though DEXAFS has lesser spatial resolution and more errors in the reported value, it offers much lower acquisition time scales to study fast processes[19]. Some examples of the DEXAFS measurement facilities are NW2A at Photon Factory, ID24 at ESRF, BL-08 at Indus-2[46]. With micro-focussed X-ray beam DEXAFS technique is also used for spatially resolved chemical characterization of complex micro and nano structured materials.[47]

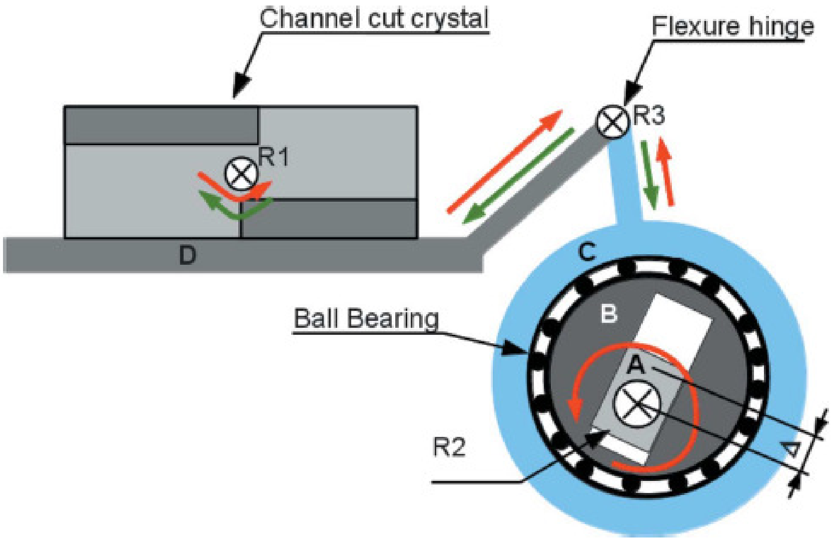

Figure 1.6: Schematic of QEXAFS monochromator (Taken from Ref. 37)

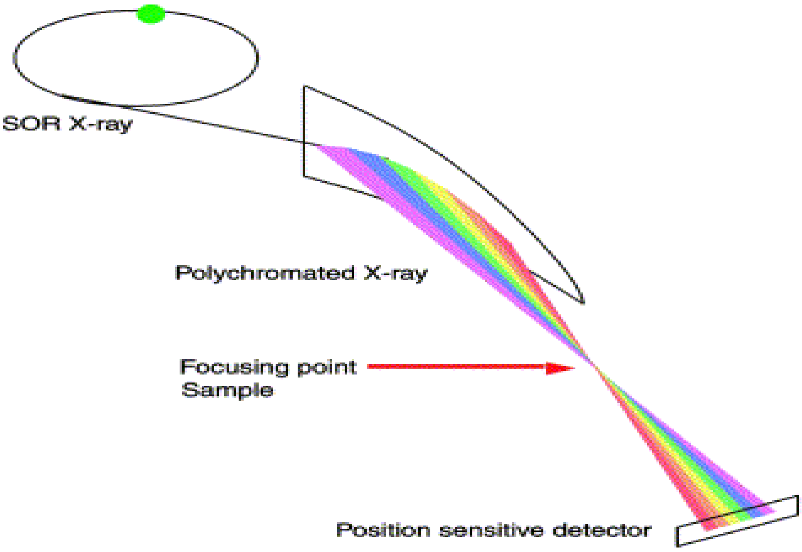

Figure 1.7: Schematic optical lay-out of a typical Dispersive EXAFS set-up.

1.3 Applications of TR-XAS

Time Resolved X-ray Absorption Spectroscopy (TR- XAS) has emerged as an important technique in the field of *in-situ* measurements due to the ability to see the structural changes in the material during a process with millisecond time resolution. Also, this technique can be applied to study the structural changes in materials that do not have long range order. This opens up the scope for a wide range of *in-situ* studies using TR-XAS. Two major applications of TR-XAS is to study the structural changes during growth of nanoparticles from solution phase and to see structural changes in catalyst samples during a chemical reaction. Recently a large number of TR-XAS studies have been reported in both of these fields, which has given insight into these processes and helped to design better materials for their applications.

1.3.1 Growth of nanoparticles

Since its invention, nanoparticles find a wide variety of applications in the field of medicine, catalysis, biotechnology, fuel cells, solar cells, sensors and environmental science[48, 49]. Nanoparticles have fascinated the scientific community due to their interesting properties that is much different from their bulk counterpart. Also, the scope of tunability of properties with size of nanoparticles attracts material physicists to study these materials. With the essence that shape and size of nanoparticles determines their properties comes the need to understand the mechanism of nucleation and growth of these particles. The *ex-situ* studies on nanoparticles gave us information about the properties once the particles are formed. However, to fabricate tailor made particles, a complete control of the formation process is inevitable. This envisages a new era of "*in-situ*" studies. Recently several *in-situ* time-resolved XAS measurements have been carried out on nanoparticles synthesized by various routes viz., Turkevich method by Polte et. al.[50] and Lin et. al.[51], Shiffrin-Brust method by Ohyama et. al.[27], X-ray irradiation of ionic liquid by Ma et. al.[52], photoreduction by Harada et. al.[20, 28, 53, 54], polyol synthesis by Boita et. al.[55],etc. Through these experiments the understanding of these processes have been improved which has ultimately helped to obtain a better yield and size distribution of the nanoparticles.

In 2010, Polte *et. al.*[50] did *in-situ* XANES measurements along with SAXS on levitated sample droplets to investigate the growth of gold nanoparticles by citrate synthesis. Though citrate synthesis was proposed by Turkevich in the year 1951, the mechanism of formation of nanoparticles through this route was not clear for a long time. From this study a four step mechanism of gold nanoparticles formation could be proposed, comprising of fast initial formation of small nuclei, coalescence of the nuclei into bigger particles, slow growth of particles sustained by ongoing reduction of gold precursor, and subsequent fast reduction ending with the complete consumption of the precursor species. In 2011, Ohyama *et. al.*[27] have carried out another experiment to understand the reduction of gold by sodium borohydride ($NaBH_4$). Au L_3 edge QEXAFS measurements were carried out in transmission mode with millisecond time resolution. The XANES spectral changes revealed that Au nanoparticles are formed by the reduction of the solution containing an equal quantity of Au^{3+} and Au^+ ions. The signature for formation of Au was observed at 4.6 s. This is one of the first reports of observation of nuclei in formation process. From the EXAFS analysis, the structure of the Au nuclei is estimated to be an Au_4 cluster with an fcc crystal system. In 2013, Ma *et. al.*[52] reported the evolution of gold nanoparticles in ionic liquid by hard X-ray irradiation. Synchrotron hard X-ray not only acts as the radiation source, which causes the reduction of Au^{3+} ions, but also acts as a probe to study the whole process in real-time by QEXAFS.They have observed a decrease in the white line intensity of the Au L_3 XANES spectra recorded during the growth of nanoparticles and the features of the spectra gradually became close to that of Au foil.From EXAFS analysis, a new hypothesis and reaction mechanism has been proposed to explain the generation progress of gold nanoparticles. The initial breaking of the Au–Cl bond differentiates this irradiation method from traditional chemical methods. Intermediates like $AuCl_3$, $AuCl_2$ and $Cl_2Au\text{-}AuCl_2$ clusters have also been predicted.

The growth of Pt nanoparticles by polyol synthesis was studied by Boita *et. al.*[55]. *In-situ* DEXAFS measurements of the reaction solution were performed at the specially designed cell. A linear combination fitting of the XANES spectra using the initial (Pt^{+4}) and final (Pt^0) spectra were done to obtain the detailed time evolution of the zerovalent Pt fraction. The XAFS analysis could distinguish three different stages in the synthesis process: a fast nucleation event, followed by diffusion-limited Ostwald ripening growth ($R \propto t^{1/3}$), where R is the radius of the particles and t is the reaction time, and subsequent slow growth and stabilization of nanoparticles. The experiment also gave an evidence of Lamer Nucleation Burst scenario.

Harada *et. al.*, on the other hand, studied the growth of metal nanoparticles by photoreduction. The precursor solution in PVP is irradiated with a 500 W super-high-pressure mercury lamp. The growth of Au, Pt, Ag, Rh and Pd nanoparticles are studied by *in-situ* EXAFS. For Au nanoparticles[53], it has been found that the photochemical reduction results in the formation of Au^{2+} intermediates and Cl radicals. Formation mechanism comprising of three main steps has been proposed: (1) The bond of Au-Cl rapidly dissociates due to the reduction from $AuCl_4^-$ to $AuCl_2^-$. (2) This is followed by reduction of $AuCl_2^-$ to Au^0 with the formation and growth of Au metal particles, the reduction from $AuCl_2^-$ to Au^0being much slower than that from $AuCl_4^-$ to$AuCl_2^-$. (3) On the prolonged photo-irradiation, $AuCl_2^-$ is completely consumed, and the growth process of Au metal particles is observed. From the Pt nanoparticles formation studies[54], it has been found that the formation in the photoreduction process is constituted of three elementary stages, reduction-nucleation, autocatalytic surface growth on nucleates and Ostwald ripening based growth. The initial nucleation stage for the formation of Pt_4 nuclei is evidenced from the CN (around 3–4) of Pt–Pt bond pair, and the aggregative particle growth including the autocatalytic reduction of Pt ionic species on the surface of Pt_4 nuclei proceeds with irradiation time to produce particles with diameter of 1−2 nm (i.e., Pt_{13} or Pt_{55}nanoparticles expected from CN around 6−7).The growth of Ag nanoparticles synthesized by photoirradiation is also studied by *in-situ* DEXAFS[28]. The study shows that the reduction rate of Ag^+ ions couldbe quantitatively evaluated from the change of X-ray absorbance $\mu(E)$ assigned to the Ag–O contribution in the XANES region whereas the temporal change of intermediate small Ag particles could be estimated by the Ag–Ag contribution. During the induction period the first-order reaction of Ag^+ ions occurred to produce Ag^0 atoms,while the subsequent nucleation and growth process concurrently proceeded after the induction period. In the nucleation and growth process after the induction period, the intermediate small Ag particles (C.N. smaller than ca. 4) were generated and they were grown up to larger particles (C.N.s equal to 4.5 ± 1.5) in the longer photoreduction process. Apart from the noble metal nanoparticles of Au, Pt and Ag, reports are available in the literature on the growth of other metal nanoparticles also. For example, formation mechanism of Rh and Pd nanoparticles by photoreduction were studied byHarada and Inada using QEXAFS[20]. The reduction rate of Rh^{3+}aqua chlorocomplexes in PVP solutions was found to be slower than that of Pd^{2+}. This is probably because Rh^{3+} chlorocomplexes were more stable thanPd^{2+} chlorocomplexes at higher concentration of chlorine ions in the aqueous solutions. In addition, the reduction process of Rh^{3+} chlorocomplexes possessed an induction period before the onset of nucleation and growth of Rh particles, although Pd^{2+} chlorocomplexes displayed no induction period, since the reduction of Pd^{2+} complexes occurred immediately after the mixing of an ethanol solution of Pd^{2+} complexes with aqueous PVP solutions.

Karim *et. al.*[56] have investigated the growth of Pd colloidal nanoparticles in a novel microfluidic reactor using in situ SAXS and XAFS with a time resolution from milliseconds to several minutes. From the results, it can be concluded that nucleation proceeds continuously and is accompanied by autocatalytic growth. Combination of SAXS and EXAFS also suggest that the capping ligands used in the synthesis plays an important role affecting the nucleation and growth of the nanoparticles.

1.3.2 Catalysis

The structure-activity correlation has become an essence to understand the performance of catalysts. In recent years, lots of attempts have been made to use more than one experimental techniques or combination of techniques which would help to get an insight into this[57-60]. This provides an in-depth understanding of the catalysis process, which in turn helps to synthesize catalysts with better performance. X-ray absorption spectroscopy (XAS) has emerged as an important technique which can give structural information about the catalysts[24, 26, 61]. The main advantage of this technique is that it can measure samples in any form i.e. crystalline, amorphous, glass, polymer, liquid, etc. and therefore can be used as a structure determining tool for a wide range of homogenous and heterogenous catalysts. *In-situ* measurements have become inevitable in the field of catalysis as they provide the exact information during the catalysis process. This has definitely given a better outlook regarding the activity and selectivity of catalysts, and also addresses the problem of deactivation of the catalyst. For example, Tibiletti *et. al.*[62] have performed *in-situ* EXAFS of oxide supported gold catalyst during water gas shift reaction. The experimental studies along with computational investigations predict that metallic gold particles rather than isolated ions are present during the reaction. Metallic gold in close contact with the oxide support has been identified as the active species in the catalyst responsible for the reaction. Newton *et. al.*[30] have investigated Pd catalyst systems during CO/NO cycling using Dispersive EXAFS and DRIFT measurements. They have developed the setup for synchronous and time resolved infra-red, XAFS, and mass spectroscopy measurements *in-situ* during reactions. The specialized reaction cum measurement cell has hotpressed BN windows for X-ray transmission and IR windows as 2 mm thick CaF_2 or ZnSe.Through these measurements, they were able to see rapid, reversible sintering and re-dispersion of the Pd catalyst during the CO/NO cycling. They were able to clearly differentiate these processes from the more simple oxidation and reduction of the Pd nanoparticles and showthat this structural change forms an integral part of the CO/NO cycle over Pd. Tromp *et. al.*[24] have investigated the deactivation of homogenous Pd catalysts in the allylic substitution reaction using combined dispersive EXAFS and UV-Visible spectroscopy. They have developed the setup for simultaneous acquisition of both Dispersive-XAFS and UV-Vis spectra during the reaction. Both time resolved techniques indicate the formation of dimers, trimers and possibly larger clusters directly from the start of the catalytic reaction leading to precipitation as palladium black. Voronov *et. al.*[29] have investigated Fischer-Tropsch reaction *in-situ* with Re promoted Co/Al_2O_3 catalysts using EXAFS at both Re L_3 and K edges. They have found local distortion of the Co environment near Re ions which may be a reason for the increased catalytic activity. Sadeqzadeh *et. al.*[63] have performed *in-situ* XRD/EXAFS measurements on Pt promoted alumina supported Co catalyst during Fischer-Tropsch reaction. They have found in the reduced Pt promoted alumina supported cobalt catalysts the presence of bimetallic Co-Pt particles. They have inferred that the hcp phase of Co is more active than the fcc phase. Also, they have reported Co sintering as the main mechanism for catalyst deactivation.

1.4 Outline of the thesis

The subsequent chapters of the thesis are arranged as follows. Chapter-2 deals with various experimental techniques used in this thesis work with brief descriptions of different equipments used and also describes the XAS data analysis technique in detail. In the beginning of this chapter, the EXAFS beamlines of Indus 2 SRS used for TR-XAS studies in the present thesis work have been described. Also, the EXAFS data analysis procedure used in the present thesis work has been extensively discussed. Other experimental techniques which are used as complementary techniques along with TR-XAS for *in-situ* studies have also been described shortly. Finally this chapter also discusses *ex-situ* techniques that are used for characterizing the materials synthesized or used in the present thesis work.

In the next three chapters (Chapters 3-5) of the thesis work, we have presented the results of the *in-situ* XAS studies during growth of nanoparticles. Chapter 3 is devoted to the *in-situ* XAS studies during growth of Au and Pt monometallic nanoparticles. Chapter 4 discusses the growth of Au-Pt bimetallic nanoparticles and Chapter 5 mentions the growth of Cu nanoparticles. These chapters elaborate the growth mechanism of nanoparticles as understood from the *in-situ* XAS measurements and also identifies the clusters formed during the growth of nanoparticles.

Chapter 6 and 7 present the applications of TR-XAS to study structural changes in catalysts during chemical reactions. Chapter 6 describes the *in-situ* XAS studies on Co based catalysts during Fischer Tropsch reactions while Chapter 7 describes the *in-situ* XAS studies on Cu doped TiO_2 catalysts during photocatalytic reduction reaction of CO_2.

Finally in Chapter-8 the conclusions drawn in all the previous chapters for the application of TR-XAS in growth of nanoparticles and catalysis have been summarized and future direction of the work has been mentioned.

Chapter 2

Experimentation and Data Analysis

In this chapter we describe the different experimental techniques used in the present thesis work. This includes the two EXAFS beamlines used for the time resolved EXAFS studies, complementary techniques which are done simultaneously with TR-XAS and different *ex-situ* techniques used for characterization of the nanoparticle samples have also been discussed. The procedure of handling and analysis of XAS and TR-XAS data have also been discussed in this chapter. The design and fabrication of various cells used for the *in-situ* TR-XAS experiments have been discussed later in subsequent chapters.

2.1 TR-XAS Experiment

As has been mentioned in Chapter-1, the pre requisite for a XAS measurement is a synchrotron source. In the present thesis work, all XAS measurements have been carried out at the energy dispersive beamline (BL-08)[46] and the energy scanning beamline (BL-09)[64, 65] at Indus-2 synchrotron source. BL-08 being a dispersive beamline offers fast data acquisition, while BL-09 has been modified from its conventional step-by-step scanning mode to a novel continuous scanning mode for achieving fast data acquisition required for TR-XAS measurements.

Indus-2 Synchrotron source

It is evident that X-ray absorption spectroscopy measurements needs a bright and tunable X-ray source and presently only synchrotron radiation sources are used to carry out XAS measurements world-wide. When a charged particle enters a magnetic field whose direction is not parallel to its initial direction of motion, it is forced to change its direction of motion, thereby emitting electromagnetic radiation. In a synchrotron, electrons of relativistic speed are forced to circulate in a storage ring by a series of bending magnets[66]. The radiation thus created is known as synchrotron radiation and is characterized by a continuous energy spectrum over a wide range of wavelengths (from infrared to hard X-rays), high intensity, strong polarization and a pulsed nature. Apart from the above bending magnet source, modern synchrotron facilities also have additional elements, so-called insertion devices, placed in the straight sections between the bending magnets. These devices constitute a series of alternating magnetic fields that force the electron beam to perform either strong (wiggler) or gentle (undulator) oscillations. The wiggler emits a broad beam of incoherent radiation characterized by increased intensity and a continuous energy spectrum extending to much higher X-ray energies compared to a bending magnet. The undulator emits a narrow beam of coherent radiation the intensity of which is amplified up to 10,000 times but only at certain energies. Based on these characteristics, the source (bending magnet, wiggler or undulator) best suited for a particular experimental technique is chosen. For the present thesis work, all XAS measurements have been carried out at Indus-2 Synchrotron facility at RRCAT, Indore, India.[67] The schematic of Indus-2 synchrotron source is shown in figure 2.1. The electron produced in a source are first accelerated using a microtron upto 40 MeV before their energy is further increased in a booster ring to 550 MeV. From here they are transferred to the Indus-2 storage ring where they are energized upto 2.5 GeV and are then stored. The synchrotron source Indus-2 was commissioned in 2005 and is presently being operated with 2.5 GeV electron energy at 200 mA beam current and a critical wavelength of about 2Å, providing a spectrum from infra-red to hard X-ray regime. The storage ring of Indus-2 is 172.4 meter (circumference) consisting of 8 unit cells each providing a 4.5 m long straight section. Each of the eight super periods has two dipole bending magnets (1.502 T), four focusing and five defocusing quadrupoles and six sextupoles. Four RF cavities are used for RF voltage of 1.5 MV to achieve 2.5 GeV energy with beam emittance of $X=5.81x10^{-8}$m.rad and $Y=5.81x10^{9}$m.rad.Indus-2 presently delivers synchrotron radiation from bending magnet source to over 15 beamlines . The insertion devices which are being installed on Indus-2 in near future include two planar undulators, one APPLE type undulator and one super conducting wavelength shifter.

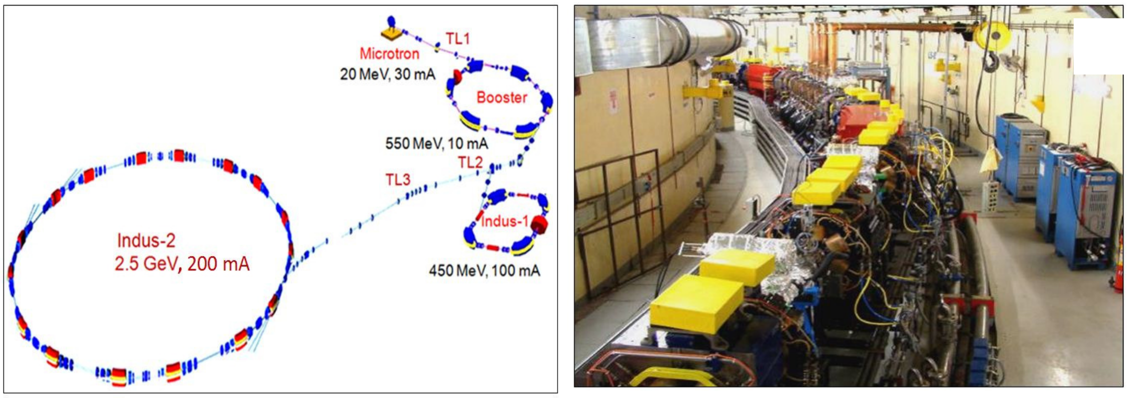

Figure 2.1: Indus-2 Synchrotron Source (2.5 GeV, 100 mA) at Raja Ramanna Centre for Advanced Technology (RRCAT), Indore, India

2.1.1 Energy Dispersive EXAFS Beamline (BL-08)

An energy dispersive EXAFS beamline had been developed and installed at a bending magnet port no. 8 of Indus-2 for X-ray absorption studies in the energy dispersive geometry[68]. The beamline works in the dispersive mode using a 460-mm-long Si (111) crystal mounted on an elliptical bender and a position-sensitive detector. The beamline covers photon energy range of 5 – 20 keV providing energy bandwidths of 0.3, 1.0 and 2.0 keV and with resolution of ~ 0.5, 1 and 2eV per pixels at photon energies of 5, 10 and 20 keV respectively. The working principal and the optical layout of the beamline is shown in Fig. 2.2 and Fig. 2.3 respectively. Here, a bent single crystal (C,C) forms part of an ellipse such that the source (S0) and the sample positions (S3) are situated at two focii of the ellipse. The elliptical optics ensures all radiation emerging from one focus (S0) reach the other focus (S3) after reflection from the crystal and offers minimum aberration.

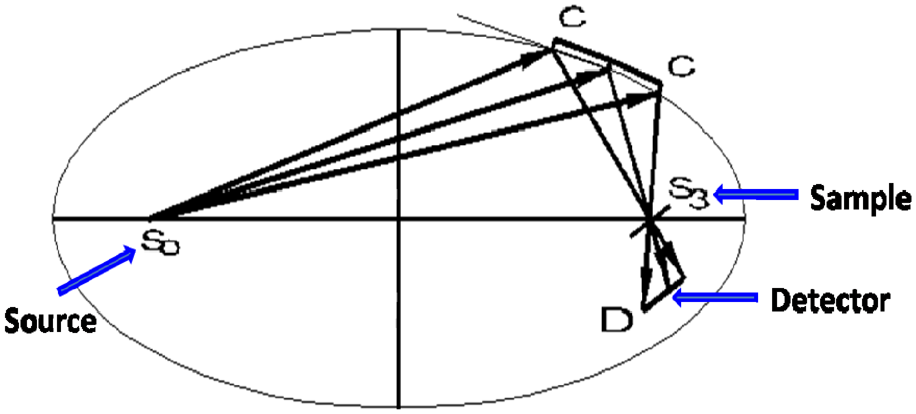

Figure 2.2: Working principle of the Energy Dispersive EXAFS beamline (BL-08) at Indus-2 SRS

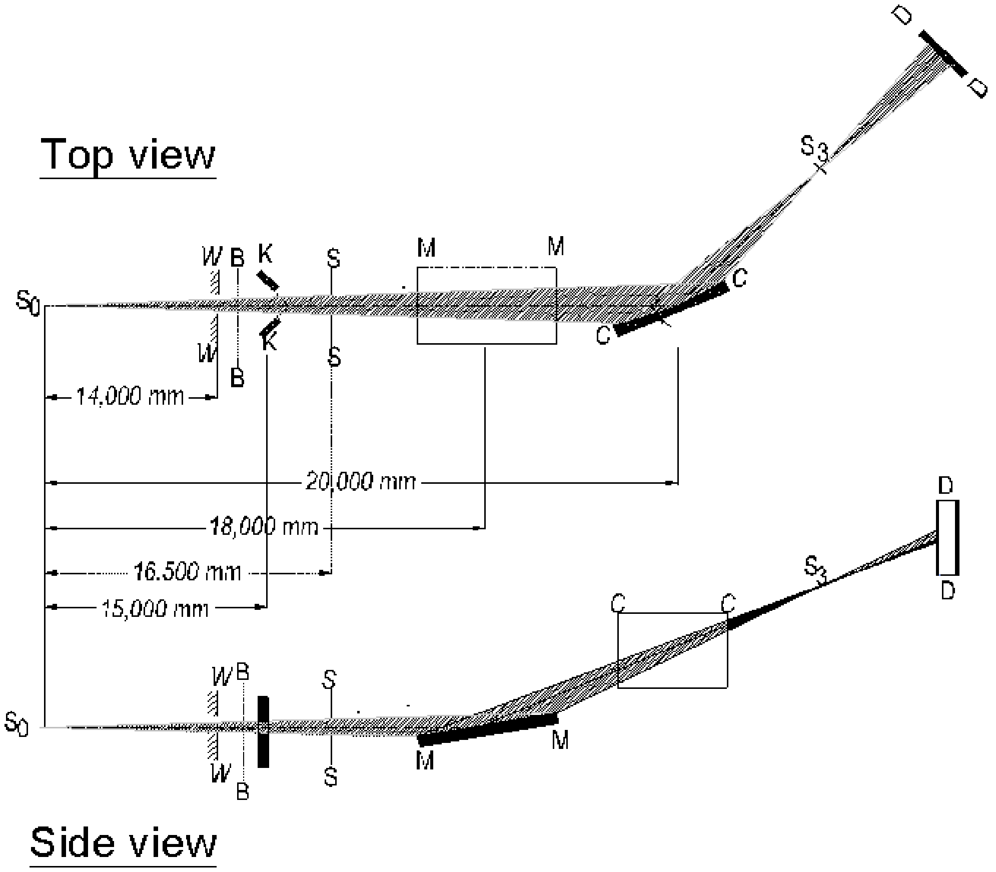

Figure 2.3: Optical layout of BL-08.

The synchrotron radiation is first passed through a Be window (B,B) of suitable thickness which isolates the ring vacuum from the beamline apart from cutting off the low energy part of the beam which in turn reduces the heat load at the optical elements of the beamline and then through the beam aperture system consisting of two copper blocks (K,K) positioned at an angle of 15° to the beam path for collimation. The collimated beam with horizontal divergence of 1.5 mrad is then made to fall on the slit system (S,S) which defines the final horizontal and vertical divergence of the synchrotron beam using two sets of water-cooled tantalum jaws. The beam emerging from the slit system with required vertical and horizontal divergences falls on a vertically focusing mirror (M, M) at a grazing angle of incidence ~ 0.2°, which cuts off the higher energy part of the synchrotron beam. After reflection from the mirror, the beam falls on a 460 mm long Si (111) crystal (C, C) mounted on a bender. Since a horizontally diverging beam falls on the long crystal, where angle of incidence of the beam varies continuously from one end of the crystal to the other, the crystal reflect a band of energy (ΔE) around a particular central energy (E_0) which depends on the angle of incidence of the beam at the centre of the crystal. The crystal being also elliptically bent, this spatially dispersed polychromatic radiation is also focused at the sample position (S3). The transmitted radiation from a sample diverges further and is detected by a position- sensitive detector (D,D). Thus, the energy dispersed absorption spectra of the sample over the whole bandwidth (ΔE) around the central energy (E_0) can be simultaneously recorded by the detector in a very short time scale of ~ 300 ms. As has been mentioned above, the elliptical shape of the ellipse is achieved by a mechanical bender, where two ends of crystal are pushed by two stepper motor driven warm shafts, while it is pivoted at two other lines using two cylindrical rods. It should be mentioned that a profiled crystal with varying height is used instead of a rectangular crystal uniform height so that perfect elliptical shape can be achieved by the bender instead of cylindrical shape. The details of the optical design of the beamline is presented elsewhere[46].

Generally, a CCD (Make: ANDOR, U.K., Model no. DW 436-F0) with 2048 × 2048 pixels each having a width of 13.5 μm is used as a position sensitive detector at BL-08. It has a theoretical resolution of 1eV/pixel, though this can be increased or decreased depending on the experimental requirements. Each element interacts with light to build up a charge – the brighter the light, and/or the longer the interaction, the more charge is registered. At the end of the measurement read out electronics pull the charge from the elements, at which point each individual charge reading is measured. CCDs require some degree of cooling to make them suitable for high grade spectroscopy. Typically this is done using either water cooling, peltier cooling (suitable for temperatures down to -90^{o}C), and liquid nitrogen cryogenic cooling. At BL-08, a water cooling system is used that maintains the detector temperature at –35^{o}C. The minimum time required by the CCD detector for data acquisition is 300 ms, however often several scans are accumulated to have better statistics in the data. In this thesis work, another position sensitive detector known as Mythen detector (Make: M/s., Dectris, Switzerland) has also been used. Mythen detector is aone dimensional X ray detector containing 1280 silicon microstrips. It operates on single photon counting mode thus leading to no readout noise. The minimum time required by the Mythen detector for data acquisition is 1 ms. A photograph of the beamline is shown in Fig. 2.4. All the works of this thesis on in-situ XAS studies on the growth of nanocrystals from solution phase have been carried out in this beamline.

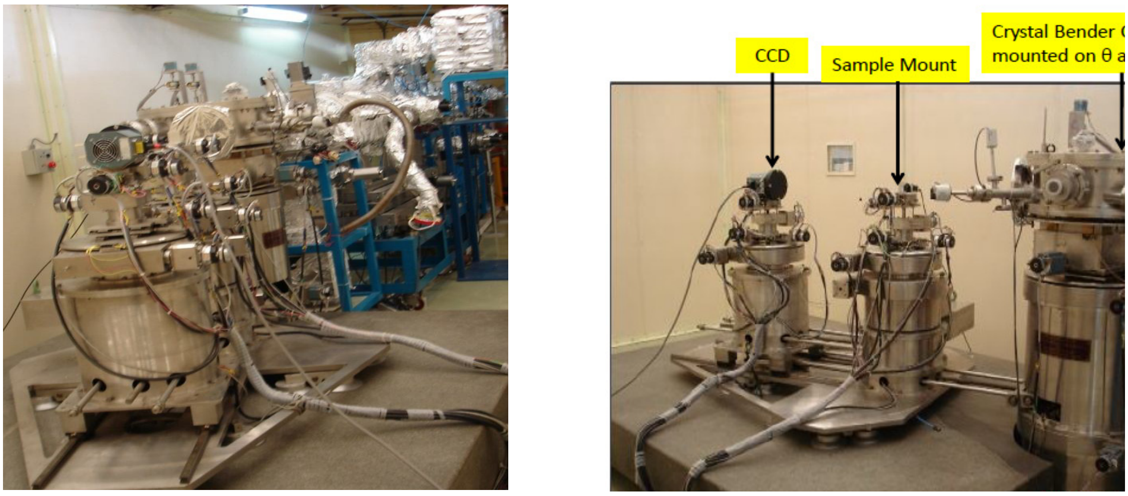

Figure 2.4: Photograph of the Energy Dispersive EXAFS beamline (BL-08).

2.1.2 Energy Scanning EXAFS beamline (BL-09)

The Energy-Scanning EXAFS beamline (BL-9) of Indus-2 SRS[64, 65], which works in the principle of conventional step-by-step scanning of a double crystal monochromator instead of a dispersive geometry used in BL-08, operates in the energy range of 4 keV-25 keV. The beamline optics consist of a Rh/Pt coated collimating meridional cylindrical mirror and the collimated beam reflected by the mirror is monochromatized by a Si(111) (2d = 6.2709 Å) based double crystal monochromator (DCM). The second crystal of DCM is a sagittal cylinder used for horizontal focussing while a Rh/Pt coated bendable post mirror facing down is used for vertical focusing of the beam at the sample position. Rejection of the higher harmonic content in the X-ray beam is performed by detuning the second crystal of the DCM to an extent so that the intensities of the higher harmonics are reduced by 99% with the loss of about half intensity of the incident flux. The role of the collimating mirror is to deliver parallel beam on the 1st crystal of the DCM. And depending on its angle w.r.t. the incident beam, it also cuts-off the higher energies. However, since the beamline is supposed to work upto 25 keV, the angle of the collimating mirror has been chosen accordingly. However, if a measurement is done at lower energy (5-8 keV), the 3rd harmonic of the energy will be present in the beam which will affect the EXAFS spectrum. This is removed by further detuning of the two crystals of the DCM from their perfect parallel configuration. Changing the angle of the collimating mirror depending on the energy range of interest to remove higher harmonics involves re-aligning of the rest of the baemline which is trouble-some and time consuming. The energy resolution $(\frac{E}{\Delta E})$ of the beamline at 10 KeV is~10^4. Fig. 2.5 shows the schematics of the beamline and Fig. 2.6 shows the actual photograph of the beamline.

This beamline operates in two modes, namely transmission mode and fluorescence mode. For recording the X-ray absorption spectra in transmission mode, the sample is placed between two 30 cm long ionization chamber detectors as shown in fig. 2.7. The first ionization chamber measures the incident flux (I_0) and the second ionization chamber measures the transmitted intensity (I_t). Absorption (μ) is calculated using formula, $\mu = \log(\frac{I_0}{I_t})$. A third ionization chamber is also used after the second ionization chamber where reference metal foils are measured for energy calibration. Appropriate gas pressure and gas mixture have been chosen to achieve 10-20% absorption in first ionization chamber and 70-90% absorption in second ionization chamber to obtain better signal to noise ratio.

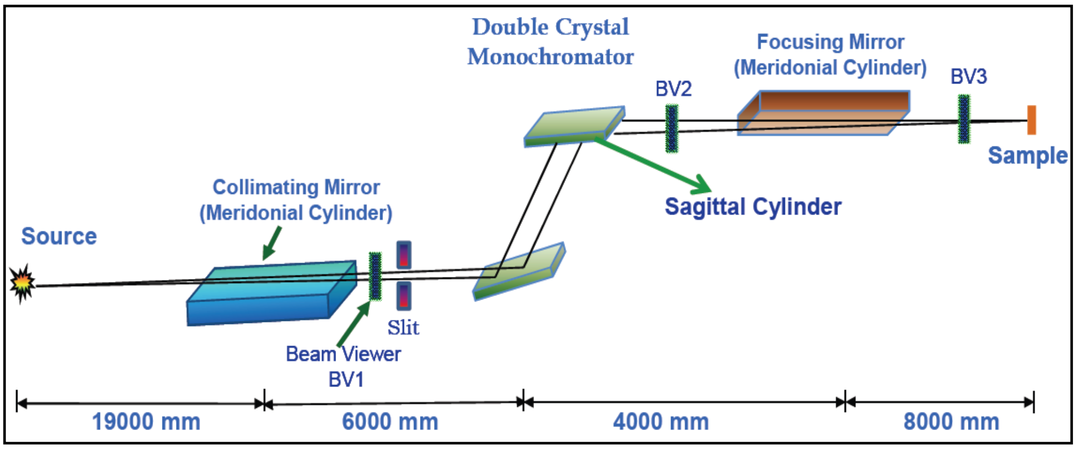

Figure 2.5: Schematic layout of Scanning EXAFS Beamline BL-09.

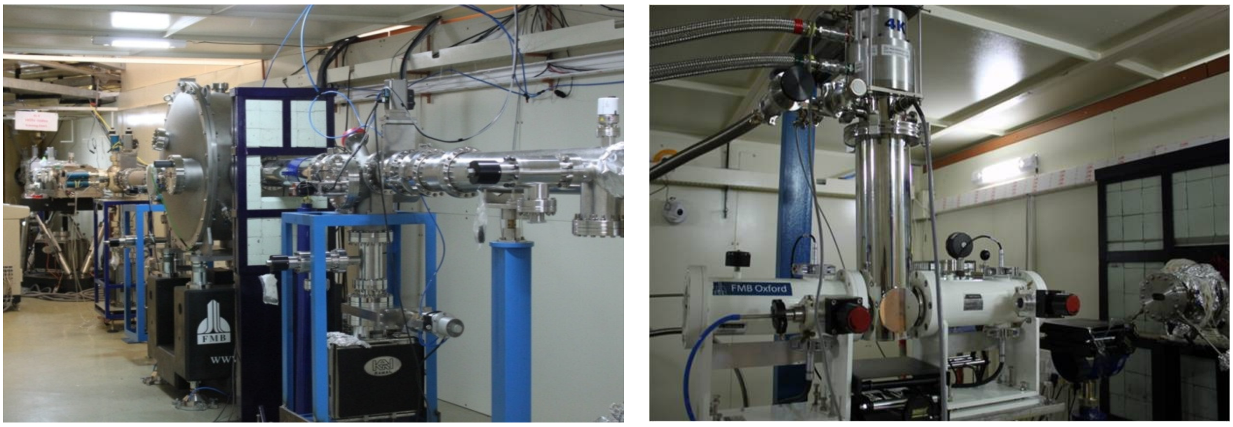

Figure 2.6: Photograph of (a) optics hutch and (b) experimental station of Scanning EXAFS Beamline BL-09.

Figure 2.7: Experimental set-up for transmission mode of EXAFS measurement.

For recording the X-ray absorption spectra in fluorescence mode, the sample is placed at 45^o to the incident X-ray beam. For measuring the florescence spectrum from the sample, a single channel Si drift detector is placed infront of the sample at 45^0. The detector is placed at right angle to the incident beam as shown in fig. 2.8so that the scattered X-ray is largely suppressed as the incident X-ray is polarized in the plane of synchrotron. An ionization chamber filled with a pre-defined gas mixture to absorb 10-20% of the incident beam was placed prior the sample stage to measure the incident beam (I_0). A proper region of interest (ROI) is selected in the detector output to selectively measure the fluorescence intensity of the absorbing atomic species (I_f). Thus the absorption co-efficient of the sample was determined by the relation ($\mu = I_f / I_0$) and the spectrum was obtained as a function of the energy by scanning the DCM of the beam line over the specified energy range.

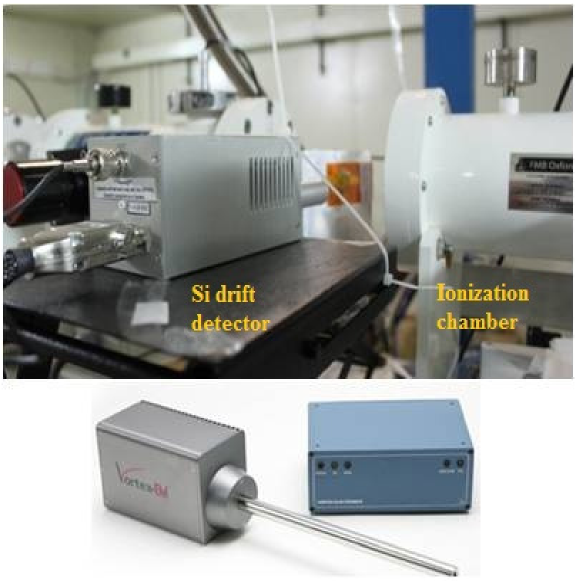

Figure 2.8: Experimental set-up for fluorescence mode of XAFS measurement.

Generally by using the step-by-step scanning of the DCM, a typical XAS data in this beamline takes 30 min. in case of transmission mode measurement and 1 hr. for fluorescence mode measurement. However, this beamline has recently been modified to carry out continuous scan XAS measurements[69] by which the data acquisition time could be reduced substantially retaining the advantage of high resolution offered by the step-by-step scan of a double crystal monochromator and therefore, it can now be used for *in situ* studies. In a DCM, energy selection is made by setting both the crystals simultaneously at a particular Bragg angle corresponding to the required energy and maintaining their parallelism, with the top surface of the first-crystal always coinciding with the centre of the goniometer. To achieve a fixed exit height between the incoming and outgoing beam in a DCM over the whole scanned energy range, the distance between the first and second crystal is adjusted using translation of the second crystal perpendicular to the crystal surfaces. As the goniometer angle is changed to change the energy, the beam reflected from the first crystal also changes the area of illumination on the second crystal. To make the beam always fall at the centre of the second crystal, the second crystal is also translated laterally using the linear stage. It was observed that this lateral movement of the 2nd crystal and the time taken to settle down the vibrations of the motors after the motion is carried out constitutes a large fraction of time for a full XAS scan. In the continuous scan mode of measurement on the other hand, this lateral motion of the 2nd crystal is restricted taking the advantage of its large length and thus the energy selection is done mainly by changing the Bragg angle by simultaneous rotational motion of the two crystals. The details of this measurement scheme have been reported elsewhere[69]. In this mode, a full EXAFS scan can be taken in 5 minutes while XANES data can be acquired in less than a 1 minute and hence this beamline has been used for *in-situ* studies on catalytic reactions in this thesis.

2.2 Analytical tools for TR-XANES

The popularity of *in-situ* and *operando* XAS techniques increases with increase in instrumental performance which often results in sub-second time resolution measurements. In these experiments XAS data were collected as a function of time while chemical or physical changes occur in the samples. Such an experiment generally results in accumulation of large number of XAS data sets and handling and analysing such a large number of data sets became a challenge for TR-XAS measurements. Different approaches are followed not only to analyze such a data set effectively, but also to differentiate different species formed during the time evolution of the sample. One of the methods is examination of isosbestic points[70]. Isosbestic points are the points where all spectra intersect. If the reaction solution contains only two species i.e. the reactant and the product, then isobestic points are the energy points where the value of the absorption coefficient is same for both the species. Therefore, even the concentration of the reactant and product varies in the reaction solution with time, the value of the absorption coefficient remains the same at these points. Presence of one or more isosbestic points thus implies the direct transformation of reactants to products without the formation of any intermediate species. However, their absence indicates the presence of intermediates in the reaction. This can give us an idea about the presence of intermediate species, but do not give any quantitative information regarding the number or structure of intermediates. For quantitative analysis, methods like Linear Combination Fitting (LCF) are used to reproduce the data set as a linear combination of known standard spectra. This can be used to identify known species formed during the reaction. More sophisticated analytical tools based on Linear Algebra like Principal Component Analysis (PCA) were used to determine the number of species formed during chemical reaction without using any standard. Chemometric method like Multivariate Curve Resolution-Alternating Least Squares (MCR-ALS) is also applied to XAS data set to identify different species formed during a reaction. These analytical tools have made the analysis and handling of TR-EXAFS data very easy and efficient.

2.2.1 Linear Combination Fitting (LCF)

Linear Combination Fitting (LCF) is used to reproduce a set of data as a linear combination of some standard data. The pre-requisite for this fitting is the linear structure of the data which is obeyed for the X-ray absorption coefficient. Therefore, the total absorption coefficient can be written as a sum of coefficients for all the species in the sample.

$$\mu_{sample} = \sum_{\mathrm{i}} x_i \; \mu_i \tag{2.1}$$

where, x_i are the fractions of the species present in the sample and μ_i are the standard XANES spectra.LCF involves modelling the spectrum for a sample of unknown chemical speciation using spectra from representative standards. LCF subroutine available in XAS data analysis programs like Athena[71] and Sixpack have been extensively used in XAS analysis. The main limitation of LCF is the need of reference spectra of all the species measured with similar energy resolution and consistent normalization. Therefore, it can be used only for systems where the species that can be present in the sample are well known. Though LCF with the just the first and last scan data may give idea about the kinetics of the reaction, however this procedure will not help to get the correct oxidation state of a species present in the reaction at any instant of time. In many situations, we are interested to know the species formed, identified by the oxidation state of an element present in it and if there are intermediates in the reaction, this is possible to determine only if we can use standards which are involved in the reaction.

2.2.2 Principal Component Analysis (PCA)

Principal Component analysis[72] (PCA) is a linear algebra based method to analyse a series of related data. Each data is represented as a vector in **n** dimensional space where **n** is the number of data point in a spectrum. If the measured data set contains **m** number of data, then it can be expressed in terms of **m** orthogonal basis vectors, referred as components. The basis vectors are the eigenvectors of the data matrix, **D(m,n)**. Ignoring the eigenvectors with small eigenvalues, minimum number of eigenvectors ($\mathbf{m_c}$) is chosen to represent the measured data set as a linear combination. These eigenvectors are known as principal components of the measured data set. To determine the least number of principal components a graphical method referred as "screen test" is generally used, where the eigenvalues are plotted in decreasing order and the number of principal components is chosen where the curve levels off to linear decline. The $\mathbf{m_c}$

number of principal components which are required to reconstruct the data set within experimental noise corresponds to the number of distinct species which contribute to the dataset. Thus, it gives us a way to determine the number of different species without any *a priori* knowledge about the identity of the species. However, the number of principal components is not necessarily equal to the number of different chemical species contained within the set of samples because the chemical species are not necessarily unique. The necessary condition for the success of PCA is the presence of distinctly different features in the spectra of each individual species. The next step in PCA is target transformation to relate the principle components to physical standards. Target transformations test the likelihood of a given standard spectrum to explain the variance in the set of spectra, and thereby identify the standards that most likely represent the data set. Because PCA relies on standard spectra, the same precautions used to interpret LCF apply here also.

Recently, PCA is used extensively for analyzing TR-XAS data[73, 74]. For example, Wang et. al.[74]has applied PCA analysis to *in-situ* TR-XAFS data of reduction and re-oxidation reaction of Cu doped Ceria. They have used theoretical modelling to identify the intermediate phases. In their study, it is evident that when fitted with two components there is a misfit in the XANES spectra which is most prominent between t=660-990 s. However, the fit quality greatly improves when three principal components are used to reproduce the spectra and the fit residuals are within noise limit. Therefore, this establishes the presence of intermediate and the time t^* when the intermediate dominates is the maxima of the residual plot when fitting is done with two components. The EXAFS spectra, μ_{int} recorded at t^* corresponds to the intermediate species. The EXAFS spectrum of the intermediate species is analyzed to identify the species.

2.2.3 Multivariate Curve Resolution with Alternating Least Squares (MCR-ALS)

MCR-ALS is a chemometric method for the resolution of spectroscopic data of time-evolving system with multi-constituents[75, 76]. The basic assumption of this method is the linear structure of the data set. The experimental data are first represented in a matrix form, called **D**(m, n), in which the m is the number of XAS spectra recorded and n is the number of data points of XAS data in terms of energy. Matrix **D** can be expressed in terms of matrix containing the concentration profiles **C**(m, k) and the matrix containing XAS spectra $\mathbf{S}^{\mathbf{T}}$(k, n) of the k species in the unknown mixture.

$$\boldsymbol{D} = \boldsymbol{C}\boldsymbol{S}^{\mathbf{T}} + \mathbf{E} \tag{2.2}$$

The matrix **E**(m,n) is the residual variation of the data. The matrices C and S^T follow physically and chemically meaningful constraints. As a first step for applying MCR-ALS, we need apriori information about the number of species which is the rank k of the matrices C and S^T. The PCA algorithm discussed in the earlier section helps us to find the rank k which is the minimum number of orthogonal components required to reproduce the data set. Once the rank is determined using PCA, the MCR-ALS algorithm can be applied with initial estimates of C and S^T matrices. The Alternating Least Square (ALS) optimization of the matrices C and S^T is done iteratively applying the following constraint.

$$\min \| D\text{-}CS^T \|^2 \tag{2.3}$$

Iterations are done alternatively on matrix C and S^T, while fixing the remaining parameters according to the following steps.

(a) Given D and the initial estimate of S^T, a minimization of C is carried out by the least square calculation considering relation (10) and the constraints for matrix C.

(b) Given D and the so-calculated C matrix, a minimization of S^T is carried out by the least square calculation considering relation (10) and the constraints for S^T.

(c) Then the reproduction of D using matrices C and S^T determined in steps (a) and (b) is done. If the convergence criterion is fulfilled, the process is finished. If not, the program goes back to step (a).

This iterative process gives the constituent species of the mixture and their concentration profiles with time. Recently, MCR-ALS has also emerged out to be as a popular analytical method which is effectively applied to the analysis of *in-situ* XAS data[77, 78].

2.3 EXAFS Data Analysis

As has been discussed in Chapter-1, the EXAFS spectra is theoretically represented by a $\chi(k)$ vs.k function described by equation 1.13. Thus to determine meaningful parameters from a EXAFS data set one has to convert the experimentally determined $\mu(E)$ vs. E spectra to a $\chi(k)$ vs.k data or more often $\chi(r)$ vs. r data by applying Fourier transformation. The experimentally generated $\chi(r)$ vs. r data is then fitted with a theoretical plot generated using eqn. 1.13 and assuming a guess structure of the sample. The steps in this data reduction and fitting process which have been followed in this thesis work are described below.

The first step of EXAFS data analysis is EXAFS data processing which includes deglitching the spectra, defining Eo, normalization of the spectra to unit edge step, background subtraction, conversion from energy to k-space, fourier transformation to r-space and generation of experimental $\chi(r)$ vs. r plots using proper window function and inverse transformation. After data processing, the EXAFS data fitting is done which includes generation of theoretical $\chi(r)$ vs. r plots using a crystallographic/amorphous model and fitting of the experimental data with the theoretical plots by nonlinear least squares fitting. The data processing has been performed using Athena software of the Demeter programme and data fitting is done using Artemis software of the Demeter programme. Demeter is a freely available programme developed by Dr. Bruce Ravel and co-workers[71]. This package is based on the IFEFFIT library[79] of numerical and XAS algorithms and it is written in the Perl programming language. This package consists of softwares like ATHENA, a program for XAS data processing, ARTEMIS, a program for analysis of extended X-ray absorption fine structure (EXAFS) data using theoretical standards computed by the FEFF program[80, 81] and HEPHAESTUS, a collection of beamline utilities based on tables of atomic absorption data.

2.3.1 Data Processing using Athena

The Athena software is used for EXAFS data processing. As such ATHENA is useful for data visualization at the beamline as well as for processing of data such as conversion of raw data to $\mu(E)$ spectra, plotting, energy calibration, alignment of data, use of reference spectra, deglitching and merging of data etc. Fig. 2.9 gives a view of the Athena software window. The X ray absorption spectra $\mu(E)$ versus E, is normalized by dividing by the size of the edge step which compensates for the uncertainties in the concentration, sample thickness and any other factor that can affect the spectrum. Edge-step of the data is determined by a linear pre-edge subtraction and regression of a quadratic polynomial beyond the edge.

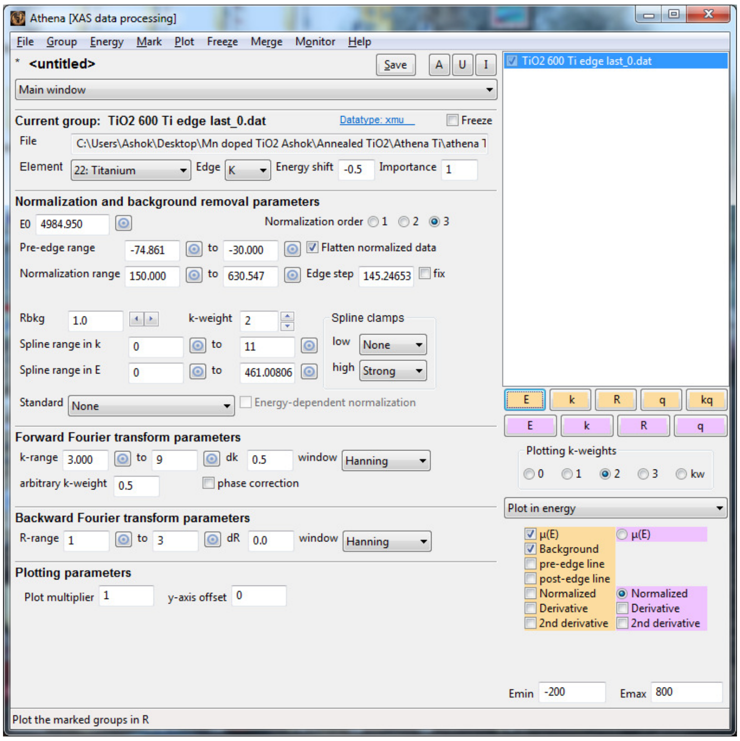

* <untitled>

Main window

Current group: TiO2 600 Ti edge last_0.dat

Datatype: xmu

☐ Freeze

File C:\Users\Ashok\Desktop\Mn doped TiO2 Ashok\Annealed TiO2\Athena Ti\athena T

Element 22: Titanium

Edge K

Energy shift -0.5

Importance 1

Normalization and background removal parameters

E0 4984.950

Normalization order ○ 1 ○ 2 ● 3

Pre-edge range -74.861 to -30.000

☑ Flatten normalized data

Normalization range 150.000 to 630.547

Edge step 145.24653 ☐ fix

Rbkg 1.0

k-weight 2

Spline clamps

low None

high Strong

Spline range in k 0 to 11

Spline range in E 0 to 461.00806

Standard None

☐ Energy-dependent normalization

Forward Fourier transform parameters

k-range 3.000 to 9

dk 0.5

window Hanning

arbitrary k-weight 0.5

☐ phase correction

Backward Fourier transform parameters

R-range 1 to 3

dR 0.0

window Hanning

Plotting parameters

Plot multiplier 1

y-axis offset 0

Plot the marked groups in R

☑ TiO2 600 Ti edge last_0.dat

Plotting k-weights

○ 0 ○ 1 ● 2 ○ 3 ○ kw

Plot in energy

☑ μ(E)

☑ Background

☐ pre-edge line

☐ post-edge line

☐ Normalized

☐ Derivative

☐ 2nd derivative

○ μ(E)

● Normalized

☐ Derivative

☐ 2nd derivative

Emin -200

Emax 800

Figure 2.9: The main window of ATHENA program.

After normalization of the data, background subtraction has been performed to isolate the EXAFS oscillations from the atomic contribution of the absorption $\mu_0(E)$, and the background absorption or scatter from other elements in the beam path. AUTOBK algorithm[82] is used for background subtraction, which determines an empirical background spline based on a distinction between data and background in terms of Fourier components. Background subtraction is accomplished by ordinary linear least squares fitting, typically using cubic spline functions as shown in Fig 2.10. The EXAFS oscillations are extracted by subtracting the isolated atom absorption $\mu_0(E)$ (which is generally unknown) from the absorption of the atom in condensed matter $\mu(E)$, and then dividing by $\Delta\mu_0(E_0)$ as given in Equation 2.4. $\Delta\mu_0(E_0)$ is the difference between pre-edge and post-edge polynomials extrapolated to the edge energy E_0 which is used as the normalization constant.

$$\boldsymbol{\chi(E) = \frac{\mu(E)-\mu(E_0)}{\Delta\mu_0(E_0)}} \tag{2.4}$$

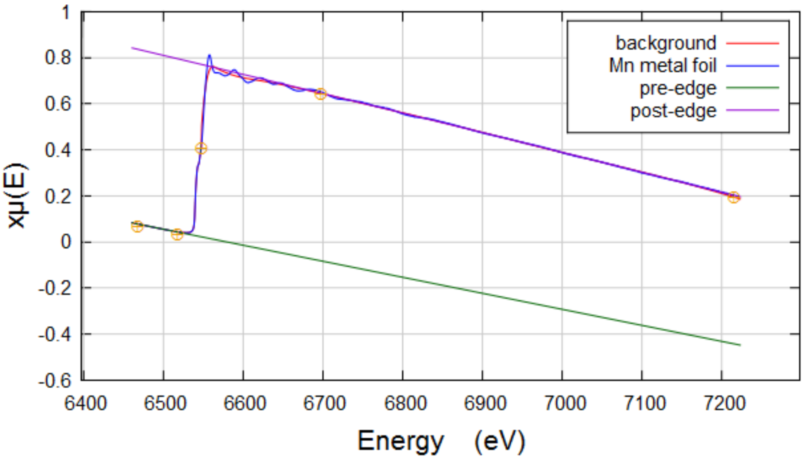

Figure 2.10: Pre-edge, post-edge polynomial and background subtraction.

Subsequently, the data in the energy scale is converted to the photoelectron wave number scale (k) as defined by,

$$\boldsymbol{k} = \sqrt{\frac{\boldsymbol{2m(E-E_0)}}{\boldsymbol{\hbar^2}}} \tag{2.5}$$

The converted k space spectrum is generally weighted by an increasing function of k (such as k, k^2or k^3) to amplify the data at high k which is of small amplitude as shown in Fig. 2.11.The functions $\chi(k)\,k^n$ are Fourier transformed in r space to generate the $\chi(r)$ versus r(or FT-EXAFS) spectra in terms of the distances from the center of the absorbing atom as shown in Fig. 2.12.The functions $\chi(k)\,k^n$ are multiplied by a window function and choosing a usable range in the k space. The region below k=2Å^{-1} is excluded because of possible complications from multiple scattering etc. The transformed data ($\chi(r)$ vs. r) actually consist of a complex function, which has real and imaginary parts, or alternatively a modulus and phase. The modulus is the most frequently used quantity, but the real and imaginary parts are also useful. They exhibit significantly more structure than the modulus does, and they don't suffer from nonlinear interference and hence during the fitting, modulus as well as real and imaginary parts should be monitored. After the raw data has been processed appropriately in ATHENA, it is used in ARTEMIS for theoretical modeling and fitting.

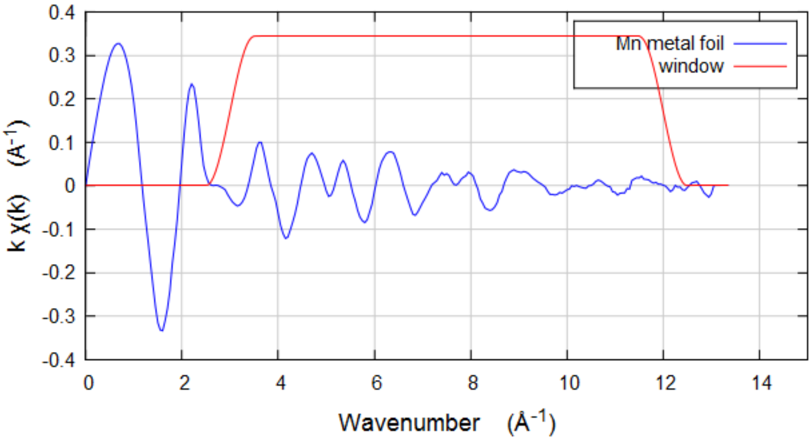

Figure 2.11: *k* space EXAFS spectrum with hanning window.

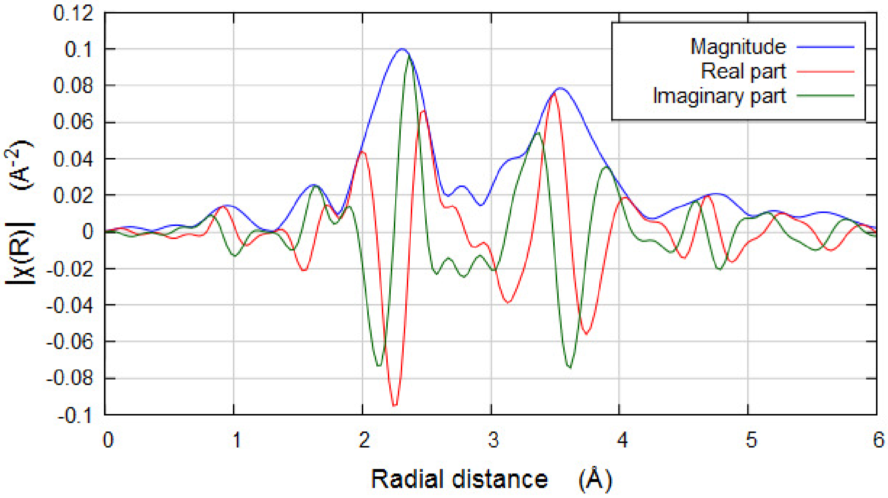

Figure 2.12: Fourier transformed EXAFS spectra alongwith real and imaginary contribution.

The ATHENA software also provides other utilities like linear combination fitting, principal component analysis, peak fitting using different line shapes (arctangent, Gaussian, Lorentzian), log ratio/phase difference analysis and generating the difference spectra. ATHENA can also import and display the results of FEFF8 calculations[81] for comparison with measured data. Additional features like self-absorption corrections for fluorescence data are also available in this software.

2.3.2 Data fitting using Artemis

ARTEMIS is a graphical interface for EXAFS data fitting in the DEMETER programme. It has access to the functionalities of the ATOMS program, which generates input file format suitable for FEFF. Fig. 2.13 shows the ARTEMIS window in its data view.

In EXAFS analysis, a theoretical EXAFS spectrum has been simulated for the system to be analyzed from an assumed model of the system containing unknown parameters whose values are determined by fitting. ARTEMIS can read crystallographic data either in the form of an ATOMS input file or a crystallographic information file (.cif) or can be supplied structure information interactively. These data are then converted into a FEFF input file. ARTEMIS includes access to the functionality of the ATOMS program, which converts crystallographic data into a format suitable for FEFF. FEFF is an *ab initio* multiple scattering code used to generate theoretical fitting standards for EXAFS analysis and simulation of XANES spectra[83]. FEFF performs its calculation in real-space on a specified cluster of atoms provided by ATOMS subroutine. $f(k)$ and $\delta(k)$ (the scattering amplitude and phase shift due to the neighbouring backscattering atom respectively) and the photoelectron mean free path $\lambda(k)$ are calculated theoretically. After the FEFF run, scattering paths are generated and information including the path distances, degeneracy, atomic species in the path, whether the path is single or multiple-scattering have been displayed. The theoretical EXAFS data is the summation of EXAFS data simulated for different scattering paths. Each scattering path has a degeneracy N (the number of equivalent atoms in single scattering paths), an effective distance r (half path-length), and a mean square variation parameter σ^2, as mentioned in the EXAFS equation (Equation 1.13). Once calculated, each of these paths can be easily modified during fitting of the experimental data to give different values of the parameters N, r, σ^2, and even E_0. The parameters that are often determined from a fit to the EXAFS spectrum affect either the amplitude of the EXAFS oscillations (N, S_0^2, σ^2) or the phase of the oscillations (ΔE_0 and Δr, the energy shift and the change in half path length respectively). Since EXAFS data is limited by a finite k and r ranges, therefore there is a limit to the number of parameters that can be extracted from the analysis of EXAFS data. Information theory is used to correlate the amount of information in the original EXAFS spectrum to the information in Fourier transform spectrum as determined from the Nyquist theorem[39]:

$$N_{ind} = \frac{2\Delta k \Delta r}{\pi} \tag{2.6}$$

where N_{ind} is the number of independent points, Δk is the Fourier transformed data rangeand $\Delta r$is the region used in EXAFS data analysis. Therefore, the number of fitting parameters of the EXAFS data should always be less than the number of independent points. The goodness of the fitting of EXAFS data is generally expressed by the R_{factor}which is defined as:

$$R_{factor} = \sum \frac{[\mathrm{Im}(\chi_{dat}(r_i) - \chi_{th}(r_i)]^2 + [\mathrm{Re}(\chi_{dat}(r_i) - \chi_{th}(r_i)]^2}{[\mathrm{Im}(\chi_{dat}(r_i)]^2 + [\mathrm{Re}(\chi_{dat}(r_i)]^2} \tag{2.7}$$

where, χ_{dat} and χ_{th} refer to the experimental and theoretical $\chi(r)$ values respectively and Im and Re refer to the imaginary and real parts of the respective quantities. In general, the value of R_{factor} factor less than 0.03 are considered as a reasonable fit.

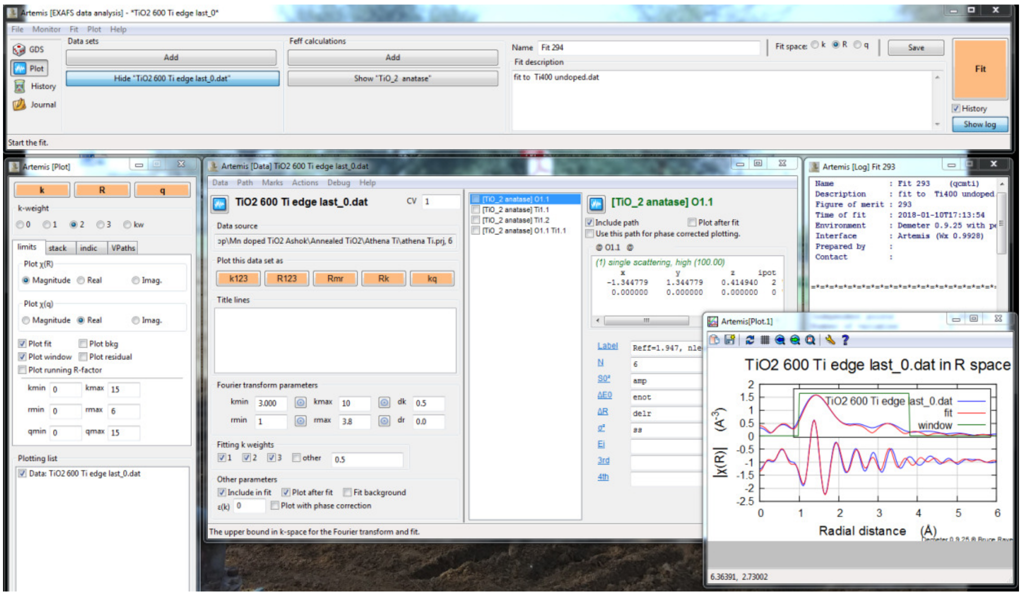

Name Fit 294

Fit space: ○ k ● R ○ q

Fit description: fit to Ti400 undoped.dat

☑ History

Start the fit.

k-weight: ○ 0 ○ 1 ● 2 ○ 3 ○ kw

Plot χ(R): ● Magnitude ○ Real ○ Imag.

Plot χ(q): ○ Magnitude ● Real ○ Imag.

☑ Plot fit ☐ Plot bkg

☑ Plot window ☐ Plot residual

☐ Plot running R-factor

kmin 0 kmax 15

rmin 0 rmax 6

qmin 0 qmax 15

Plotting list: ☑ Data: TiO2 600 Ti edge last_0.dat

TiO2 600 Ti edge last_0.dat CV 1

Data source: ɔp\Mn doped TiO2 Ashok\Annealed TiO2\Athena Ti\athena Ti.prj, 6

Plot this data set as

Title lines

Fourier transform parameters

kmin 3.000 kmax 10 dk 0.5

rmin 1 rmax 3.8 dr 0.0

Fitting k weights: ☑ 1 ☑ 2 ☑ 3 ☐ other 0.5

Other parameters: ☑ Include in fit ☑ Plot after fit ☐ Fit background

ε(k) 0 ☐ Plot with phase correction

The upper bound in k-space for the Fourier transform and fit.

☐ [TiO_2 anatase] O1.1
☐ [TiO_2 anatase] Ti1.1
☐ [TiO_2 anatase] Ti1.2
☐ [TiO_2 anatase] O1.1 Ti1.1

[TiO_2 anatase] O1.1

☑ Include path ☐ Plot after fit

☐ Use this path for phase corrected plotting.

@ O1.1 @

```
(1) single scattering, high (100.00)
     x           y           z         ipot
 -1.344779    1.344779    0.414940    2
  0.000000    0.000000    0.000000    0
```

Label Reff=1.947, nle

N 6

S0² amp

ΔE0 enot

ΔR delr

σ² ss

Ei

3rd

4th

```
Name            : Fit 293     (qcmti)
Description     : fit to  Ti400 undoped
Figure of merit : 293
Time of fit     : 2018-01-10T17:13:54
Environment     : Demeter 0.9.25 with pe
Interface       : Artemis (Wx 0.9928)
Prepared by     :
Contact         :

=*=*=*=*=*=*=*=*=*=*=*=*=*=*=*=*=*=*=*=*:
```

6.36391, 2.73002

Figure 2.13: Main window of ARTEMIS program.

2.4 Complementary Techniques

It has been mentioned in Chapter-1, that TR-XAS has emerged out to a very effective technique for understanding the structural changes in a sample during a chemical reaction. However, no technique is self sufficient and every technique helps us to understand only a part of the system. In case of complicated studies where many species are involved, the analysis and conclusion become very challenging. Therefore, it is always better to rely on more than one technique to have a broad and better understanding of the processes. With this point of view often several other techniques have been complemented with TR-XAS for simultaneous measurements to get a better insight into the reaction procedure. UV-Vis spectroscopy is often complemented with XAS measurement while studying the growth of nanoparticles. Growth of gold and platinum nanoparticle formation has been studied simultaneously by these techniques by several researchers. Stotzel *et. al*. have used QEXAFS and UV-Vis techniques simultaneously to monitor the growth of TiO_2 nanoparticles[22]. This combination of techniques gives information not only about the local structure of different species in the solution but also about their optical properties. Polte *et. al.*[50] have combined XANES and SAXS to study the growth of gold nanoparticles, which has helped to determine the changes in oxidation states of gold cations concurrently with shape, size and polydispersity of the nanoparticles formed. *In-situ* XRD and XAS are combined to observe the ZnO nanoparticle encapsulation into Zeolite-Y with heating upto 550°C[84]. This combination gave insight into short range and long range structural changes in the samples. Many other techniques were also complemented to TR-XAS like IR spectroscopy[26], Raman spectroscopy[25], Mass spectrometry[26], etc. Briois *et. al.*[25] studied oxidation of ethanol by Cerium based catalysts using combined Quick-XANES, UV-Vis and Raman spectroscopies. Newton *et. al.*[26] complemented FT-IR, Dispersive EXAFS and Mass spectrometry techniques to investigate the structural changes in Rh-based catalysts during NO reduction of CO. These three techniques helped to correlate the surface speciation, local structure and catalyst activity of the catalysts. Complementary techniques give a broader view of the system and focus on different aspects of it which in turn results in more consolidated conclusions. In the present work we have complemented UV-Vis spectroscopy with TR-XAS for studying growth of nanoparticles, while for *in-situ* catalysis studies we have complemented online gas chromatography measurements with TR-XAS.

2.4.1 UV-Visible Spectroscopy

UV-Visible spectroscopy deals with the absorption or reflectance spectroscopy in the UV and visible spectral region[85].Absorption of visible and UV radiation in both atoms and molecules is associated with excitation of electrons from lower to higher energy levels. Since the energy levels are quantized, only lightwith the precise amount of energy can cause transitions from one level to another will be absorbed. The absorption follows Beer-Lambert Law. This law states that whenever a beam of monochromatic light is passed through a sample with an absorbing substance, the decreasing rate of the radiation intensity along with the thickness of the absorbing solution is actually proportional to the concentration of the sample and the incident radiation. UV-Vis spectroscopy has applications in several fields. For example, this technique can be used to identify functional groups, known compounds, configurations of geometrical isomers, purity of substances, etc. Also, this technique finds application in nanoparticle characterisation. Some nanoparticles, e.g. gold nanoparticles show the surface plasmon resonance (SPR) peak in the UV or visible region of the spectrum. The surface plasmon resonance originates due to collective resonant oscillations of the free electrons at the metal surface in presence of incident light. The position of the SPR peaks in wavelength scale and their intensities are related to the size, shape and surface chemistry of the nanoparticles. Therefore, studying the SPR peaks using UV-Vis spectroscopy can provide information regarding the size, shape and surface of nanoparticles. UV-Vis spectroscopy measurement can be done in two modes: Scanning and Dispersive. In scanning mode, the instrument has a monochromator which is a grating or a prism and it monochromatise the light from the UV Visible source. This monochromatic light falls on the sample and the transmitted intensity is measured using a photodetector. By adjusting the monochromator different wavelengths are selected and the absorption spectrum of the sample is generated.

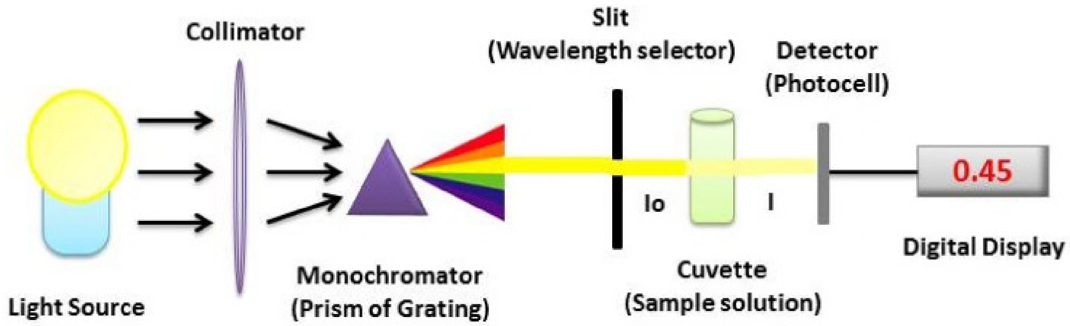

Figure 2.14: Schematics of UV Visible spectrophotometer.

However, for fast measurement of the UV-Visible spectra dispersive mode of measurements are used, where the whole range of wavelengths are focused on the sample and the transmitted intensity is collected and measured using a position sensitive detector as shown in fig. 2.15. In the present work we have used Deuterium and Halogen light source covering wavelength range of 200-2500 nm and a Fiber Optic spectrometer (Make: Avantes, Netherlands). The photograph of the source and spectrometer are shown in fig. 2.16. It should be noted here that the optics of XAS measurement set-up and UV-Vis spectroscopy are similar, both the techniques deal with measurement of absorption coefficient in X-ray and optical wavelength regime respectively . using Beer-Lambert law. . Similar types of optical components (collimator, monochromator, slits etc.) are used in both the cases and both the techniques can be used in scanning and dispersive modes.

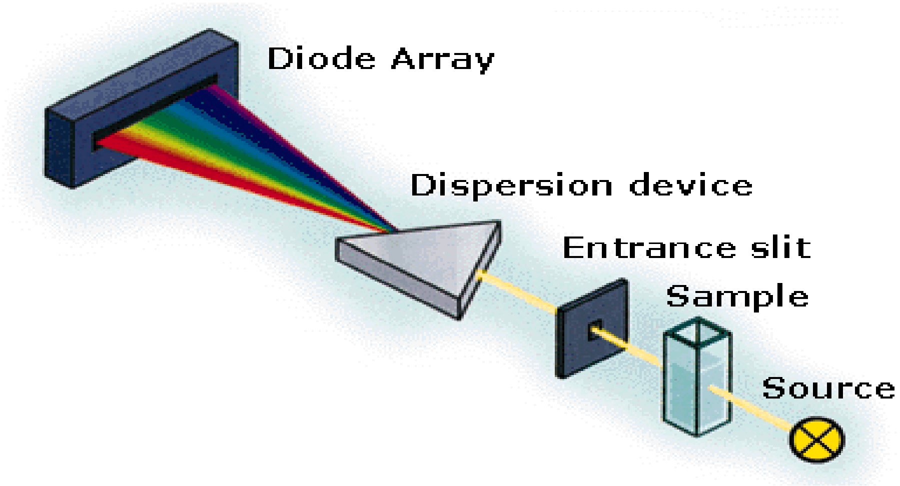

Figure 2.15: Schematics of Fiber optics based UV Visible spectrometer

(a) (b)

Figure 2.16: (a) Photograph of Avalight DHc light source (b) Photograph of AvaSpec-ULS2048L-USB2 Fiber optics based UV Visible spectrometer

2.4.2 Gas chromatography

Gas chromatography is an analytical technique that helps in identifying various gaseous components in a sample and gives a quantitative estimate about the concentration of various components[86]. In gas chromatography there is a mobile phase which is an inert gas and a stationary phase which is a layer of liquid or polymer on a solid support inside a metal tube known as column. The injected sample interacts with the stationary phase and different components in the sample elutes at different times through the stationary phase, called the retention time. The separated components get detected by the detector. Different detectors used in GC are thermal conductivity detector (TCD) , flame ionization detector(FID), electron capture detector (ECD) and mass spectrometer (MS) which responds to the physicochemical property of the analyte.

Figure 2.17: Photograph of Gas Chromatograph (Make: Netel India Ltd.).

Photograph of the GC system (Make: Netel India Ltd.) used in the *in-situ* probing of heterogenous catalysts included in this thesis work is shown in Fig. 2.17. The GC has one TCD detector and two FID detectors. The oven and injector temperatures are kept at 50ºC for all measurements. Packed columns Molecular Sieve 5A has been used for detection of H_2, N_2, CO and CH_4 gases, while Porapak N column has been used for detection of CO_2 and CH_4 gases. An autosampling valve has been used before the GC to enable online detection of gases. The schematic of the working principal of the autosampling valve has been shown in Fig. 2.18. When the valve is in position A, the sample flows through the external loop to the vent and the carrier gas flows through the GC columns. When the valve is switched to position B, the sample in the external loop along with the carrier gas is injected into the column for analysis.

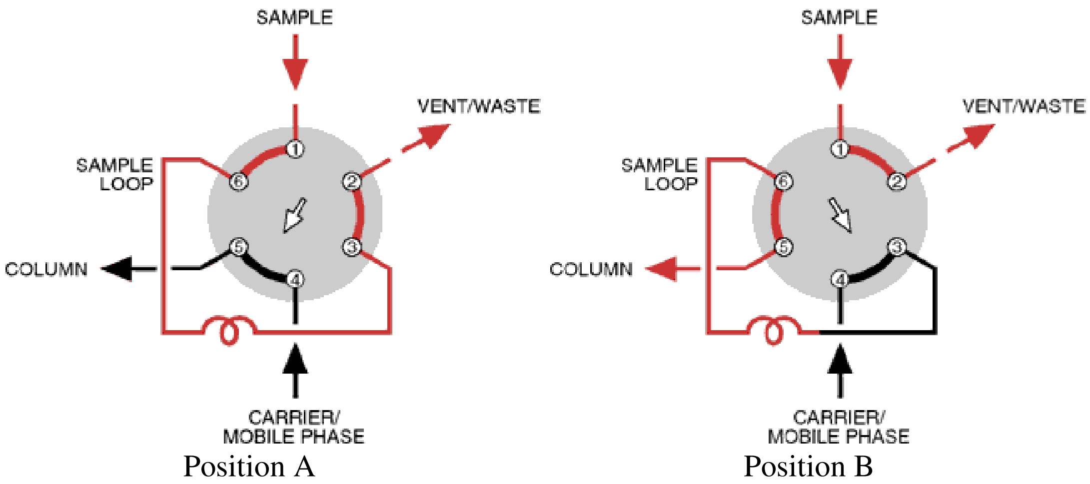

Figure 2.18: Schematics of autosampling valve working principal.

2.5 *Ex-situ* techniques

2.5.1 X-ray Diffraction

X-ray diffraction[87] (XRD)is an analytical technique used for the identification of crystalline phases of various materials and the quantitative phase analysis subsequent to the identification. The diffraction of X-rays from a crystalline solid is governed by Bragg's law, $n\lambda = 2d\sin\theta$ where n is an integer, λ is the characteristic wavelength of the X-rays impinging on the crystallize sample, d is the inter-planar spacing between rows of atoms, and θ is the angle of the X-ray beam with respect to these planes. An X-ray diffraction spectrum consists of a set of diffracted intensities and the angles at which they are observed. This diffraction pattern can be thought of as a chemical fingerprint, and chemical identification can be performed by comparing this diffraction pattern to a database of known patterns. In this thesis work, theX-ray diffractometer (Bruker D8 Advance diffractometer) with Cu Kα radiation (λ = 1.54 Å) and a LYNXEYE detector have been used.

Figure 2.19: Photograph of X-ray diffractometer (Bruker D8 Advance diffractometer).

2.5.2 X-ray Photoelectron Spectroscopy

X-ray Photoelectron Spectroscopy[88] (XPS) is based on photoelectric effect. It is a surface sensitive technique and provides information about elemental composition, chemical state and electronic state. When X-rays of energy hν falls on a sample, photoelectons are emitted from the sample surface. The kinetic energy and number of photoelectrons emitted is measured by an electron energy analyzer.

The kinetic energy of the emitted photoelectron is given by,

$$K.E. = h\nu - B.E. - \Phi s \tag{2.8}$$

where, $B.E.$ is the binding energy of the electron in atomic orbital from which the electron originates and Φs is the work function dependent on both the spectrometer and the material. The schematic representation of the working principle of an XPS instrument is shown in fig. 2.20. The XPS spectrum is obtained as a plot of the number of detected photoelectrons per energy interval versus their kinetic energy. Since the mean free path of the electrons in solids is less than

10 nm, a majority of the detected electrons originate from the top few atomic layers makes this technique surface sensitive. Since the core levels of each element have unique binding energies, XPS can be used to identify and determine the concentration of the elements at the surface. Variation in the elemental binding energies (chemical shifts), arising from differences in the chemical potential (Madelung potential) and polarizability of compounds can be used to identify chemical states of the elements in materials being analyzed. In this thesis work, *ex-situ* X-ray Photoelectron spectroscopy measurements were carried out using a SPECS X-Ray Phototelectron Spectroscopy (XPS) set up with a PHOBIOS 100/150 Delay Line Detector (DLD) and Al Kα (1486.6eV) dual anode as the source. As an internal reference for the absolute binding energy, the C-1s peak (284.5 eV) was used. The Au-Pt bimetallic particles were etched in the preparation chamber using an IQE-IIA Specs model ion source unit having ion energy of 2 keV, operating at a filament current of 6 mA. The XPS spectra were recorded on the as-prepared sample as well as on the etched sample after different periods of etching.

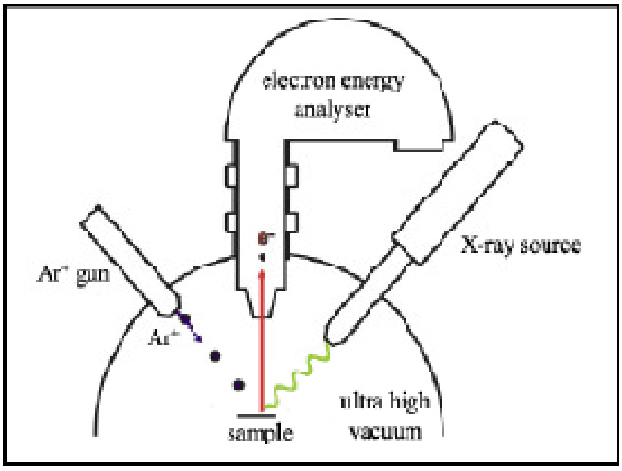

Figure 2.20: Block diagram of XPS instrument.

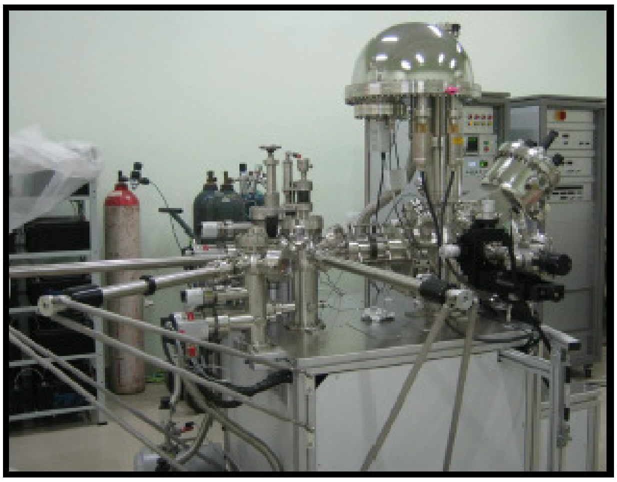

Figure 2.21: Photograph of XPS instrument.

2.5.3 Transmission Electron Microscopy

Optical microscopy has limited ability to resolve objects because of the wavelength of light used. Transmission Electron Microscopy (TEM) uses electron beam of much shorter wavelength as a probe and hence details of a specimen can be observed to a much higher magnification level than the conventional optical microscopes[89]. In TEM a beam of high energy electrons is transmitted through a thin sample to form an image. TEM consists of an electron gun which produces the electron beam, magnetic lenses for focusing of the beam and fluorescent screen or CCD detector for recording the image. When the high energy electron beam falls on the sample, part of the beam gets transmitted through the sample and part of it is scattered. The transmitted beam is focused by the objective lens into an image screen or CCD camera to generate the image. Incident electrons that are scattered by atoms elastically in the specimen which is crystalline forms a pattern of spots, each spot corresponds to a specific atomic spacing. This pattern can then yield information about the orientation, atomic arrangements and phases present in the area being examined. The conventional diffraction mode used in TEM is called selected area diffraction (SAED). The spherical aberrations of the objective lens limit the area of the selected object to few hundred nanometers. SAED patterns of a crystal permit to obtain the symmetry of its lattice and calculate its inter-planar distances using Bragg's law. This is useful to confirm the identification of a phase, after assumptions generally based on the literature of the studied system and on chemical analyses.

In the present thesis work, ex-situ TEM images of the nanoparticles were collected using a CM200 machine with Tungsten filament operated at an acceleration voltage of 200 kV with a resolution of 2.4 Å. Metal nanoparticles, after the completion of reaction have been collected, washed, centrifuged and then re-dispersed in water by ultrasonicating for 20 minutes. A drop of this solution was placed on a copper grid, dried at room temperature and then imaged by TEM.

Figure 2.22: Photograph of the Transmission Electron Microscope (CM200) used in this thesis work.

2.5.4 High Resolution Transmission Electron Microscopy

High resolution Transmission Electron Microscopy is similar to Transmission Electron Microscopy except that it gives an atomic scale resolution. It uses both the transmitted and the scattered electron beams to create an interference image which is a phase contrast image and can be as small as the unit cell of crystal. In the present thesis work, the High Resolution Scanning

Transmission Electron Microscope (HR-STEM) images on the above samples have been acquired with a probe-corrected 80-300 Titan TEM at 300 KV using HAADF detector. Metal nanoparticles, after completion of the reaction have been collected, washed, centrifuged and then re-dispersed in water by ultrasonicating for 20 minutes. A drop of this solution was placed on a copper grid, dried at room temperature and then imaged by TEM.EDS (Energy Dispersive Spectroscopy) line scan for elemental mapping has been done on a nanocrystal in the same set-up using EDAX 30mm Si-Li detector by tilting the sample by 20º to maximize the collection of X-rays. In EDS line scan, the electron beam moves along a line on the sample surface and measures the count of the characteristics fluorescent X-rays coming out of the elements present in the sample as a function of the beam position. The count rate is measured in the selected windows of the spectrum corresponding to the characteristic X-ray energies of the particular element expected in the sample. The variation of the X-ray count rate in the selected window corresponding to a particular element gives the changes in concentration of that element over the line of scanning.

Chapter 3

In-situ XAS studies on growth of Au and Pt monometallic nanoparticle

Noble metal nanoparticles are important due to their uniqueness in properties and wide variety of applications in different fields among which gold and platinum seek special attention. They have applications in biotechnology, catalysis and optoelectronics[90-94]. Properties of these nanoparticles are highly dependent on their size and shape, thus accentuating the importance of their synthesis process. Though Gold and Platinum nanoparticles are one of the widely studied nano-systems which have been subjected to various studies, initial stages of nucleation and growth of these nanoparticles remain unexplored for a long time mainly due to scarcity of suitable experimental techniques which can explore the initial stages of growth. As has been elaborately discussed in the Introduction (Chapter-1), Time Resolved X-ray absorption spectroscopy (TR-XAS), which include both XANES and EXAFS, can simultaneously give insight into the structural changes in the species during the growth of nanoparticles from solution phase, as well as in the oxidation states of the metal cations. In the present study, we have combined XAS and UV-Vis spectroscopy to study the growth of Gold and Platinum nanoparticles stabilized by block copolymer. Block copolymers consist of two or more chemically distinct polymeric units connected by covalent or non-covalent bonds. Block copolymer forms a crown ether structure which engulfs metal ions and acts as both reducing and stabilizing agents. The present *in-situ* studies have given direct insight into the growth mechanism of these nanoparticles from their respective precursors. However, there is no effect of X ray beam on the nanoparticle synthesis. This has been verified by keeping the precursor solution in the beam for 2 hours and observing any change in the EXAFS spectra recorded.

3.1 Synthesis of Block copolymer stabilized Au and Pt nanoparticles

Gold nanoparticles have been synthesized by mixing 2.5 ml of 60mM Chloroauric acid ($HAuCl_4.3H_2O$) with 1.5 ml of 100mM trisodium citrate (Na_3Ct) and 1 ml of 10 mM P85 block copolymer. The solution is kept undisturbed at room temperature. After ~ 10 minutes the colour of the solution starts changing to red and after ~ 15 min the colour becomes dark violet as shown in Fig. 3.1(a) manifesting formation of Au nanoparticles. The concentration of gold in the final solution is 30 mM.

Similarly, Platinum nanoparticles were synthesized by mixing 2.5 ml of 60mM Chloroplatinic acid ($H_2PtCl_6.6H_2O$) with 2.5 ml of 500mM Ascorbic Acid (AA) and 1 ml of 10 mM P85 block copolymer and by heating the mixture to 50°C. The solution first becomes colourless and in 12 minutes it changes to brown and then black as shown in Fig. 3.1(b) depicting formation of Pt nanoparticles.

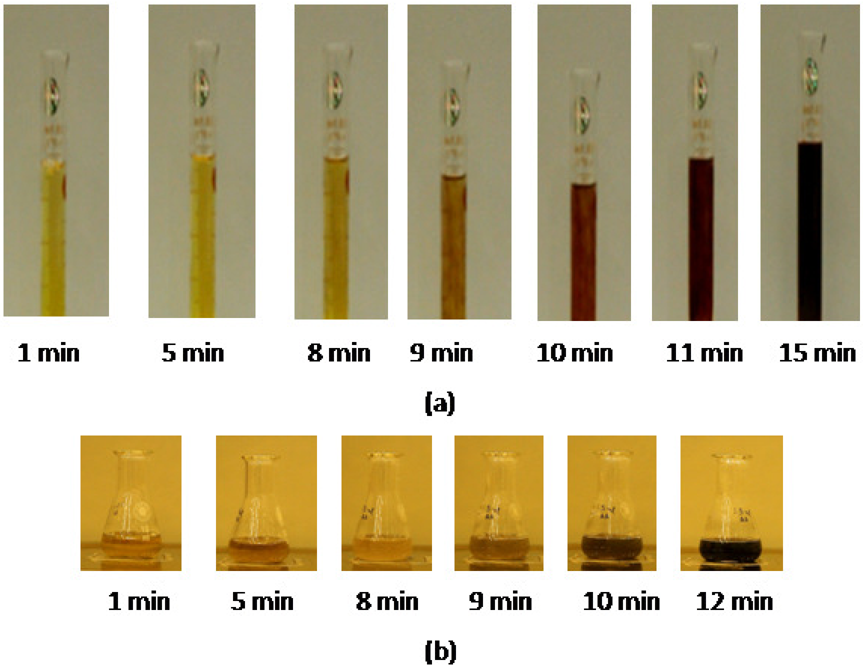

Figure 3.1: Changes in colour of (a) Au nanoparticle precursor solution and (b) Pt nanoparticle precursor solution with time after mixing the reducers.

TEM micrograph of gold nanoparticles formed by completely reducing $HAuCl_4$ by sodium citrate and P85 block copolymer is shown in Fig.3.2(a). The figure shows that the Au nanoparticles formed are faceted (almost spherical) in shape and the size of most of the particles lies between 20 to 30 nm. Fig. 3.2 (b) shows the TEM image of Pt nanoparticles obtained from the solutions after completion of the reaction which shows that the fully formed nanoparticles are mostly spherical in size with average size of ~20 nm. The size of both gold and platinum nanoparticles agrees well with the final particle size obtained from EXAFS measurements discussed later in this chapter (Fig.3.8 and Fig. 3.14).

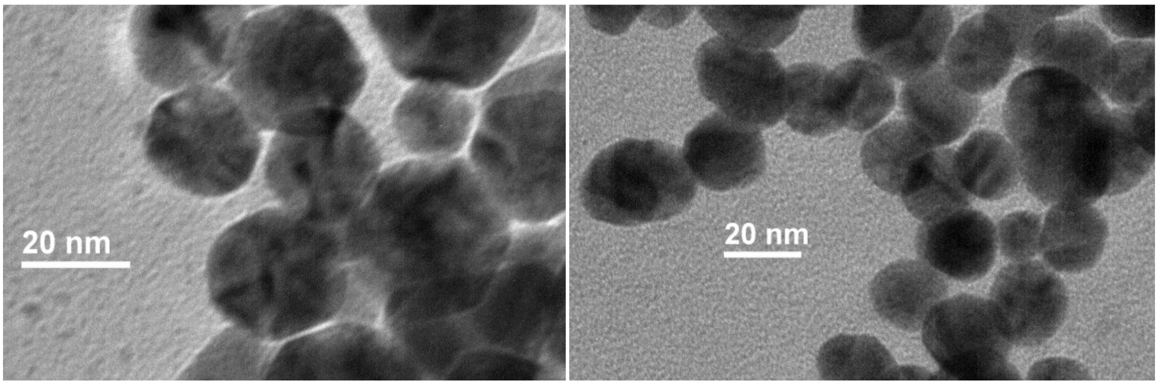

(a) (b)

Figure 3.2: (a) TEM micrograph of fully formed Au nanoparticles (b) TEM micrograph of fully formed Pt nanoparticles

3.2 *In-situ* EXAFS measurement cell for one pot synthesis

For *in-situ* EXAFS measurement the synthesis process has been carried out in a specially designed teflon reaction cell having paths for both X-rays and UV-Vis radiation in mutually perpendicular directions. UV-Vis absorption measurement has been carried out simultaneously with the XAS measurements using an optical fiber based spectrometer (Make: M/s., Avantes, Netherlands). X-ray is transmitted through Kapton windows while the optical light is passed using optical fibres which are capped with teflon ferrules and are directly immersed into the solution. The cell has been designed and fabricated in such a way that the optical paths can vary from 5 mm to 20 mm for X-rays and from 2 mm to 20 mm for UV-Vis radiation. The volume of the cell varies according to the adjustment of the kapton windows and optical fibers. However, for the present experiment where Kapton windows are adjusted 10 mm apart and the teflon ferrules are adjusted such that optical fibers are positioned 5 mm apart, the volume of the cell is approximately 8 ml. The sample mount of the beamline has been modified so that the *in-situ* reaction cell can be placed on a magnetic stirrer-cum-heater for mixing and heating the reaction solution. The precursor is taken in the teflon reaction cell and the respective reducer is injected into it through teflon tube using a computer-controlled motor-driven syringe pump (Make: KD Scientific, USA). The syringe pump works in the "infuse only" operation mode with flow rates from 5pl/min to 220 ml/min. The reducer is injected at a speed of 5ml. min^{-1} and the reaction solution is stirred with a speed of about 60 rpm to have a homogenous solution. Time t=0 is the time when the reducing agent is put in the reaction solution using the syringe pump. This is the time when the reaction starts and the EXAFS measurement is also recorded w.r.t. this time. As has been mentioned in the previous section, for synthesis of Au nanoparticles the reaction solution remains at room temperature while in case of formation of Pt nanoparticles the solution is heated to 50°C. The schematic diagram of the experimental set up for simultaneous time resolved EXAFS measurement and UV-Visible absorption measurement has been shown in Fig 3.3 and the actual photograph has been shown in Fig 3.4.

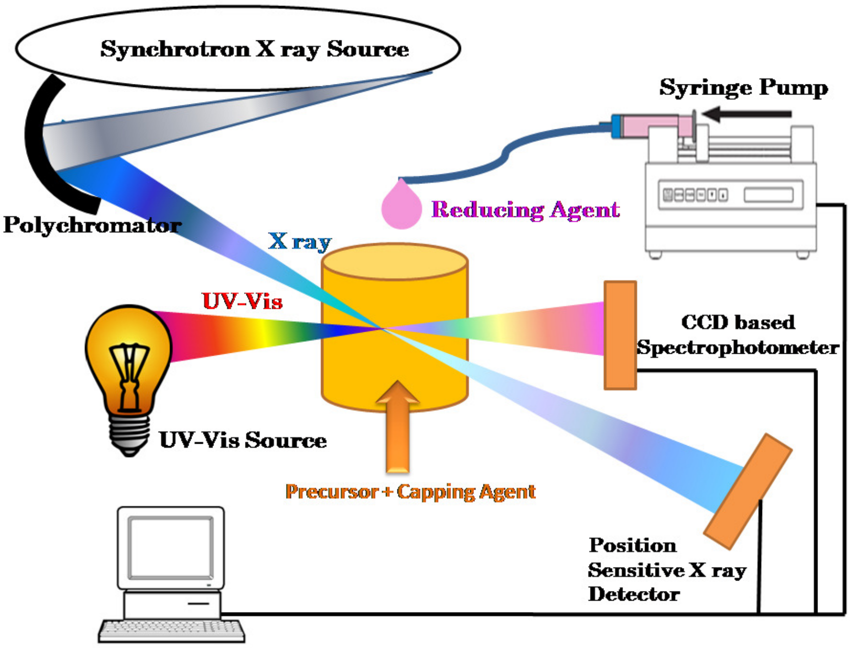

Figure 3.3: Schematic diagram of the experimental setup for simultaneous time resolved EXAFS measurement and UV-Visible absorption measurement of one-pot synthesis processes.

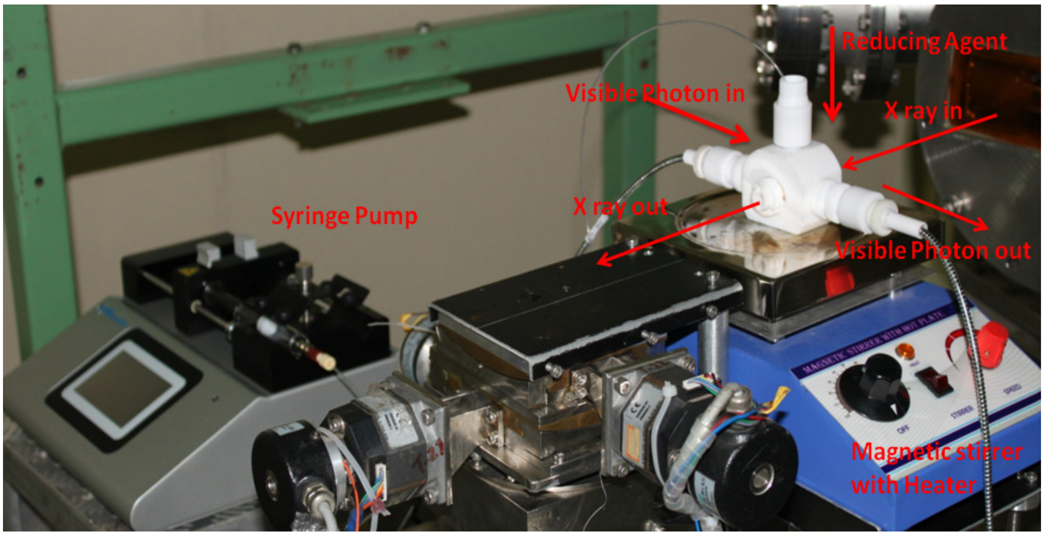

Figure 3.4: Photograph of the experimental setup for simultaneous time resolved EXAFS measurement and UV-Visible absorption measurement of one-pot synthesis processes.

3.3 Growth of Block Copolymer stabilized Au nanoparticles

3.3.1 *In-situ* XANES studies

Fig 3.5 shows *in-situ* time-resolved XANES spectra of the gold precursor reaction solution measured at Au L_3 edge. It can be seen that the near edge spectrum of $HAuCl_4$ shows a white line at 11923 eV which is due to electronic transition from the $2p_{3/2}$ to 5d state. This white line is a characteristic of Au^{+3} and disappears for metallic Au due to fully filled 5d states. The decrease in the intensity of the white line and finally its disappearance with time suggests reduction of $HAuCl_4$ and formation of metallic gold nanoparticles. After 90 min from the start of the reaction the spectrum fully resembles that of metallic gold spectrum.

As has been mentioned by Helmbrecht *et. al.*[95], the Au L_3 edge data does not show a linear shift with change in oxidation state of Au due to the overlapping of the 2p-5d transition peak with the edge. Thus a linear combination fit of the time resolved XANES spectra were performed considering $HAuCl_4$ and Au foil spectra as standards of the +3 and +0 states to obtain a quantitative measure of the presence of the two species in the reaction solution at a particular reaction time as shown in Fig. 3.6. From the linear combination fit of the time resolved XANES spectra, it has been observed that after 10 minutes ~ 50 % of the Au cations are in the metallic (+0) state and after 90 minutes ~ 87 % of the Au cations get reduced to +0 state. Similar approach has been followed by other workers[27, 50, 55] also for *in-situ* observation of nucleation and growth of Au and Pt nanoparticles from solution phases using XANES measurement.

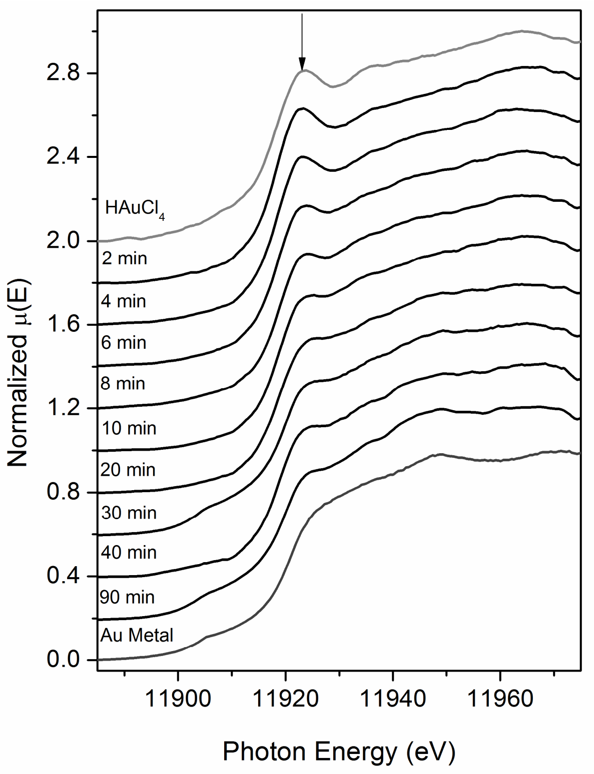

Figure 3.5: *In-situ* XANES spectra measured at Au L_3 edge at different time intervals during growth of Au nanoparticles

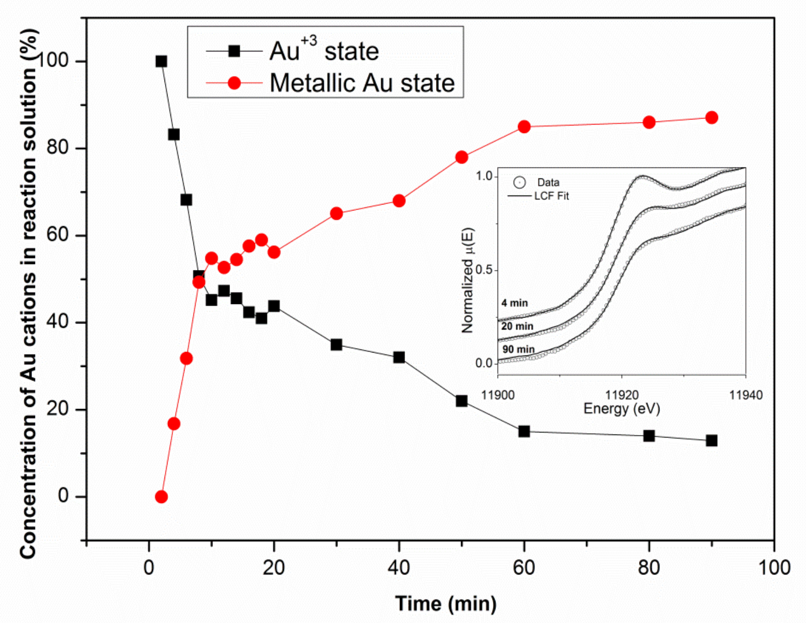

Figure 3.6: Linear combination fit results of *in-situ* XANES spectra at Au L_3 edge recorded during growth of Au nanoparticles. Inset: linear combination fitting of selected data.

3.3.2 *In-situ* EXAFS studies

Fig. 3.7 shows the $k^2\chi(k)$versus k plots taken at different intervals of time during the growth of gold nanoparticles. The k range used for Fourier Transform is 3-9.5 Å^{-1} and the $|\chi(r)|$ versus r plots and the Re[$\chi(r)$] versus r plots are shown in Fig. 3.8 and Fig. 3.9 respectively. The first peak (~1.8 Å) corresponds to Au-Cl bond and the second peak (~2.6 Å) corresponds to Au-Au bond. The$\chi(r)$versus r plots have been fitted assuming an Au-Cl path and an Au-Au path. The R_{factor} values of all fits are less than 0.01 which ensures good fit. The value of Debye Waller factors (σ^2) have been kept fixed at 0.002 and 0.001 for Au-Cl and Au-Au bonds respectively which have been found by fitting the data of the Au precursor (having only Au-Cl bonds) and Au nanoparticles formed after 90 min. of reaction (having only Au-Au bonds) respectively. The values of Debye-Waller factors are kept constant to reduce the number of parameters during fitting and to obtain a more reliable fit. Similarly,ΔE_0 values obtained from the fitting of the EXAFS data of the precursor and the end products (0 min. and 90 min. data respectively) are used for the two paths and kept constant during fitting.

In case of EXAFS fitting, the maximum number of independent points is generally given by the Nyquist criteria $N_{ind} = \frac{2\Delta k \Delta r}{\pi}$. In this case, $\Delta k = 9.5 - 3 = 6.5$ and $\Delta r = 3 - 1 = 2.$, yielding $N_{ind} = 8.3$. Since the Debye Waller factors andΔE_0values of the various paths are kept constant, only four parameters are varied (bond distance and coordination number for two paths) during the fitting which is much less than the maximum no. of independent points. Similar approach has also been taken by other researchers also while analysing EXAFS data of nanoparticles. For example, Ma *et. al.*[52] in their study of X-ray induced formation of gold nanoparticles have varied only coordination number and bond lengths and kept the Debye-Waller factor constant while fitting the EXAFS data. Similarly, Yao *et. al.*[96] while studying formation mechanism of Rh nanocubes by *in-situ* dispersive EXAFS measurements have also kept the Debye-Waller factor fixed. Harada and Kamigaito[54] have also found that the Debye-Waller factor for Pt-Pt bond, in case of growth of Pt nanoparticles, do not show any time dependence and is close to that of bulk Pt.

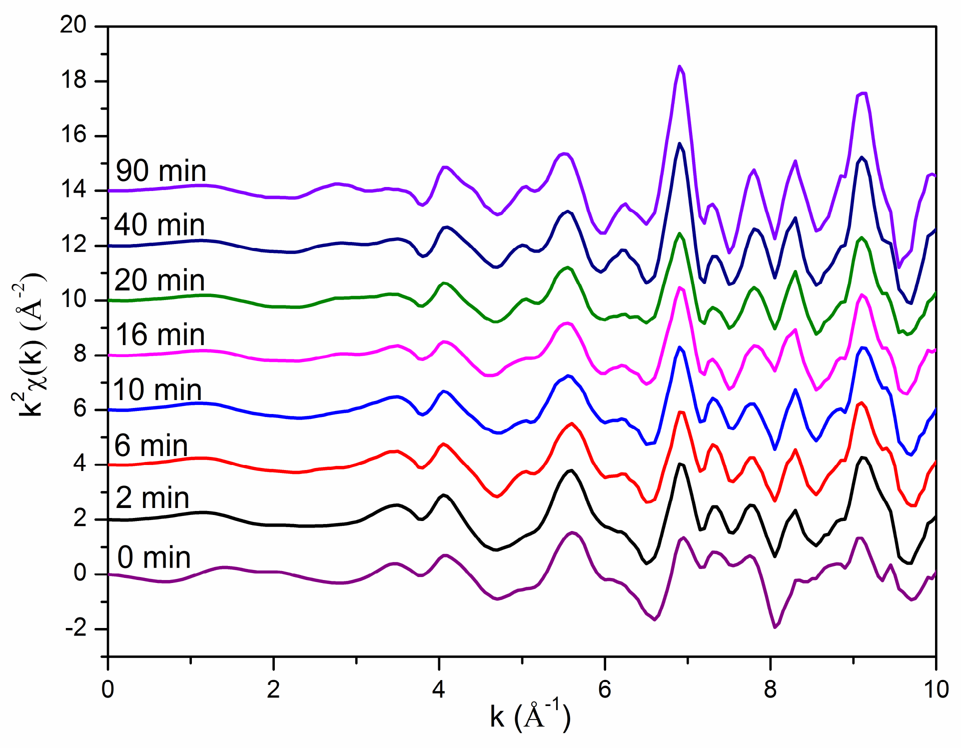

Figure 3.7: *In-situ* EXAFS $\chi(k)$versus k spectra measured at Au L_3 edge at different time intervals during growth of Au nanoparticles

It can be observed from Fig. 3.8 that within two minutes a small peak appears corresponding to Au-Au bond. The bond lengths of both Au-Cl and Au-Au bonds do not change significantly during the reaction. Fig 3.10 shows the variation of coordination number of both the bonds which shows that Au-Au coordination remains near 5 till 10 minutes and subsequently it increases and reaches the coordination of ~11 at about 70 minutes. The Au-Cl bond coordination, on the other hand, decreases till 20 minutes, after which it starts increasing again.

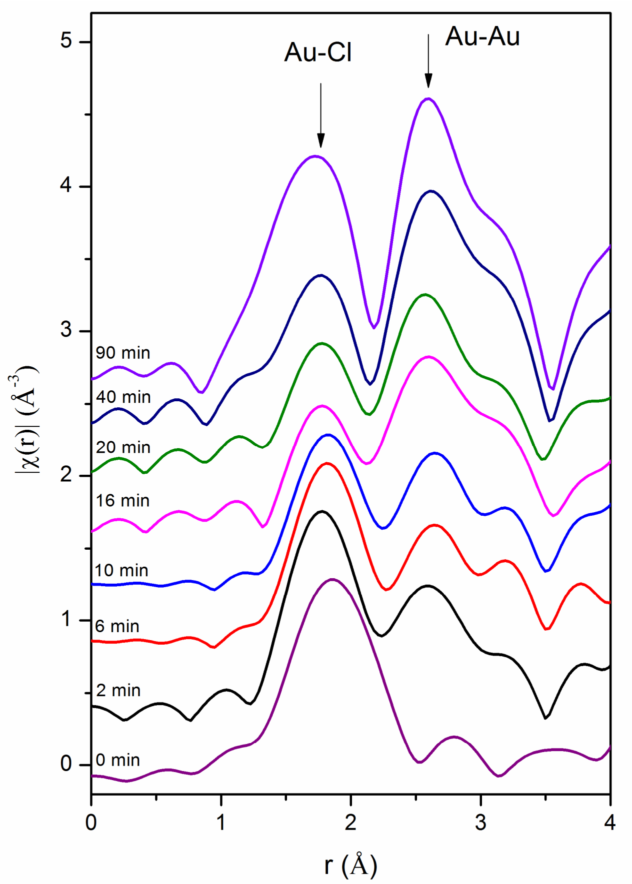

Figure 3.8: *In-situ* EXAFS $|\chi(r)|$ versus r spectra measured at Au L_3 edge at different time intervals during growth of Au nanoparticles

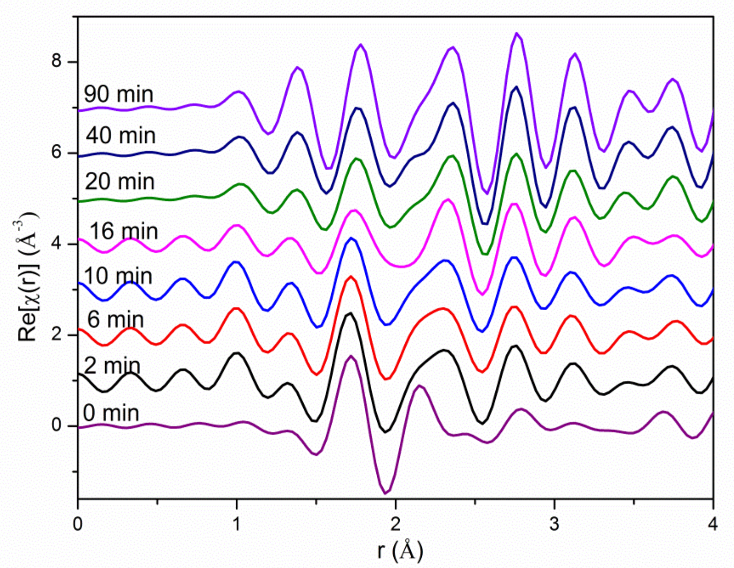

Figure 3.9: *In-situ* EXAFS Re[$\chi(r)$] versus r spectra measured at Au L_3 edge at different time intervals during growth of Au nanoparticles

It should also be mentioned here that EXAFS cannot directly yield information on particle sizes and one way to overcome this problem is to carry out EXAFS and SAXS measurements simultaneously, as had been done by Polte *et.al.*[50]. However, in that case SAXS measurement has to be carried out in transmission mode and EXAFS in fluorescence mode and there might be a possibility that the two techniques probe different sample volumes.

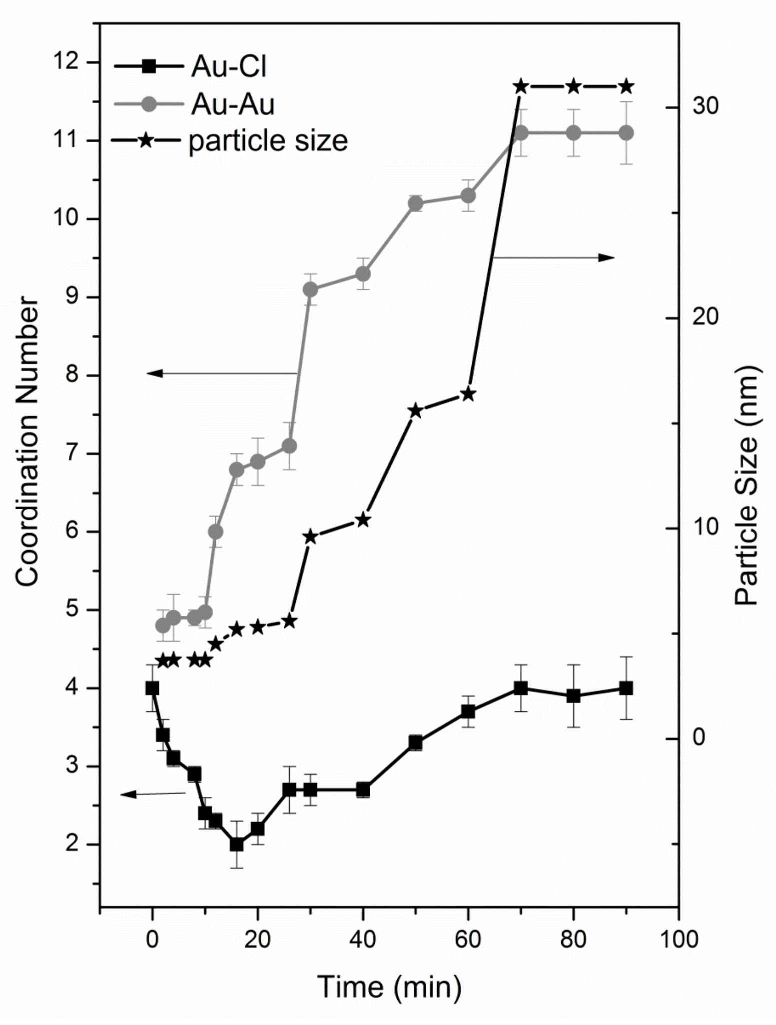

Figure 3.10: Variation of Au and Cl co-ordinations around Au sites and particle size obtained from EXAFS measurements during growth of Au nanoparticles.

In the present case we have carried out EXAFS and XANES both in transmission mode and obtained particle sizes from the coordination numbers determined from EXAFS analysis as described below[97]. Assuming the nanoparticles to be spherical, Calvin *et. al.*[98] devised a formula to correlate the coordination number and the particle size as:

$$n_{nano} = \left[1 - \frac{3}{4}(\frac{r}{R}) + \frac{1}{16}(\frac{r}{R})^3\right] n_{bulk} \qquad (3.1)$$

where,r is the distance between the nearest neighbor atoms, R is the particle radius, n_{nano} is the coordination number for the nanoparticles and n_{bulk} is the bulk coordination number. Using the values of Au-Au coordination numbers given in Fig.3.10 as a function of time, particle sizes have been obtained for Au nanoparticles using eqn. (3.1) and are plotted as a function of time in Fig. 3.10. However, it should be noted here that the particle size determined by this method is based on the assumption that particles are spherical and hence gives good proximity to the final particle size as determined by TEM, but it fails to predict the cluster sizes formed during the initial stages of growth due to their non-spherical shapes.

3.3.3 *In-situ* UV-Visible spectroscopy studies

Fig. 3.11 shows the visible absorbance spectra during the growth of gold nanoparticles. The absorbance increases with time and a peak appears between 520 nm to 540 nm which corresponds to the surface plasmon resonance (SPR) peak of the gold nanoparticles. The intensity or height of the SPR peak has been plotted in fig. 3.12 as a function of time. The peak maxima also shifts from 527 nm to 540 nm during the initial phase of the reaction indicating the increase in particle size. The variation of peak position has also been plotted in fig. 3.12 as a function of time.

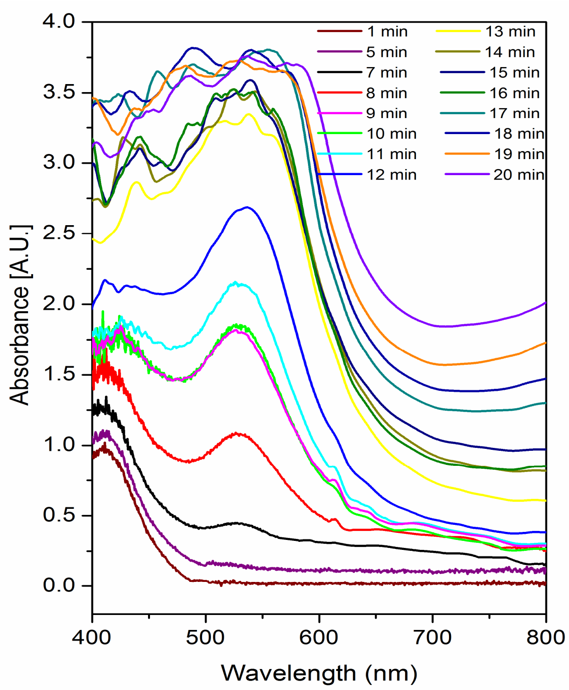

Figure 3.11: UV-Vis spectra recorded in the wavelength range of 400-800 nm at different time intervals during growth of Au nanoparticles.

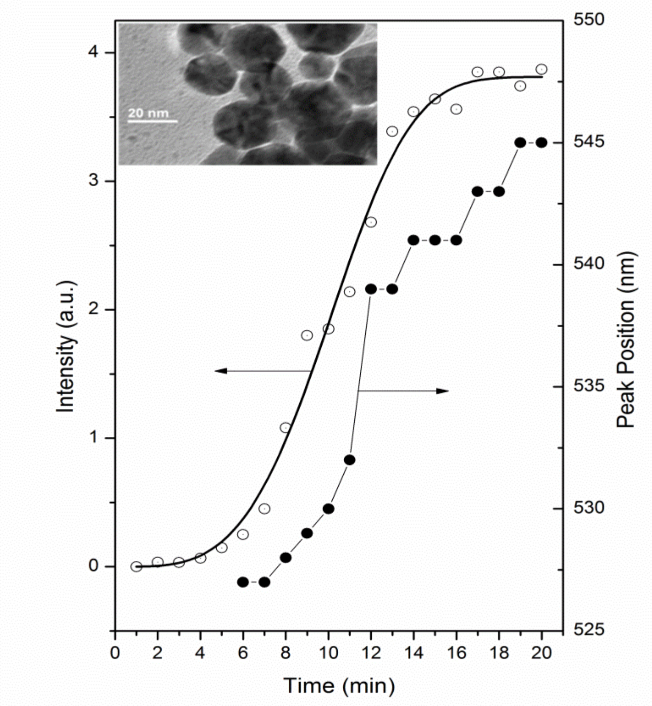

Figure 3.12: Variation of intensity and position of the Au surface plasmon peak in the UV-Vis spectra measured during growth of Au nanoparticles.

3.3.4 Growth Mechanism

As suggested by Sakai and Alexandridis[99], the growth mechanism of block copolymer stabilized gold nanoparticle is governed by three main stages: (1) reduction of metal ions by block copolymer, (2) absorption of block copolymer on gold cluster and reduction of metal ions on the surface and (3) growth of gold nanoparticles stabilized by block copolymer. In our case, as can be seen from fig. 3.10, within 2 minutes of the start of the reaction Au clusters are formed. This gives evidence of fast reduction of gold precursor and formation of large number of nuclei which further grows into particles. The fast reduction of the precursor is also evident from the XANES spectra given in fig.3.5 and this phenomenon is similar to Lamers Nucleation Mechanism [100] which suggests very fast nucleation and slow growth. In the next 10 minutes Au-Au coordination remains same at 4.9 while Au-Cl bond breaks, which corresponds to the 1st stage of nucleation and growth discussed above. Au-Au coordination of 4.9 is close to the average coordination number of three dimensional Au clusters of 12 atoms with C_{2v} symmetry[101, 102]. These Au_{12} clusters act as seeds for further growth and after 10 minutes, with the onset of the 2nd stage, when the block copolymer gets adsorbed on the surface of Au_{12} clusters, there is an increase of Au-Au coordination to 6.8 in next 15 minutes which corresponds to Au_{13} magic number icosahedron clusters. Au_{13} clusters are highly stable as they fulfill the first geometrical shell closing. They exist in three preferred geometries planar, cuboctahedral and icosahedral with average coordination numbers of 4, 5.5 and 6.5 respectively. Theoretically the most stable Au_{13} structure is the planar, however it has been found experimentally that the ligated Au_{13} icosahedron clusters are most stable due to ligand induced charge transfer[101]. After 25 minutes the coordination number again shows a jump from 7 to 9 which may correspond to the cuboctahedral Au_{147} clusters. Au_{147} clusters are also magic number clusters which show very high stability due to the closing of third geometrical structure[103]. After 30 minutes the Au nanoparticle growth starts and in 70 minutes, it reaches the size of 31 nm with coordination approaching bulk value of 12. Hence the 3rd stage of the growth process is found to begin after 30 min. from the start of the reaction and the stabilization of these nanoparticles occurs along with the growth process. Therefore, growth of gold nanoparticle occurs through the formation of Au_{12} clusters which grows into Au_{13} icosahedron clusters and subsequently to cuboctahedral Au_{147} clusters which finally grows into spherical gold nanoparticles. It can also be seen from fig. 3.10 that the first shell coordination around Au site does not decrease below 2 even though the XANES spectra show the presence of mostly metallic Au state and after 20 minutes, Au-Cl bond coordination increases. Such high value of coordination of the Au-Cl shell has also been observed by Ma *et. al.*[52] and Yao *et.al.*[96] during formation of Au nanoparticls by reduction of $HAuCl_4$, even after sufficiently long time of the reduction reaction and this phenomenon has been attributed to chloride capping of Au nanoparticles after formation.

The first two stages of the growth process as described above can also be corroborated by the time resolved UV-Vis spectroscopy studies. As can be seen from fig. 3.12, the nature of variation of the intensity of the surface plasmon peak upto 20 minutes of growth process exactly follows the pattern of variation of Au coordination number as shown in fig. 3.10. The growth process cannot be probed further by UV-Vis spectroscopy since the absorption becomes too high for detection of the transmitted beam.

3.4 Growth of Block Copolymer stabilized Pt nanoparticles

3.4.1 *In-situ* XANES studies

Fig. 3.13 shows the *in-situ* time resolved XANES spectra of the platinum nanoparticle precursor solution measured at Pt L_3 edge. The near edge spectrum of H_2PtCl_6 shows a white line at 11571 eV which is due to electronic transition from the $2p_{3/2}$ to 5d state. This white line is a characteristic of Pt^{+4} ions and disappears for metallic Pt due to fully filled 5d states. The decrease in the intensity of the white line and finally its disappearance with time suggests reduction of H_2PtCl_6 and formation of metallic platinum nanoparticles. After 90 min. from the start of the reaction, the XANES spectrum completely resembles that of metallic platinum. A linear combination fit of the time resolved XANES spectra were performed considering the spectra of H_2PtCl_6 and Pt foil as standards of the +4 and +0 states as shown in Fig. 3.14, from which it has been observed that in 6 min 50% of the Pt cations are found to be in the metallic (+0) state and after 90 minutes ~ 82% of the Pt cations get reduced to +0 state.

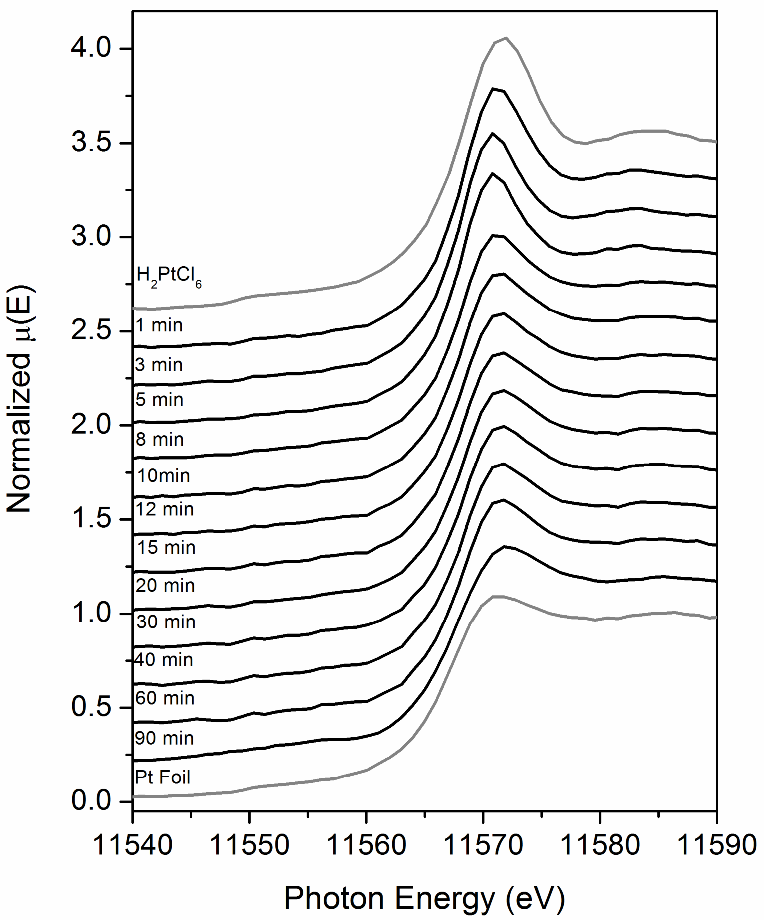

Figure 3.13: *In-situ* XANES spectra measured at Pt L_3 edge at different time intervals during growth of Pt nanoparticles

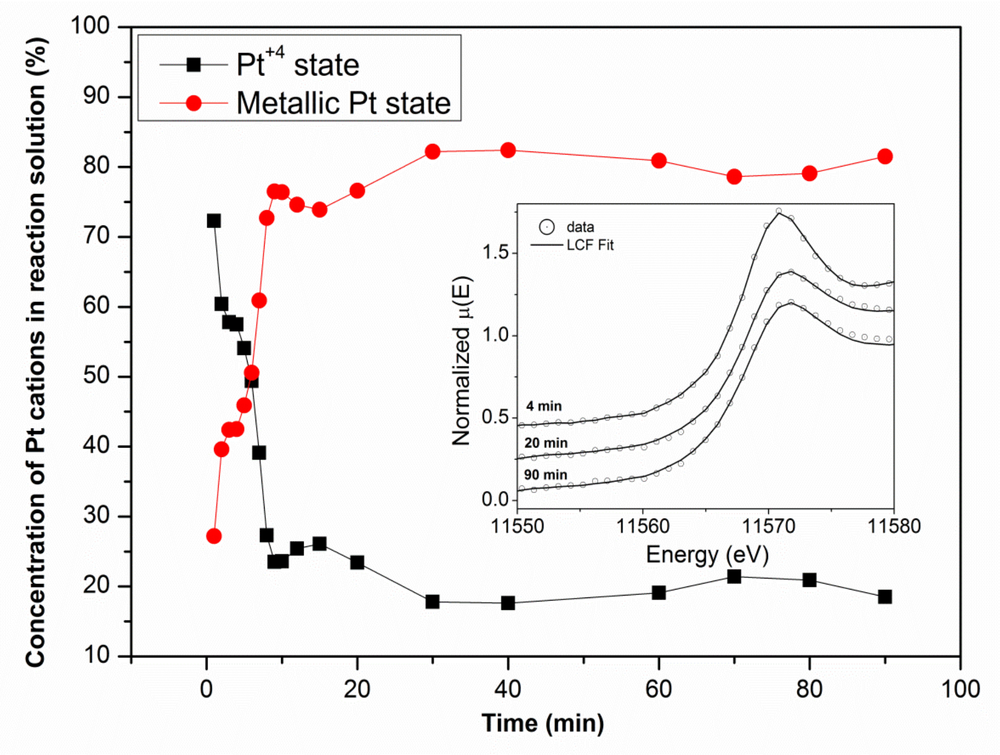

Figure 3.14: Linear combination fit results of *in-situ* XANES spectra at Pt L_3 edge recorded during growth of Pt nanoparticles. Inset: linear combination fitting of selected data.

3.4.2 *In-situ* EXAFS studies

The $\chi(k)$ vs. k plots shown in Fig. 3.15, have been derived from the $\mu(E)$ vs. Espectra following the steps described in the section 2.3. The$\chi(k)$ spectra is weighted by k^2 and the functions$\chi(k)k^2$ are Fourier transformed in the k range 2-10 Å^{-1} to generate the$\chi(r)$ versus r (or FT-EXAFS) plots in terms of the real distances from the center of the absorbing atom.

Fig. 3.16 shows the $|\chi(r)|$ versus r plots at different time intervals during the growth of platinum nanoparticles. The first peak (~1.8 Å) corresponds to Pt-Cl bond and the second peak (~2.4Å) corresponds to Pt-Pt bond. The$\chi(r)$ versus r plots have been fitted assuming a Pt-Cl path and a Pt-Pt path. The value of Debye Waller factors (σ^2) have been kept fixed to 0.005 and 0.004 for Pt-Cl and Pt-Pt bond respectively. The R_{factor} values for all the fittings are less than 0.01

which ensures good fit of the data. The EXAFS fittings of the |$\chi(r)$| versus r data at few selected time intervals have been shown in Fig. 3.17. The bond length of both Pt-Cl and Pt-Pt bonds do not change significantly during the reaction however, the coordination numbers change with time and the variations of coordination number of both the bonds are shown in Fig. 3.18. Using Calvin's approach[98] the size of the Pt nanoparticles have been obtained from Pt-Pt coordination numbers through eqn. (3.1) the and have also been plotted as a function of time in Fig.3.18.

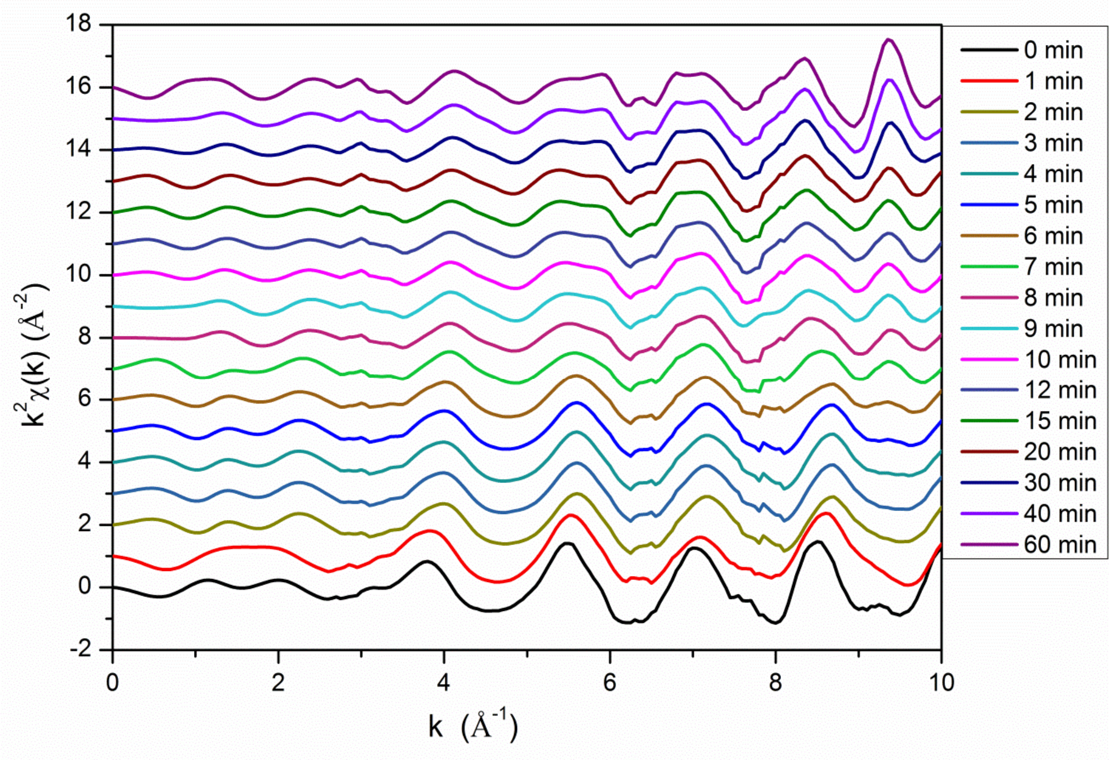

Figure 3.15: *In-situ* EXAFS $\chi(k)$versus k spectra measured at Pt L_3 edge at different time intervals during growth of Pt nanoparticles

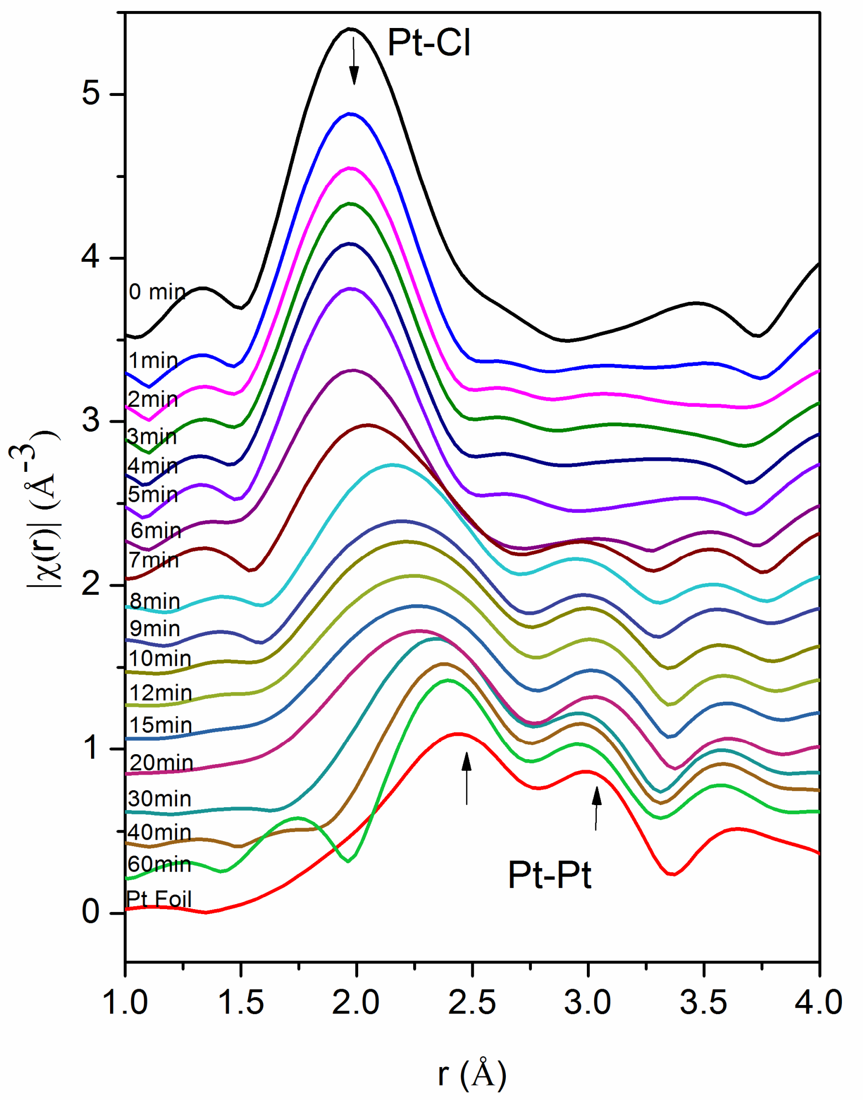

Figure 3.16: *In-situ* EXAFS $|\chi(r)|$ versus r spectra measured at Pt L_3 edge at different time intervals during growth of Pt nanoparticles

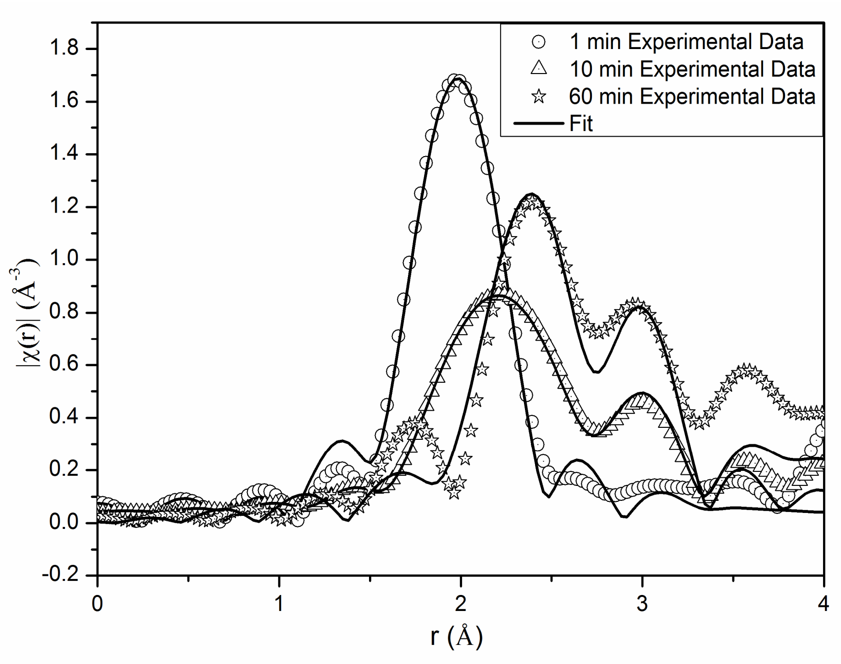

Figure 3.17: EXAFS fitting of the experimental |*χ(r)*| versus *r* data at few selected time intervals during the growth of Pt nanoparticles.

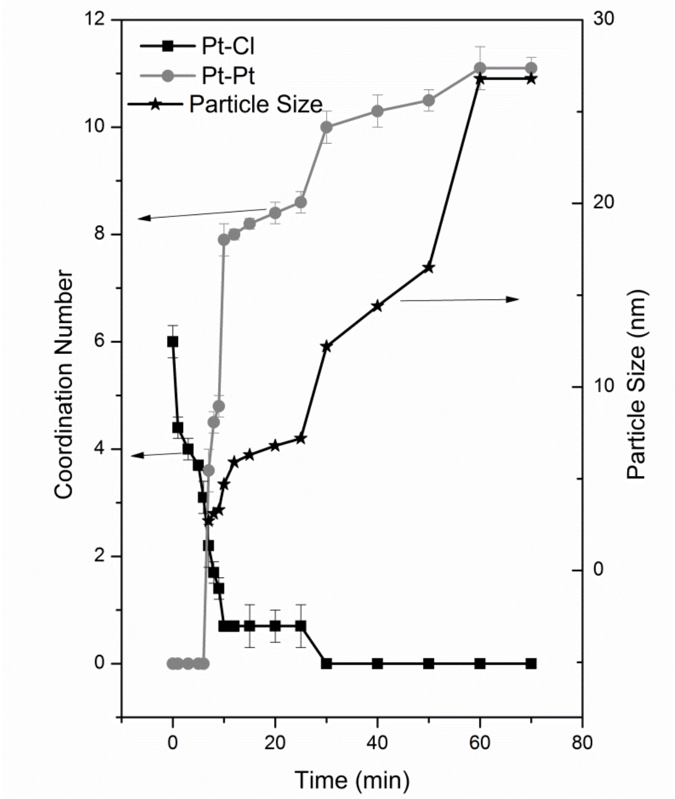

Figure 3.18: Variation of Pt and Cl co-ordinations around Pt sites and particle size obtained from EXAFS measurements during growth of Pt nanoparticles.

3.4.3 *In-situ* UV-Visible spectroscopy studies

Fig. 3.19 shows the evolution of the UV-visible absorbance spectra during the growth of platinum nanoparticles. The spectrum at 1 min. shows two peaks at 328 nm and 394 nm due to $PtCl_6^{2-}$ whose intensity decreases with time in the first 5 minutes and while the reaction proceeds further, the total absorbance increases. Fig.3.20 shows the variation of the intensity of absorbance at 324nm, 394nm and 450nm with time. The increase in intensity at 450 nm wavelength manifests the growth of Pt nanoparticles.

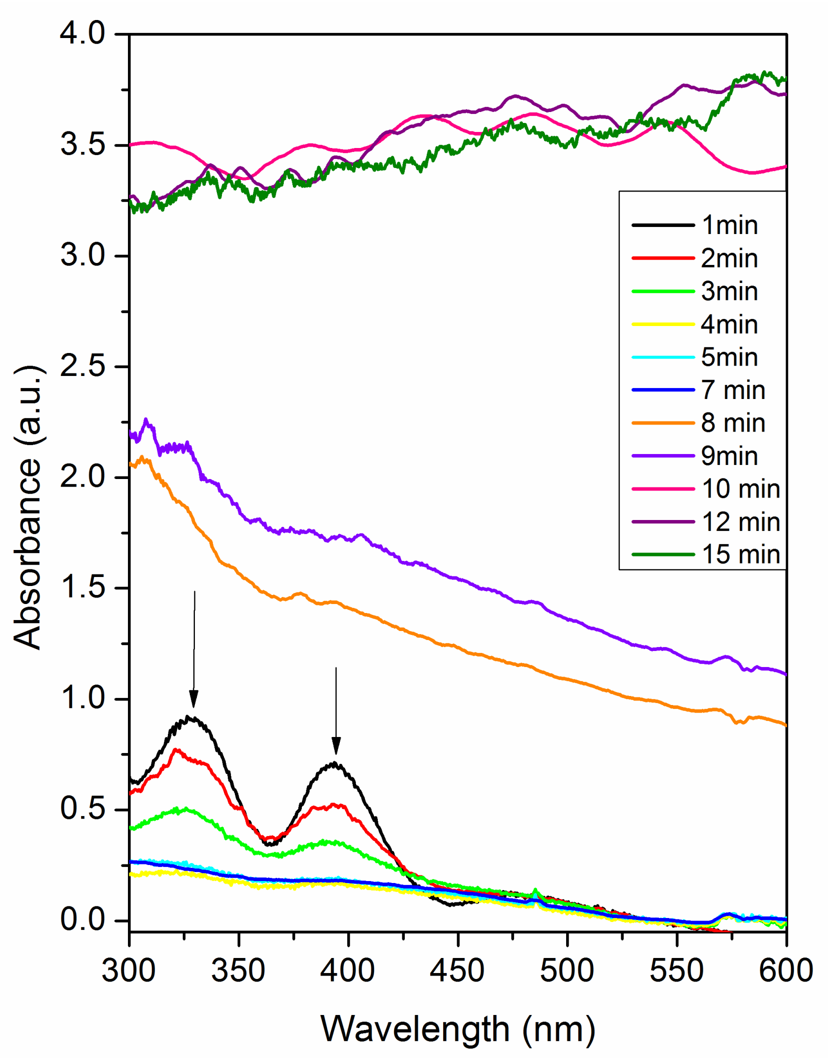

Figure 3.19: UV-Vis spectra recorded in the wavelength range of 300-600 nm at different time intervals during growth of Pt nanoparticles.

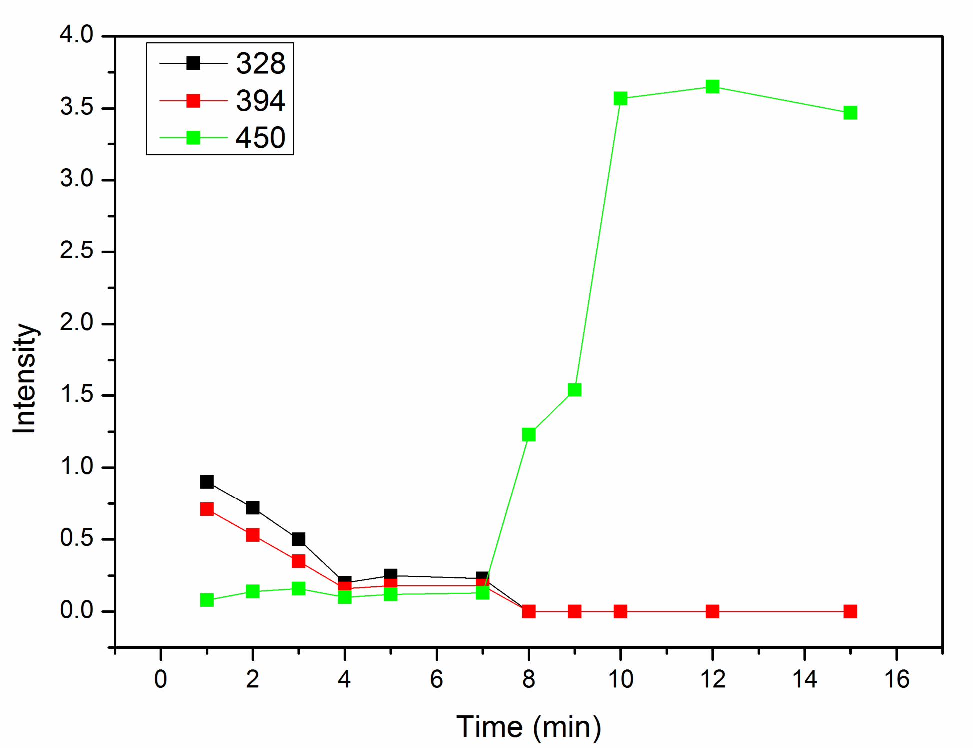

Figure 3.20: Variation of intensity of absorption at 328, 394 and 450 nm in the UV-Vis spectra measured during growth of Pt nanoparticles.

3.4.4 Growth Mechanism

The formation process of Pt nanoparticles can also be divided in three stages similar to that of gold nanoparticles. As can be seen from Fig. 3.18, the Pt-Cl bond breaks from the start of the reaction signifying the reduction of the precursor H_2PtCl_6. The Pt-Cl bond coordination suddenly drops from 6 to 4 after which it gradually decreases. This may indicate the reduction of $Pt^{IV}Cl_6^{2-}$ ions to $Pt^{II}Cl_4^{2-}$ ions. It has already been found that the $Pt^{IV}Cl_6^{2-}$ ions inhibit the formation of Pt nanoparticles[54]. Therefore in the reduction process Pt^{+4} is first reduced to Pt^{+2} and then to Pt^{+0}. After 7 minutes, a small peak appears in Fig.3.16 along with an increase in Pt-Pt coordination in Fig. 3.18 showing formation of Pt-Pt bond. This sudden jump in Pt-Pt coordination corresponds to the phenomenon of Lamer's nucleation burst[24]. This is similar to the growth of gold nanoparticles discussed in the earlier section. However in case of gold the Lamer

Nucleation occurs within 2 minutes from the start of the reaction, while platinum shows the nucleation burst at 7 minutes from the start. This difference may be due to the difference in the reduction potential of the two noble metal precursors i.e. $Au^{III}Cl_4^-$ having a higher reduction potential than $Pt^{IV}Cl_6^{2-}$. From 7 to 9 minutes Pt-Pt coordination remains around 4.5 indicating the formation of Pt_{12} clusters[104] which manifest the 1st stage of the reaction. The 2nd stage starts at 10 minutes with a drastic increase in the Pt-Pt coordination to 7.9 which possibly corresponds to formation of cubo-octahedral Pt_{55} clusters. Pt_{55} is a magic cluster with the closing of second geometrical shell. A cubooctahedron structure of 55 atoms has average coordination number 7.8, while the icosahedrons structure with 55 atoms have 8.5 as average coordination[105]. In the third stage, Pt-Pt coordination increases to its bulk value of 11 till 60 minutes through a slower process similar to the Au case. Therefore, during the growth of Pt nanoparticles, initially Pt_{12} clusters are formed which grows into cuboctahedral Pt_{55} clusters which further grows into spherical Pt nanoparticles. The formation of Pt_{55} clusters during the growth of Pt nanoparticles has also been reported by Harada and Kamigaito.[54] The first two stages of growth of the Pt nanoparticles can also be corroborated by UV-Vis spectroscopy, where as can be seen from Fig. 3.20, the intensity at 450 nm grows almost similarly as the coordination number (Fig.3.18) upto 10 minutes of reaction.

3.5 Comparison of growth of Au and Pt nanoparticles

The growth kinetics of both types of nanoparticles are found to be similar and are found to follow the three stages viz., (i) reduction of metal ions by block copolymer and formation of small cluster of typical 5 coordinations, (ii) absorption of block copolymer and reduction of metal ions on the surface of the cluster and increase in cluster size and (iii) growth of nanoparticles stabilized by block copolymer. This can be observed that the time scale involved in the 2nd and 3rd stages of the nanoparticle formation are similar for both gold and platinum nanoparticles. This may be due to the fact that these stages are mainly governed by the block copolymer which is same in both the cases. This also consolidates the role of the block copolymer in the formation of these nanoparticles. However, the 1st stage of nucleation takes place earlier in case of Au than in case of Pt due to the difference in the reduction potential of the respective precursors. In both the cases, 12 atoms clusters are formed which act as seeds for further growth. However, for gold, these 12 atoms cluster first grows into the magic number 13 atoms cluster and then 147 atoms clusters which further grows into gold nanoparticles. For platinum the 12 atoms cluster grows into the magic number 55 atoms cluster which further grows into platinum nanoparticles. The first two stages of the growth of Au and Pt nanoparticles as obtained by in-situ XAS measurements are also corroborated by simultaneous *in-situ* measurement of UV-Vis spectroscopy.

3.6 Conclusion

A set-up has been developed at the energy dispersive EXAFS beamline (BL-08) at Indus-2 SRS at RRCAT, Indore, India for *in-situ* XAS measurements on chemical processes using a specially designed teflon cell with one optical path for X-ray in the direction of synchrotron beam and another in the perpendicular direction for visible radiation. Using the above set-up the growth of Au and Pt nanoparticles from their respective chloride precursors using block copolymer based reducer-cum-stabilizer have been studied by simultaneous *in-situ* measurement of XAS and UV-Vis spectroscopy. The growth kinetics of both types of nanoparticles are found to be almost similar and are found to follow the three stages viz., (i) reduction of metal ions by block copolymer and formation of small cluster of typical 5 coordinations, (ii) absorption of block copolymer and reduction of metal ions on the surface of the cluster and increase in cluster size and (iii) growth of gold nanoparticles stabilized by block copolymer. This can be observed that the time scale involved in the 2nd and 3rd stages of the nanoparticle formation are similar for both gold and platinum nanoparticles. This may be due to the fact that these stages are mainly governed by the block copolymer which is same in both the cases. This also consolidates the role of the block copolymer in the formation of these nanoparticles. However, the 1st stage of nucleation takes place earlier in case of Au than in case of Pt due to the difference in the reduction potential of the respective precursors. In both the cases, 12 atoms clusters are formed which act as seeds for further growth. However, for gold, these 12 atoms cluster first grows into the magic number 13 atoms cluster and then 147 atoms clusters which further grows into gold nanoparticles. For platinum the 12 atoms cluster grows into the magic number 55 atoms cluster which further grows into platinum nanoparticles. The first two stages of the growth of Au and Pt nanoparticles as obtained by *in-situ* XAS measurements are also corroborated by simultaneous *in-situ* measurement of UV-Vis spectroscopy.

Chapter 4

In-situ XAS studies on growth of Au-Pt bimetallic nanoparticle

In recent years, bimetallic nanoparticles have attracted considerable attention in the scientific community due to their unique properties and multiple functionalities in the field of catalysis, electrochemistry and environmental science[106-110]. In catalysis, bimetallic nanoparticles show improved activity and selectivity compared to their monometallic constituents[111-115]. For example, Au-Pt bimetallic nanoparticles show higher CO oxidation activity relative to Au and Pt monometallic nanoparticles [116]. Hamed *et. al.*[117] have shown that Au-Pt nanoparticles with dendritic Pt shells and Au cores show high activity as an electrocatalyst for methanol oxidation reaction also. Zhang *et. al.*[118] have showed higher activity of Au/Pt bimetallic alloys for aerobic glucose oxidation. These studies inculcate the idea that alloying Au with Pt improves the activity and selectivity of the catalyst. However, the performance of the catalyst also depends on the shape, size and configuration of the bimetallic nanoparticles. The bimetallic nanoparticles can exist in a wide range of sizes (1-100nm), can adopt different shapes (spherical, polyhedral, nanorods, dendritic and tripods) and can exist in different configurations (random, intermetallic, core-shell, etc.)[119-121]. Existence of these particles in a wide spectrum of size, shape and configuration opens up the scope of material engineering to tailor material properties based on various applications. Since the size, shape and configuration in which the bimetallic nanoparticles exist solely depend on the synthesis route which in turn affect the properties of the nanoparticles, therefore a rigorous *in-situ* study of the synthesis process is extremely important to synthesize tailor-made bimetallic nanoparticles. *In-situ* XAS can provide information on how the bimetallic nanoparticles are formed which in turn will be helpful to design and synthesize nanoparticles of desired properties. For example, Chen *et. al.*[122] have performed *in-situ* EXAFS on Pd-Au nanoparticles which revealed the formation of Pd–Au bimetallic clusters with various Pd–Au atomic stackings by properly performing hydrazine reduction and redox trans-metalation reactions. In most cases bimetallic nanoparticles are synthesized by a two step process where the seeds are first formed and then coated with the shell. However recently, Hamed *et. al.*[123] have developed a one-pot synthesis technique of Au-Pt bimetallic alloys using block copolymers as surfactants. This surfactant assisted synthesis is not only convenient and environment friendly, but can also give rise to nanostructures in the shell. Therefore, *in-situ* study of this synthesis route can provide some more insight which can help to make this more application oriented.As has been discussed in the Introduction (Chapter-1), XAS is an excellent technique with local structure sensitivity, element specificity and high spatial resolution and hence is very suitable to study the bimetallic nanoparticle system . The local structure information of different elements of the bimetallic nanoparticles can be obtained through XAS analysis which can throw light on the structure and configuration of these nanoparticle systems. *In-situ* XAS can provide information on how these bimetallic nanoparticles are formed which in turn will be helpful to design and synthesize nanoparticles of desired properties.

In the previous chapter (Chapter-3), we have presented the results of our investigations on the growth of block copolymer stabilized gold and platinum monometallic nanoparticles. We were able to identify the different stages of growth and stabilization, including the various clusters formed during the growth of nanoparticles. In the present chapter, we are taking one step ahead to throw light on the growth of Au-Pt bimetallic nanoparticles stabilized by block copolymer. In the present study, the Au-Pt bimetallic nanoparticles are synthesized following the one-pot synthesis route using ascorbic acid as the reducing agent and P85 block copolymer as the stabilizing agent. The synthesis process has been investigated by *in-situ* XAS (XANES and EXAFS) and UV-Vis measurements simultaneously. *Ex-situ* High Resolution Transmission Electron Microscopy (HRTEM) along with Energy Dispersive Spectroscopy (EDS) line scan and X-ray photo-electron spectroscopy (XPS) measurements with *in-situ* etching have also been carried out on the samples to complement the results.

4.1 Synthesis of Block copolymer stabilized Au-Pt bimetallic nanoparticle

Gold-platinum core-shell nanoparticles have been synthesized by mixing 2 ml of 60mM Chloroauric acid ($HAuCl_4.3H_2O$), and 2 ml of 60mM Chloroplatinic acid ($H_2PtCl_6.6H_2O$) with 1 ml of 1 M Ascorbic Acid (AA) and 1 ml of 10 mM P85 block copolymer. The solution is stirred continuously at room temperature. As soon as the reducing agent AA was added to the solution, the colour of the solution immediately turned into dark violet manifesting growth of Au nanoparticles. After ~ 20 sec. the colour of the solution starts changing to brown and after ~50 sec. the colour becomes black as shown in Fig. 4.1 manifesting formation the Pt shells on Au cores.

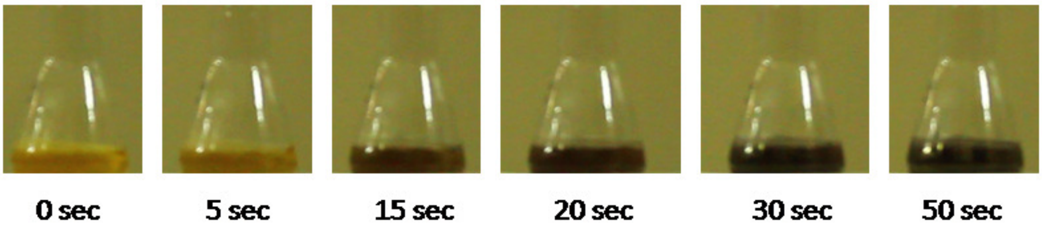

Figure 4.1: Photographs showing colour of the solution at different stages during formation of Au@Pt core shell nanoparticles.

4.2 *In-situ* studies during growth of Au-Pt bimetallic nanoparticles

For the present *in-situ* studies, the synthesis process has been carried out in a specially designed teflon reaction cell having paths for both X-rays and UV-Vis radiation in mutually perpendicular directions. The detailed description of the *in-situ* cell has been provided in section

3.2 of the previous Chapter and the schematics and photograph of the setup have been given in Fig. 3.3 and Fig. 3.4 respectively. The precursors (Chloroauric, Chloroplatinic acid and P85 block copolymer) are taken in the teflon reaction cell and the reducer (ascorbic acid) is injected into it through teflon tube using a computer-controlled motor-driven syringe pump. The reducer is injected at a speed of 5ml. min.$^{-1}$ and the reaction solution is stirred at a speed of about 60 rpm to have a homogenous solution. For *in-situ* XAS measurements, the teflon reaction cell has been placed at the sample position of the beamline and the kapton windows of the cell were adjusted to obtain an optical path length of 10 mm for X-rays through the solution. For XAS measurement at Au and Pt L_3 edges, the radiation transmitted through the sample is detected by a position sensitive Mythen detector (Make: M/s., Dectris, Switzerland) described in Chapter-2.For each spectrum the exposure time has been fixed to 1 second to improve the signal to noise ratio and XAS spectra have been recorded at every second foran hour.

4.2.1 *In-situ* XANES studies

Fig. 4.2a shows the *in-situ* time-resolved XANES spectra of the reaction solution measured at Au L_3 edge. It can be seen that the near edge spectrum of 0 sec data shows a white line at 11923 eV which is due to electronic transition from the $2p_{3/2}$ to 5d state. This white line is a characteristic of Au^{+3}state and disappears for metallic Au due to fully filled 5d states. The decrease in the intensity of the white line and finally its disappearance with time suggests reduction of $HAuCl_4$ and formation of metallic gold nanoparticles. It should be noted here that though Au and Pt XAS spectra were taken in every 1 sec. in the present experiment, in Fig. 4.2 the XANES spectra for the instants where significant changes were observed in XANES white line features at Au and Pt edges are only shown for clarity of the figures.

A linear combination fit of the time resolved XANES spectra were performed using the ATHENA code of IFEFFIT software package[79] in the energy range of -20 to 30 eV around the Au L3 absorption edge considering XANES spectra of $HAuCl_4$ and Au foil as standards of the +3 and +0 states. This has been done to obtain a relative quantitative measure of the presence of the two species in the reaction solution at a particular reaction time. The values of the weights of the two species were constrained between 0 and 1 and their sum was forced to 1.The goodness of fit has been determined by the parameter R_{factor}[39], defined in Chapter-1and R_{factor} of all the linear combination fitting at Au L_3 edge is less than 0.01. The linear combination fitting of selected time intervals have been shown in Fig. 4.4(a). Fig. 4.3a shows the percentage of the two phases present in the reaction solution as a function of time obtained from the linear combination fitting of the time resolved XANES spectra. From Fig.4.3a, it has been observed that within 6 sec. ~ 99% of the Au cations are in the metallic (+0) state and after 10 sec. ~ 100% of the Au cations get reduced to +0 state.

Fig. 4.2b shows the *in-situ* time resolved XANES spectra of the reaction solution measured at Pt L_3 edge. The near edge spectrum of the 0 sec. data shows a white line at 11571 eV which is due to electronic transition from the $2p_{3/2}$ to 5d state. This white line is a characteristic of Pt^{+4} ions and disappears for metallic Pt due to fully filled 5d states. The decrease in the intensity of the white line with time suggests reduction of H_2PtCl_6 and formation of metallic Pt. A linear combination fit of the time-resolved XANES spectra were performed considering H_2PtCl_6 and Pt foil spectra as standards of the +4 and +0 states. The linear combination fitting of selected time intervals have been shown in Fig. 4.4(b).The R_{factor} of all the linear combination fitting at Pt L_3 edge is less than 0.01. Figure 4.3b shows the percentage of the two phases present in the reaction solution at different times obtained from the linear combination fitting of the time-resolved XANES spectra. It can be seen that that within 10 sec. ~ 6 % of the Pt cations are in the metallic (+0) state and after 200 sec. ~ 78 % of the Pt cations get reduced to +0 state.

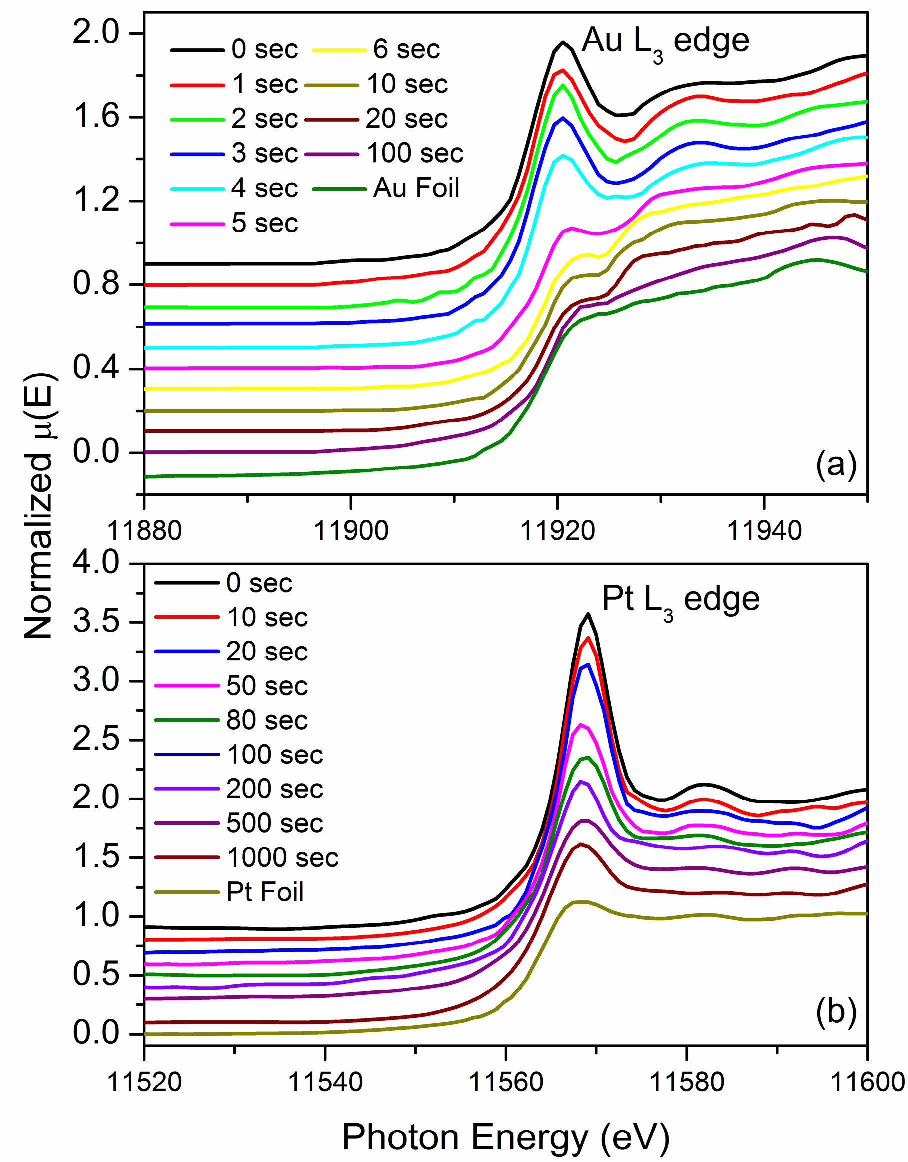

Figure 4.2: *In-situ* XANES spectra at (a) Au and (b) Pt L_3 edge recorded at different time intervals during the growth of Au@Pt nanoparticles.

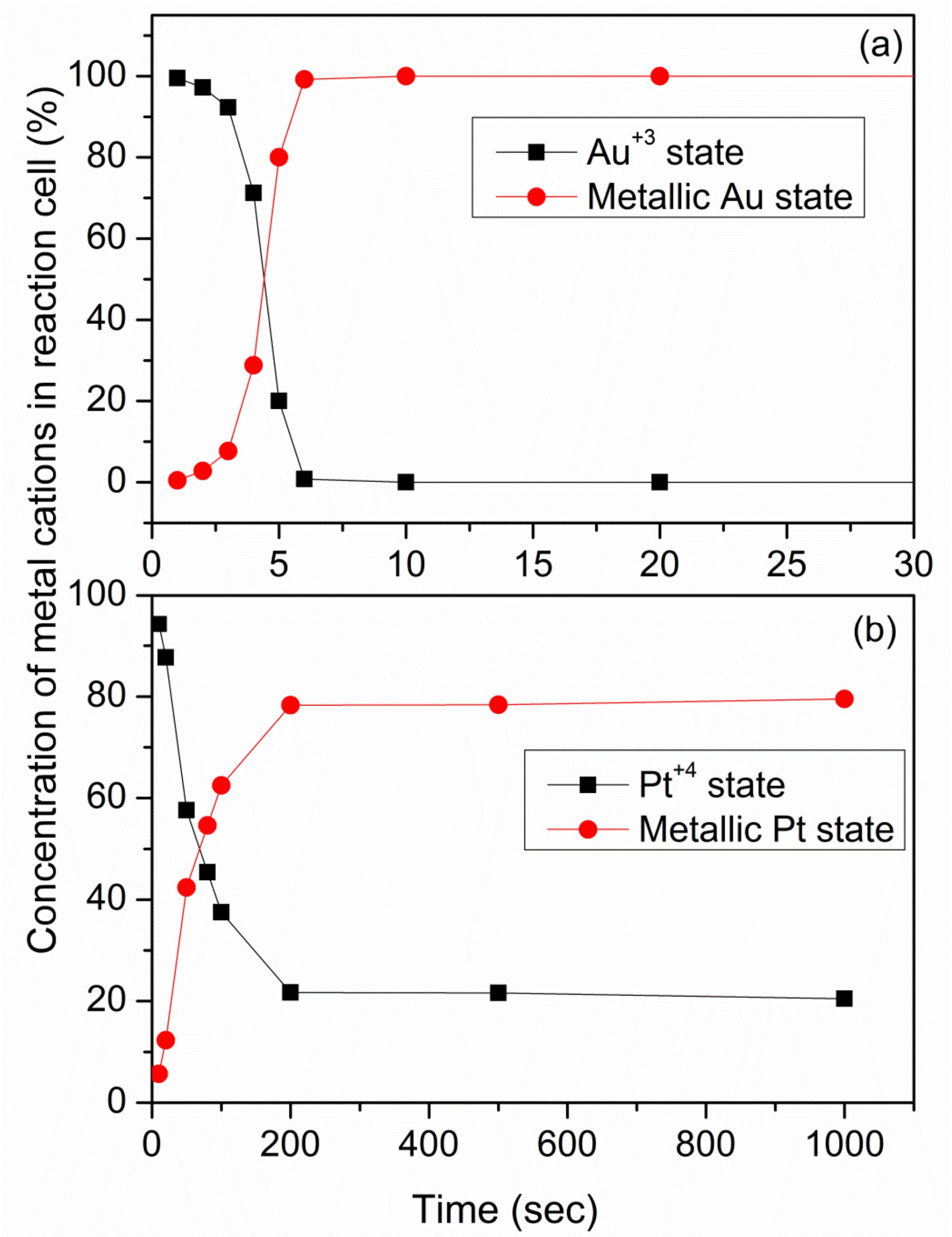

Figure 4.3: Linear combination fit results of *in-situ* XANES spectra at (a) Au and (b) Pt L_3 edge recorded during growth of Au@Pt nanoparticles.

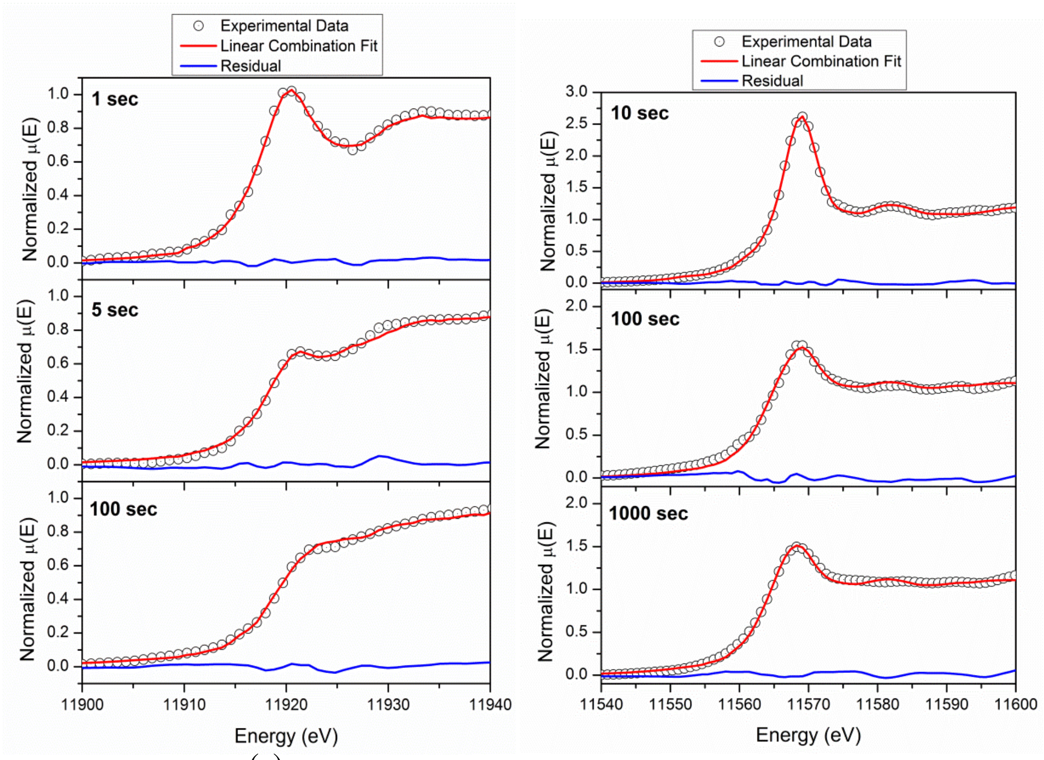

(a) (b)

Figure 4.4: Linear combination fitting of *in-situ* XANES spectra at selected time interval at (a) Au and (b) Pt L_3 edge recorded during growth of Au@Pt nanoparticles.

4.2.2 *In-situ* EXAFS studies

Figure 4.5 shows the experimental *in-situ* X-ray absorption ($\mu(E)$ versus E) spectra recorded during the growth of Au-Pt bimetallic nanoparticles simultaneously at Au and Pt L_3 edges. EXAFS oscillations have been extracted from the EXAFS spectra following the standard procedure described in the experimental section. The EXAFS oscillations, $\chi(k)$ is weighted by k^2 to amplify the oscillation at high k and the functions $\chi(k)k^2$are Fourier transformed using k range of 2-10 Å^{-1} for Au edge and 2-8.5 Å^{-1} for Pt edge to generate the $\chi(r)$ versus r (or FT-EXAFS) spectra.

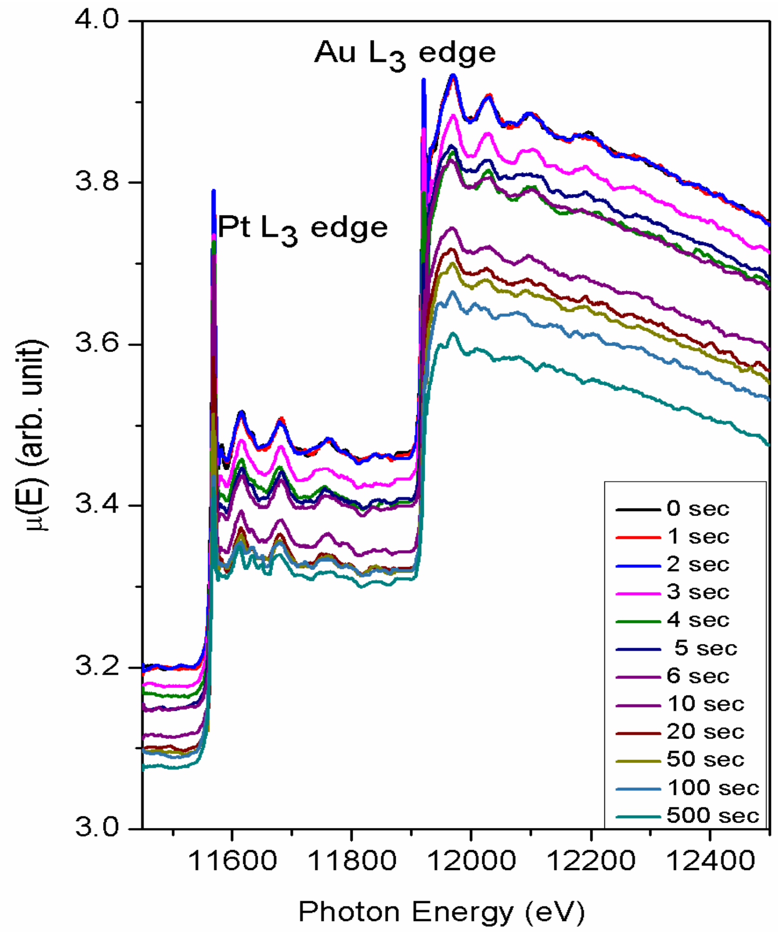

Figure 4.5: *In-situ* X ray absorption spectra at Pt and Au L_3 edges recorded at different time intervals during growth of Au@Pt nanoparticles.

Fig. 4.6(a) shows the $\chi(r)$ versus r plots at Au L_3 edge at different time during the growth of gold platinum bimetallic nanoparticles. The first peak (~1.8 Å) corresponds to Au-Cl bond and the peaks between 2-3 Å correspond to Au-Au and Au-Pt bond. The $\chi(r)$ versus r plots have been fitted assuming an Au-Cl path, Au-Pt path and Au-Au path. While fitting the data bond lengths and coordination numbers of the above three shells have been varied, however, the value of Debye Waller factors (σ^2) have been kept fixed at 0.002 for Au-Cl path and at 0.004 for Au-Au and Au-Pt paths which have been found by fitting the data of the Au precursor (having only Au-Cl bonds) and Au nanoparticles formed after 90 min. of reaction (having only Au-Au and

Au-Pt bonds) respectively. The value of S_o^2 has been kept fixed at 1 for all the paths of all the data at both Au and Pt L_3 edges as obtained from the fitting of the EXAFS data of the respective precursors. The parameter ΔE_0, on the other hand is kept same for all the paths of a data, however it is varied during the fitting of each data. For Au L_3edge, the value of ΔE_0 is found to vary in the range of 4.5-7 eV over the data of different time instants, while for Pt L_3edge data, the value of ΔE_0 is found to vary in the range of 3-5 eV. The best fit results have been presented in Tables 4.1 for Au L_3 edge data.

Table 4.1: Au L_3 edge EXAFS Fitting Results

Time(s)	Au-Cl (σ^2 =0.002 Å^2)		Au-Au (σ^2 =0.004 Å^2)		Au-Pt (σ^2=0.004 Å^2)	
	r (Å)	N	*r* (Å)	N	*r* (Å)	N
0	2.35±0.02	4.0±0.1	-	-	-	-
1	2.34±0.01	3.7±0.3	-	-	-	-
2	2.36±0.02	3.7±0.5	-	-	-	-
3	2.36±0.02	3.6±0.4	-	-	-	-
4	2.34±0.01	3.3±0.6	-	-	-	-
5	2.33±0.01	2.0±0.4	-	-	-	-
6	2.31±0.02	1.8±0.1	-	-	-	-
10	2.33±0.02	1.8±0.3	-	-	-	-
15	2.31±0.03	2.0±0.3	-	-	-	-
20	2.31±0.01	1.6±0.2	-	-	-	-
30	2.31±0.03	1.6±0.2	-	-	-	-
40	2.35±0.01	1.7±0.2	2.95±0.02	2.6±0.6	-	-
50	2.34±0.05	1.6±0.4	3.01±0.03	2.8±0.4	-	-
60	2.36±0.03	1.3±0.4	3.03±0.05	3.5±0.4	-	-
70	2.35±0.05	1.0±0.6	2.97±0.03	4.4±0.2	-	-
80	2.34±0.05	0.6±0.5	2.99±0.04	5.4±0.3	-	-
90	-	-	2.93±0.03	6.4±0.3	-	-
95	-	-	2.90±0.02	6.4±0.5	2.67±0.04	2.4±0.5
100	-	-	2.90±0.05	7.3±0.3	2.67±0.02	2.4±0.2
110	-	-	2.89±0.01	7.4±0.4	2.65±0.02	2.3±0.4
120	-	-	2.88±0.05	7.4±0.6	2.63±0.05	2.3±0.5
140	-	-	2.90±0.01	7.2±0.7	2.66±0.04	2.3±0.7
150	-	-	2.91±0.03	7.3±0.5	2.63±0.05	2.2±0.4
180	-	-	2.88±0.05	9.2±0.2	2.66±0.06	3.2±0.2
200	-	-	2.88±0.05	9.6±0.6	2.63±0.05	4.8±0.2
230	-	-	2.88±0.01	9.7±0.7	2.65±0.03	4.9±0.7
280	-	-	2.86±0.02	9.6±0.6	2.67±0.04	4.7±0.7

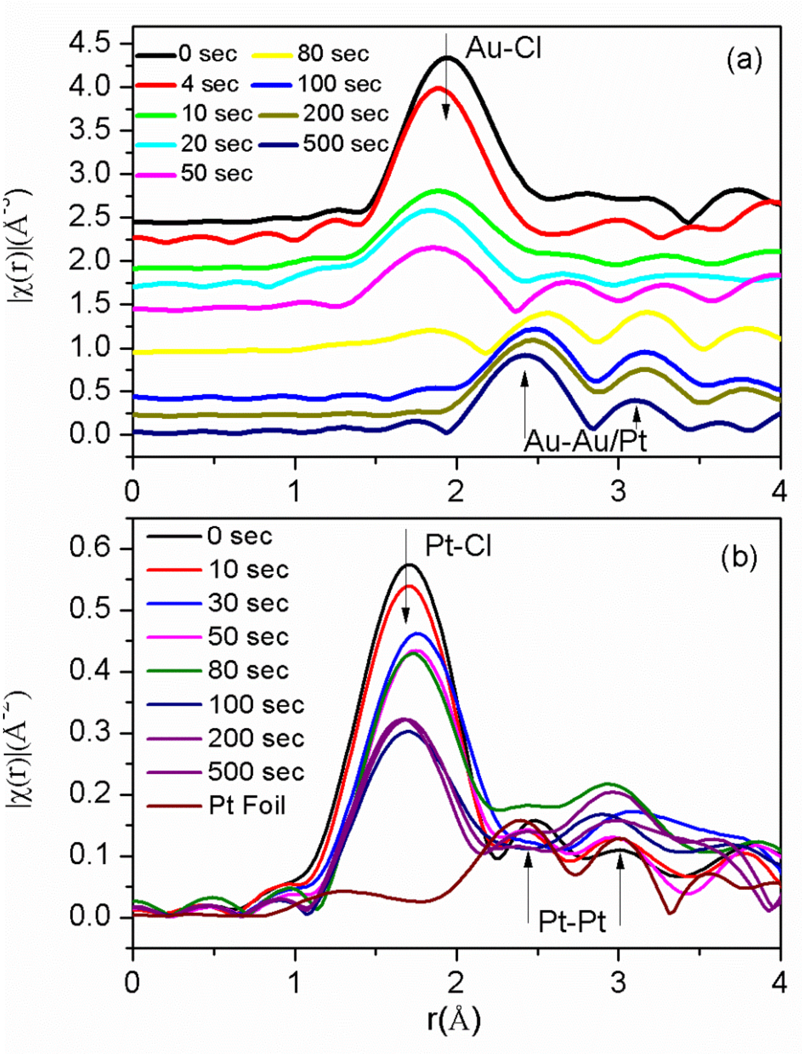

Figure 4.6: $\chi(r)$ versus r plot (FT-EXAFS spectra) measured at (a) Au and (b) Pt L_3 edge recorded at different time intervals during growth of Au@Pt nanoparticles.

It should be noted here that the Pt L_3 edge oscillations at high k range will have an effect on the Au L_3 edge data since the difference in the two edges are less than 500 eV. However, as has been shown by Chen *et. al.*[124], interference of Pt L_3 edge oscillations in the Au L_3 edge data results in the appearance of peaks at low r<2Å, whereas peaks due to Au and Pt shells generally appear at r>2Å. We have also found that Au L_3 edge FT-EXAFS data of the gold precursor without any Pt precursor in the solution and the 0 sec. data of the reaction solution containing both Au and Pt precursors resemble each other at lower r range without any extra peak in the mixed precursor case. Therefore we can say that Pt L_3 edge oscillations have not significantly affected the Au L_3 edge data in this case.

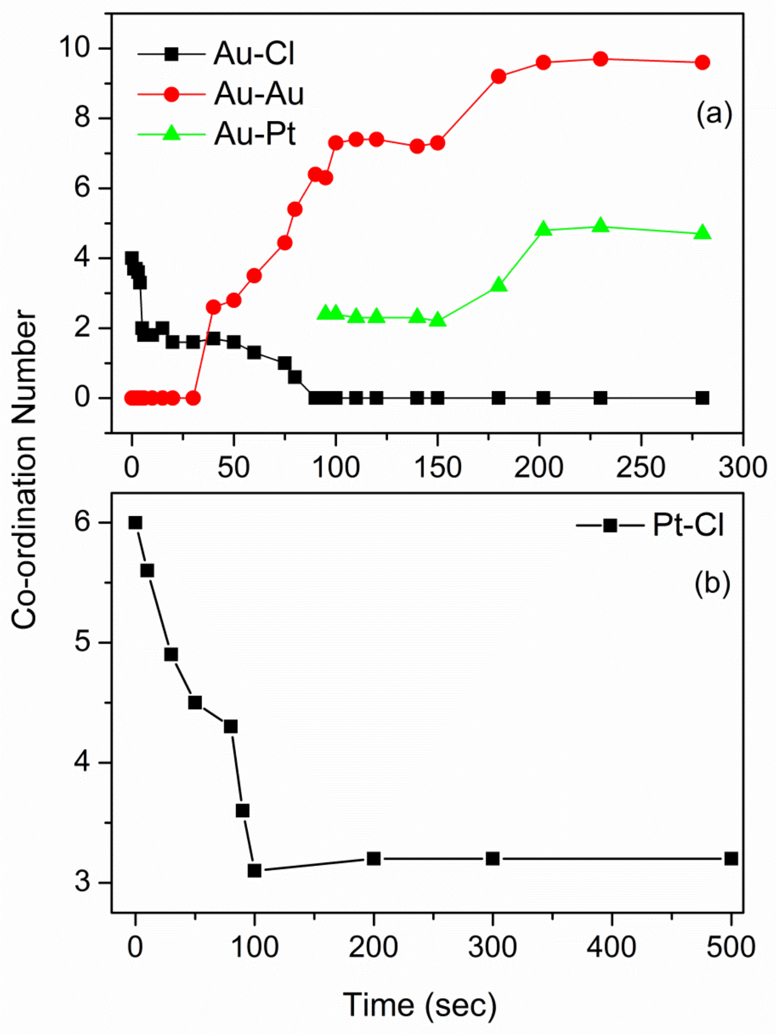

Figure 4.7: Variation of co-ordination numbers of (a) Au-Cl, Au-Au, Au-Pt bonds and (b) Pt-Cl bonds as a function of reaction time during growth of Au@Pt nanoparticles.

Fig. 4.7a shows the variation of coordination numbers of the three shells (Au-Cl, Au-Pt and Au-Au) with time. It can be seen from Table 4.1 that the bond lengths corresponding to the Au-Cl and Au-Pt shells do not change significantly during the reaction, however the Au-Au bond length decreases from ~3 Å to 2.88 Å with time. Similar phenomenon has also been observed by Yao *et. al.*[125] during the growth of gold nanocrystals from $HAuCl_4$ precursor. The above authors have shown by linear combination fit of theoretically simulated XANES spectra of $HAuCl_4$ precursor and Au_2Cl_6 dimers that this initial observation of higher values of the Au-Au bond length is possibly due to the partial reduction of $HAuCl_4$, presence of Cl^{-1} ions surrounding the Au atoms and formation of Au-Cl dimmers. However, as reaction proceeds the specific surface area per Au atom decreases, which in turn reduces the capping efficiency of Cl^{-1} ions and Au-Au bond lengths thus approaches its nominal value of 2.88 Å. It can also be noted that the Au-Pt bond distance obtained is ~2.65 Å which is less than nominal Pt-Pt bond distance of 2.76 Å. However, in solution while studying formation of Pt nanoparticles reduced by methanol in presence of citrate, Lin *et. al.* have also reported Pt-Pt bond length value of 2.68 Å[51].

Fig. 4.6b shows the $\chi(r)$ versus r plots at Pt L_3 edge at different time during the growth of Au-Pt bimetallic nanoparticles. The first peak (~1.8 Å) corresponds to Pt-Cl bond and the peaks between 2-3Å corresponds to Pt-Au and Pt-Pt bonds. It should be noted that Au L_3 edge appears only 355 eV above the Pt L_3 edge, therefore the energy range measured above Pt L_3 edge is limited and we can get a k range only upto 8.5 $Å^{-1}$ for Pt L_3 edge EXAFS data. Since the k range is short, we could get the information regarding first shell (Pt-Cl) only around the Pt sites. Thus in this case, the $\chi(r)$ versus r plots have been fitted in the range of 1-2.3 Å assuming a Pt-Cl path only. The R_{factor} of all fits are less than 0.01 which ensures good fit. Fig. 4.7b shows the variation of coordination number of the Pt-Cl bond. The best fit results have also been presented in Tables 4.2. for Pt L_3 edge data.

Table 4.2: Pt L_3 edge EXAFS Fitting Results

Time(s)	Pt-Cl (σ^2 =0.002 $Å^2$)	
	r(Å)	N
0	2.23±0.02	6±0.4
10	2.22±0.04	5.6±0.5
30	2.25±0.05	4.9±0.3
50	2.25±0.04	4.5±0.5
80	2.23±0.06	4.3±0.6

90	2.24±0.02	3.6±0.5
100	2.23±0.06	3.1±0.7
200	2.23±0.04	3.2±0.5
300	2.23±0.02	3.2±0.6
500	2.22±0.02	3.2±0.6

Recently, Frenkel *et. al.*[126] have suggested a method to determine the homogeneity of bimetallic systems from EXAFS analysis by correlating Cowley's short range order parameter with the homogeneity of bimetallic systems. Cowley short range order parameter is given by:

$$\alpha = 1 - \frac{N_{AB}/N_{AM}}{x_B} \tag{4.1}$$

where, x_B is the molar concentration of B-type atoms in A-B bimetallic alloy. N_{AB} is the average coordination number of B type atoms around A type atoms and N_{AM} is the average coordination number of metal neighbors around A type atoms. Cowley parameter (α) can vary from -1 to 1 and can be used to determine the positive and negative degree of clustering in bimetallic alloys. Positive value of α indicates that the bimetallic system is heterogeneous in nature. For homogenous alloy, the value of α lies between α_{min} and 0, where $-1<\alpha_{min}<0$. In our case, we have $N_{AuPt}=4.8$, $N_{AuM}= 4.8+9.6=14.4$, $x_B/x_A= 0.78$ (From XANES), therefore $\alpha= 0.24$. The above values of coordination numbers for different bonds have been taken after 200 sec. from the start of the reaction since it has been found that the coordination numbers do not change after that. The positive value of α obtained in this case indicates that Au and Pt are not homogenously mixed, instead they form heterogeneous configuration consistent with a core-shell structure.

4.2.3 *In-situ* UV-Visible spectroscopy studies

Fig. 4.8 shows the UV-Vis spectra of the reaction solution recorded at a time interval of 1 second during the growth of bimetallic nanoparticles. It has been observed that at 25 sec. a hump appears near 540 nm which corresponds to the Surface Plasmon Resonance (SPR) peak of gold nanoparticles. The intensity of the Au SPR peak increases till 50 sec. which indicates the fact that gold nanoparticles are formed in the solution. However at 100 sec. it can be seen that the Au SPR peak intensity decreases and it splits into a double hump. As time proceeds further the intensity of this peak decreases and finally after 160 sec. the SPR signal almost vanishes. This decrease in the intensity of the Au SPR peak and finally its disappearance indicates the formation of Pt shells on Au cores[123, 127-129]. Thus, from the *in-situ* UV-Vis measurements we get the evidence of formation of core-shell type structure for bimetallic Au-Pt system. It should be noted here that Pt nanoparticles do not show any characteristic SPR peak. Further explanation of the appearance of two peaks or hump in the SPR spectra has been given later in section 4.4.

4.3 *Ex-situ* studies

4.3.1 Transmission Electron Microscopy

The low resolution TEM image of fully formed Au-Pt bimetallic particles extracted from the solution after 60 min. of reaction has been shown in Fig. 4.9 while Fig. 4.10 shows the particle size distribution histogram which reveals that most of the particles are ~ 3-5 nm in size though few particles of larger sizes are also seen. Fig 4.11(a) shows the *ex-situ* HR-STEM image of a Au-Pt nanoparticle which reveals a lattice spacing of ~0.23 nm corresponding to {111} planes. The d spacings of Au and Pt {111} planes are 2.35 Å and 2.26 Å respectively which are very close and it is not possible to distinguish between them by seeing the lattice spacing in HRTEM micrograph. Hence to distinguish between Au and Pt regions in the particle, EDS line scan has been done, which is explained later in this section. It should be noted that the HRTEM/EDS measurements have been taken on few nanoparticles, however in the following the result has been given for a representative nanoparticle, chosen from the higher side of the size distribution curve because of the clarity of the result. It does not anyway hamper the generalisation of the result. .

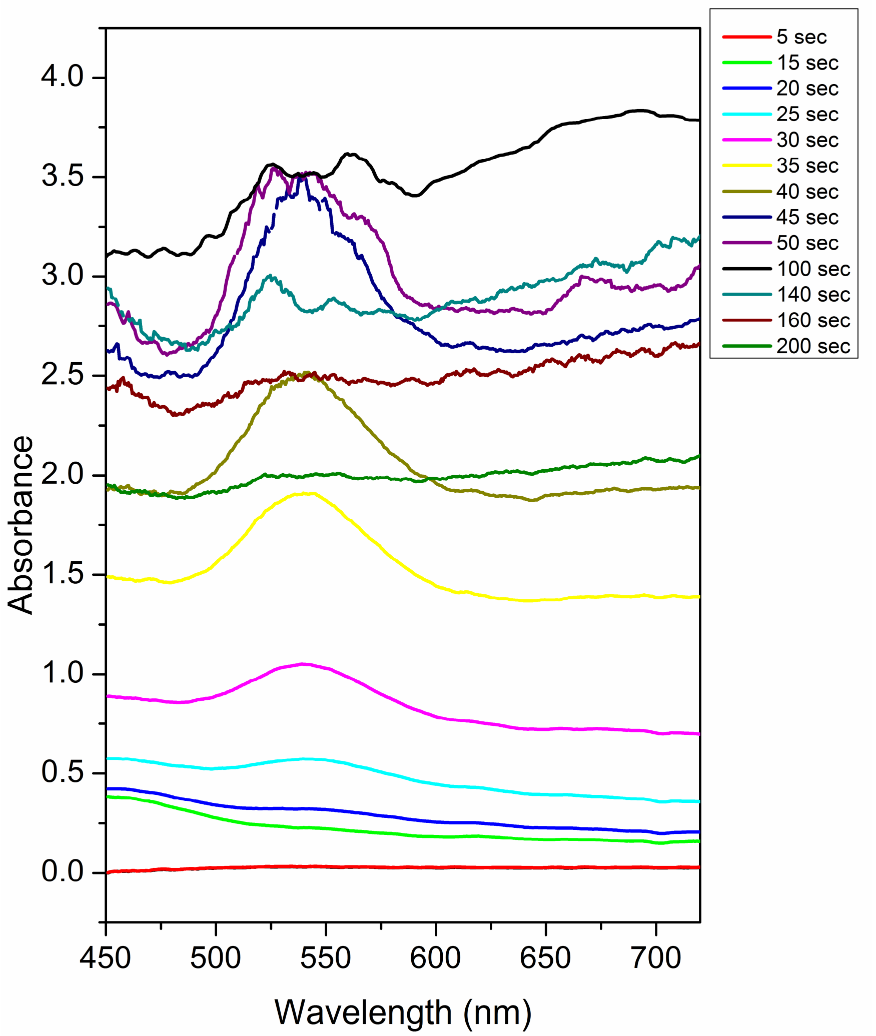

Figure 4.8: *In-situ* UV-Vis spectra recorded at different time intervals during growth of Au@Pt nanoparticles.

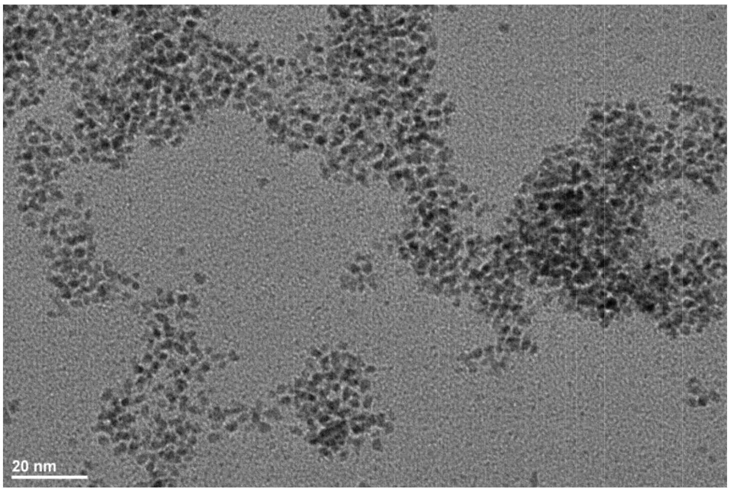

Figure 4.9: TEM image of Au-Pt bimetallic particle

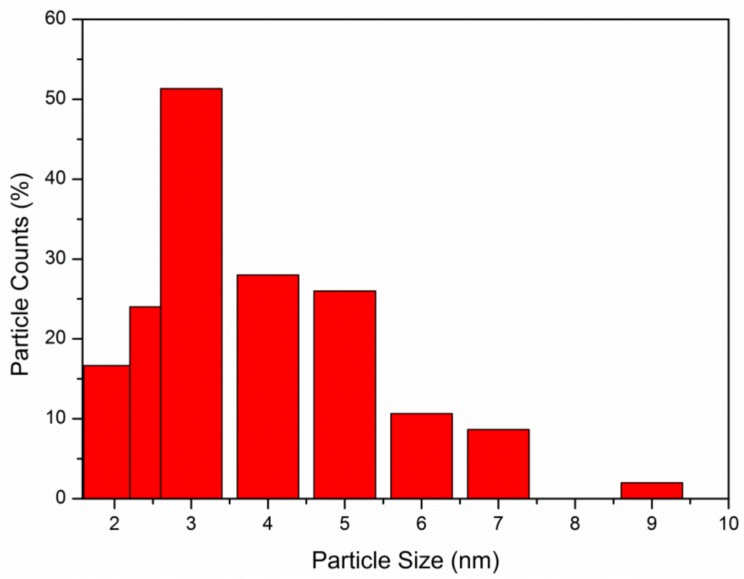

Figure 4.10: Particle size histogram of Au-Pt bimetallic particles

It should be noted that the particle sizes obtained in case of these bi-metallic nanoparticles are significantly less than that of the monometallic Au and Pt nanoparticles reported in Chapter 3. Such small sizes for Au-Pt core shell nanoparticles have been reported by many researchers also[118, 124, 130]. Zhang *et. al.*[118] for example, have reported that the smaller particle size of the Au-Pt bimetallic nanoparticles results in higher catalytic activity for aerobic glucose oxidation. The activity increases gradually with decrease in Au-Pt particle size from 10 nm to 3 nm and increases drastically for particle size less than 3 nm since in this regime, the proportion of the surface atoms, that play the main role in catalysis, increases significantly.

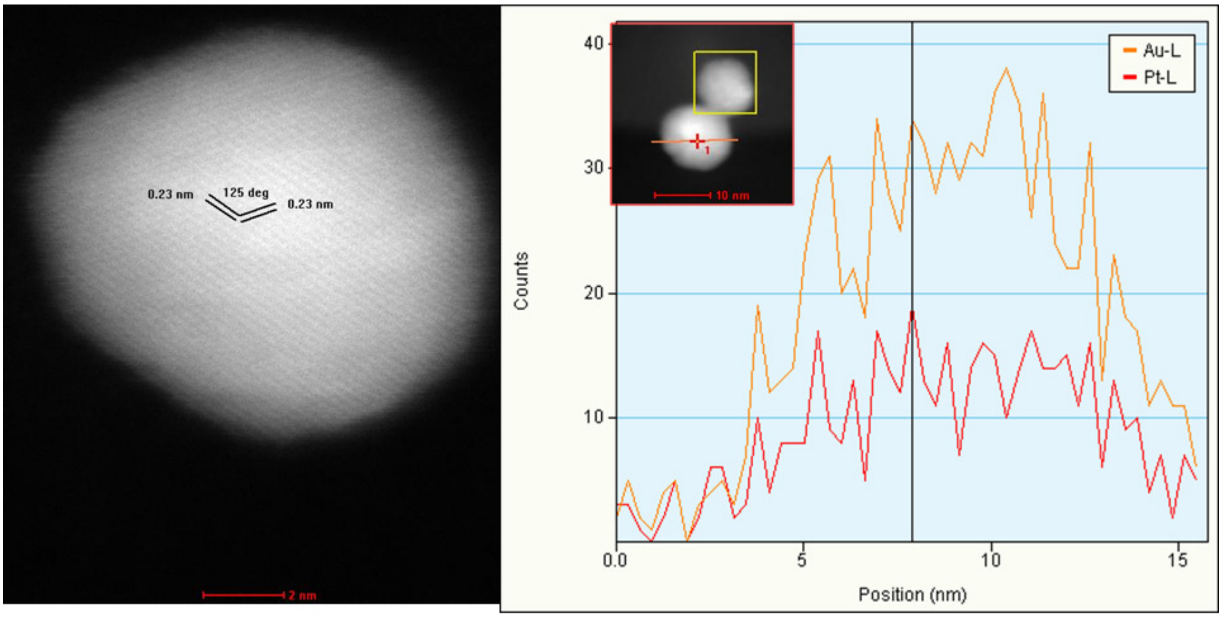

(a) (b)

Figure 4.11: (a) HR-STEM micrograph and (b) EDS line scan on fully formed Au-Pt bi-metallic nanocrystal.

The EDS line scan on a representative nanoparticle is shown in Fig. 4.11(b), which indicates higher concentration of Au at the central portion than Pt manifesting a nearly core-shell type structure. Our EDS line scan spectrum resembles the spectra reported by several other researchers on Au-Pt core-shell structure[118, 131-133], however, it should be mentioned here that in the EDS line scan we have not observed any region where Pt concentration is higher than that of Au. This suggests that the core may be of Au, but the shell is not entirely of Pt, instead it may be a bimetallic shell of both Au and Pt or a thick Au core and a thin Pt shell. It should be noted here that the core-shell image contrast could not be seen in the HRTEM micrograph due to nearly same atomic numbers of Au and Pt.

4.3.2 X-ray Photoelectron Spectroscopy

To get further insight into the structure of the particles, *ex-situ* X-ray photoelectron spectroscopy (XPS) measurements were carried out. Au-Pt bimetallic particles were etched with Ar^+ ions for different time intervals and the XPS spectra were recorded to see if the surface composition changes with etching. Fig.4.12a represents the XPS spectra for the Au-4f orbital for different etching times. The as-prepared sample with no etching shows two Au 4f peaks ($4f_{5/2}$ and $4f_{7/2}$) with a difference in binding energy of 3.6 eV which is a characteristic of Au[134]. However in this as-prepared sample Au is more electronegative as compared to elemental Au and there is an increment in the binding energy of Au with an increase in etching time. It has been observed that after an etching of 105 min, the binding energy of Au -$4f_{7/2}$ is ~84.0 eV which is a characteristic of Au^0.

Fig. 4.12b is the representative XPS spectra for the Pt 4f orbitals. It has been observed that binding energy corresponding to Pt $4f_{7/2}$ in the as-prepared sample (71.33 eV) and the difference in binding energies of Pt$4f_{7/2}$ and Pt$4f_{7/2}$ peaks is very close to that of Pt 0 state[134]and there is again an increment in the binding energies of Pt 4f peaks as etching time is increased.

In the as-prepared sample Au is more electronegative due to fact that in this case the XPS signal of Au mostly comes from the Au/Pt interface of the Au core and Pt shell structure, and there is a definite electronic interaction at the Au-Pt interface. With the increase in etching time, as more and more Pt shell is removed by etching we obtain enhanced signature of metallic Auof the core and the binding energy of Au 4f peaks increases. It is also corroborated with the nature of variation of binding energy of Pt 4f peaks, where we find that Pt was initially present as Pt metal and its binding energy increases as we approach the Au/Pt interface by etching.

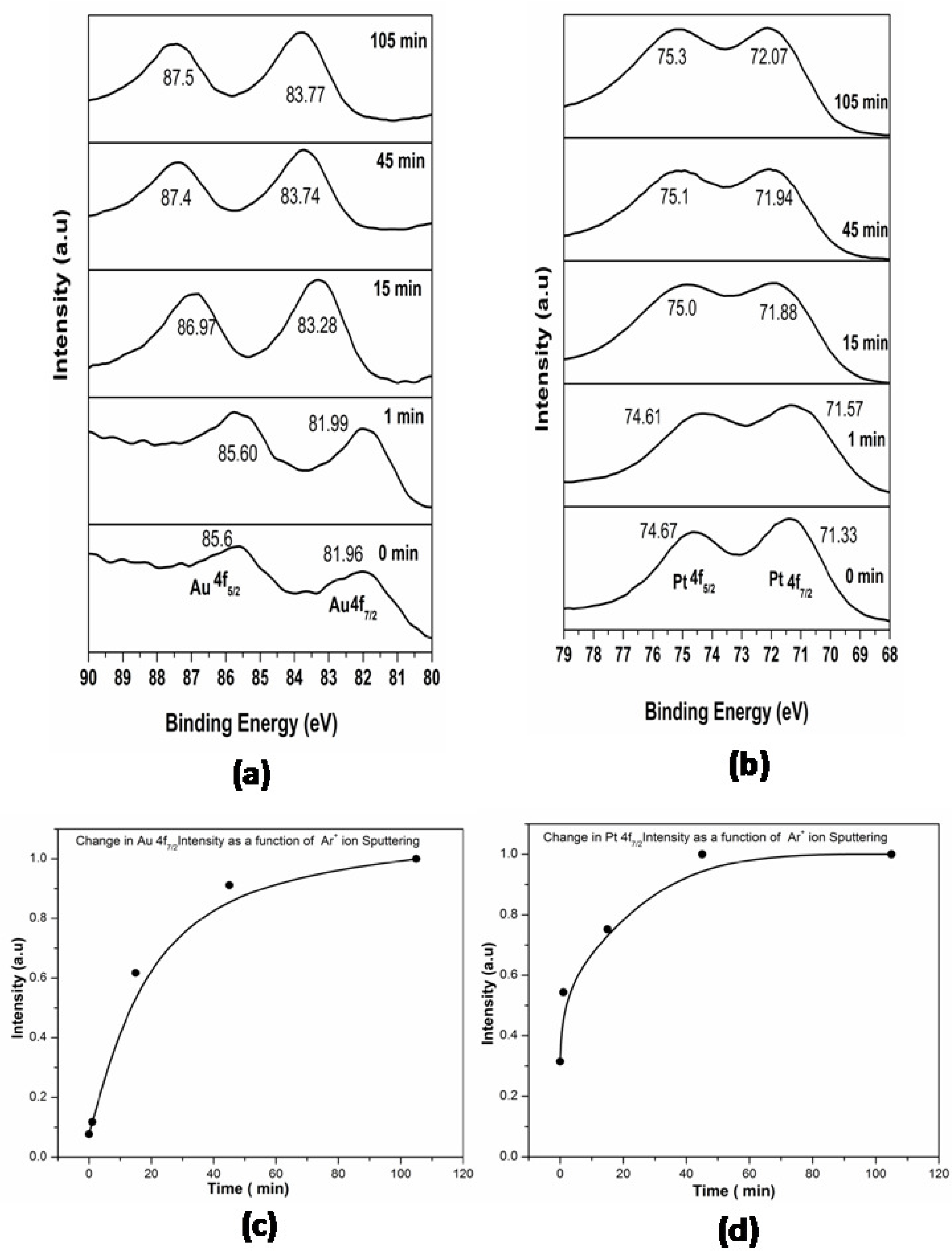

Figure 4.12: a) XPS Spectra of Au-4f with different sputtering time 0 min, 1 min, 15 min, 45 min and 105 min. (b)XPS Spectra of Pt-4f with different sputtering time 0 min, 1 min, 15 min, 45 min and 105 min. (c) Variation of intensity as a function of sputtering time of the Au-$4f_{7/2}$ XPS peak after background correction using a Shirley Background and normalisation w.r.t. the intensity after 105 min. etching and (d) Variation of intensity as a function of sputtering time of the Pt-4f $_{7/2}$ XPS peak after background correction using a Shirley Background and normalisation w.r.t. the intensity after 105 min. etching.

Fig. 4.12 (c) and (d) show the variation of intensities of Au $4f_{7/2}$ and Pt $4f_{7/2}$ peaks, with increase in etching time. The intensities are obtained after background correction and are normalized with respect to the intensity value at the maximum etching time. Intensities of both Au and Pt peaks increase with etching due to removal of the surfactants, however, it has been found that with etching the relative increase in intensity of the Au $4f_{7/2}$ peak is much higher as compared to that of the Pt $4f_{7/2}$ peak. This implies that Au is mostly present at the core and Pt at the shell of the nanoparticles. Thus XPS results also corroborate with the EDS line scan results as discussed in the previous section that the nanoparticles formed here are having a thick Au core and thin Pt shell.

4.4 Growth of Au-Pt bimetallic nanoparticles

From the XANES analysis at the Au and Pt L_3 edge (Fig. 4.3), it can be observed that the Au cations get reduced to metallic state within 10 sec., however the reduction of Pt cations in this duration is only 5%. The reduction of H_2PtCl_6 is much slower and even after a sufficiently long time of 1000 sec., only 78% of Pt is reduced to metallic state. This gives an indication that the Au seeds are formed immediately after adding the reducing agent and the Pt reduction occurs slowly on the surface of the Au seeds.

From the time resolved EXAFS analysis at Au L_3 edge (Fig. 4.7a), it can be seen that the Au-Cl co-ordination number shows a sudden drop from 4 to 2 at 5 sec. This may correspond to the reduction of Au^{+3} to Au^{+1} in the early stages of the reaction which has been mentioned by many researchers during the growth of Au nanoparticles.[27, 54] After 80 sec. there is no peak corresponding to the Au-Cl bond. At 40 sec. we see the appearance of Au-Au peak with a sudden jump in the Au-Au coordination. The Au-Au coordination monotonically increases upto 7 till

100 sec. At 100 sec., there is the appearance of Au-Pt coordination shell. The Au-Au and Au-Pt coordinations remain same till 150 sec., after which there is a sudden jump in the Au-Au coordination from 7 to 9 and the Au-Pt coordination increases monotonically to 4.7.

As suggested by Sakai and Alexandridis[99], and discussed in Chapter-3 also, the growth mechanism of block copolymer stabilized nanoparticles is governed by three main stages: (1) reduction of metal ions by block copolymer or additional reducing agent, (2) absorption of block copolymer on cluster and reduction of metal ions on the surface and (3) growth of nanoparticles stabilized by block copolymer. As in case of the monometallic nanoparticles described in Chapter-3, these three stages can also be identified for Au-Pt bimetallic nanoparticles. Till 40 sec. from the start of the reaction, the reduction of gold precursor occurs which corresponds to the first stage described above. After 40 sec. there is a sudden jump of Au-Au coordination to 2.6 which may indicate the formation of Au_4 cluster[27]. This situation is similar to Lamer Nucleation Burst[24] where the monomer concentration increases in the solution and as it crosses the critical value suddenly the nuclei are formed with a jump in the nearest neighbour coordination. Subsequently, the Au-Au coordination number increases signifying the growth of these Au_4 clusters accompanied by the reduction of Au-Cl coordination till 100 sec. This corresponds to the second stage of the process. After 100 sec. the appearance of Au-Pt coordination signifies the formation of the shell. However the co-ordination number of Au-Au and Au-Pt remains constant till 150 sec. which may indicate the formation of a layer containing both Au and Pt between Au core and Pt shell. At this stage, the Au-Au coordination of 7.3 is close to the coordination number of Au_{55}cubo-octahedral cluster which is a stable cluster due to the second geometrical shell closing[105]. After 150 sec., there is again a sudden jump in Au-Au coordination to 9.6 which is close to the icosahedral Au_{147} cluster which is a stable cluster with third geometrical shell closing[103]. The Au-Pt coordination number also monotonically increases till 200 sec. signifying the growth of the Pt shell. This corresponds to the third stage of the reaction as per the above model. From the Pt L_3 edge EXAFS data (Fig.4.7b), it can also be seen that the after 100 sec. there is no further reduction of Pt precursor and subsequently there is a slight increase in the Pt-Cl coordination which may correspond to the stabilization of the nanoparticles.

It should be noted here that as per the above proposition, Au precursor is first reduced and Au_4 clusters are formed as has been confirmed by *in-situ* XANES and EXAFS studies and further growth of Au and Pt takes place on these clusters which act as seeds. However, as has been observed by Esfahani et. al.[117, 123], deposition rate of Au is much higher than that of Pt. Therefore block copolymers preferentially attaches to $AuCl_4^-$ and reduces it on the surface of the clusters resulting in growth of Au clusters. As the concentration of $AuCl_4^-$ ions decreases in the solution $PtCl_6^-$ ions are available for attachment to the polymer and this results in the formation of Pt shell. Thus Au_{55} clusters are formed prior to Pt shell formation. However, there is also an intermediate stage when both Au and Pt are simultaneously reduced by the block copolymer. This results in a layer of Au-Pt alloy between Au core and Pt shell. This signature of an Au-Pt alloy interface has also been found by *ex-situ* XPS measurements described in subsection 4.3.2.

It should also be noted that, though the size of the nanoparticles as shown by HR-STEM is~<10 nm, the SPR peak in the *in-situ* UV-Vis spectra shown in fig.4.8, initially appears at 540 nm which corresponds to much larger particles. However, as the reaction proceeds the SPR peak shows a blue shift and at 50 sec. it appears at 520nm corresponding to <10 nm particle size. Similar phenomenon of appearance of SPR peak at higher wavelength and its blue shift during the reaction has been found by other workers also[135]. This can be attributed to the effect of the block copolymers engulfing the gold particles resulting in formation of branched intermediates during the reaction. It should be noted that from *in-situ* EXAFS measurements also discussed above, we have seen that Au-Au peaks starts increasing from 50 sec. onwards. The gold particles formed before 50 sec. corresponds to the initial stage of growth corresponding to the "reduction of metal ions by block copolymer" stage as mentioned above and at this stage gold particles or clusters must be covered with the block copolymer. As the reaction proceeds we start obtaining spherical like nanoparticles with fewer branches and from 50 sec. onwards the SPR peak start appearing at 520 nm corresponding to particles of 10 nm size. However, it can be seen from fig.4.7 that from 50 sec. onwards another peak also starts appearing at 560 nm along with the peak at 520 nm. It has been observed from *in-situ* EXAFS studies that in this time interval a layer containing both Au and Pt between Au core and Pt shell also appears. *Ex-situ* XPS studies also suggest that there is a Au-Pt mixed phase at the interface of the core and shell which has different electronic configuration than that of Au and the peak at 560 nm may correspond to this phase. Subsequently, the SPR peaks vanish from 150 sec. onwards as the Pt shell starts covering the Au nanoparticles. *In-situ* EXAFS measurements also show that the Au-Pt coordination starts increasing from 150 sec. onwards.

4.5 Comparison of growth of Au-Pt bimetallic nanoparticles with growth of Au and Pt monometallic nanoparticles

In this section, we try to compare the formation of Au and Pt monometallic nanoparticles discussed in Chapter 3 with that of Au-Pt bimetallic nanoparticles discussed above. In all the cases we have identified the three stages of growth as suggested by Sakai and Alexandridis[99]. However, for monometallic nanoparticles the process is much slower than that of the bimetallic nanoparticles. This may be due to the use of ascorbic acid as reducing agent in the later case, which is comparatively stronger than sodium citrate used for the synthesis of gold nanoparticles.

The use of stronger reducing agent results in faster reduction of the precursor and formation of smaller nuclei. In case of growth of Pt monometallic nanoparticles, the Pt precursor couldn’t be reduced at room temperature with ascorbic acid as reducing agent and the reaction solution had to be heated to start the reduction of the precursor. However, in the bi-metallic case, Pt precursor is reduced at room temperature only. Though the reduction is much slower than that of gold precursor, the reduction is facilitated by the formation of small Au clusters which act as seeds for the surface reduction of the Pt precursor. For the case of Au and Pt monometallic nanoparticles, 13-atom clusters are formed which acts as nuclei for further growth, however for Au-Pt bimetallic nanoparticles 4-atom clusters act as nuclei for growth. This results in smaller bimetallic nanoparticle as compared to the monometallic case. Au_{147} cluster has been identified in the growth of Au monometallic nanoparticles, which further grow into Au nanoparticles. In case of Au-Pt bimetallic nanoparticles, Au_{147} clusters are also formed which get covered with the Pt shells.

4.6 Conclusion

Au-Pt bimetallic nanoparticles have been synthesized through a one-pot synthesis route from their respective chloride precursors using block copolymer as a stabilizer. Using the set-up for simultaneous *in-situ* time-resolved XAS and UV-Vis measurements at the Energy Dispersive EXAFS beamline (BL-08) at Indus-2 SRS at RRCAT, Indore, India, the growth of Au-Pt bimetallic nanoparticles from their respective chloride precursors using block copolymer stabilizer have been studied. The measurements have been carried out in a specially designed teflon cell with one optical path for X-ray in the direction of synchrotron beam and another in the perpendicular direction for visible radiation. From the *in-situ* measurement of UV-Vis spectroscopy, it has been observed that Au seeds are formed with the appearance of Au SPR peak and vanishes when the Pt shell starts forming on the Au core. This confirms the formation of core shell like structure in Au-Pt bimetallic alloy. *Ex-situ* studies by HRTEM with EDS line scan and XPS measurements with *in-situ* etching on the fully formed nanoparticles also ascertain their core-shell type nature. However, simultaneous *in-situ* XAS measurement gives a detail microscopic account of the phenomenon which shows that Au precursor get reduced within 10 sec. and Au_4 clusters are formed which act like nuclei for the further growth and the Pt reduction occurs slowly on the surface of the Au nuclei. The study of the formation process shows how the difference in the reduction potential of the two precursors could be used successfully to get the core shell configuration of bimetallic alloy in a controlled fashion using a one–pot synthesis method.

Chapter 5

In-situ XAS studies on growth of Cu nanoparticles

Transition metal nanoparticles are important due to their uniqueness in properties and wide variety of applications in different fields as optical, electronic, catalytic and magnetic materials[136-139]. Properties of these nanoparticles are highly dependent on their size and shape, and often are very different from their corresponding bulk materials. Copper is important because of its high natural abundance, low handling cost and application in diverse fields[140]. In many applications, efforts have been made to replace noble metal based systems with Cu based systems to make the technology cost effective[141, 142]. However, the main challenge faced in metallic Cu based systems is their high affinity towards oxidation. Therefore, several efforts have been made to increase the stability of metallic Cu nanoparticles and reducing their reactivity towards oxygen, water and other chemicals[143, 144]. Due to the availability of Cu in multiple oxidation states (Cu^0, Cu^{+1}, Cu^{+2},Cu^{+3}), it can participate in many reactions enabling reactivity in both one and two electron pathways. Therefore, Cu based nanoparticles are widely used as catalysts for Photocatalysis, Electrocatalysis, Gas phase reactions and Oxidation-Reduction reactions[140]. With such a wide application of this system, the importance of synthesis routes comes into picture, through which not only the properties of the system can be controlled but also efforts can be made to reduce the susceptibility of the system towards oxidation.In thischapter, we present the study of growth of Cu nanoparticles synthesized by chemical reduction method using PVP as a stabilizing agent under constant N_2 bubbling using a specialized flow set-up. The flow setup facilitates online monitoring of Cu nanoparticles formation using *in-situ* X ray Absorption Spectroscopy measurement while creating the required reaction conditions for their growth.

5.1 Synthesis of Cu nanoparticles

Cu nanoparticles have been synthesized by mixing aqueous solution of copper acetate [$Cu(OAc)_2$] (0.5M) with Poly(N-vinyl-2-pyrrolidone) (PVP). NaOH is first added to this solution which makes its colour bright blue and cloudy manifesting formation of $Cu(OH)_2$ species. Subsequently $NaBH_4$ is added which makes the colour of the solution immediately changed to dark green and within next 3-4 minutes the colour further changes to brown and finally to black manifesting formation of Cu nanoparticles. The synthesis was carried out under continuous nitrogen flow with stirring and mixing of the reactants.

5.2 Flow setup for *in-situ* XAS studies

An *in-situ* EXAFS measurement cell has been reported in section 3.2 of Chapter-3, where the growth reactions were carried out in the specially designed cell and *in-situ* XAS spectra were recorded in the same cell as the reaction proceeds. However, such an experimental setup is generally useful only for one-pot synthesis and has very less flexibility in terms of creating different environmental conditions. In reference to this problem, a new setup has been designed where the reaction chamber and measurement chamber are separated enabling *in-situ* XAS measurements on variety of species grown or synthesized under various reaction conditions.Fig.5.1 shows the schematics of the flow setup for *in-situ* XAS measurement. In this setup, a reaction vessel, which is a three neck flask with two side nozzles, is used for adding, stirring and mixing the reactants. Two necks of the flask are used for continuous N_2 flow through the reaction vessel. The third neck is used for adding reactants using a computer controlled syringe pump. The two side nozzles are connected to the inlet and outlet of a peristaltic pump.

The reaction product is pumped to the *in-situ* XAS measurement cell from the reaction vessel through viton tubes using the peristaltic pump.

The *in-situ* XAS measurement cell is made of teflon and permits a continuous flow of the reaction solution. The cell comprises of a spacer which is mounted between two discs with Kapton windows fixed by four screws. A set of spacers of different thickness varying from 5mm to 20 mm, enables the adjustment of the X-ray path length in the solution. Depending on the absorption edge and the concentration of the cations in the reaction solution, the thickness of the spacer is decided to get the appropriate XAS edge jump. The spacer contains an inlet and outlet of outer diameter of 6 mm for connecting the viton tube. Photograph of the *in-situ* XAS measurement cell is shown in Figure 5.2. The peristaltic pump is chemically resistant and the pump rate is adjustable over a wide range. The peristaltic pump and the syringe pump, both are operated and controlled through the computer.

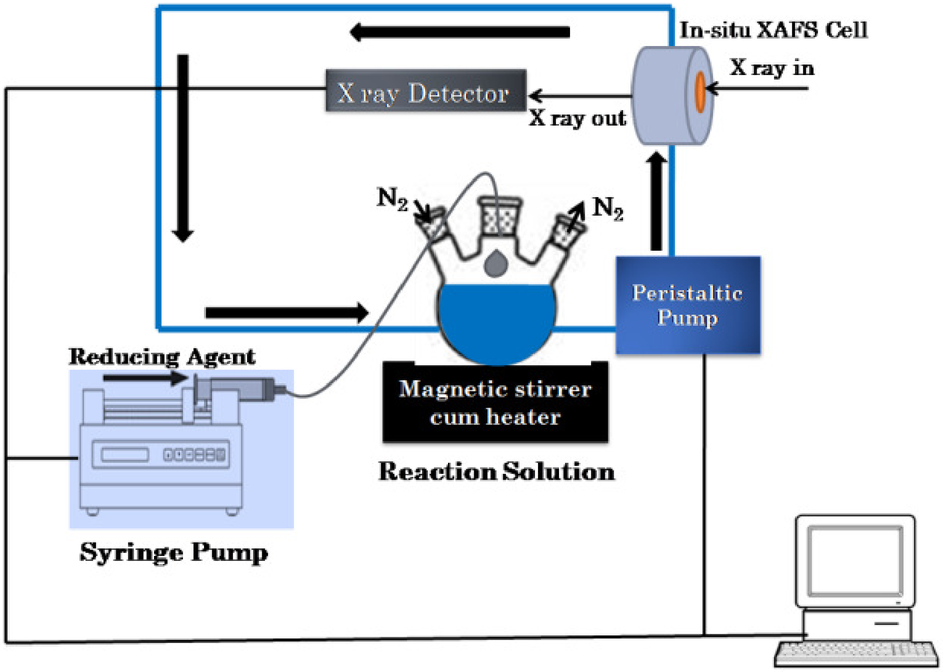

Figure 5.1: Schematics of Flow setup for *in-situ* XAS studies

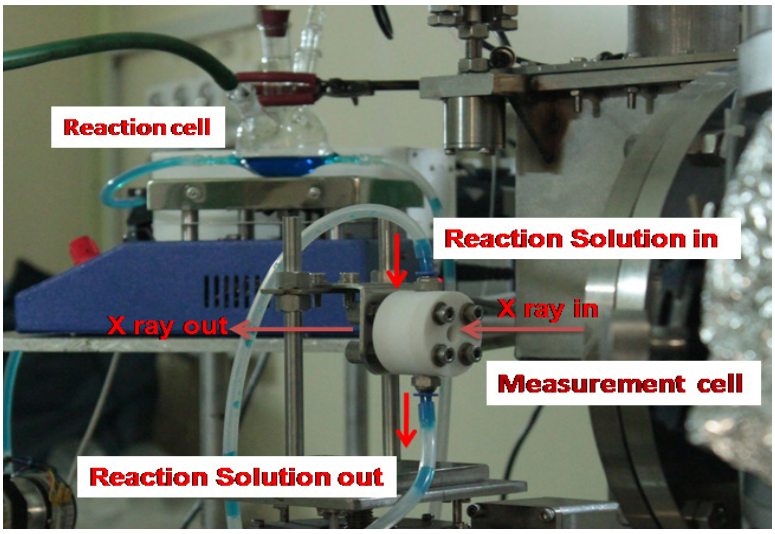

Figure 5.2: Photograph of the Reaction Vessel and *in-situ* XAS measurement cell

Time-resolved XAS measurement has been carried out at the energy dispersive EXAFS beamline (BL-8) at the Indus-2 synchrotron source[46] which has been discussed in details in Chapter-2. For *in-situ* XAS study of Cu nanoparticle formation, the teflon measurement cell has been placed at the sample position and the 5 mm spacer thickness was used to obtain an optical path length of 5 mm for X-ray through the solution. The copper acetate solution and PVP have been taken in the reaction vessel, subsequently NaOH was added to the solution and the $NaBH_4$ reducer was injected using the computer-controlled motor driven syringe pump. The solution in the reaction vessel was continuously stirred using a magnetic stirrer and N_2 gas is bubbled through the reaction vessel. The reaction solution was pumped to the measurement cell with a flow rate of 200 ml/min using the peristaltic pump which ensures turbulence–less steady flow of the liquid. *In-situ* XAS measurements have been carried out for an hour at regular time intervals of 1 s starting from the instant of adding the $NaBH_4$ reducer to the precursor mixture.

5.3 *In-situ* XANES study

Figures 5.3 shows the *in-situ* XANES and derivative spectra (inset a) at Cu K-edge recorded during the synthesis of Cu nanoparticles. As the reaction proceeds the absorption edge shifts from 8986 eV to 8979 eV, accompanied by a decrease in intensity of the white line peak at 8998 eV, which indicates the reduction of Cu^{2+} to metallic Cu. At 750 s a significant hump appears at 8982 eV, this may correspond to the formation of Cu^{+1} species. The derivative XANES spectra (inset(a) of fig.5.3) also show that as the reaction proceeds, the intensities of the peaks at 8985 eV and 8992 eV decrease and a new peak appears at 8979 eV, indicating formation of Cu metal nanoparticles, whose intensity increases with time and becomes very prominent after 1hr. This is also evident from inset (b) of Fig. 5.3 which clearly shows a significant shift in the absorption edge of the 1 hr. spectrum towards lower energy. However, the hump at the rising portion of the absorption edge and the oscillations above the absorption edge of the 1 hr. XANES spectrum (Fig. 5.3) are less prominent than that of a Cu foil which indicates that the reduction to Cu (0) may not be complete. This has also been found in the XRD data, which gives evidence for the presence of Cu_2O phase along with metallic Cu.

5.3.1 Linear Combination Fitting

Though the above observation gives us an idea of the reduction sequence of the synthesis process, to have a better insight we have carried out quantitative analysis of the time evolution of the XANES data. Linear Combination Fitting (LCF) is generally used to reproduce the data set as a linear combination of known standard spectra and thus can be used to identify known species formed during the reaction. Fig 5.4 shows the XANES and derivative spectra (inset) of Cu metal, Cu_2O and CuO references at Cu K-edge.

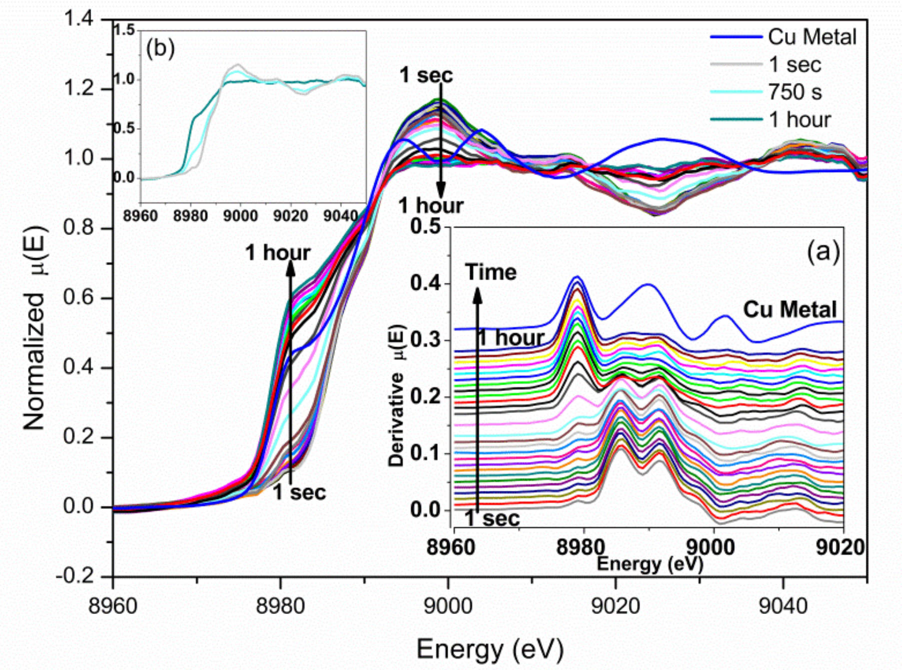

Figure 5.3: *In-situ* XANES spectra of the reaction solution measured at Cu K edge at different time intervals after mixing reducer in the precursor solution. Inset (a): Derivative of XANES spectra recorded during synthesis of Cu nanoparticles Inset (b): 1 sec., 750 sec. and 1 hr. spectra shown separately.

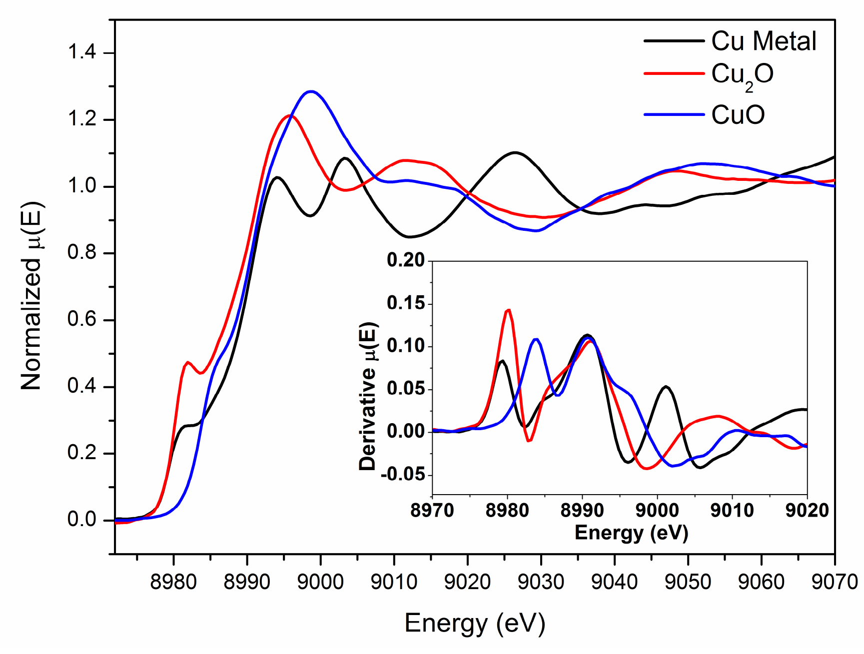

Figure 5.4: XANES spectra of Cu Metal, Cu_2O and CuO standards.

The LCF fitting of the *in-situ* XANES data have been carried out from -20 to 30 eV around the edge using CuO and metallic Cu as standards. It has been observed that the fitting of the data using these two standards are very poor and after 550 s the data could not be fitted using two standards, therefore there is a strong probability of presence of an intermediate species. Since, there are reports suggesting the reduction of Cu^{+2} to Cu through the formation of Cu^{+1}, which has been indicated by our XRD measurements also as discussed later in this chapter, we have attempted to fit the data using Cu_2O as an intermediate phase[76, 145]. It has been observed that the Linear Combination fitting of the XANES data using Cu metal, Cu_2O and CuO as references has improved the fitting quality significantly compared to the LCF fitting using Cu metal and CuO. Fig.5.5 shows the experimental XANES spectra at 550s and its LCF fit using the different combinations of the standards. However, the LCF method depends on the use of standard spectra and since we are not able to reproduce the experimental spectra perfectly, therefore may not be able to give the correct information regarding the intermediate species formed during the reduction process. This is evident from fig. 5.5 which shows poor fit of the experimental data with the LCF generated theoretical spectra.

5.3.2 Principal Component Analysis

To gain further insight into the intermediates formed during the reduction of Cu^{2+} to metallic Cu, the XANES spectra have been analyzed by Principal Component Analysis which has been discussed in details in sub-section 2.2.2 of Chapter 2. Following the work of Wang *et. al.*[74] PCA has been applied to the *in-situ* XANES spectra recorded during the formation of the PVP stabilized Cu nanoparticles. In case of the present data set, PCA analysis range of the XANES data was chosen from 8954 eV to 9025 eV. PCA was performed using Athena programme of the "Demeter" software package[71]. Fig. 5.6 shows the first five components sorted in descending order of their respective eigenvalues among which the first two components have been found to have most significant contributions to reproduce the spectra. However, the contribution of the third component also appears to be above the noise level. To determine the number of significant components, the data were fitted with 2, 3 and 4 principal components and the fit residuals were plotted in Fig. 5.7.

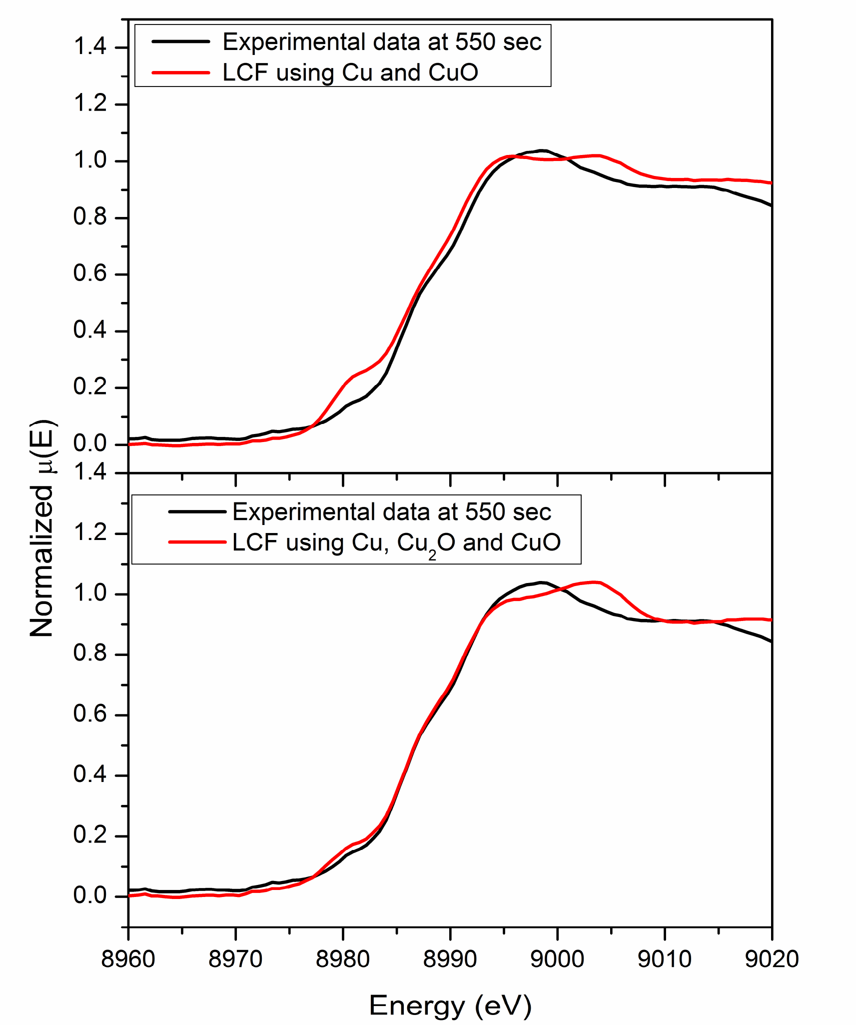

Figure 5.5: Linear Combination Fitting of the 550 s experimental data using different combination of Cu Metal, Cu_2O and CuO standards.

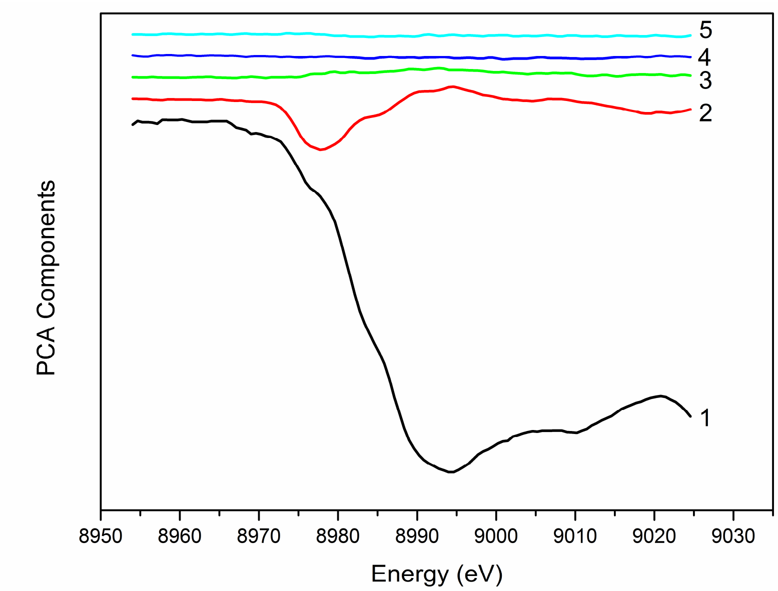

Figure 5.6: First five components of PCA analysis of the TR-XANES spectra recorded during growth of Cu nanoparticles.

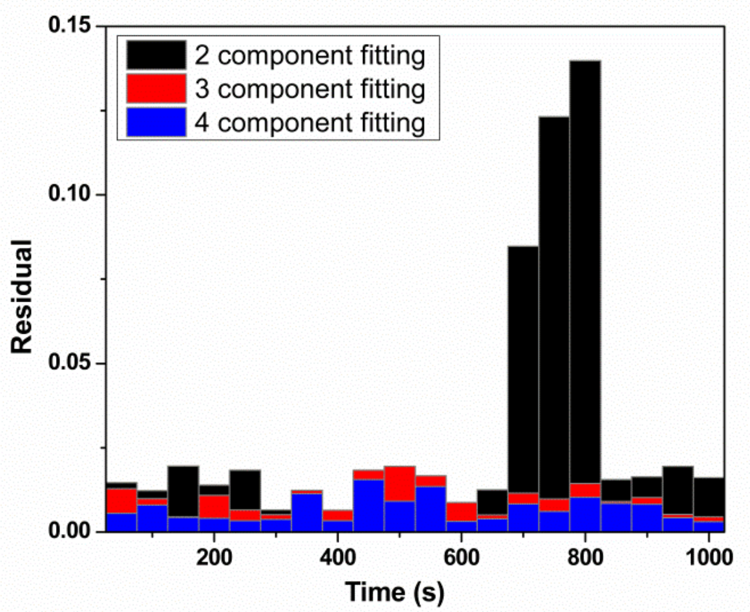

Figure 5.7: Fit residuals of the two, three and four Principal Component fitting of the TR-XANES spectra recorded during growth of Cu nanoparticles.

From Fig. 5.7 it is evident that the value of the residual for 2-component fitting is maximum around t= 700-800 s which indicates the presence of an intermediate species during this period. The fit quality improves significantly with the 3-component fitting and the value of the residual is within statistical noise level. Therefore, the analysis of the residuals from PCA not only predicts the presence of intermediate phase but also quantitatively estimates the time duration when the intermediate phase exists during the growth of Cu nanoparticles i.e. 700-800 s from the start of the reaction.

5.3.3 Multivariate Curve Resolution with Alternating Least Squares (MCR-ALS)

To further determine the structure and concentration profile of the intermediates during the reaction, MCR-ALS analysis which has been discussed in details in sub-section 2.2.3 of Chapter 2, has been done on the XANES data. Recently, MCR-ALS has emerged out to be a popular analytical method which is effectively applied to the analysis of *in-situ* XAS data. Cassinelli *et al.* have employed MCR-ALS to TR-XAS data for monitoring the activation of copper-alumina catalyst[76] and ethanol dehydrogenation reaction[146, 147]. They were successful in determining copper speciation during reduction of the catalyst and also obtained an in-depth information about the reduction process. Staniuk *et. al.*[78] have also used MCR-ALS to study the growth of Cu based nanoparticles in organic solvents and predicted the nucleation of Cu_2O and its consecutive reduction to Cu. Martini *et al.*[77] have studied Cu speciation and reducibility in Cu-CHA zeolite catalyst using MCR-ALS.

In the present work, MCR-ALS analysis of the *in-situ* XANES data has been performed using the commercial software The Unscrambler X (CAMO, Norway). The number of components as determined by PCA analysis in the previous subsection is 3 in the reaction mixture during the formation of Cu nanoparticles. This value has been used for the k rank of the C and S^T matrices in the MCR-ALS analysis. MCR-ALS analysis has been started using three guess spectra which are (i) the spectrum of the reaction solution recorded at 1s from the start of the reaction, (ii) spectrum recorded at 750 s where the intermediate dominated as predicted by PCA, and (iii) spectrum recorded at 3600 s when the reaction ends. Using these three guessed spectra the MCR-ALS applied on a large number of XANES data set evenly distributed over the whole time scale, gives three best fit absorption spectra of the pure constituents of the reaction solution which are shown in fig. 5.8 (along with their derivatives shown in the inset) while the concentration profiles of these pure constituents are shown in Fig. 5.9. The XANES features of the constituent 1 is found to be similar to $Cu(OH)_2$ with a shoulder peak at 8987 eV[145], which is formed at the start of the reaction. The constituent 3 is similar to metallic Cu with edge energy at 8979 eV which is the end product of the reaction. The constituent 2 is the intermediate species formed during 600 to 850 s after the start of the reaction. As evident from the absorption and their derivative spectra shown in fig.5.8, the absorption edge of constituent 2 lies in-between that of constituent 1 and 3, which are Cu^{+2} and Cu^0 species respectively suggesting that constituent 2 can be a Cu^{+1} species. The absorption edge of constituent 2 is 8980 eV which is same as that of Cu_2O. The formation of Cu^{+1} during the reduction of Cu^{+2} to Cu^0 has also been reported by Nishimura *et. al.*[145], Cassinelli *et. al.*[76] and Staniuk *et al.*[78] From the concentration profile plot (Fig. 5.9) it can be concluded that the reaction occurs in two steps: (i) formation of Cu^{+1} species from Cu^{+2} reduction after 500 s and (ii) reduction of Cu^{+1} to Cu^0 after 750 s from the start of the reaction. The Linear Combination Fitting using the pure constituent spectra determined from MCR-ALS gives very good fit of the experimental data (R_{factor}<0.005) as seen in Fig. 5.10.

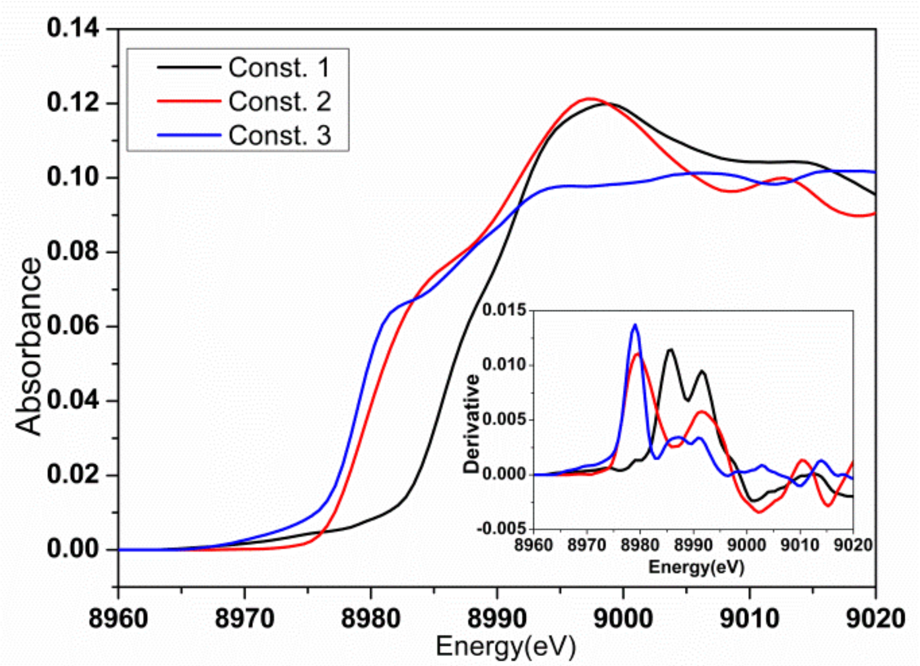

Figure 5.8: Constituent spectra predicted by MCR-ALS analysis of the TR-XANES spectra recorded during growth of Cu nanoparticles.

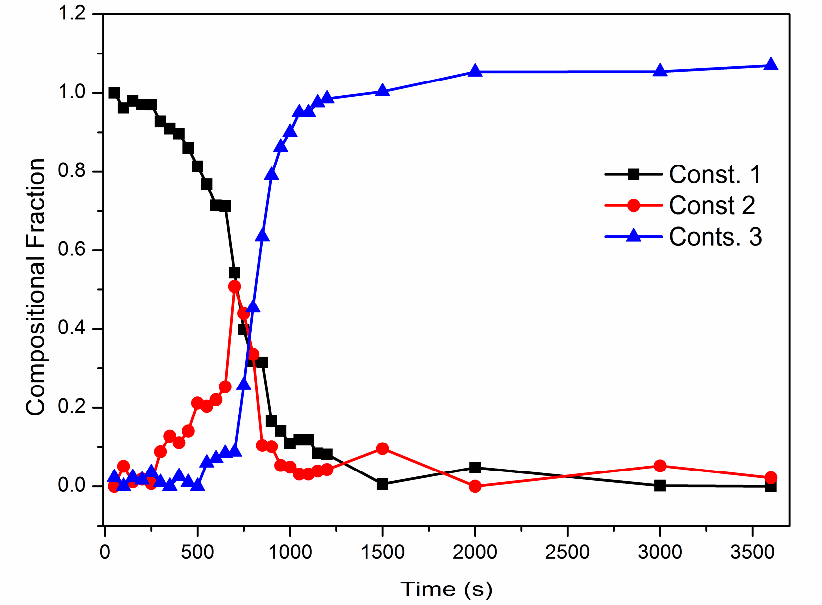

Figure 5.9: Concentration profiles of the constituents as determined by MCR-ALS analysis of the TR-XANES spectra recorded during growth of Cu nanoparticles.

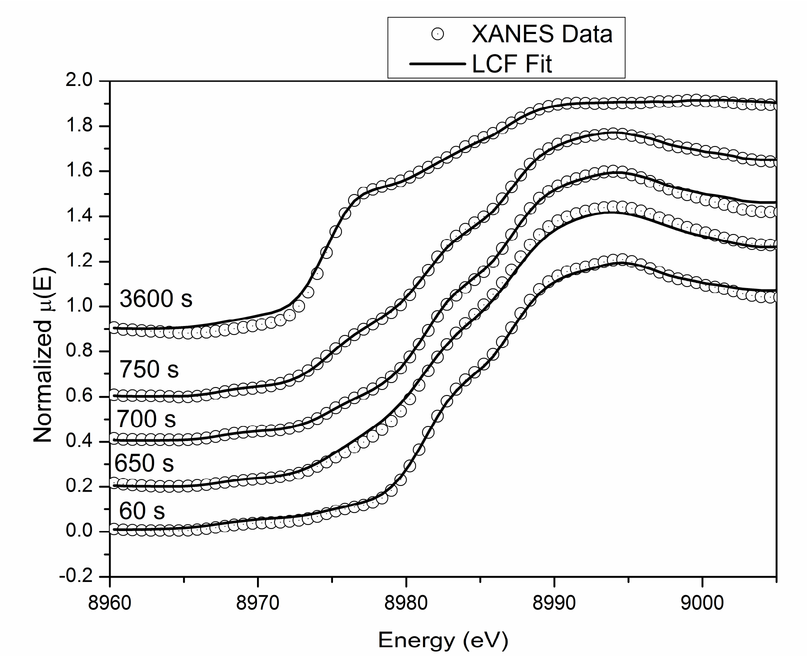

Figure 5.10: LCF fitting of the experimental XANES spectra using the MCR-ALS predicted constituent spectra as standards.

5.4 *In-situ* EXAFS study

EXAFS analysis of the constituents of the reaction solution as determined from the XANES analysis has been done for local structure information of the constituents. The XAS spectra of constituent 1 and 3 are same as the XAS spectra recorded at 1s and 3600 s. Finally, the EXAFS spectrum recorded at 750 s has been used to extract the exact structure of the intermediate i.e. constituent 2. Using the LC fitting parameters of the XANES spectra (Fig. 5.10), the XAS spectrum of the intermediate was extracted from the XAS spectrum of the solution measured at 750 s using the following relationship:

$$XAS_{\text{int}\,ermediate} = \frac{(Expt.data)_{750s} - c_1(XAS)_{const1} - c_3(XAS)_{const3}}{c_2} \tag{5.1}$$

where, *c*'s are the weights of the respective constituents in the XANES LC fitting of the experimental data.

From the XAS spectrum of the intermediate thus obtained, the EXAFS oscillations have been extracted following the standard procedure[3, 4, 39]. The EXAFS oscillations, $\chi(k)$ is weighted by $k^2$to amplify the oscillations at high $k$and the functions $\chi(k)k^2$are Fourier transformed using k range of 2-9 Å^{-1} to generate the$\chi(r)$ versus $r$plots (or FT-EXAFS spectra). The $\chi(r)$ versus r plots of the intermediate species extracted using MCR-ALS analysis along with the data recorded at 1s and 3600 s have been shown in Fig.5.11. The 1 s and the intermediate plots show peaks between 1-2 Å and fitted with a Cu-O path. The plot at 3600 s shows a peak between 2-3 Å and fitted with a Cu-Cu path. The best fit theoretical plots of the experimental data obtained as above have also been shown in Fig.5.11.

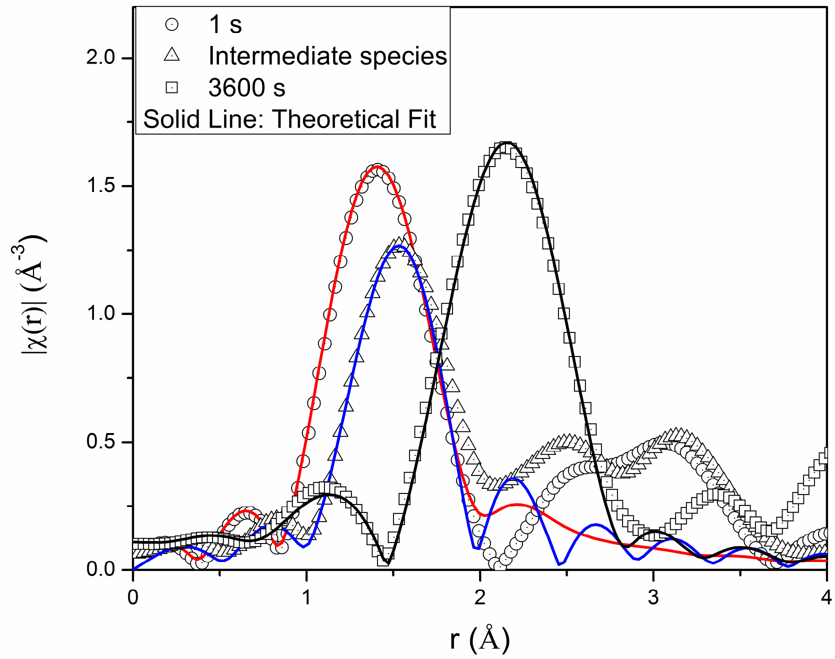

Figure 5.11: The FT-EXAFS spectra of the three constituent species of the reaction solution as predicted by MCR-ALS analysis of the TR-XANES data.

The above EXAFS analysis shows that the initial spectrum recorded at 1s corresponds to a Cu-O bond at 1.94 Å with coordination number of 4. This is in agreement with $Cu(OH)_2$ structure of the precursor[148]. The final spectrum recorded at 3600 s corresponds to a Cu-Cu bond distance of 2.51Å with coordination number of 9 which also agrees with crystallographic parameters of fcc Cu. It should be noted that the coordination number is less than its bulk value of 12 due to nanoparticle nature of the samples[149, 150]. The intermediate species as predicted by MCR-ALS analysis gives a Cu-O bond at 1.98 Å with coordination number of 2.4. The oxygen coordination around 2 is consistent with Cu_2O environment, however the Cu-O bond distance is higher than that of Cu_2O structure which should ideally be 1.85Å[151]. This higher bond distance may be due to the ligands attached to the Cu^{+1} species in the reaction solution.

It should be noted that in the above EXAFS analysis the information has been extracted by only 1st shell fitting due to limited k range of the data available from the solution phase measurements. However, that has not affected the identification of the species in any way. Similar approach has been followed by other workers also in analysis of EXAFS data extracted for intermediate reaction species by MCR-ALS analysis of time-resolved XAS data of Cu nanoparticles derived from solution phase[76, 152].

5.5 *Ex-situ* XRD and TEM Measurements

Figure 5.12 shows the XRD pattern of Cu nanoparticles synthesized using $NaBH_4$ and PVP. Most of the XRD peaks are identified to metallic Cu and Cu_2O phases. The peak at 29.8° corresponds to Cu_2O (110) peaks while the peak at 24° corresponds to $Cu(OH)_2$ phase. The other sharp peaks could not be identified which might be due to reflections from some large particles. Nishimura *et.al.*[145] have also observed strong peaks at $2\theta < 40°$ region in the XRD pattern of the Cu nanoparticles prepared by similar route, which they have attributed to reflections from large particles. There is no signature of CuO phase in case of the present samples.

The average crystallite sizes (D) of the Cu nanoparticles are calculated from the most prominent peakat $2\theta = 43.39^o$ using the Debye-Scherrer formula[153].

$$D = \frac{0.9 \times \lambda}{\beta Cos\theta} \tag{5.2}$$

where, λ is the X ray wavelength, β is the FWHM of the diffraction peak in radian and θ is the diffraction angle. The average crystallite size from XRD is 19.1 nm. Fig. 5.13 shows the TEM image of Cu nanoparticles.

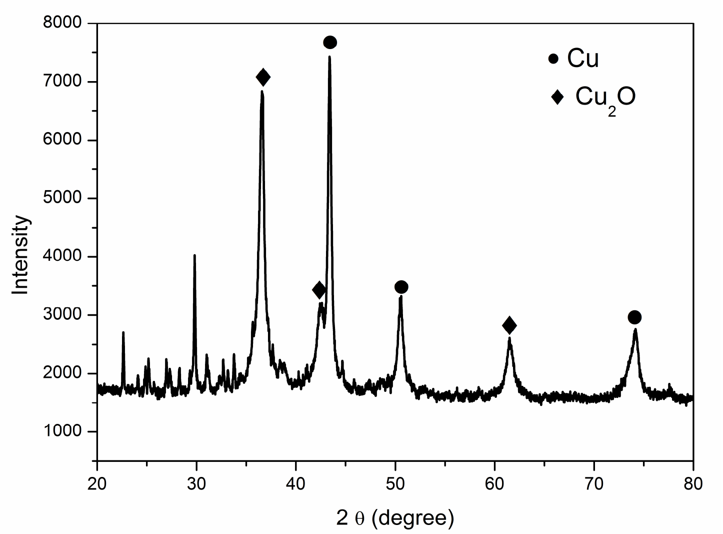

Figure 5.12: *Ex-situ* XRD spectra of the Cu nanoparticles.

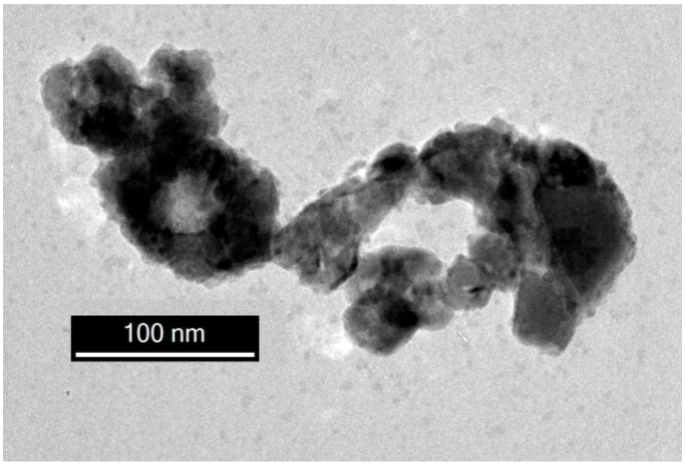

Figure 5.13: *Ex-situ* TEM micrograph of the Cu nanoparticles.

5.6 Reduction Mechanism

The Linear Combination Fitting of the XANES spectra recorded during the growth of Cu nanoparticles using standards gives a poor fitting. This gives an indication of formation of intermediate species during the reduction of Cu precursor to Cu metal. From PCA, it has been confirmed that the reduction reaction involves three species and the intermediate species exist between 700-800 s. MCR-ALS analysis gives the XANES spectra of the three species and their concentration profiles during the reaction. Therefore, it has been concluded that the copper acetate precursor changes to copper hydroxide [$Cu(OH)_2$] on addition of NaOH. On further addition of $NaBH_4$, $Cu(OH)_2$ reduces to metallic Cu in two steps: (i) formation of Cu^{+1} species from Cu^{+2} reduction after 500 s and (ii) reduction of Cu^{+1} to Cu^0 after 750 s from the start of the reaction. The EXAFS analysis of the intermediateCu^{+1}species confirms the presence of 2 oxygen atoms around the first coordination shell of Cu cation which nearly matches with the local environment of Cu_2O and hence supports the above conjecture.

5.7 Conclusion

Cu nanoparticles have been synthesized from copper acetate using $NaBH_4$ as a reducing agent and PVP as a stabilizing agent. XRD and TEM measurements confirm the presence of metallic Cu nanoparticles of size between 19 nm. *In-situ* XAS measurement has been done during the formation of Cu nanoparticles using a specialized flow setup. Principal Component Analysis (PCA) and Multivariate Curve Resolution with Alternating Least Squares (MCR-ALS) analysis techniques have been successfully applied to Cu K-edge XANES data recorded during the growth of Cu nanoparticles. From PCA, it has been confirmed that the reduction reaction involves three species. MCR-ALS analysis gives the XANES spectra of the three species and their concentration profiles during the reaction. It has been concluded that the reduction reaction occurs in two steps: (i) formation of Cu^{+1} species from Cu^{+2}reduction after 500 s and (ii) reduction of Cu^{+1} to Cu^0 after 750 s from the start of the reaction. The EXAFS spectra of the intermediate species have been extracted and the analysis confirms the presence of 2 oxygen atoms around the first coordination shell of Cu cation in the intermediate species which nearly matches with the local environment of Cu_2O. Thus the present chapter describes preparation of Cu nanoparticles under controlled environment, *in-situ* XAS measurement of the reaction species in a flow set-up arrangement and successful application of statistical procedures in analyzing the time-resolved XAS data to identify the intermediate species formed in the reaction. This methodology described here will be helpful in controlling the reaction parameters and hence the reduction process for synthesis of nanoparticles with tailored properties.

Chapter 6

In-situ XAS studies on Fischer Tropsch reaction with Co catalysts

Studies on structure-activity correlation is essential today to understand the performance of catalysts[57-60] and in this context, X-ray absorption spectroscopy (XAS), including EXAFS and XANES has emerged out as an important technique which can give structural information about the catalysts[19, 24, 61]. Since this technique does not need a crystalline sample and can probe samples in any form i.e. crystalline, amorphous, glass, polymer, liquid, etc., therefore it can be used as a structure determining tool for a wide range of homogenous and heterogenous catalysts.

Several *ex-situ* EXAFS experiments have been performed to obtain information about the structure of catalysts, which is then correlated with their catalytic performance. For example, Majeed *et. al.*[154] have studied the correlation of Mo dopant and photocatalytic activity of TiO_2 through EXAFS and photocatalysis studies. Cizmer *et. al.*[155] have also studied the correlation between structure and activity of Cu modified TiO_2-SiO_2 nanoparticles using EXAFS. Haandel*et. al.*[156] investigated the effect of organic additives on the activity of (Co)Mo/Al_2O_3 catalyst using EXAFS studies. Many such experiments have been done where EXAFS studies gave insight into the role of dopant or additives in the catalyst material to improve the activity which in turn helped in designing and fabricating tailor made catalysts.

However, as has been discussed in the earlier chapters, with the improvements in the performance of synchrotron beam lines and fast data acquisition systems, an EXAFS spectrum of 1000 eV energy range can now be measured in much faster time scale[42, 157] enabling *in-situ* or *operando* measurements on catalytic reactions where time-resolved XAS spectra of catalyst samples are recorded during the reaction. Presently, *in-situ* measurements have become inevitable in the field of catalysis as they provide the exact information during the catalysis process. This has definitely given a better outlook regarding the activity and selectivity of catalysts and also addresses the problem of deactivation of the catalyst accurately.

In-situ EXAFS measurements have been successfully used in many important catalytic systems in the past. For example, Tibiletti*et. al.*[62] have performed *in-situ* EXAFS of oxide supported gold catalyst during water gas shift reaction to identify the active species in the catalyst responsible for the reaction. Voronov *et. al.*[29] have investigated Fischer-Tropsch reaction with Co-Re/Al_2O_3 catalysts. Newton *et. al.*[30] have investigated Pd catalyst systems during CO/NO cycling. Grunwaldt and Clausen[158] have combined XRD and EXAFS with on line gas analysis and studied Cu based catalysts for methanol synthesis. Quick EXAFS and Raman measurements were simultaneously performed for Fischer-Tropsch reaction with Co/alumina catalysts[159]. Newton *et. al.*[26] have investigated the behaviour of Rh catalysts *in-situ* during NO reduction by CO with FT-IR, dispersive EXAFS and mass spectrometry.

One of the techniques which is often complemented with Time resolved XAS (TR-XAS) for studying heterogenous catalysis is Gas chromatography (GC). The online monitoring of the gaseous species using GC during an *in-situ* XAS measurement of the catalyst provides the exact information regarding the reaction which in turn decides the activity of the catalysts, while TR-XAS gives information regarding structural changes in the catalyst. Therefore, a combination of TR-XAS and GC can give insight into the structure-activity correlation of the catalyst system.

Unlike the previous *in-situ* studies on growth of nanoparticles discussed in earlier chapters, which have been carried out in the Energy Dispersive EXAFS beamline (BL-08) at Indus-2 synchrotron source, this study on *in-situ* study on catalytic reaction process, has been carried out in the Energy Scanning EXAFS beamline (BL-09) at Indus-2[64, 65].This beamline, as has been discussed in detail in Chapter-2, uses a double crystal monochromator (DCM) which normally works in conventional step-by-step scanning mode. However, recently a continuous mode EXAFS facility has been successfully commissioned in this beamline for fast data acquisition[69]. In the present chapter, we describe the development of an *in-situ* or *operando* XAS measurement setup for studying heterogenous catalysis processes with online gas monitoring using GC at the above beamline where EXAFS measurements have been carried out in the continuous mode. This setup has been used for *in-situ* study of Fischer Tropsch reaction using Co_3O_4 nanoparticles supported on SBA-15 as catalyst. The reaction has been performed in a specially designed cell with facility for heating and reaction under various gaseous environments. The structure and activity of the catalyst have been studied at different reaction temperatures. Deactivation of the catalyst has also been investigated in an attempt to find out the factors responsible for this.

6.1 Synthesis of the catalyst

Synthesis of Co_3O_4 nanoparticles has been carried out following the hydrothermal method reported by Dong *et. al.*[160]. In a typical synthesis 1g of $Co(CH_3COO)_2.4H_2O$ is dissolved in 50ml of deionized water under stirring to get a transparent solution. Subsequently 5ml of 25% NH_3 is added to it under vigorous stirring and the stirring is continued for 10min to form a homogeneous slurry. The resulting solution is then transferred into a teflon lined autoclave which is heated to 150ºC for 3h. Afterwards, the autoclave is allowed to be cooled down to room temperature naturally and the black precipitate is collected by centrifuge, washed with water and absolute ethanol and dried at 60ºC. A colloidal solution of Co_3O_4 nanoparticles obtained by dispersing the above precipitate in minimum amount of water and a desired amount of SBA-15 was added to the colloidal solution of Co_3O_4 nanoparticles to achieve 20wt.% of Co metal loading. The slurry formed was stirred for 2h, centrifuged, and washed with water and ethanol and dried at 60°C for 12h. Fig. 6.1 shows the XRD data of the as prepared Co_3O_4/SBA-15 catalyst. All the peaks in the XRD data matches with that of Co_3O_4 phase. The average crystallite sizes (D) of the Co_3O_4 nanoparticles are calculated from the most prominent peak at $2\theta = 37^o$ using the Debye-Scherrer formula[153].

$$D = \frac{0.9\times\lambda}{\beta Cos\theta} \tag{5.2}$$

where, λ is the X ray wavelength, β is the FWHM of the diffraction peak in radian and θ is the diffraction angle. The average crystallite size from XRD is 11 nm.

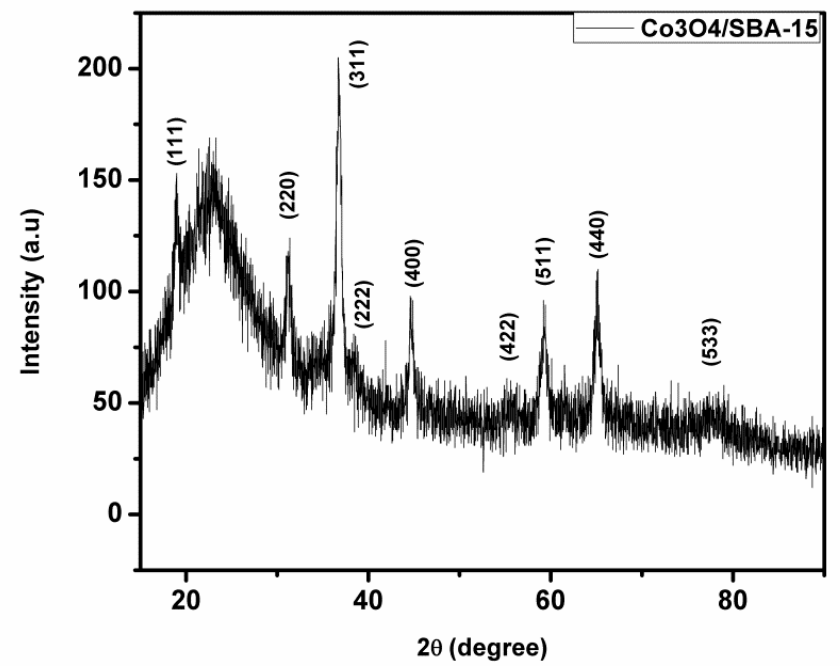

Figure 6.1: XRD data of the as prepared Co_3O_4/SBA-15 catalyst.

6.2 Fischer Tropsch Reaction

Fischer Tropsch reaction produces long chain hydrocarbons from syngas which is a mixture of carbon monoxide and hydrogen. This reaction is important in fuel industries as a source of synthetic fuel. Chemical production of liquid fuel is one of the alternatives to circumvent the problem of dwindling crude oil reserve. Fischer Tropsch synthesis is good alternate for the production of fuel from syngas, which can be made available from coal, natural gas, biomass etc.[161]. Co supported catalysts are generally used for Fischer Tropsch reaction[29, 162]. However, catalyst deactivation and deselectivation are major problems related to the Fischer Tropsch reaction. Many factors are reported as a reason for catalyst deactivation and deselectivation. Some of them are poisioning, sintering, surface carbon formation, carbidization, cobalt reoxidation, cobalt support mixed compound formation, etc[159]. Most of these studies suggest that deactivation and deselectivation are not governed by a single process and are dependent on the reaction condition.

Fischer Tropsch reaction involves hydrogenation of CO to produce hydrocarbons such as alkanes, alkenes, oxygenates etc. as described in the following:

$$\text{Parrafins : } (2n + 1)H_2 + nCO \longrightarrow C_nH_{2n+2} + nH_2O \tag{6.1}$$

$$\text{Olefines : } 2nH_2 + nCO \longrightarrow C_nH_{2n} + nH_2O \tag{6.2}$$

$$\text{Alcohols : } 2nH_2 + nCO \longrightarrow C_nH_{2n-1}OH + (n-1)H_2O \tag{6.3}$$

Supported cobalt catalyst in metallic state is mostly favourable for Fischer Tropsch synthesis at low temperature. In this work SBA-15 supported Co_3O_4 nanoparticle synthesized as mentioned in section 6.1 has been used for Fischer Tropsch reaction under flow condition at atmospheric pressure. 50 mg of the SBA-15 supported as-prepared oxide catalyst was palletized into a 12 mm thin pellet which is used as a sample in a S.S. cell described later for the Fischer Tropsch reaction. The oxide catalyst was first reduced by heating it to 400ºC with a ramp rate of 10º/min under 20ml/min H_2 flow. The temperature of the sample was maintained at 400ºC for 5 hours for reduction of the oxide catalyst into metallic Co catalyst. After reduction of the as-prepared catalyst into metallic cobalt, the temperature of the cell is reduced to the reaction temperature in presence of H_2 and on attaining the desired temperature, H_2 gas flow is reduced. The catalytic reaction is subsequently monitored at few different temperatures viz. 240ºC, 260ºC, 280ºC and 320ºC with the syngas in H_2:CO ratio of 3:1 and N_2 as internal standard. The flow of CO, H_2 and N_2 gases were maintained at 2 ml/min, 6 ml/min and 1ml/min respectively during the catalytic reaction. The structural changes of the catalyst sample during the reaction have been studied at the above mentioned temperatures with *in-situ* X-ray absorption spectroscopy.

6.3 *In-situ* XAS-GC Setup for heterogenous catalysis

For *in-situ* XAS measurements, a stainless steel reaction chamber is used with Be windows for X-ray transmission. The sample is mounted on a SS block which can be heated with two cartridge heaters, each having power of 200 W. The window flanges and the top flange of the chamber are water cooled. The temperature of the sample can go upto 400ºC. A thermocouple has been introduced in the cell from the top flange and is fixed at the sample holder touching the sample. The temperature at the sample position was controlled within ±1° of the set value using temperature controller coupled with the power supply of the cartridge heaters. The chamber is provided with two 1/4″ S.S. tubes for the inlet and outlet of reaction gases. The inlet of the reaction chamber is connected to a gas manifold where the gas flow can be controlled using three separate mass flow controllers (MFC's) and shut-off valves. The outlet of the reaction chamber is connected to a computer-controlled Gas Chromatograph (GC) (Netel, India make) through a 6 port auto-sampling valve, for the detection of the product gases. The 6 port auto-sampling valve has a sample loop of 1 ml and the gas in the sample loop goes to the GC for analysis, while the rest of the outgas goes to the vent. The product gases (H_2, N_2, CO and CH_4) are detected using a molecular sieve 5A column and using Ar as a carrier gas for GC. CO conversion percentage is calculated from the GC data using the following formula[163]:

$$\%\mathrm{CO}_{\mathrm{conv.}} = \frac{\left((\mathrm{CO}_{(\mathrm{in})}-\mathrm{CO}_{(\mathrm{out})}\times\frac{\mathrm{N}_{2(\mathrm{in})}}{\mathrm{N}_{2(\mathrm{out})}}\right)\times 100}{\mathrm{CO}_{(\mathrm{in})}} \tag{6.4}$$

where, $CO_{(in)}$, $CO_{(out)}$, $N_{2(in)}$ and $N_{2(out)}$ are concentrations of CO and N_2 gases at the inlet and outlet of the reaction chamber respectively as measured by the gas chromatograph. A schematic of the experimental setup along with the photograph of the reaction cell has been shown in Fig 6.2.

Time Resolved X ray absorption spectroscopy measurements of the catalyst sample at Co K edge were carried out in transmission mode at the Scanning EXAFS Beamline (BL-9) at the Indus-2 Synchrotron Source, discussed in details in Chapter-2. For *in-situ* XAS measurements in the transmission mode, the reaction chamber with the sample is placed between two ionization chamber detectors. The first ionization chamber measures the incident flux (I_0) and the second ionization chamber measures the transmitted intensity (I_t) and the absorbance of the sample is obtained as ($\mu = \exp(-\frac{I_t}{I_0})$). As has been mentioned earlier, for the above measurement the beamline has been operated in the recently developed continuous scan mode which enables time-resolved study in minute scale retaining the advantage of high resolution offered by the step-by-step scan of a double crystal monochromator. This measurement mode is based on restricted movement of the 2nd crystal of the double crystal monochromator and energy selection is done by only changing the Bragg angle by simultaneous rotational motion of the two crystals. The measurement scheme has been briefly discussed in Chapter-2 and the details have been reported elsewhere[69]. In this mode, a full EXAFS scan is taken in 5 minutes while XANES data can be acquired in less than a 1 minute. EXAFS oscillations have been extracted from the X ray absorption spectra $\mu(E)$ versus E, following the standard procedure[3, 4, 39]. The EXAFS oscillations, $\chi(k)$ is weighted by k^2 and the functions $\chi(k)\,k^2$ are Fourier transformed using k range of 2-10 Å^{-1} to generate the $\chi(r)$ versus r (or FT-EXAFS) plots.

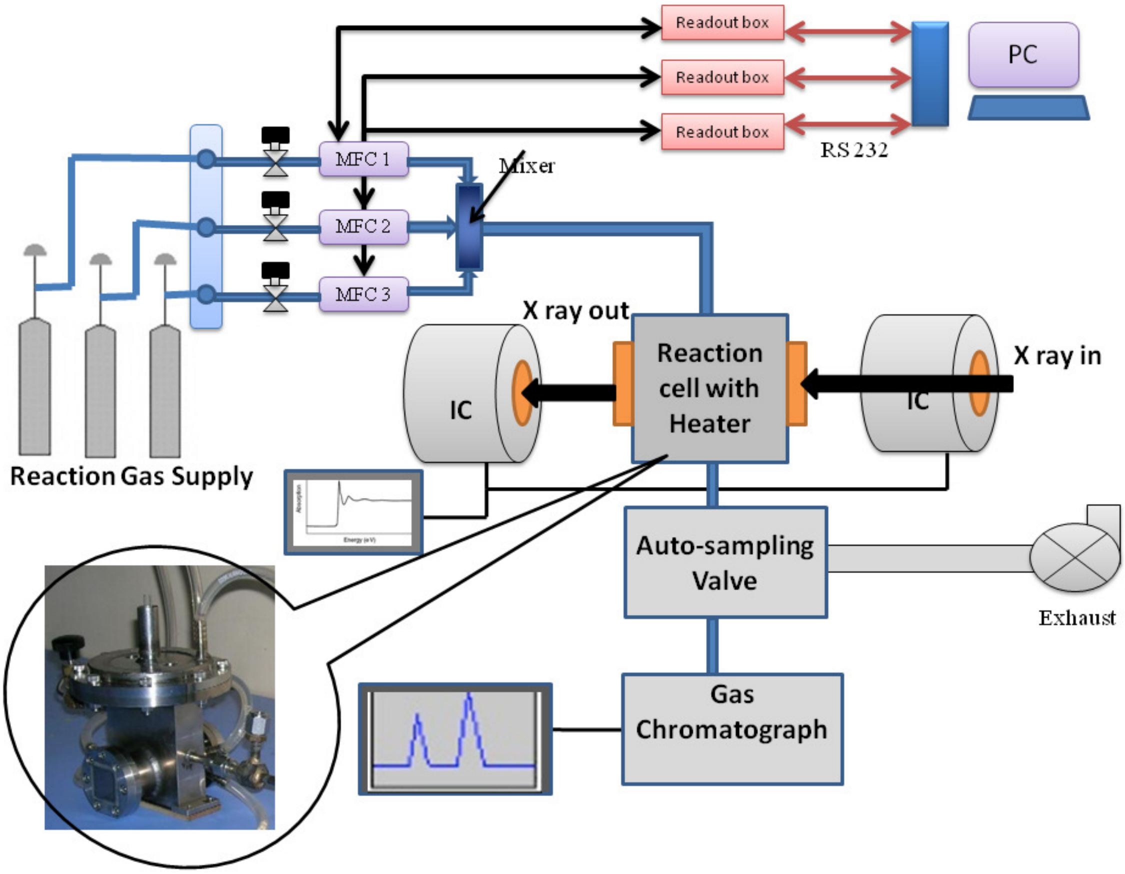

Figure 6.2: Schematic of the experimental setup for *in-situ* XAS-GC measurement during heterogenous catalysis along with the photograph of the reaction cum measurement cell.

6.4 *In-situ* XAS studies during activation of the catalyst

Fig. 6.3 (a) and (b) show the *in-situ* XANES spectra measured during the reduction of the as-prepared oxide catalyst sample and the inset in Fig. 6.3(a) shows the XANES spectra of Co standards i.e., Co_3O_4, CoO and Co metal. From the figure, it is evident that the XANES features of the as-prepared sample resemble that of Co_3O_4. During reduction at 350ºC the spectrum shifts to lower energy with XANES features resembling that of CoO spectra. As the temperature is increased to 400ºC, intensity of the white line decreases and after 5 hours of heating at 400ºC the absorption edge matches with that of metallic Co foil with reduced intensity of the white line. Therefore, the *in-situ* XANES measurement during the reduction of the as-prepared sample indicates that as the temperature is increased, the as-prepared Co_3O_4 catalyst first reduces to CoO and then to metallic Co.

The *in-situ* EXAFS spectra recorded during the reduction of the as-prepared oxide catalyst sample have been shown in Fig 6.4 (a) and (b). The EXAFS spectrum of the as-prepared sample resembles that of Co_3O_4 (shown in the inset of Fig. 6.4(a)) with a Co-O peak at 1.4 Å and a Co-Co peak at 2.3 Å. As the temperature is increased during reduction of the catalyst, the intensities of both the peaks decrease and the peaks shift towards higher *r* values. This may be due to the formation of CoO during the reduction process as also can be seen from the XANES spectra analysis. As the temperature attains 400ºC, after 1 hour a new peak starts appearing near 2 Å which represents the Co-Co bond of metallic Co. At 400ºC with time, the intensity of the Co-Co peak at 2 Å increases and the intensity of the other peaks decreases. After 5 hours at 400ºC, the EXAFS spectrum has only one prominent peak near 2 Å which resembles the features of metallic Co as seen from the inset. Therefore, it can be concluded that the sample at kept at 400ºC for 5 hours is completely reduced to metallic Co with no signature of CoO or Co_3O_4 phases in the EXAFS and XANES spectra. The formation of CoO during the hydrogen activation of Co_3O_4 catalyst has also been reported by other researchers[159, 162, 164].

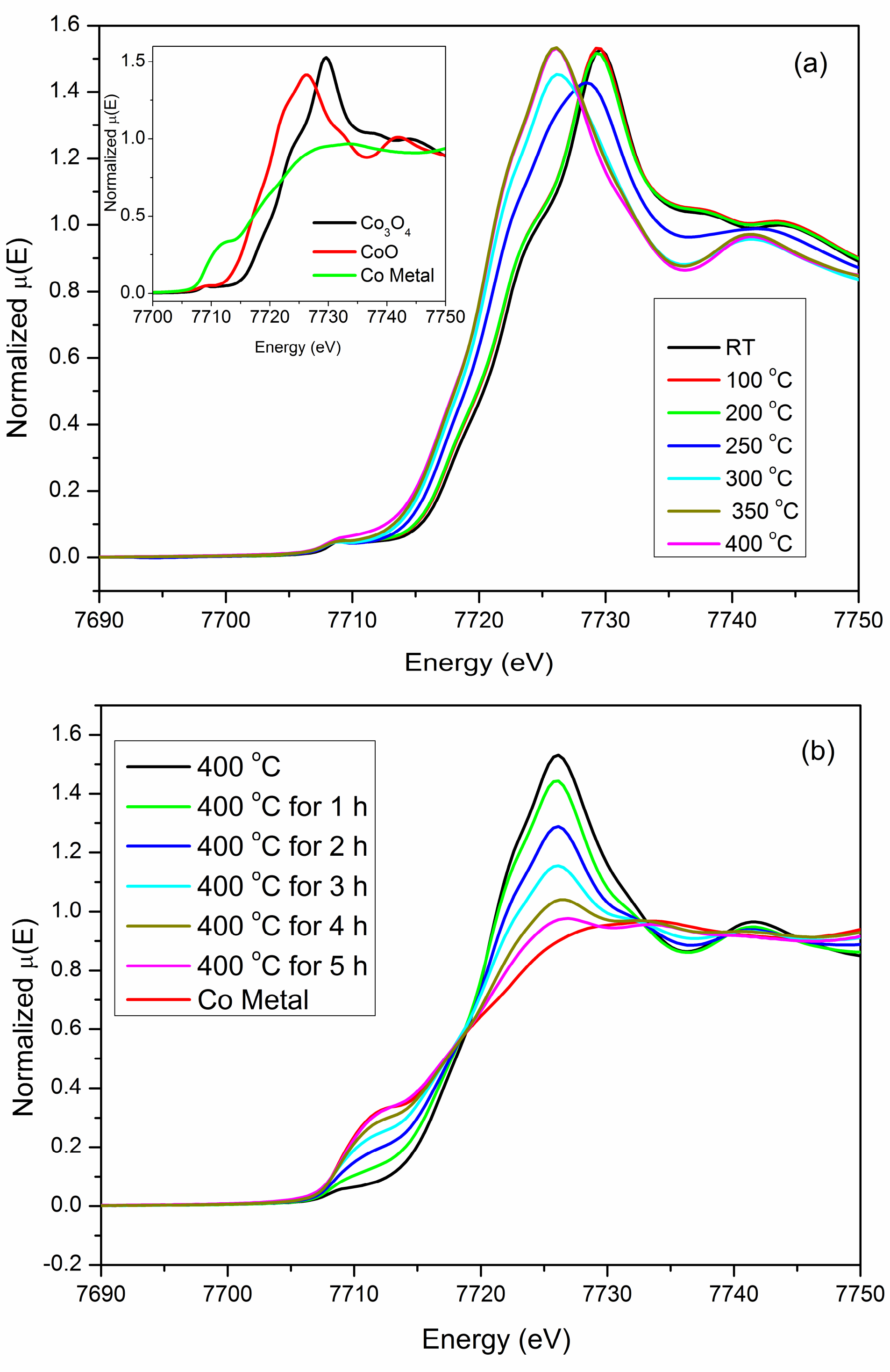

Figure 6.3: (a) *In-situ* XANES spectra recorded at different temperatures during the reduction of the as-prepared oxide catalyst sample. Inset: XANES spectra of Co standards i.e., Co_3O_4, CoO and Co metal. (b) *In-situ* XANES spectra recorded at 400 ºC at different time intervals during the reduction of the as-prepared oxide catalyst sample.

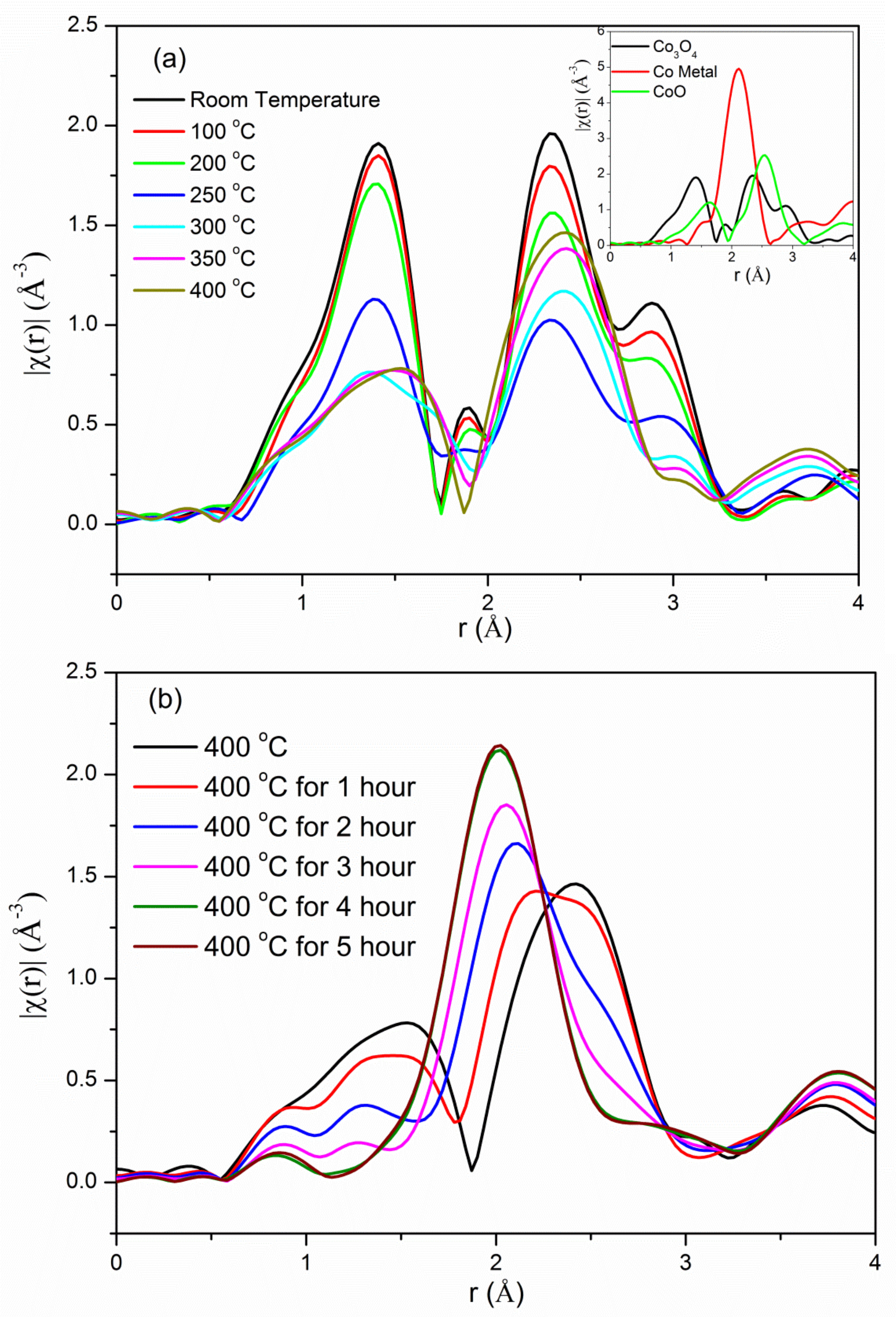

Figure 6.4: (a) *In-situ* EXAFS spectra recorded at different temperatures during the reduction of the as-prepared oxide catalyst sample. Inset: EXAFS spectra of Co standards i.e., Co_3O_4, CoO and Co metal.(b) *In-situ* EXAFS spectra recorded at 400 ºC at different time intervals during the reduction of the as-prepared oxide catalyst sample.

6.5 *In-situ* XAS studies during Fischer Tropsch reaction

The reduced sample is then exposed to the reactant gases and the structural changes during reaction have been studied. Fig. 6.5 and fig. 6.6 show the changes in the radial distribution function and $\chi(k)$ versus k spectra of the catalyst sample undergoing reaction at different temperatures respectively.From figure 6.5, it is evident that at 240ºC and 260ºC the structure of the catalyst does not change. The variation in the peak intensity is due to the temperature effect of the disorder factor (σ^2). At 280ºC the Co-Co peak near 2 Å shows some variation with time as the reaction proceeds. However, there is no signature of appearance of Co-O peak even at this temperature, which manifests that CoO is not formed. The variation in the Co-Co peak intensity may be due to disorder in the catalyst system which originates as the activity of the sample increases significantly with temperature.

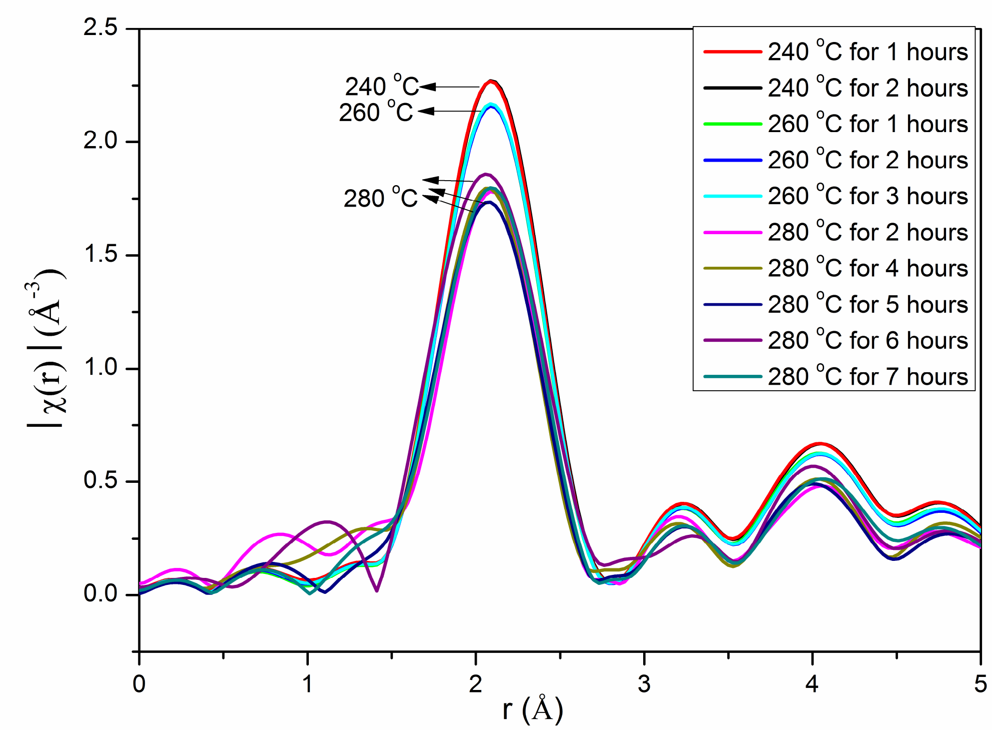

Figure 6.5: Variation in the EXAFS radial distribution function of the catalyst sample undergoing FT reaction at different temperatures.

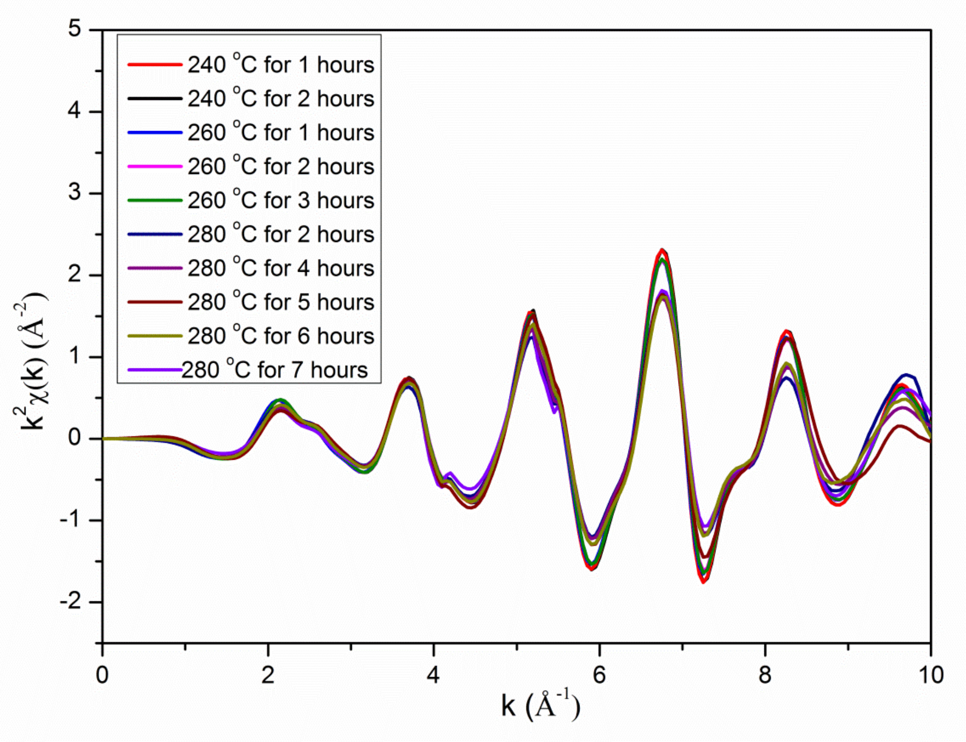

Figure 6.6: Variation in the *χ(k)*versus *k* spectra of the catalyst sample undergoing FT reaction at different temperatures.

6.6 *In-situ* XAS studies during deactivation of the catalyst

Fig. 6.7 shows the percentage of CO conversion at 280ºC for 7 hours and at 320ºC for 10 hours. It has been found from the figure that, when the temperature is increased from 280° C to 320ºC, there is a drastic increase in the CO conversion from 20% to 54%. The CO conversion percentage remains almost constant for 7 hours at 280ºC, however it monotonically decreases with time from 54% to 41% at 320ºC. The intensities of the methane peak and CO peak in the gas chromatograph data decrease and increase respectively, with time at 320ºC as shown in Fig. 6.8. This suggests that there is a decline in the performance of the catalyst at 320ºC or in other words the catalyst is deactivating.

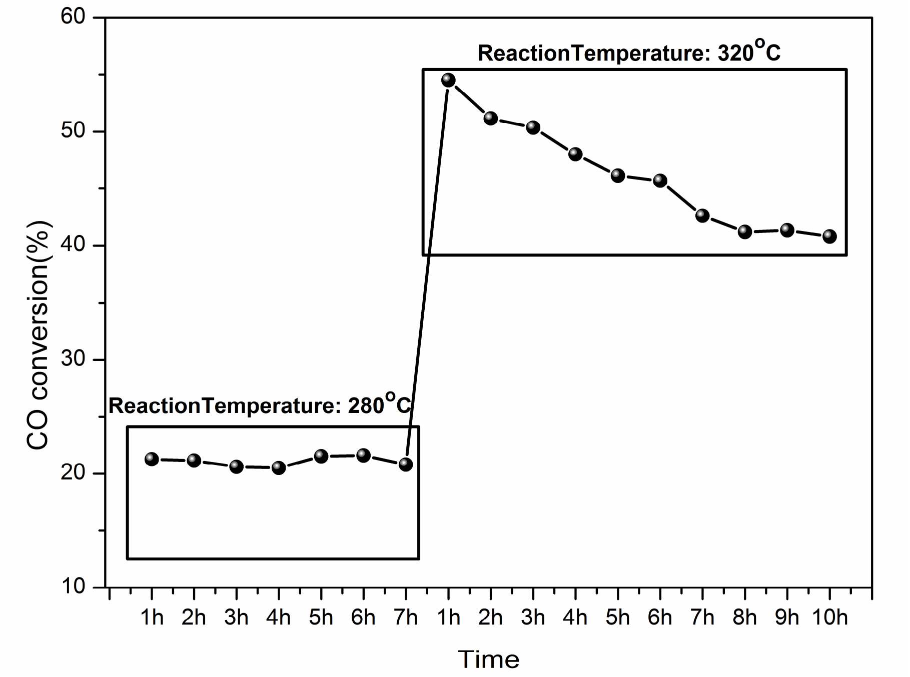

Figure 6.7: CO conversion percentage at 280ºC and at 320ºC with time.

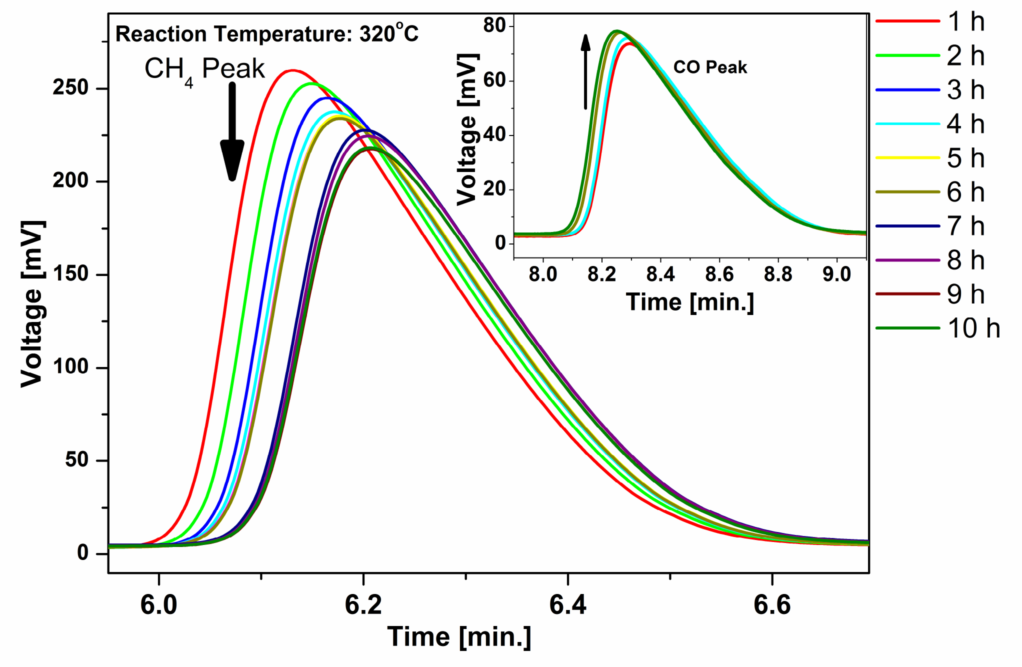

Figure 6.8: Gas chromatograph data showing the variation in methane peak intensity. Inset: Gas chromatograph data showing the variation of CO peak intensity.

Fig. 6.9 shows the XANES spectra recorded during the deactivation of the catalyst at 320ºC which shows decrease of the white line intensity at 7726 eV with time. This suggests further reduction of the catalyst due to the reaction gases. Linear combination fitting (LCF) of the XANES spectra with metallic Co and CoO as standards has been performed in the energy range of -20 eV to 30 eV around the absorption edge of the normalized μ spectra. The values of the LCF weights are restricted between 0 and 1, and sum of all the weights is also constrained to 1. The R_{factor} of the LCF fittings are less than 0.004. From the results of the LCF fitting (Fig. 6.10), it can be observed that the metallic Co percentage increases and the CoO percentage decreases with time as the reaction proceeds at 320°C. This observation rules out the possibility of formation of CoO during the reaction which might act as a contributing factor for deactivation. The EXAFS spectra (Fig. 6.11) resemble that of metallic Co and the intensity of the Co-Co peak near 2 Å increases with time. There is no signature of Co-O bonds in the EXAFS spectra. Therefore, the EXAFS results corroborate with the XANES analysis results confirming that no CoO phase is formed during the deactivation of the catalyst.

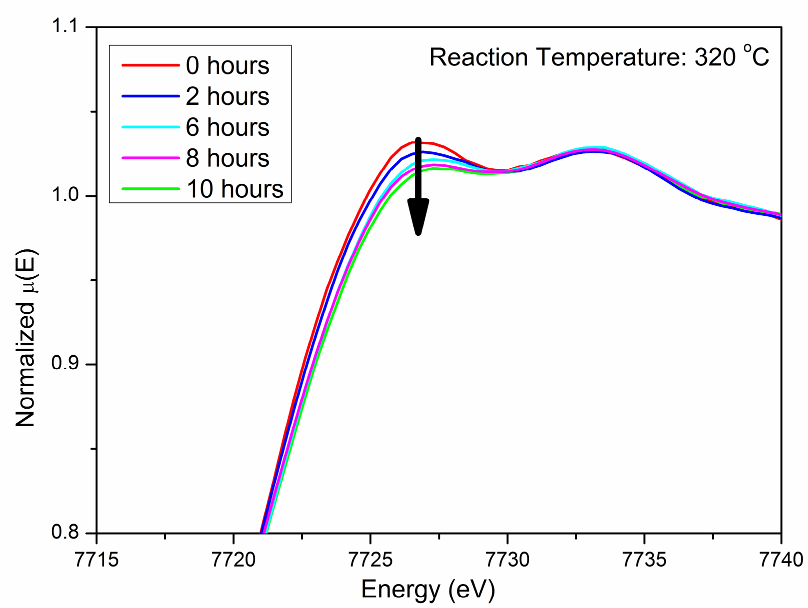

Figure 6.9: *In-situ* XANES spectra recorded during the deactivation of the catalyst at 320°C.

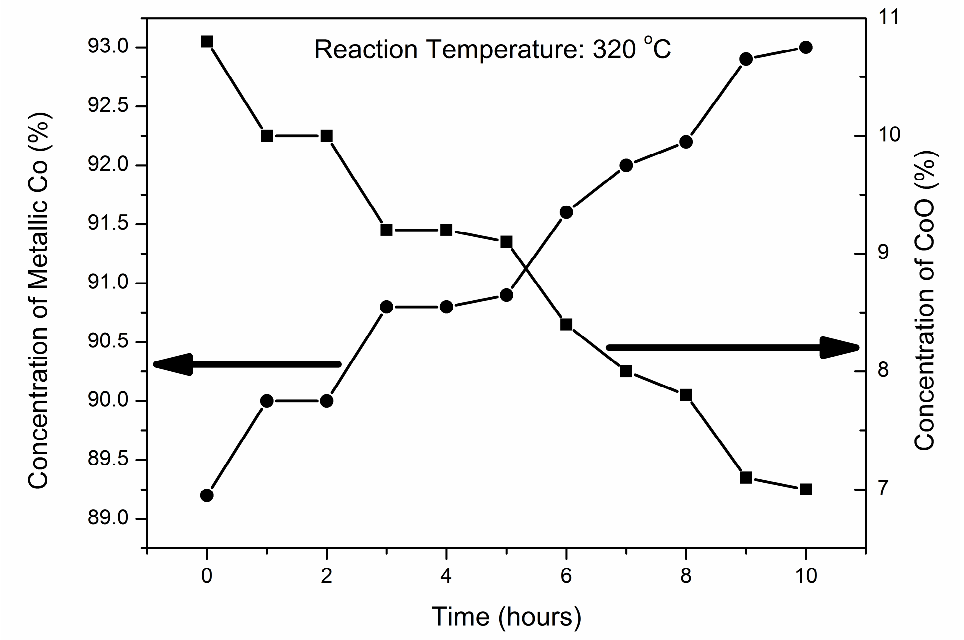

Figure 6.10: Results of Linear combination fitting of the *in-situ*XANES spectra recorded during the deactivation of the catalyst at 320ºC with metallic Co and CoO as standards.

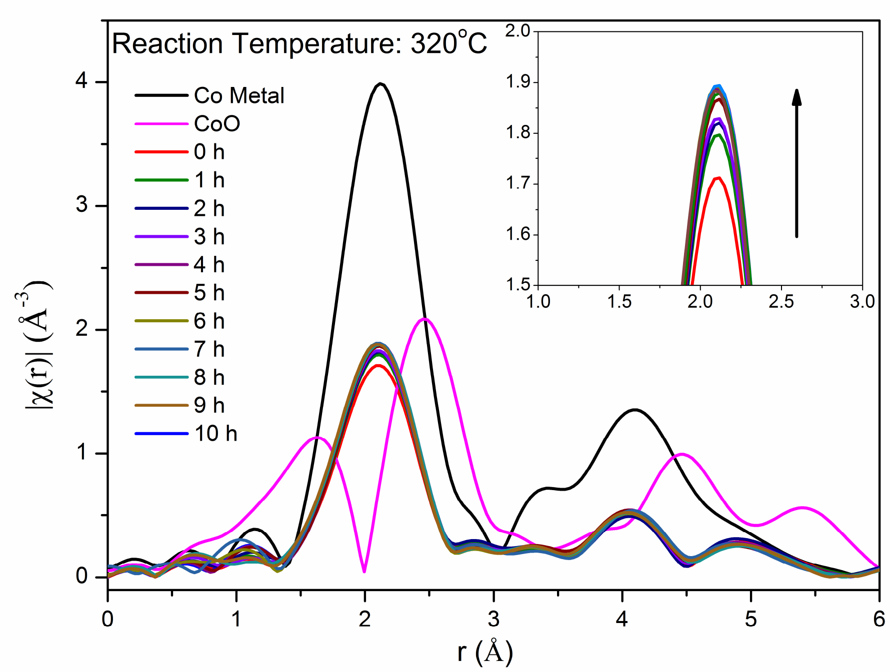

Figure 6.11: *In-situ* EXAFS spectra recorded during the deactivation of the catalyst at 320ºC. Inset: Enlarged view of the peak at 2 Å in the *in-situ* EXAFS spectra recorded during the deactivation of the catalyst at 320ºC

Many researchers have tried to find out the reason for deactivation of Co based catalyst in Fischer Tropsch reaction. Rochet *et. al.*[159].have found that the Co catalyst deactivates due to re-oxidation of the catalyst in the presence of water produced in the Fischer Tropsch reaction which is however ruled out in the present case from the above observation. Another common cause of deactivation of catalysts is sintering, i.e., increase in particle size during reaction[165] leading to loss in surface area and hence deactivation. Sadeqzadeh *et. al.*[63] have also found through *in-situ* XRD/EXAFS measurements that hcp phase of Co is more active than the fcc phase and Co sintering is the main mechanism for catalyst deactivation. However, sintering generally leads to an increase in the intensity in the metal-metal peak in the FT-EXAFS spectra and hence in coordination number[158]. The experimental EXAFS spectra of the present catalyst sample during the deactivation of the catalyst at 320ºC have been fitted from 1.5-3 Å assuming a Co-Co shell at 2.50(12×) Å (not shown here) and the fitting results have been tabulated in Table 6.1. From the EXAFS fitting results it can be inferred that the Co-Co bond length does not change with time during the deactivation of the catalyst at 320ºC. There is an increase in the Co-Co coordination number with time during the deactivation of the catalyst at 320ºC, however the change is not significant and comparable to the error limits of ±10%. Hence it may not imply any sintering of the catalyst during the reaction. Also, the increase in coordination number may be due to an increase in the metallic Co phase in the catalyst as determined from the LCF fitting of the XANES spectra (Fig.6.10).

Table 6.1: Co K edge EXAFS fitting results during the deactivation of the catalyst at 320ºC.

Time (h)	Co-Co Path		
	r(Å)	N	σ^2(Å^2)
0	2.46 ±0.01	9.1 ±1.4	0.0113 ±0.0017
1	2.46 ±0.01	9.6 ±1.2	0.0115 ±0.0015

2	2.46 ±0.01	9.9 ±1.4	0.0116 ±0.0016
3	2.46 ±0.01	10.0 ±1.2	0.0117 ±0.0014
4	2.46 ±0.01	9.9 ±1.0	0.0113 ±0.0012
5	2.46 ±0.01	10.0 ±1.0	0.0116 ±0.0012
6	2.46 ±0.01	10.1 ±0.9	0.0114 ±0.0013
7	2.46 ±0.01	10.1 ±1.0	0.0113 ±0.0011
8	2.46 ±0.01	10.2 ±1.0	0.0122 ±0.0012
9	2.46 ±0.01	9.7 ±0.8	0.0108 ±0.0011
10	2.46 ±0.01	10.1 ±0.9	0.0116 ±0.0011

Passos *et. al.*[164, 166]have studied Co based catalysts for ethanol steam reforming reactions. They have however observed that CoO enables the catalyst surface cleaning by oxidation of the deposited carbon and a very low Co^{+2}/Co ratio in the catalyst sample leads to deactivation of the catalyst due to surface carbon deposition. Under the Fischer Tropsch reaction conditions, many reactions occur. One of these is Boudouard reaction which is as follows:

$$CO+CO \longrightarrow C + CO_2$$

which may lead to formation of carbon.

In our case, the percentage of Co^{2+} in the activated catalyst is also low (around 11%) and there is no further increase in the percentage of Co^{2+} due to re-oxidation during deactivation. Therefore, the process of deactivation may be attributed to carbon formation on the surface of the catalyst during the reaction which does not get removed due to low concentration of CoO species in the sample. This has also been confirmed through Raman spectroscopic measurement on the deactivated catalyst. The Raman spectrum of the deactivated catalyst is shown in Fig. 6.12 which gives two broad peaks typical of coke deposits. Similar spectra have been observed by Passos *et.*

al.[164] on spent catalysts of ethanol steam reforming reaction after deactivation due to surface carbon deposits.

It should be mentioned here that Moodley *et.al.*[167] have also identified carbon deposition as one of the deactivation mechanism of cobalt-basedFischer–Tropsch synthesis catalysts by characterizing the spent catalyst using both surfacecharacterization technique like X-ray photoelectron spectroscopy and bulk characterization tools like temperature programmed(TPO/TPH) techniques and transmission electron microscopy.

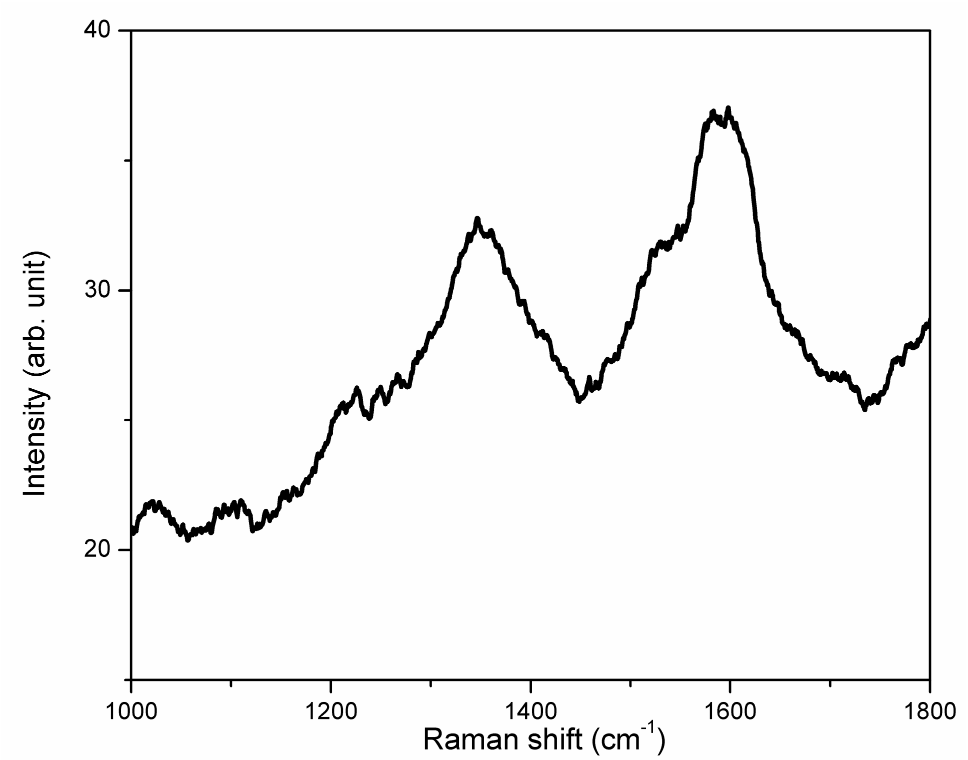

Figure 6.12: *Ex-situ* Raman spectrum of the deactivated catalyst

6.7 Conclusion

A facility has been set up at the Energy Scanning EXAFS beamline (BL-09) at RRCAT, Indore, India for *in-situ* studies of structure-activity correlation during catalytic reaction using simultaneous measurements of X-ray absorption spectroscopy (XAS) and gas chromatography. XAS provides information regarding structural changes in the catalyst during the reaction, while gas chromatography monitors the product gases of the reaction, which in turn gives information regarding the activity of the catalyst. Using the above facility SBA-15 supported Co_3O_4 nanoparticle catalysts has been studied *in-situ* during Fischer Tropsch reaction for methane generation by the reaction of CO and H_2. The catalyst is first reduced by heating it at 400ºC for 5 hours under H_2 ambient and it has been found from XANES measurements that the as-prepared catalyst first reduces to CoO and then to metallic Co during reduction. The activity of the reduced catalyst is subsequently been observed at few different temperatures viz., 240ºC, 260ºC, 280ºC and 320ºC and it has been found by XANES and EXAFS measurements that the structure of the catalyst does not show any significant change during the Fischer Tropsch reaction at these temperatures and remains in the metallic Co phase. It has further been observed that as the reaction temperature increases from 280ºC-320ºC the activity of the catalyst increases significantly. However, at 320ºC the Co catalyst shows deactivation with time. The catalyst has been studied for 10 hours at 320ºC and an attempt has been made to understand the process of deactivation using XANES and EXAFS analysis. From the structural analysis results it has been observed that there is no signature of formation of CoO phase during the reaction which might be responsible for the deactivation of the catalyst. Therefore, there is a strong possibility that the deactivation of the catalyst is caused due to carbon formation on the surface of the catalyst which does not get removed due to very low concentration of CoO in the reduced sample. This has been confirmed from *ex-situ* Raman spectroscopy measurement of the deactivated catalyst.

Chapter 7

In-situ XAS studies during photocatalytic reduction of CO_2 using Cu doped TiO_2 catalyst

In the present world where the depletion of fossil fuels has become a major concern, the search of alternating methods to produce fuels has attracted considerable attention. Photocatalytic reduction of CO_2 has emerged as an important technique in this regard as it produces renewable and sustainable fuel from green house gas like CO_2. The consumption of fossil fuels leads to emission of CO_2, which with water and sunlight driven photocatalyst can again be converted to fuel. This therefore, not only ensures production of fuel but also effective utilisation of combustion gas like CO_2, which is a responsible factor for global warming.

Recently a lot of studies have been reported on the photocatalytic reduction of CO_2[168-170]. TiO_2 has emerged out as a popular photocatalyst for this process[171, 172]. However, the lack of photoresponse in the visible region due to its wide band gap (3.2 eV for anatase TiO_2) and the high rate of recombination of the photogenerated electron-hole pair reduces the efficiency of TiO_2as a catalyst. To cope with these problems, often different metals have been doped into TiO_2 which have increased the CO_2 photoconversion rate. The dopants apart from creation of additional energy levels inside the forbidden gap and thus reducing its band gap also create charge carrier traps in the TiO_2 lattice which reduces the recombination of charge carriers. Among others, Cu doped TiO_2 has shown high activity for the photocatalytic reduction of CO_2[173, 174]. However, the reaction mechanism involved in this process is not very well understood. In order to commercialize this fuel production technology, a detail understanding and control over the catalytic process is required. In this regard *in-situ* XAS can be a useful technique to give information about the structural changes in the catalyst during the photocatalytic reduction of CO_2.

7.1 Synthesis of Cu doped TiO_2 photocatalyst

Cu doped TiO_2 catalysts have been synthesized by a modified sol-gel process in which the required stoichiometric amount of $Cu(NO_3)_2.3H_2O$ (Aldrich, 97%) was initially dissolved in nano pure water at room temperature and neutral pH. The copper nitrate solution was maintained at 0°C by external application of ice-salt mixture. Ti(IV) iso-propoxide solution in iso-propanol (IPA) was added to the copper nitrate solution, drop wise in a controlled manner over a period of 1h, with vigorous stirring until the formation of a uniform gel. This gel was stirred further for 1h to ensure the incorporation of copper precursor in the titanium gel phase. The gel was kept for nucleation for 12h in the dark, and then IPA is removed by keeping the gel in a Petri dish for 12h. The mass was then dried in an oven at 100°C for 4h. The resulting solid mass was crushed and calcined at 500°C for 3h. The required amount of Cu (5.0 and 10 atom %) doping was achieved by adding stoichiometric amount of copper nitrate solution and Ti (IV) iso-propoxide. Subsequently in this chapter, the 5% and 10% Cu doped TiO_2samples would be referred to as Cu5 andCu10 respectively.

7.2 *In-situ* XAS-GC measurement setup for photocatalytic reactions

The experimental setup for *in-situ* XAS measurements during photocatalytic reactions consists of a specially designed reaction-cum-measurement cell which consists of quartz and glass windows for shining UV and visible radiation on the sample in addition to the Kapton windows for X-ray transmission. Two valves are provided at the inlet and outlet of the chamber so that it can be converted to a closed reactor for studying the photocatalytic reactions discussed in this study. Measured proportions of CO_2 and water vapor, have been taken in syringes and inserted in the chamber through an inlet port blanked with a septum while measured amount of the product gases is periodically collected in a syringe from the chamber through an outlet port blanked with a septum and is fed to a computer-controlled Gas Chromatograph (GC) (Netel, India make). The product gases (CO_2 and CH_4) are detected using a Porapak N column and using He as a carrier gas for GC. For the photocatalytic reaction a 250 W white light lamp with wavelength range 350-700nm and luminous flux of 35000 Lm, has been used to shine light on the catalyst sample placed inside the chamber through a glass window. The schematic of the experimental setup along with the photograph of the reaction cell has been shown in Fig 7.1 and the actual photograph of the experimental setup has been shown in Fig 7.2.This setup has been used to study photocatalytic reduction of CO_2 using 5% and 10% Cu doped TiO_2 as catalyst.

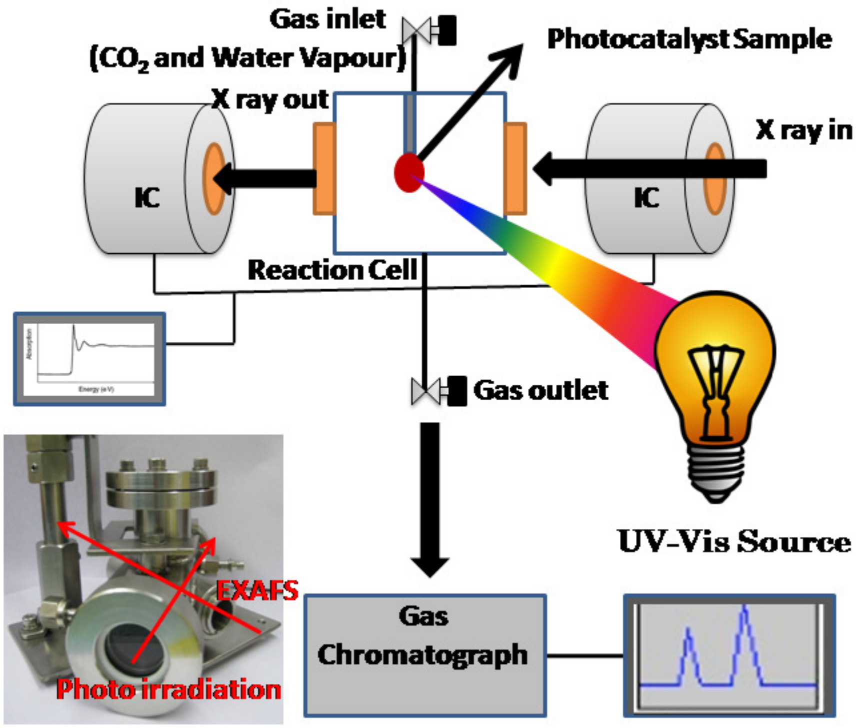

Figure 7.1: Schematic Diagram of the experimental setup for *in-situ* XAS measurement during photocatalytic reactions along with the photograph of the reaction cell.

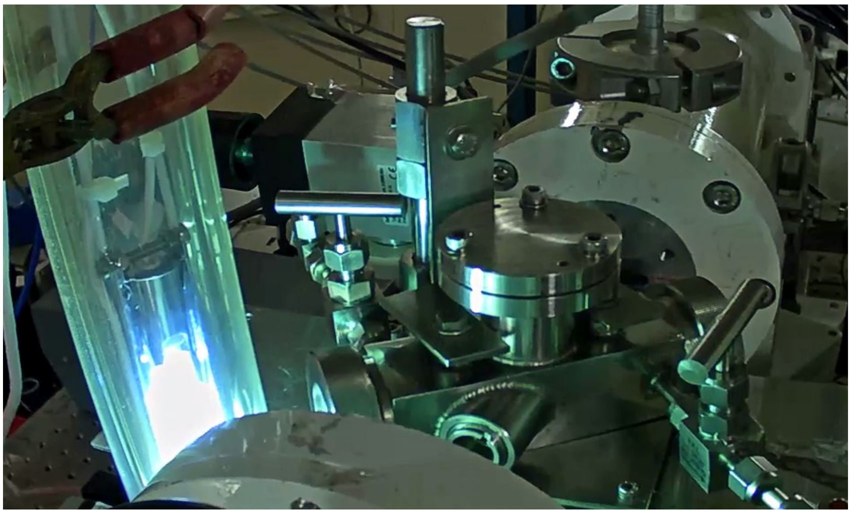

Figure 7.2: Actual photograph of the experimental setup for *in-situ* XAS measurement during photocatalytic reactions.

7.3 *In-situ* XAS studies during adsorption of CO_2 and water vapour

For *in-situ* XAS measurements in the transmission mode, the *in situ* reaction cell with the sample is placed between two ionization chamber detectors in the beamline. For Cu K edge measurements, 50 mg of the catalyst samples are pelletized and for Ti K edge measurements 20 mg of the samples are uniformly spread over a kapton tape. The sample is loaded into the *in-situ* cell and 300 ml of CO_2 and 16 ml of water vapour have been inserted into the cell as discussed above. To get an insight into the adsorption of CO_2 and water vapour on the catalyst sample, *in situ* XAS measurement at both Ti and Cu K edges have been recorded during the exposure of the catalyst sample to CO_2 and water vapour without illuminating the visible light.

7.3.1 *In-situ* XAS studies at Ti K edge

Fig. 7.3 (a) and (b) show the *in-situ* XANES spectra measured at Ti K edge during the adsorption of CO_2 and water vapour on the Cu5 and Cu10 catalyst samples respectively. From the figure, it is evident that there is no significant changes in the Ti K edge XANES spectra during the adsorption of CO_2 and water vapour on Cu doped TiO_2 catalyst samples. The XANES features of both the samples match with that of anatase TiO_2 (shown in inset of Fig. 7.3 (a)).

The EXAFS spectra have been extracted using the standard procedure described in section 2.3. The $\chi(k)$ spectra is weighted by k^2 and the functions $\chi(k)\,k^2$ are fourier transformed in the k range 2-9 Å^{-1} to generate the $\chi(r)$ versus r (or FT-EXAFS) plots. The experimental $\chi(r)$ versus r plots of the Cu doped TiO_2 samples at Ti K edge have been fitted with theoretically simulated $\chi(r)$ versus r plots generated assuming anatase TiO_2 structure. The structural parameters for the anatase TiO_2 structure are obtained from the reported values in the literature[175]. Following this structure, the experimental data have been fitted from 1-3.7 Åassuming one Ti-O shell at 1.97(6×) Å and two Ti-Ti shells at 3.04(4×) Å and 3.79(4×) Å.The experimental $\chi(r)$ versus r plots of the Cu5 and Cu10 samples at Ti K edge along with best fit theoretical plots carried out as above have been shown in Fig. 7.4 (a) and (b) respectively and the fitting results have been tabulated in Table 7.1.

From the EXAFS analysis results at Ti K edge (Table 7.1), it is evident that the variation of the Ti-Ti bond lengths and coordination numbers are within the error bars. However, the Ti-O bond length decreases with the adsorption of CO_2 and water vapour for both the samples. For both the as prepared samples, the Ti-O coordination number values are less than the theoretical values of anatase TiO_2 structure (i.e. 6). This suggests the presence of oxygen vacancies in the TiO_2 lattice near the Ti cations. The Ti-O coordination increases on adsorption of CO_2 and it decreases on adsorption of water vapour. Therefore, from the XANES and EXAFS analysis at Ti K edge it can be inferred that the effective charge of Ti cations do not change during the adsorption of CO_2 and water vapour. However, the Ti-O bond lengths and coordination numbers change which suggests that the oxygen vacancies near the Ti sites participate in the adsorption process. The oxygen vacancies decrease on adsorption of CO_2 and it again increase on adsorption of water vapour.

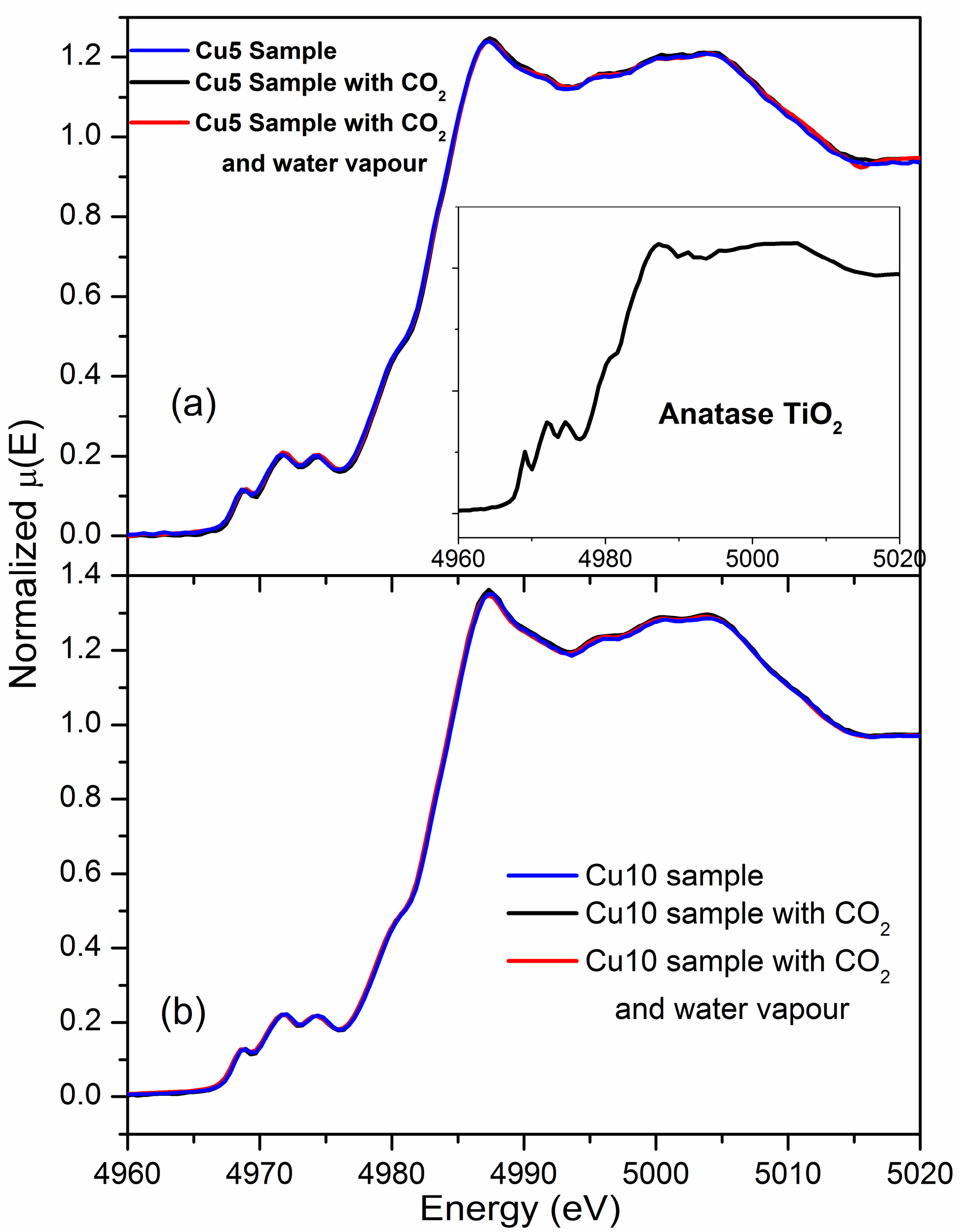

Figure 7.3: (a) *In-situ* XANES spectra measured at Ti K edge during the adsorption of CO_2 and water vapour on Cu5 catalyst sample. Inset: Ti K edge XANES spectrum of anatase TiO_2 (b) *In-situ* XANES spectra measured at Ti K edge during the adsorption of CO_2 and water vapour on Cu10 catalyst sample.

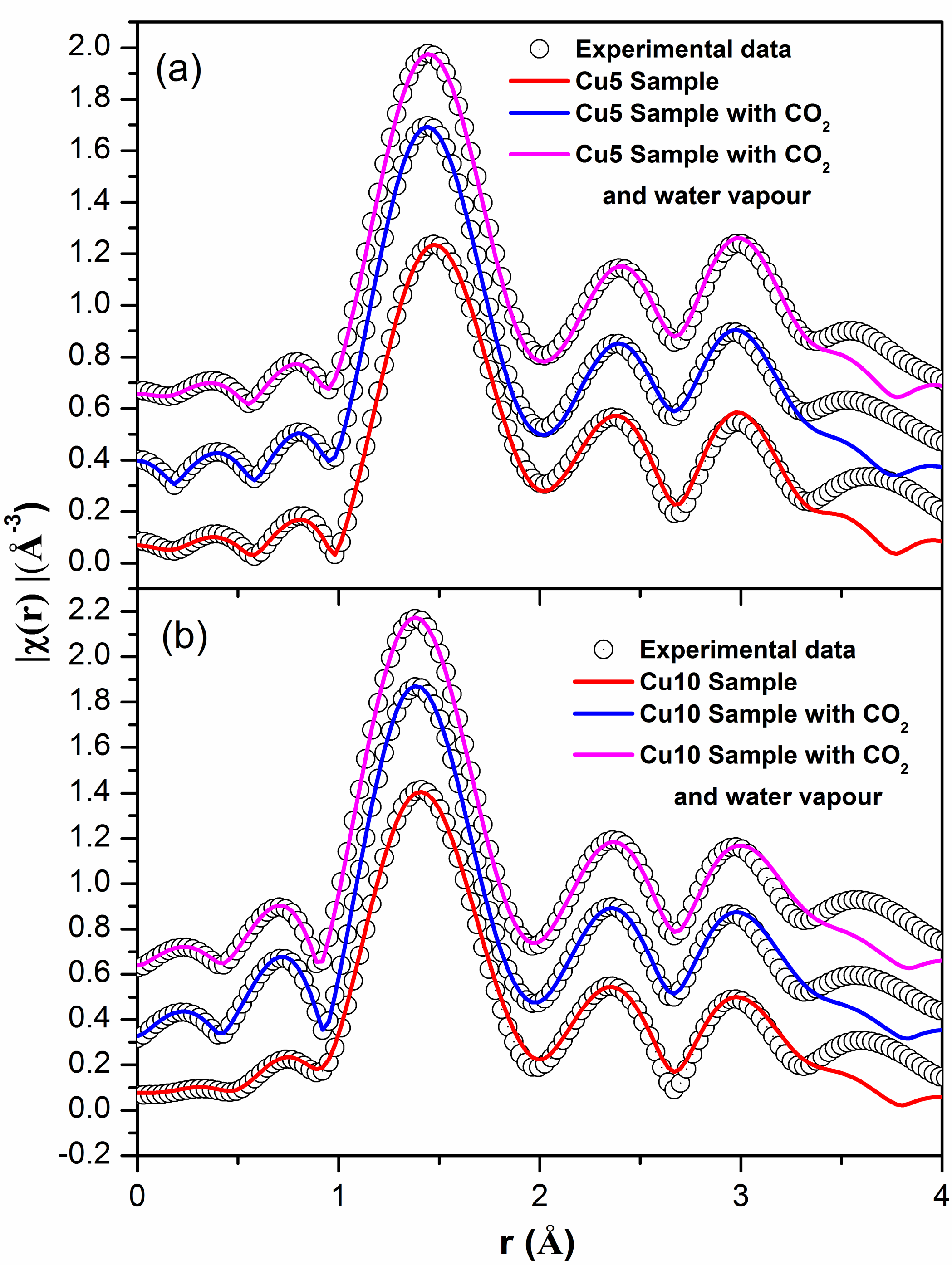

Figure 7.4:(a)*In-situ* EXAFS spectra measured at Ti K edge during the adsorption of CO_2 and water vapour on Cu5 catalyst sample. (b) *In-situ* EXAFS spectra measured at Ti K edge during the adsorption of CO_2 and water vapour on Cu10 catalyst sample. Open circles: experimental data and solid lines: best theoretical fit.

Table 7.1: Ti K edge EXAFS fitting of Cu doped TiO_2samples during adsorption of CO_2 and water vapour

	Ti-O1			Ti-Ti1			Ti-Ti2		
	r(Å)	N	σ^2(Å^2)	r(Å)	N	σ^2(Å^2)	r(Å)	N	σ^2(Å^2)
Cu5	1.94 ±0.01	5.5 ±0.2	0.0061 ±0.0011	2.94 ±0.02	4.1 ±0.4	0.0109 ±0.0020	3.69 ±0.02	3.4 ±0.5	0.0026 ±0.0023
Cu5 with CO_2	1.92 ±0.01	5.9 ±0.2	0.0049 ±0.0010	2.93 ±0.01	4.4 ±0.5	0.0086 ±0.0018	3.71 ±0.02	3.4 ±0.5	0.0022 ±0.0021
Cu5 with CO_2& water vapour	1.90 ±0.01	5.6 ±0.1	0.0043 ±0.0007	2.92 ±0.01	4.2 ±0.3	0.0076 ±0.0012	3.71 ±0.01	3.4 ±0.3	0.0012 ±0.0011
Cu10	1.97 ±0.04	5.4 ±0.2	0.0052 ±0.0015	2.96 ±0.02	4.2 ±0.5	0.0050 ±0.0027	3.74 ±0.02	4.1 ±0.6	0.0036 ±0.0030
Cu10 with CO_2	1.94 ±0.01	5.8 ±0.1	0.0043 ±0.0010	2.96 ±0.01	4.1 ±0.4	0.0075 ±0.0019	3.75 ±0.02	4.3 ±0.5	0.0034 ±0.0021
Cu10 with CO_2& water vapour	1.94 ±0.01	5.6 ±0.1	0.0041 ±0.0012	2.97 ±0.02	4.2 ±0.4	0.0085 ±0.0024	3.76 ±0.02	3.8 ±0.7	0.0019 ±0.0014

7.3.2 *In-situ* XAS studies at Cu K edge

Fig. 7.5 (a) and (b) show the *in-situ* XANES spectra measured at Cu K edge during the adsorption of CO_2 and water vapour on Cu5 and Cu10 catalyst samples respectively. The inset in both Fig. 7.5 (a) and (b) gives an enlarged view of the absorption edge. It has been found from the spectra that the effective charge of Cu in the samples increases during CO_2 adsorption and decreases during H_2O adsorption. This suggests that Cu cations play an important role in both CO_2 and H_2O adsorption.

The EXAFS spectra have been extracted using the standard procedure described in section 2.3. The $\chi(k)$ spectra is weighted by k^2 and the functions$\chi(k)k^2$ are fourier transformed in the k range 2-10 Å^{-1} to generate the$\chi(r)$ versus r plots shown in Fig 7.6. It can be observed from Fig 7.6 that the peak at 1.4 Å corresponds to the Cu-O path, however the features between 2-3 Åare due to contributions from higher coordination shells. These features vary significantly for both Cu5 and Cu10 samples on adsorption of CO_2 and water vapour, but could not be fitted with any model due to the broadness of the peaks. The significant variations of the EXAFS features in

Fig 7.6 suggest that the local environment around the Cu cations change during the adsorption of CO_2 and water vapour. The experimental $\chi(r)$ versus r plots of the Cu doped TiO_2 samples at Cu K edge have been fitted from 1-2 Åwith an Cu-O shell at 1.97(6×) Å assuming Cu replacing Ti in the anatase TiO_2 structure[175].The experimental $\chi(r)$ versus r plots of the Cu5 and Cu10 samples at Cu K edge along with best fit theoretical plots carried out as above have been shown in Fig. 7.6 (a) and (b) respectively and the fitting results have been tabulated in Table 7.2. From the EXAFS analysis results, it can be inferred that the Cu-O coordination number decreases on adsorption of CO_2 and water vapour for both the samples. This implies the creation of oxygen vacancies near Cu cations due to both adsorption of CO_2 and water vapour. It should also be noted that the Cu-O bond length does not vary significantly for the Cu5 sample during adsorption of CO_2 and water vapour, though for the Cu10 sample the Cu-O bond length increases on adsorption of CO_2 and water vapour. From the XANES and EXAFS analysis, it is evident that the effective charge and local environment of Cu cations change significantly upon adsorption of CO_2 and water vapour, which indicates the participation of Cu cations in the adsorption process.

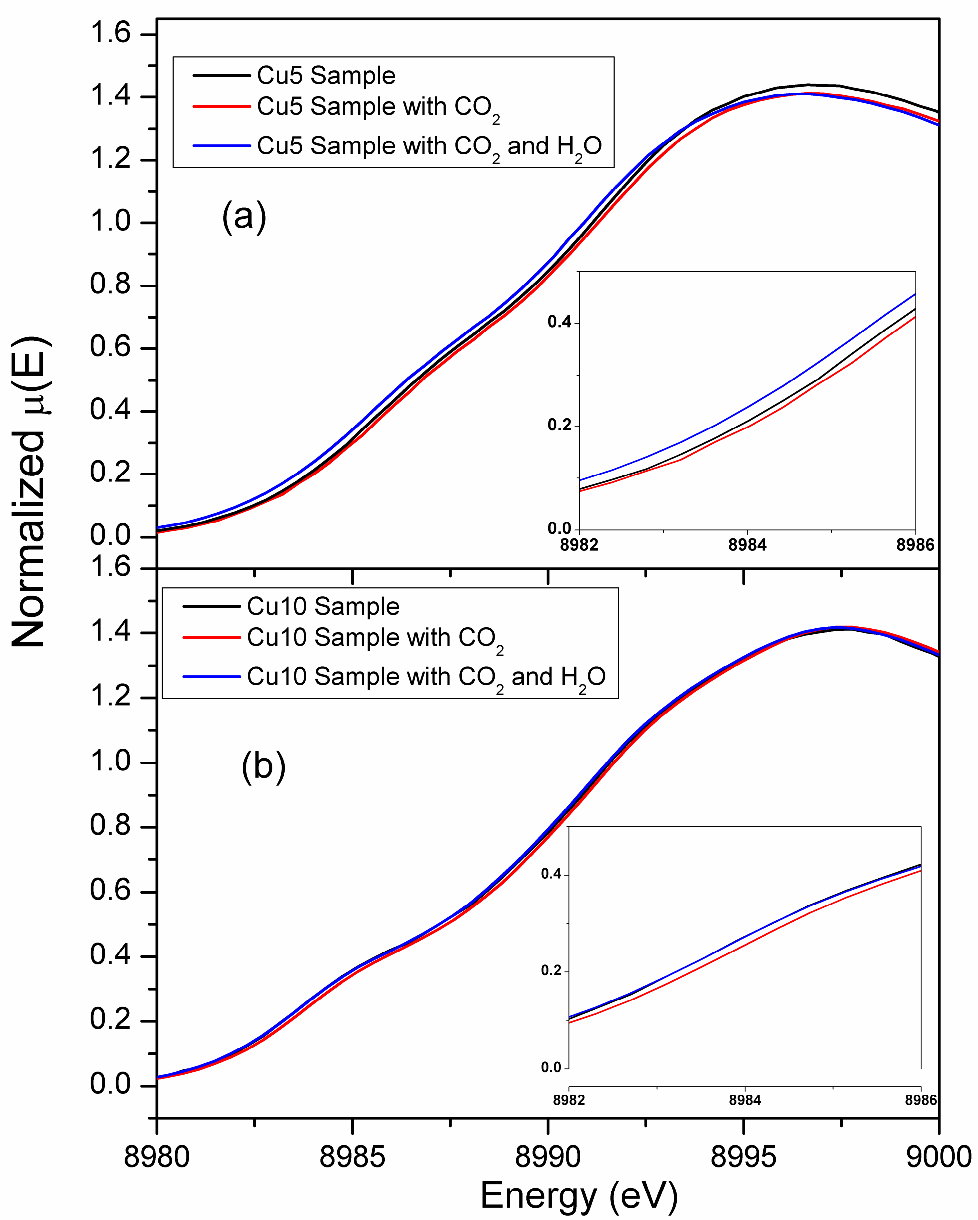

Figure 7.5:(a) *In-situ* XANES spectra measured at Cu K edge during the adsorption of CO_2 and water vapour on Cu5 catalyst sample. Inset: enlarged view of the absorption edge (b) *In-situ* XANES spectra measured at Cu K edge during the adsorption of CO_2 and water vapour on Cu10 catalyst sample. Inset: enlarged view of the absorption edge.

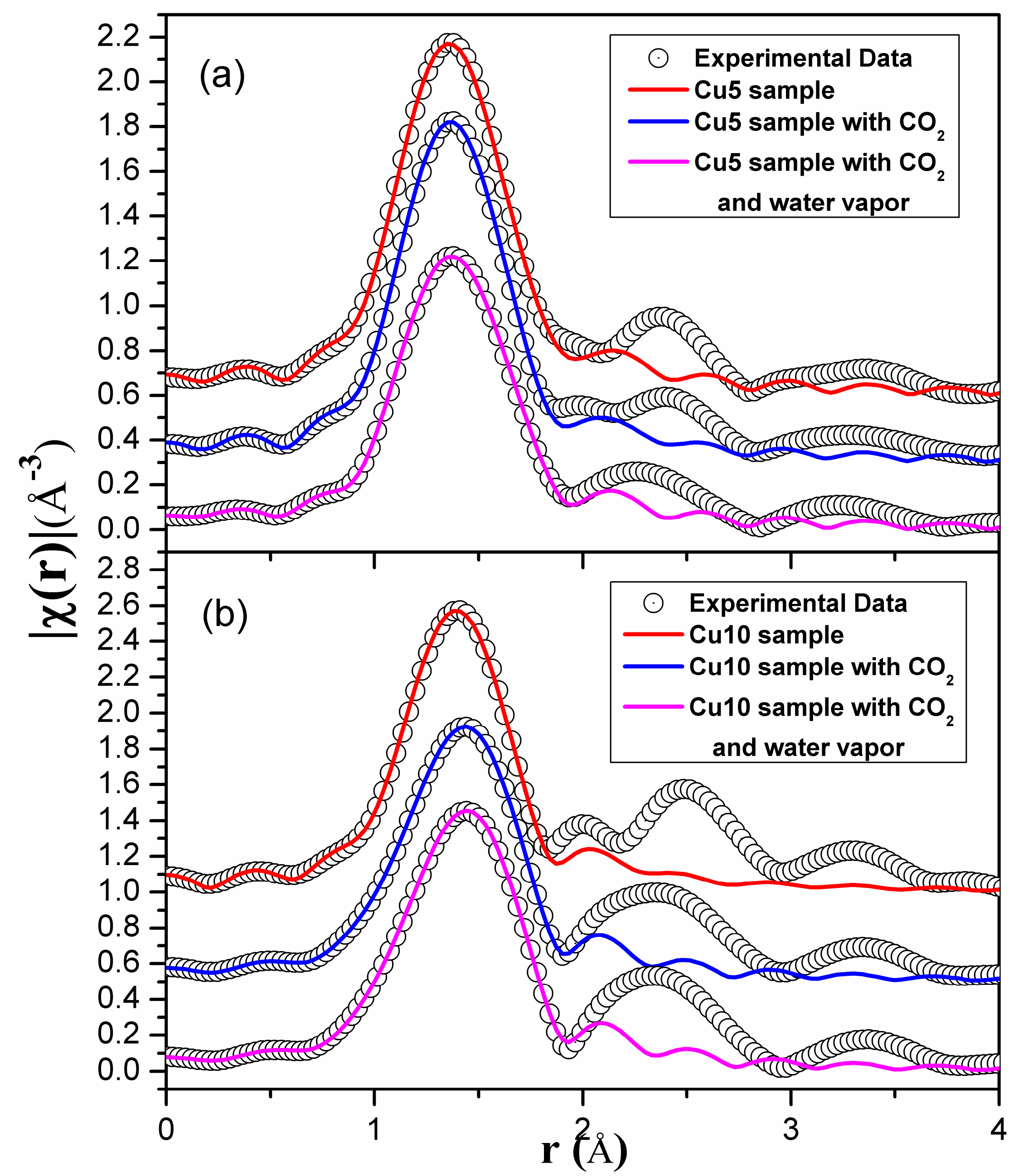

Figure 7.6: *In-situ*EXAFS spectra measured at Cu K edge during the adsorption of CO_2 and water vapour on Cu5 catalyst sample. (b) *In-situ* EXAFS spectra measured at Cu K edge during the adsorption of CO_2 and water vapour on Cu10 catalyst sample. Open circles : experimental data and solid lines: best theoretical fit.

Table 7.2: Cu K edge EXAFS fitting of Cu doped TiO_2 samples during adsorption of CO_2 and water vapour

	Cu-O		
	r(Å)	N	σ^2(Å^2)
Cu5	1.92 ±0.03	5.2 ±0.2	0.0044 ±0.0023
Cu5 with CO_2	1.91 ±0.03	4.8 ±0.1	0.0036 ±0.0015
Cu5 with CO_2& water vapour	1.92 ±0.02	4.7 ±0.2	0.0057 ±0.0008
Cu10	1.91 ±0.01	5.0 ±0.3	0.0036 ±0.0008
Cu10 with CO_2	1.93 ±0.01	4.6 ±0.2	0.0039 ±0.0021
Cu10 with CO_2& water vapour	1.94 ±0.02	4.7 ±0.2	0.0042 ±0.0026

7.4 *In-situ* XAS studies during photocatalytic reduction of CO_2

After inserting CO_2 and water vapour in the cell, the catalyst sample is illuminated with visible radiation and the photocatalysis reaction has been monitored for 8-12 hours by *in-situ* XAS measurements at both Ti and Cu K edges. The product gases have been monitored every hour during the reaction using the Gas Chromatograph.

7.4.1 *In-situ* XAS studies at Ti K edge

Fig. 7.7 (a) and (b) show the *in-situ* XANES spectra measured at Ti K edge during the photocatalytic reduction of CO_2 with Cu5 and Cu10 catalyst samples respectively. The inset in both the figures give an enlarged view of the pre-edge region which shows three small peaks termed as A1, A2 and A3. The peaks A1 and A2 correspond to 3d-4p hybridized state transition and peak A3 corresponds to 4p-4s transition. In anatase TiO_2, the A1 peak corresponds to the four Ti neighbors of the first Ti-Ti shell and the peak A2 is related to the Ti neighbors of the second Ti-Ti shell. Peak A3 arises due to Ti 4p hybridization with Ti 4s and/or O 2p orbitals[176, 177]. From the figure, it is evident that the Cu10 sample does not show any significant changes.

However, for the Cu 5 sample, the pre edge peaks A1, A2 and A3 increase in intensity and moves towards higher energy as the reaction proceeds. The increase in the pre edge peak intensities is often associated with distortion in the TiO_6 octahedra of anatase TiO_2 which results in higher orbital mixing between Ti and O[178].

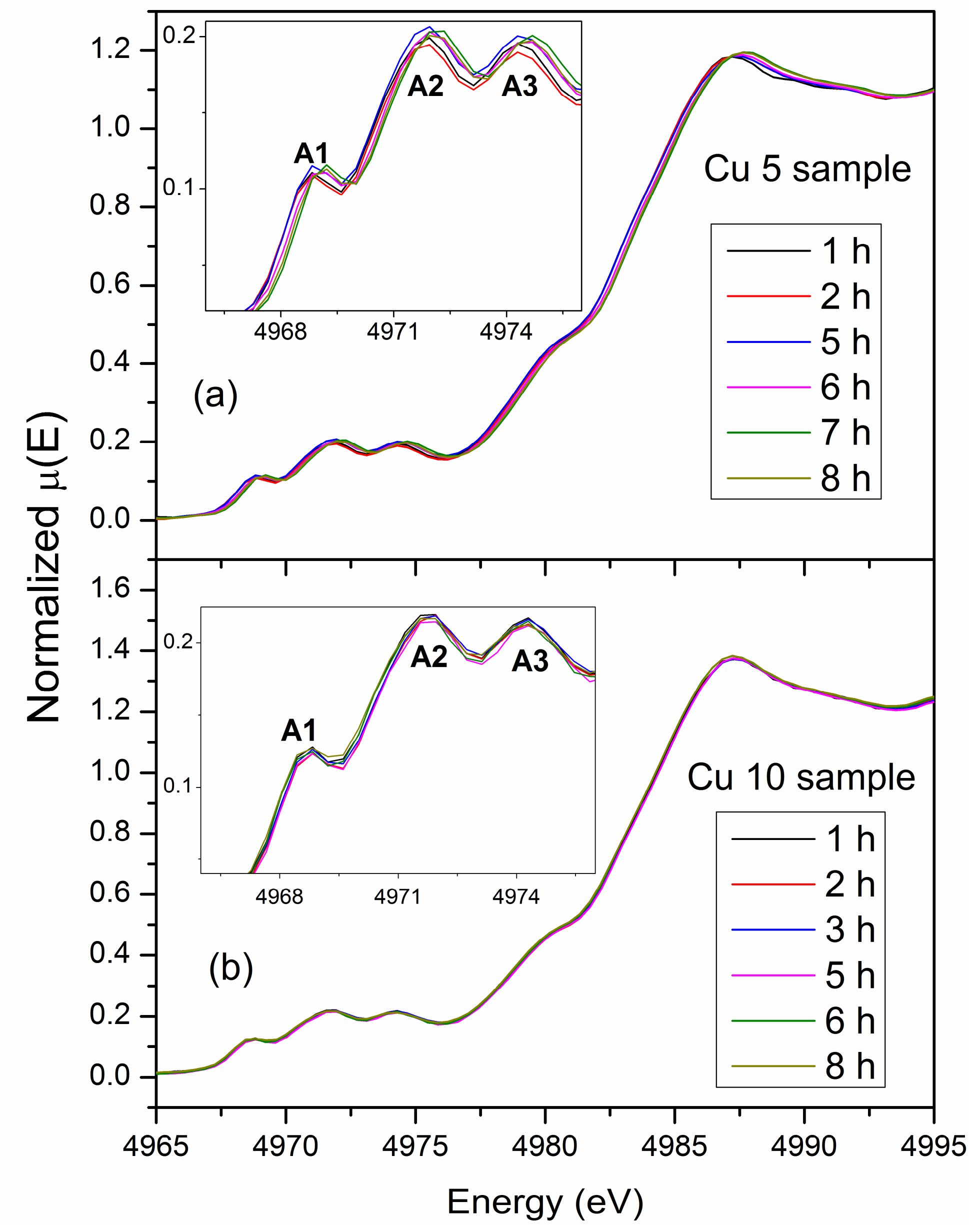

Figure 7.7:(a) *In-situ* XANES spectra measured at Ti K edge of Cu5 catalyst sample during the photocatalytic reduction of CO_2. Inset: enlarged view of pre-edge peaks (b) *In-situ* XANES spectra measured at Ti K edge of Cu10 catalyst sample during the photocatalytic reduction of CO_2. Inset: enlarged view of pre-edge peaks.

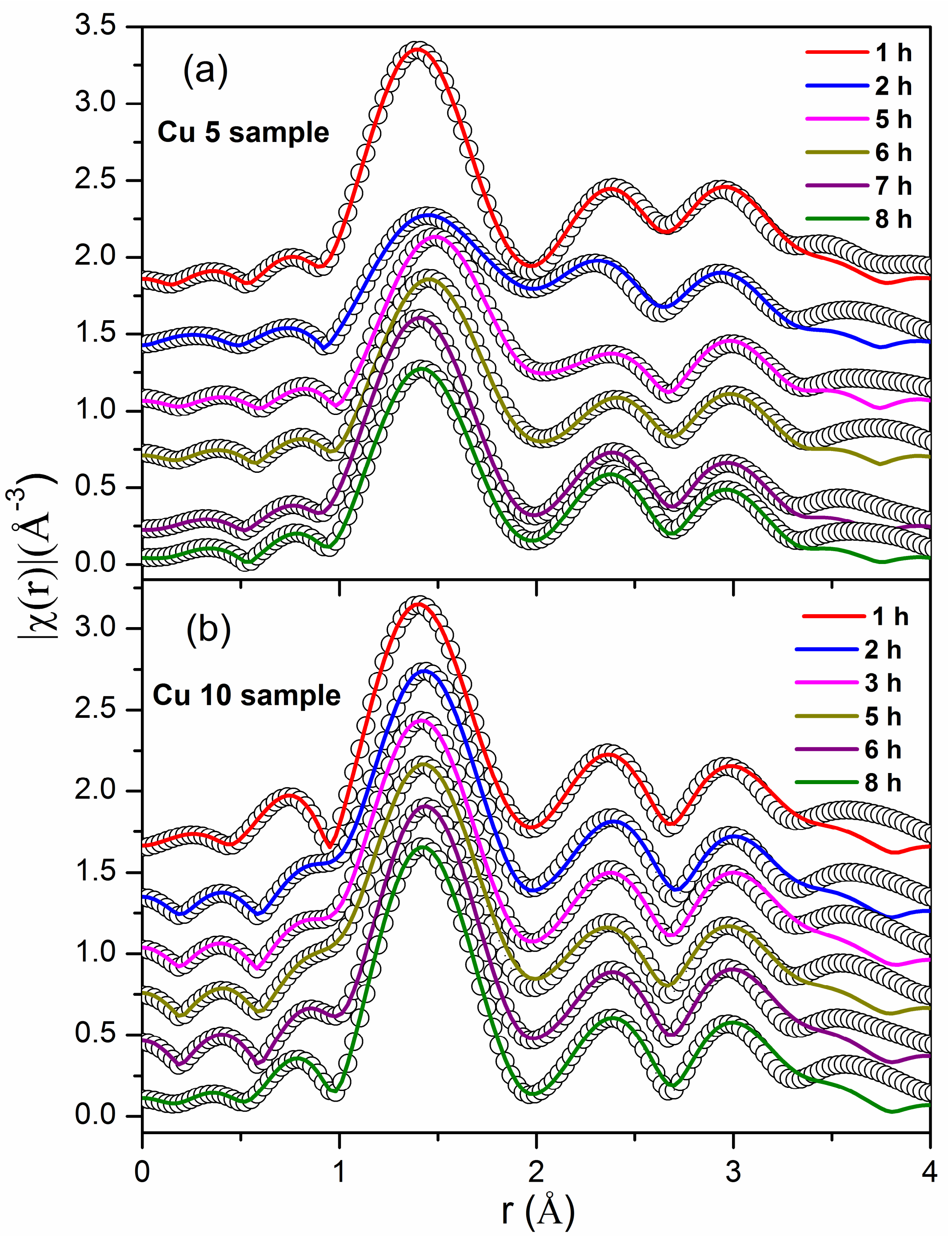

Figure 7.8: (a)*In-situ*EXAFS spectra measured at Ti K edge of Cu5 catalyst sample during the photocatalytic reduction of CO_2. (b) *In-situ*EXAFS spectra measured at Ti K edge of Cu5 catalyst sample during the photocatalytic reduction of CO_2. Rounds: experimental data and solid lines: best theoretical fit.

Table 7.3: Ti K edge EXAFS fitting of Cu5 sample during the photocatalytic reduction of CO_2.

Reaction Time(h)	Ti-O1			Ti-Ti1			Ti-Ti2		
	r(Å)	N	σ^2(Å^2)	r(Å)	N	σ^2(Å^2)	r(Å)	N	σ^2(Å^2)
1	1.90 ±0.01	5.3 ±0.2	0.0028 ±0.0007	2.94 ±0.01	3.6 ±0.3	0.0055 ±0.0013	3.72 ±0.01	3.2 ±0.3	0.0015 ±0.0005
2	1.91 ±0.01	5.6 ±0.3	0.0106 ±0.0015	2.91 ±0.01	3.5 ±0.3	0.0045 ±0.0015	3.69 ±0.02	3.6 ±0.5	0.0048 ±0.0023
5	1.91 ±0.01	5.8 ±0.2	0.0067 ±0.0008	2.91 ±0.01	3.9 ±0.3	0.0087 ±0.0013	3.69 ±0.01	3.9 ±0.5	0.0070 ±0.0020
6	1.89 ±0.01	6.0 ±0.4	0.0063 ±0.0012	2.93 ±0.01	3.9 ±0.3	0.0088 ±0.0015	3.72 ±0.01	3.9 ±0.5	0.0069 ±0.0021
7	1.90 ±0.01	6.1 ±0.2	0.0052 ±0.0011	2.93 ±0.01	3.9 ±0.3	0.0082 ±0.0013	3.71 ±0.01	3.5 ±0.5	0.0059 ±0.0019
8	1.91 ±0.01	6.2 ±0.2	0.0073 ±0.0008	2.93 ±0.01	3.9 ±0.3	0.0075 ±0.0013	3.71 ±0.02	3.6 ±0.5	0.0056 ±0.0019

Table 7.4: Ti K edge EXAFS fitting of Cu10 sample during the photocatalytic reduction of CO_2.

Reaction Time(h)	Ti-O1			Ti-Ti1			Ti-Ti2		
	r(Å)	N	σ^2(Å^2)	r(Å)	N	σ^2(Å^2)	r(Å)	N	σ^2(Å^2)
1	1.95 ±0.01	5.4 ±0.1	0.0038 ±0.0009	2.97 ±0.01	4.1 ±0.4	0.0068 ±0.0018	3.75 ±0.02	4.0 ±0.5	0.0033 ±0.0021
2	1.96 ±0.01	5.6 ±0.3	0.0045 ±0.0011	2.97 ±0.01	4.1 ±0.5	0.0069 ±0.0020	3.75 ±0.02	3.4 ±0.6	0.0029 ±0.0018
3	1.96 ±0.01	5.5 ±0.3	0.0041 ±0.0010	2.97 ±0.01	3.9 ±0.4	0.0067 ±0.0019	3.76 ±0.02	4.2 ±0.6	0.0029 ±0.0020
5	1.96 ±0.01	5.6 ±0.3	0.0043 ±0.0012	2.95 ±0.02	4.1 ±0.5	0.0069 ±0.0023	3.73 ±0.02	3.9 ±0.6	0.0028 ±0.0015
6	1.95 ±0.01	5.7 ±0.2	0.0042 ±0.0009	2.96 ±0.01	4.3 ±0.5	0.0079 ±0.0018	3.74 ±0.01	3.9 ±0.5	0.0024 ±0.0019
8	1.95 ±0.01	5.8 ±0.2	0.0038 ±0.0009	2.96 ±0.01	4.1 ±0.5	0.0075 ±0.0020	3.74 ±0.02	3.7 ±0.5	0.0022 ±0.0016

The experimental $\chi(r)$ versus r plots of the Cu doped TiO_2 samples at Ti K edge have been fitted using the same procedure described in sub-section 7.3.1. The experimental $\chi(r)$ versus r plots of the Cu5 and Cu10 samples at Cu K edge along with best fit theoretical ones have been shown in Fig. 7.8 (a) and (b) respectively and the fitting results have been tabulated in Table 7.3 and Table 7.4.From the EXAFS analysis results, it is evident that the coordination numbers of the Ti-O bond increases as the reaction proceeds. However, the Ti-O and Ti-Ti bond length do not change significantly during the reaction. The increase in the Ti-O coordination number implies the decrease in oxygen vacancies near Ti cations, which suggests that the oxygen vacancies play a role in the photocatalytic reduction of CO_2.

7.4.2 *In-situ* XAS studies at Cu K edge

Fig. 7.9 (a) and (b) show the *in-situ* XANES spectra measured at Cu K edge during the photocatalytic reduction of CO_2 with Cu5 and Cu10 catalyst samples respectively. From the above figures, it can be observed that the absorption edge in general shifts towards lower energy with time during the photocatalytic reduction of CO_2 for both the catalyst samples. This implies that the effective charge of Cu decreases during the photocatalytic reduction of CO_2. However, at certain time intervals there is a slight increase in the Cu effective charge as evident from the shift of absorption edge to higher energy shown in Fig. 7.10.

The experimental $\chi(r)$ versus r plots of the Cu doped TiO_2 samples at Cu K edge have been fitted using the same procedure described in sub-section 7.3.2. The experimental $\chi(r)$ versus r plots of the Cu5 and Cu10 samples at Cu K edge along with best fit theoretical plots have been shown in Fig. 7.11 (a) and (b) respectively and the fitting results have been tabulated in Tables7.5 and 7.6. From the EXAFS analysis results it can be seen that the Cu-O bond lengths and coordination numbers do not vary significantly during the photocatalytic reduction of CO_2 for both Cu5 and Cu10 samples. Therefore, it can be concluded from the XANES and EXAFS analysis that the effective charge of Cu decreases during the photocatalytic reduction of CO_2, but there is no change in the local environment of Cu cations.

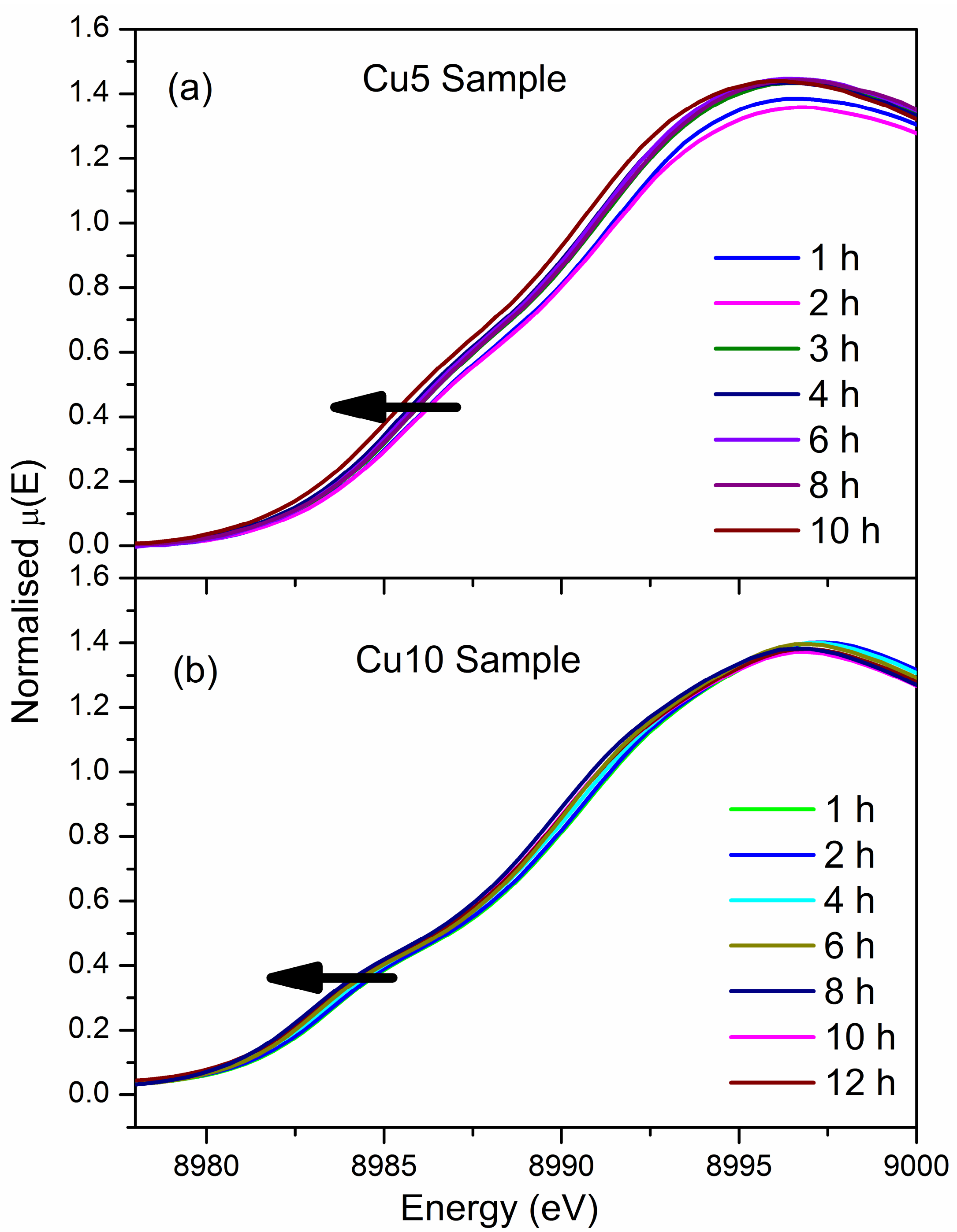

Figure 7.9:(a) *In-situ* XANES spectra measured at Cu K edge of Cu5 catalyst sample during the photocatalytic reduction of CO_2. (b) *In-situ* XANES spectra measured at Cu K edge of Cu10 catalyst sample during the photocatalytic reduction of CO_2.

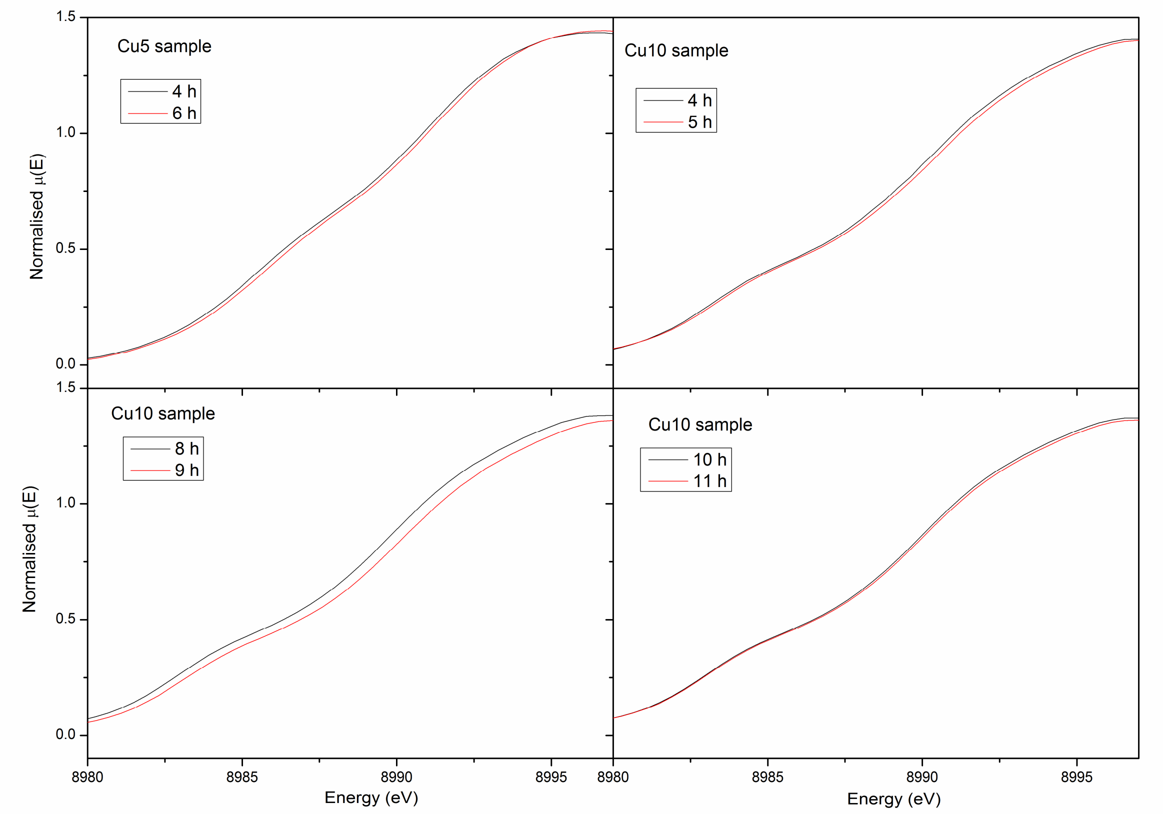

Figure 7.10:*In-situ* XANES spectra measured at Cu K edge of Cu5 and Cu 10 catalyst sample at some selected time intervals during the photocatalytic reduction of CO_2.

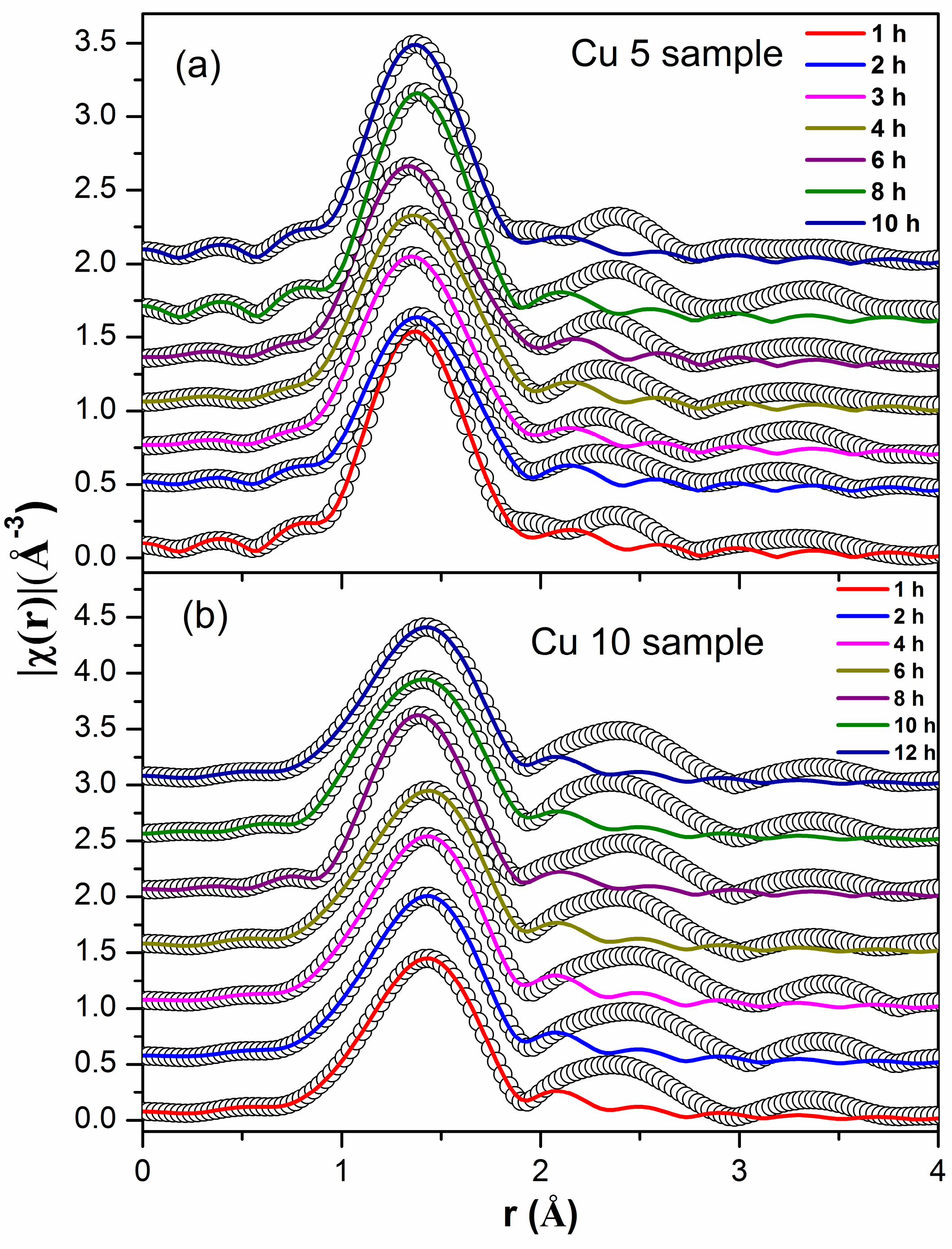

Figure 7.11:(a)*In-situ*EXAFS spectra measured at Cu K edge of Cu5 catalyst sample during the photocatalytic reduction of CO_2. (b) *In-situ*EXAFS spectra measured at Cu K edge of Cu5 catalyst sample during the photocatalytic reduction of CO_2. Open circles : experimental data and solid lines: best theoretical fit.

Table 7.5: Cu K edge EXAFS fitting of Cu5 sample during the photocatalytic reduction of CO_2.

Reaction Time (h)	Cu-O		
	r(Å)	N	σ^2(Å^2)
1	1.92 ±0.02	4.8 ±0.3	0.0033 ±0.0006
2	1.93 ±0.02	4.7 ±0.3	0.0059 ±0.0011
3	1.92 ±0.01	4.9 ±0.4	0.0054 ±0.0015
4	1.93 ±0.01	4.9 ±0.4	0.0055 ±0.0015
6	1.92 ±0.02	4.9 ±0.6	0.0056 ±0.0023
8	1.92 ±0.01	5.0 ±0.3	0.0031 ±0.0014
10	1.91 ±0.03	4.7 ±0.5	0.0034 ±0.0025

Table 7.6: Cu K edge EXAFS fitting of Cu10 sample during the photocatalytic reduction of CO_2.

Reaction Time (h)	Cu-O		
	r(Å)	N	σ^2(Å^2)
1	1.93 ±0.01	5.1 ±0.7	0.0048 ±0.0022
2	1.92 ±0.03	5.3 ±0.4	0.0053 ±0.0014
3	1.92 ±0.03	5.2 ±0.4	0.0051 ±0.0010
4	1.92 ±0.03	5.4 ±0.7	0.0054 ±0.0005
5	1.92 ±0.02	5.2 ±0.4	0.0050 ±0.0004
6	1.93 ±0.01	5.2 ±0.7	0.0054 ±0.0021
7	1.92 ±0.02	5.4 ±0.3	0.0048 ±0.0008
8	1.92 ±0.02	5.2 ±0.4	0.0037 ±0.0013
9	1.93 ±0.02	5.1 ±0.8	0.0050 ±0.0023
10	1.93 ±0.01	5.2 ±0.6	0.0054 ±0.0015
11	1.93 ±0.02	5.1 ±0.5	0.0037 ±0.0006
12	1.93 ±0.01	5.0 ±0.7	0.0051 ±0.0017

7.5 Gas Chromatograph Measurements

From the Gas Chromatograph (GC) measurements, it has been confirmed that CH_4 is produced during the photocatalytic reduction of CO_2. Fig. 7.12 shows the variation of CH_4 concentration with time during the photocatalytic reduction of CO_2 as determined from the GC measurements. The methane peak appears after 2 hrs and 3 hrs from the start of the reaction for 50 mg of the Cu5 and Cu10 samples respectively.

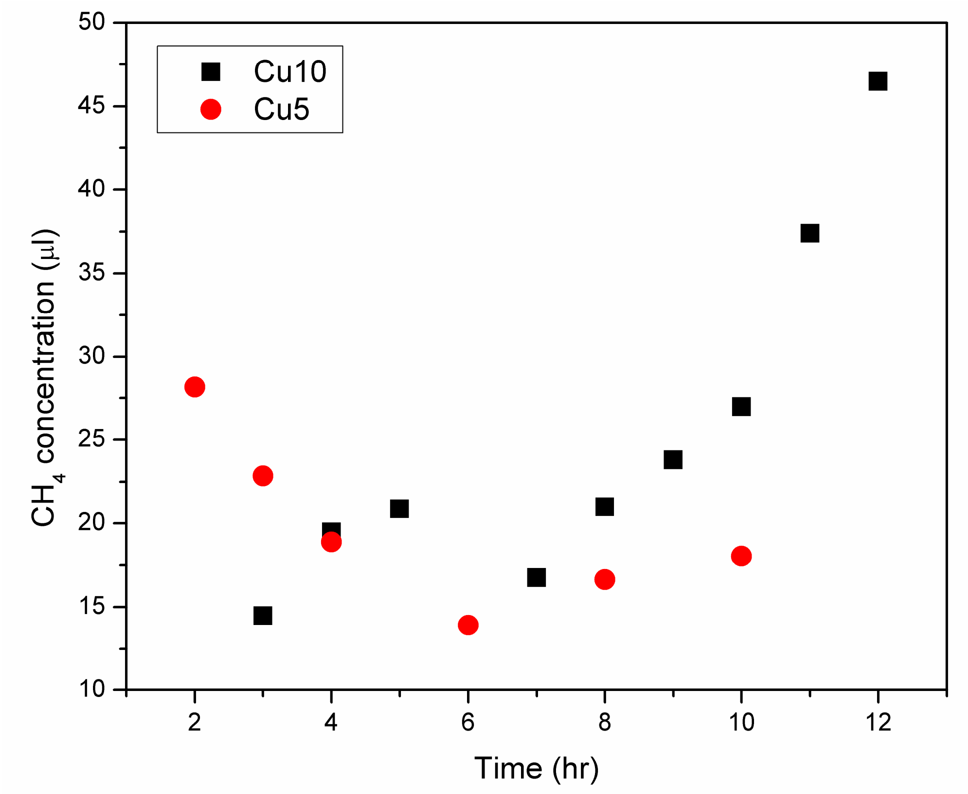

Figure 7.12: Concentration of CH_4produced during the photocatalytic reduction of CO_2.

7.6 Reaction Mechanism

Many studies have been carried out in order to understand the reaction mechanism involved during the photocatalytic reduction of CO_2[172]. Karamian *et. al.*[170] have proposed some reaction mechanism of the photocatalytic reduction of CO_2 and tried to explain the effect of different reducing agents on the photocatalytic reduction process. Tan *et. al.*[171] studied the photocatalytic reduction of CO_2 with TiO_2 pellets and proposed that the photogenerated electron and holes are created on the surface of TiO_2. These charge carriers react with adsorbed water and CO_2, thus generating OH and carbon radicals. Carbon radicals are formed by the dissociation of CO_2 with CO as an intermediate and H^+ ions are formed when the OH radicals further oxidize the water. The carbon radicals react with H^+ and electrons from the photocatalyst to form CH_4. Similarly, many studies have been done to understand the enhanced photocatalytic activity of Cu doped TiO_2[179-181].For example, Liu *et. al.*[179] have performed *in situ* DRIFT measurements to investigate the activation and dissociation of CO_2 on Cu doped TiO_2 catalysts. This study has helped to identify the different reaction intermediates formed during the reduction of CO_2.

In the present study it has been found that during the adsorption of CO_2 and H_2O, the oxygen vacancies decrease near the Ti sites, which suggest that the oxygen vacancy defect sites adsorb the CO_2 and H_2O molecules. The electron in the oxygen vacancy defect sites can be transferred to the CO_2 molecules and CO_2^- species may be formed. The CO_2^- species may decompose to CO giving the extra oxygen to the vacancy site. This results in decrease in the oxygen vacancies as found from EXAFS results. The formation of CO from CO_2^- on decomposition has been confirmed by many other researchers also[174, 180, 182]. In case of H_2O adsorption on the other hand, more oxygen from the lattice diffuse to the surface forming OH radicals and results in the increase in oxygen vacancies. Many literatures suggest that the Ti^{+3} cations present in the TiO_2 lattice also acts as a site for adsorption[173, 182]. However, in our case, we didn't find any change of effective charge of Ti cations during adsorption. Therefore, we assume that the oxygen vacancies near Ti^{+4} cations and not the Ti^{+3} cations participate in the adsorption process. The effective charge of the Cu cations increases during the adsorption of CO_2. This may be due to transfer of electrons from surface Cu cations to the adsorbed CO_2

species forming CO_2^- radicals. The effective charge on Cu however decreases during adsorption of water vapour which suggests that electrons are transferred to Cu cations during the process of generation of OH^- radicals.

On photo-illumination, the Ti-O coordination number decreases from 5.6 to 5.3 for Cu5 sample and 5.6 to 5.4 for Cu10 sample. This suggests the generation of oxygen vacancies near the Ti cations on photo-illumination. The partial regeneration of surface oxygen vacancies on Cu/TiO_2 catalyst has also been observed by Liu *et. al.*[180] The holes created in the TiO_2 lattice oxidise the surface oxygen atoms to O_2, thus forming oxygen vacancies. These defect sites are however further used for the activation and dissociation of CO_2 as discussed above, which results in decrease in the oxygen vacancies as time proceeds during the photoreduction of CO_2. The effective charge of Cu also decreases during photo-illumination of the catalyst which suggests the photo generated electrons get transferred to the Cu cations. Thus Cu acts as electron trapping agent in the TiO_2 lattice. The trapped electrons are transferred to the adsorbed CO_2 and results in the dissociation of CO_2. However, the trapped electrons can also be transferred to H^+ or O_2. The transfer of electrons from Cu sites to the adsorbed species results in re-oxidation of Cu cations[183]. This has been observed at certain time intervals when the effective charge of Cu increases as shown in Fig. 7.10. Liu *et. al.*[180] have also found the formation of Cu^+-CO species during photoirradiation which suggests the activation and dissociation of CO_2 at the Cu sites. Neatu et. al.[182] have also found that Cu bonding to CO leads to the selective formation of CH_4.

7.7 Conclusion

A facility has been set up at the Energy Scanning EXAFS beamline (BL-09) at RRCAT, Indore, India for *in-situ* structure-activity correlation studies on catalysts during photocatalytic reaction using simultaneous measurements of X-ray absorption spectroscopy (XAS) and gas chromatography (GC). Using this setup, the photocatalytic reduction reaction of CO_2 and water vapour to form methane (CH_4) in the presence of Cu doped TiO_2 catalysts has been studied. It has been inferred from the Cu and Ti K edge XANES and EXAFS measurement that the oxygen vacancies present in the samples near Ti and Cu cations are the sites for CO_2 and water vapour adsorption in the catalysts. The photo generated electrons get transferred to the Cu cations which act as electron traps in the TiO_2 lattice. The trapped electrons are transferred to the adsorbed CO_2 and results in the formation of CO_2^- which further dissociates to form carbon radicals. These carbon radicals react with H obtained from reduction of water vapour and form CH_4On photo-illumination, oxygen vacancies are also created in the lattice, which are further used for the activation and dissociation of CO_2 or H_2O. Therefore, *in-situ* XAS measurement gives an understanding of the CO_2 and H_2O adsorption process on the Cu doped TiO_2 catalyst and photoreduction of CO_2 to CH_4. Both Cu cations and oxygen vacancies present near Ti cations play important roles in the photo-reduction of CO_2 to CH_4. The production of CH_4 during photocatalytic reduction of CO_2 has been confirmed simultaneously by Gas Chromatography (GC) measurements.

Chapter 8

Conclusions and Future Work

This thesis work focuses on the application of Time Resolved X-ray Absorption spectroscopy (TR-XAS) for *in-situ* studies during growth of nanoparticles and catalysis. Various *in-situ* cells have been designed and different experiments have been carried out to understand the growth mechanism or reaction mechanism involved in these processes. This chapter discusses the final conclusions of all the experiments and the future perspective of the work.

8.1 *In-situ* XAS studies during growth of nanoparticles

For *in-situ* XAS measurements on one-pot nanoparticle synthesis processes, a set-up has been developed at the energy dispersive EXAFS beamline (BL-08) at Indus-2 SRS at RRCAT, Indore, India using a specially designed teflon cell with one optical path for X-ray in the direction of synchrotron beam and another in the perpendicular direction for visible radiation. Using the above set-up the growth of Au, Pt and Au@Pt nanoparticles from their respective chloride precursors using block copolymer based reducer-cum-stabilizer have been studied by simultaneous *in-situ* measurement of XAS and UV-Vis spectroscopy. The growth process of these nanoparticles are found to follow the three stages viz., (i) reduction of metal ions by block copolymer and formation of small cluster (ii) absorption of block copolymer and reduction of metal ions on the surface of the cluster and increase in cluster size and (iii) growth of nanoparticles stabilized by block copolymer. This can be observed that the time scale involved in the 2nd and 3rdstages of the Au and Pt monometallic nanoparticle formation are similar which suggest that these stages are mainly governed by the block copolymer which is same in both the cases. This also consolidates the role of the block copolymer in the formation of these nanoparticles. However, the 1st stage of nucleation takes place earlier in case of Au than in case of Pt due to the difference in the reduction potential of the respective precursors. In both the cases, 12 atoms clusters are formed which act as seeds for further growth. However, for gold, these 12 atoms cluster first grows into the magic number 13 atoms cluster and then 147 atoms clusters which further grows into gold nanoparticles. For platinum the 12 atoms cluster grows into the magic number 55 atoms cluster which further grows into platinum nanoparticles. The first two stages of the growth of Au and Pt nanoparticles as obtained by *in-situ* XAS measurements are also corroborated by simultaneous *in-situ* measurement of UV-Vis spectroscopy.

The Au-Pt bimetallic nanoparticles have been synthesized through a one-pot synthesis route from their respective chloride precursors using block copolymer as a stabilizer. From the *in-situ* measurement of UV-Vis spectroscopy, it has been observed that Au seeds are formed with the appearance of Au SPR peak and vanishes when the Pt shell starts forming on the Au core. This confirms the formation of core shell like structure in Au-Pt bimetallic alloy. *Ex-situ* studies by HRTEM with EDS line scan and XPS measurements with *in-situ* etching on the fully formed nanoparticles also ascertain their core-shell type nature. However, simultaneous *in-situ* XAS measurement gives a detail microscopic account of the phenomenon which shows that Au precursor get reduced within 10 sec. and Au_4 clusters are formed which act like nuclei for the further growth and the Pt reduction occurs slowly on the surface of the Au nuclei. The study of the formation process shows how the difference in the reduction potential of the two precursors could be used successfully to get the core shell configuration of bimetallic alloy in a controlled fashion using a one–pot synthesis method.

A flow set-up has been developed at the energy dispersive EXAFS beamline (BL-08) at Indus-2 SRS at RRCAT, Indore, India for studying growth of nanoparticles under different reaction conditions. *In-situ* XAS measurement has been done during the formation of Cu nanoparticles under inert atmosphere using this specialized flow setup. Cu nanoparticles have been synthesized from copper acetate using $NaBH_4$ as a reducing agent and PVP as a stabilizing agent. XRD and TEM measurements confirm the presence of metallic Cu nanoparticles of size between 19 nm. Principal Component Analysis (PCA) and Multivariate Curve Resolution with Alternating Least Squares (MCR-ALS) analysis techniques have been successfully applied to Cu K-edge XANES data recorded during the growth of Cu nanoparticles. From PCA, it has been confirmed that the reduction reaction involves three species. MCR-ALS analysis gives the XANES spectra of the three species and their concentration profiles during the reaction. It has been concluded that the reduction reaction occurs in two steps: (i) formation of Cu^{+1} species from Cu^{+2} reduction after 500 s and (ii) reduction of Cu^{+1} to Cu^0 after 750 s from the start of the reaction. The EXAFS spectra of the intermediate species have been extracted and the analysis confirms the presence of 2 oxygen atoms around the first coordination shell of Cu cation in the intermediate species which nearly matches with the local environment of Cu_2O. Therefore, using PCA and MCR-ALS analysis of *in-situ* XAS spectra recorded during the synthesis of Cu nanoparticles, the intermediates formed have been identified and their concentration profile has been estimated. This methodology will be helpful in controlling the reaction parameters and hence the reduction process for synthesis of nanoparticles with tailored properties.

8.2 *In-situ* XAS studies during catalysis

A facility has been set up at the Energy Scanning EXAFS beamline (BL-09) at Indus-2 SRS, RRCAT, Indore, India for *in-situ* studies of structure-activity correlation during catalytic reaction using simultaneous measurements of X-ray absorption spectroscopy (XAS) and gas chromatography. XAS provides information regarding structural changes in the catalyst during the reaction, while gas chromatography monitors the product gases of the reaction, which in turn gives information regarding the activity of the catalyst. Using the above facility SBA-15 supported Co_3O_4 nanoparticle catalysts has been studied *in-situ* during Fischer Tropsch reaction for methane generation by the reaction of CO and H_2. The catalyst is first reduced by heating it at 400ºC for 5 hours under H_2 ambient and it has been found from XANES measurements that the as-prepared catalyst first reduces to CoO and then to metallic Co during reduction. The activity of the reduced catalyst is subsequently been observed at few different temperatures viz., 240ºC, 260ºC, 280ºC and 320ºC and it has been found by XANES and EXAFS measurements that the structure of the catalyst does not show any significant change during the Fischer Tropsch reaction at these temperatures and remains in the metallic Co phase. It has further been observed that as the reaction temperature increases from 280ºC-320ºC the activity of the catalyst increases significantly. However, at 320ºC the Co catalyst shows deactivation with time. The catalyst has been studied for 10 hours at 320ºC and an attempt has been made to understand the process of deactivation using XANES and EXAFS analysis. From the structural analysis results it has been observed that there is no signature of formation of CoO phase during the reaction which might be responsible for the deactivation of the catalyst. Therefore, there is a strong possibility that the deactivation of the catalyst is caused due to carbon formation on the surface of the catalyst which does not get removed due to very low concentration of CoO in the reduced sample. This has been confirmed from *ex-situ* Raman spectroscopy measurement of the deactivated catalyst.

Similarly, another facility has been set up at the Energy Scanning EXAFS beamline (BL-09) at Indus-2 SRS, RRCAT, Indore, India for *in-situ* studies during photocatalytic reaction using simultaneous measurements of X-ray absorption spectroscopy (XAS) and gas chromatography. Using this setup, the photocatalytic reduction reaction of CO_2 has been studied using Cu doped TiO_2 catalysts. It has been inferred from the XANES and EXAFS analysis that the oxygen vacancies near Ti cations and Cu cations are the sites for CO_2 and water vapour adsorption. The photo generated electrons get transferred to the Cu cations which acts as a electron trap in the TiO_2 lattice. The trapped electrons are transferred to the adsorbed CO_2 and results in the dissociation of CO_2. On photoillumination, oxygen vacancies are also created in the lattice, which are further used for the activation and dissociation of CO_2 or H_2O. Therefore, in situ XAS measurement gives an understanding of the CO_2 and H_2O adsorption on the Cu doped TiO_2 catalyst and photoreduction of CO_2 to CH_4. Both Cu cations and oxygen vacancies near Ti cations play important role in the photoreduction of CO_2 to CH_4. The production of CH_4 during photocatalytic reduction of CO_2 has been confirmed from the GC measurements.

8.3 Future work

The present thesis work can be extended in future for the application of time resolved XAS in other fields like *in-situ* studies during growth of thin films and *in-situ* studies during charging-discharging of rechargeable batteries. The *in-situ* studies during growth of thin films will give an insight into the thin film formation process which in turn will help to fabricate better thin film devices. Similarly, *in-situ* studies during charging-discharging of rechargeable batteries will provide information regarding the structural changes in the anode or cathode materials during the charging-discharging process. This information will facilitate to fabricate efficient batteries with higher charge holding capacity and compatibility with higher number of charging - discharging cycles before break-down.

References

1. E. A. Stern, Physical Review B **10** (8), 3027-3037 (1974).
2. D. E. Sayers, E. A. Stern and F. W. Lytle, Physical Review Letters **27** (18), 1204-1207 (1971).
3. D. C. Konigsberger and R. Prince, *X-Ray Absorption: Principles, Applications, Techniques of EXAFS, SEXAFS and XANES*. (Wiley, New York, 1988).
4. G. Bunker, *Introduction to XAFS: A Practical Guide to X-ray Absorption Fine Structure Spectroscopy*. (Cambridge University Press, Cambridge, 2010).
5. T. Mizutani, S. Ogawa, T. Murai, H. Nameki, T. Yoshida and S. Yagi, Applied Surface Science **354**, 397-400 (2015).
6. H. Zheng, R. K. Smith, Y.-w. Jun, C. Kisielowski, U. Dahmen and A. P. Alivisatos, Science **324** (5932), 1309 (2009).
7. S. B. Simonsen, I. Chorkendorff, S. Dahl, M. Skoglundh, J. Sehested and S. Helveg, Journal of the American Chemical Society **132** (23), 7968-7975 (2010).
8. F. Vigier, C. Coutanceau, F. Hahn, E. M. Belgsir and C. Lamy, Journal of Electroanalytical Chemistry **563** (1), 81-89 (2004).
9. L. J. Burcham, G. Deo, X. Gao and I. E. Wachs, Topics in Catalysis **11** (1), 85-100 (2000).
10. S. E. R. Tay, A. E. Goode, J. Nelson Weker, A. A. Cruickshank, S. Heutz, A. E. Porter, M. P. Ryan and M. F. Toney, Nanoscale **8** (4), 1849-1853 (2016).
11. B. Abécassis, F. Testard, O. Spalla and P. Barboux, Nano Letters **7** (6), 1723-1727 (2007).
12. B. L. Caetano, C. V. Santilli, F. Meneau, V. Briois and S. H. Pulcinelli, The Journal of Physical Chemistry C **115** (11), 4404-4412 (2011).
13. T. D. Hatchard and J. R. Dahn, Journal of The Electrochemical Society **151** (6), A838-A842 (2004).
14. B. T. Young, D. R. Heskett, J. C. Woicik and B. L. Lucht, Journal of Spectroscopy **2018**, 7 (2018).
15. M. Kubin, J. Kern, M. Guo, E. Källman, R. Mitzner, V. K. Yachandra, M. Lundberg, J. Yano and P. Wernet, Physical Chemistry Chemical Physics **20** (24), 16817-16827 (2018).
16. T.-S. Wu, L.-Y. Syu, S.-C. Weng, H.-T. Jeng, S.-L. Chang and Y.-L. Soo, Journal of Synchrotron Radiation **25** (5), 1395-1399 (2018).
17. D. Koziej, Chemistry of Materials **28** (8), 2478-2490 (2016).
18. R. Frahm, T. W. Barbee and W. Warburton, Physical Review B **44** (6), 2822-2825 (1991).
19. M. A. Newton, A. J. Dent and J. Evans, Chemical Society Reviews **31** (2), 83-95 (2002).
20. M. Harada and Y. Inada, Langmuir **25** (11), 6049-6061 (2009).
21. Y. Makimura, T. Sasaki, H. Oka, C. Okuda, T. Nonaka, Y. F. Nishimura, S. Kawauchi and Y. Takeuchi, Journal of The Electrochemical Society **163** (7), A1450-A1456 (2016).
22. J. Stötzel, D. Lützenkirchen-Hecht, R. Frahm, C. V. Santilli, S. H. Pulcinelli, R. Kaminski, E. Fonda, F. Villain and V. Briois, The Journal of Physical Chemistry C **114** (14), 6228-6236 (2010).
23. I. J. Shannon, T. Maschmeyer, G. Sankar, J. M. Thomas, R. D. Oldroyd, M. Sheehy, D. Madill, A. M. Waller and R. P. Townsend, Catalysis Letters **44** (1), 23-27 (1997).

24. M. Tromp, J. R. A. Sietsma, J. A. van Bokhoven, G. P. F. van Strijdonck, R. J. van Haaren, A. M. J. van der Eerden, P. W. N. M. van Leeuwen and D. C. Koningsberger, Chemical Communications (1), 128-129 (2003).
25. V. Briois, D. Lützenkirchen-Hecht, F. Villain, E. Fonda, S. Belin, B. Griesebock and R. Frahm, The Journal of Physical Chemistry A **109** (2), 320-329 (2005).
26. M. A. Newton, B. Jyoti, A. J. Dent, S. G. Fiddy and J. Evans, Chemical Communications (21), 2382-2383 (2004).
27. J. Ohyama, K. Teramura, Y. Higuchi, T. Shishido, Y. Hitomi, K. Kato, H. Tanida, T. Uruga and T. Tanaka, ChemPhysChem **12** (1), 127-131 (2011).
28. M. Harada, Y. Inada and M. Nomura, J Colloid Interface Sci **337** (2), 427-438 (2009).
29. A. Voronov, N. E. Tsakoumis, N. Hammer, W. van Beek, H. Emerich and M. Rønning, Catalysis Today **229**, 23-33 (2014).
30. M. A. Newton, C. Belver-Coldeira, A. Martínez-Arias and M. Fernández-García, Nature Materials **6**, 528 (2007).
31. G. Nusinovich, R. Pu, O. Sinitsyn, A. Kesar, T. Antonsen Jr, Y. Dimant and V. Granatstein, presented at the APS Meeting Abstracts, 2010 (unpublished).
32. G. Bunker, *Introduction to XAFS A Practical Guide to X-ray Absorption Fine Structure Spectroscopy*. (Cambridge University Press, New York, 2010).
33. D. C. K. R. Prince, *X-Ray Absorption: Principles Applications Techniques of EXAFS SEXAFS and XANES* (Wiley, New York 1988).
34. Jeroen A. van Bokhoven and C. Lamberti, *X-Ray Absorption and X-Ray Emission Spectroscopy: Theory and Applications*. (John Wiley & Sons, Ltd, West Sussex, 2016).
35. S. Calvin, *XAFS for Everyone*. (CRC Press, New York, 2013).
36. M. R. Claudia S. Schnohr, *X-Ray Absorption Spectroscopy of Semiconductors*. (Springer-Verlag Berlin Heidelberg, 2015).
37. P. Willmott, *An Introduction to Synchrotron Radiation: Techniques and Applications*. (John Wiley & Sons, Ltd, West Sussex, 2011).
38. Z. Sun, W. Yan, T. Yao, Q. Liu, Y. Xie and S. Wei, Dalton Transactions **42** (38), 13779-13801 (2013).
39. S. Kelly, D. Hesterberg and B. Ravel, Methods of soil analysis. Part **5**, 387-463 (2008).
40. E. Fonda, A. Rochet, M. Ribbens, L. Barthe, S. Belin and V. Briois, Journal of Synchrotron Radiation **19** (3), 417-424 (2012).
41. R. Frahm, M. Richwin and D. Lützenkirchen-Hecht, Physica Scripta **2005** (T115), 974 (2005).
42. O. Muller, M. Nachtegaal, J. Just, D. Lutzenkirchen-Hecht and R. Frahm, Journal of Synchrotron Radiation **23** (1), 260-266 (2016).
43. V. Briois, C. L. Fontaine, S. Belin, L. Barthe, M. Th, V. Pinty, A. Carcy, R. Girardot and E. Fonda, Journal of Physics: Conference Series **712** (1), 012149 (2016).
44. C. Prestipino, O. Mathon, R. Hino, A. Beteva and S. Pascarelli, Journal of Synchrotron Radiation **18** (Pt 2), 176-182 (2011).
45. P. L. Lee, M. A. Beno, G. Jennings, M. Ramanathan, G. S. Knapp, K. Huang, J. Bai and P. A. Montano, Review of Scientific Instruments **65** (1), 1-6 (1994).
46. D. Bhattacharyya, A. K. Poswal, S. N. Jha, Sangeeta and S. C. Sabharwal, Nucl. Instrum. Meth. Phys. Res.A **609**, 286 (2009).

47. D. F. Sanchez, A. S. Simionovici, L. Lemelle, V. Cuartero, O. Mathon, S. Pascarelli, A. Bonnin, R. Shapiro, K. Konhauser, D. Grolimund and P. Bleuet, Scientific Reports **7** (1), 16453 (2017).
48. M. R. Bockstaller, Angewandte Chemie International Edition **43** (43), 5723-5724 (2004).
49. S. B. Sant, Materials and Manufacturing Processes **27** (12), 1462-1463 (2012).
50. J. Polte, T. T. Ahner, F. Delissen, S. Sokolov, F. Emmerling, A. F. Thünemann and R. Kraehnert, Journal of the American Chemical Society **132** (4), 1296-1301 (2010).
51. C.-S. Lin, M. Khan, R. and S. Lin, D., Journal of Colloid and Interface Scvience **299**, 678-685 (2006).
52. J. Ma, Y. Zou, Z. Jiang, W. Huang, J. Li, G. Wu, Y. Huang and H. Xu, Physical Chemistry Chemical Physics **15** (28), 11904-11908 (2013).
53. M. Harada and H. Einaga, Langmuir **23** (12), 6536-6543 (2007).
54. M. Harada and Y. Kamigaito, Langmuir **28** (5), 2415-2428 (2012).
55. J. Boita, L. Nicolao, M. C. M. Alves and J. Morais, Physical Chemistry Chemical Physics **16** (33), 17640-17647 (2014).
56. A. M. Karim, N. Al Hasan, S. Ivanov, S. Siefert, R. T. Kelly, N. G. Hallfors, A. Benavidez, L. Kovarik, A. Jenkins, R. E. Winans and A. K. Datye, The Journal of Physical Chemistry C **119** (23), 13257-13267 (2015).
57. B. M. Weckhuysen, Chemical Communications (2), 97-110 (2002).
58. H. Topsøe, Journal of Catalysis **216** (1), 155-164 (2003).
59. M. Hunger and J. Weitkamp, Angewandte Chemie International Edition **40** (16), 2954-2971 (2001).
60. M. Manzoli, F. Vindigni, T. Tabakova, C. Lamberti, D. Dimitrov, K. Ivanov and G. Agostini, Journal of Materials Chemistry A **5** (5), 2083-2094 (2017).
61. J. G. Mesu, A. M. J. van der Eerden, F. M. F. de Groot and B. M. Weckhuysen, The Journal of Physical Chemistry B **109** (9), 4042-4047 (2005).
62. D. Tibiletti, A. A. Fonseca, R. Burch, Y. Chen, J. M. Fisher, A. Goguet, C. Hardacre, P. Hu and D. Thompsett, The Journal of Physical Chemistry B **109** (47), 22553-22559 (2005).
63. M. Sadeqzadeh, H. Karaca, O. V. Safonova, P. Fongarland, S. Chambrey, P. Roussel, A. Griboval-Constant, M. Lacroix, D. Curulla-Ferré, F. Luck and A. Y. Khodakov, Catalysis Today **164** (1), 62-67 (2011).
64. S. Basu, C. Nayak, A. K. Yadav, A. Agrawal, A. K. Poswal, D. Bhattacharyya, S. N. Jha and N. K. Sahoo, Journal of Physics: Conference Series **493** (1), 012032 (2014).
65. A. K. Poswal, A. Agrawal, A. K. Yadav, C. Nayak, S. Basu, S. R. Kane, C. K. Garg, D. Bhattachryya, S. N. Jha and N. K. Sahoo, AIP Conference Proceedings **1591** (1), 649-651 (2014).
66. P. Willmott, in *An Introduction to Synchrotron Radiation* (John Wiley & Sons, Ltd, 2011), pp. 39-86.
67. http://www.rrcat.gov.in/technology/accel/indus2.html.
68. D. Bhattacharyya, A. K. Poswal, S. N. Jha, Sangeeta and S. C. Sabharwal, Nuclear Instruments and Methods in Physics Research Section A: Accelerators, Spectrometers, Detectors and Associated Equipment **609** (2), 286-293 (2009).
69. A. K. Poswal, A. Agrawal, H. K. Poswal, D. Bhattacharyya, S. N. Jha and N. K. Sahoo, Journal of Synchrotron Radiation **23** (6), 1518-1525 (2016).

70. X. Wang, J. C. Hanson, A. I. Frenkel, J.-Y. Kim and J. A. Rodriguez, The Journal of Physical Chemistry B **108** (36), 13667-13673 (2004).
71. B. Ravel and M. Newville, Journal of Synchrotron Radiation **12** (4), 537-541 (2005).
72. S. R. Wasserman, P. G. Allen, D. K. Shuh, J. J. Bucher and N. M. Edelstein, Journal of Synchrotron Radiation **6** (3), 284-286 (2007).
73. A. I. Frenkel, O. Kleifeld, S. R. Wasserman and I. Sagi, The Journal of Chemical Physics **116** (21), 9449-9456 (2002).
74. Q. Wang, J. C. Hanson and A. I. Frenkel, The Journal of Chemical Physics **129** (23), 234502 (2008).
75. A. Voronov, A. Urakawa, W. v. Beek, N. E. Tsakoumis, H. Emerich and M. Rønning, Analytica Chimica Acta **840**, 20-27 (2014).
76. W. H. Cassinelli, L. Martins, A. R. Passos, S. H. Pulcinelli, C. V. Santilli, A. Rochet and V. Briois, Catalysis Today **229**, 114-122 (2014).
77. A. Martini, E. Borfecchia, K. A. Lomachenko, I. A. Pankin, C. Negri, G. Berlier, P. Beato, H. Falsig, S. Bordiga and C. Lamberti, Chemical Science **8** (10), 6836-6851 (2017).
78. M. Staniuk, D. Zindel, W. van Beek, O. Hirsch, N. Kränzlin, M. Niederberger and D. Koziej, CrystEngComm **17** (36), 6962-6971 (2015).
79. M. Newville, Journal of Synchrotron Radiation **8** (2), 322-324 (2001).
80. S. I. Zabinsky, J. J. Rehr, A. Ankudinov, R. C. Albers and M. J. Eller, Physical Review B **52** (4), 2995-3009 (1995).
81. A. L. Ankudinov, B. Ravel, J. J. Rehr and S. D. Conradson, Physical Review B **58** (12), 7565-7576 (1998).
82. M. Newville, P. Līviņš, Y. Yacoby, J. J. Rehr and E. A. Stern, Physical Review B **47** (21), 14126-14131 (1993).
83. J. J. Rehr, J. J. Kas, F. D. Vila, M. P. Prange and K. Jorissen, Physical Chemistry Chemical Physics **12** (21), 5503-5513 (2010).
84. F. Meneau, G. Sankar, N. Morgante, S. Cristol, C. R. A. Catlow, J. M. Thomas and G. N. Greaves, Nuclear Instruments and Methods in Physics Research Section B: Beam Interactions with Materials and Atoms **199**, 499-503 (2003).
85. H.-H. Perkampus, *UV-VIS Spectroscopy and its Applications*. (Springer Science & Business Media, 2013).
86. V. G. Berezkin, V. R. Alishoyev and I. B. Nemirovskaya, Journal of Chromatography Library **10**, 1-31 (1977).
87. B. D. Cullity and S. R. Stock, *Elements of X-ray Diffraction*. (Pearson Education, 2014).
88. D. Briggs and M. Seah, *Practical surface analysis: by auger and x-ray photoelectron spectroscopy*. (Wiley, 2003).
89. D. B. Williams and C. B. Carter, in *Transmission electron microscopy* (Springer, 1996), pp. 3-17.
90. J. J. Storhoff, R. Elghanian, R. C. Mucic, C. A. Mirkin and R. L. Letsinger, Journal of the American Chemical Society **120** (9), 1959-1964 (1998).
91. G. C. Bond, C. Louis and D. T. Thompson, Imperial College Press: London **6** (2006).
92. C.-K. Tsung, J. N. Kuhn, W. Huang, C. Aliaga, L.-I. Hung, G. A. Somorjai and P. Yang, Journal of the American Chemical Society **131** (16), 5816-5822 (2009).
93. R. Narayanan and M. A. El-Sayed, Journal of the American Chemical Society **126** (23), 7194-7195 (2004).

94. L. Catherine and P. Olivier, *Gold nanoparticles for physics, chemistry and biology.* (Imperial College Press, London, 2012).
95. C. Helmbrecht, D. Lützenkirchen-Hecht and W. Frank, Nanoscale **7** (11), 4978-4983 (2015).
96. S. Yao, Y. Yuan, C. Xiao, W. Li, Y. Kou, P. J. Dyson, N. Yan, H. Asakura, K. Teramura and T. Tanaka, The Journal of Physical Chemistry C **116** (28), 15076-15086 (2012).
97. A. I. Frenkel, A. Yevick, C. Cooper and R. Vasic, Annual Review of Analytical Chemistry **4** (1), 23-39 (2011).
98. S. Calvin, M. Miller, R. Goswami, S.-F. Cheng, S. Mulvaney, L. Whitman and V. Harris, Journal of applied physics **94** (1), 778-783 (2003).
99. T. Sakai and P. Alexandridis, The Journal of Physical Chemistry B **109** (16), 7766-7777 (2005).
100. V. K. LaMer and R. H. Dinegar, Journal of the American Chemical Society **72** (11), 4847-4854 (1950).
101. M. P. Johansson, A. Lechtken, D. Schooss, M. M. Kappes and F. Furche, Physical Review A **77** (5), 053202 (2008).
102. D. Schooss, P. Weis, O. Hampe and M. M. Kappes, Philosophical Transactions of the Royal Society of London A: Mathematical, Physical and Engineering Sciences **368** (1915), 1211-1243 (2010).
103. V. Petkov, N. Bedford, M. R. Knecht, M. G. Weir, R. M. Crooks, W. Tang, G. Henkelman and A. Frenkel, The Journal of Physical Chemistry C **112** (24), 8907-8911 (2008).
104. V. Kumar and Y. Kawazoe, Physical Review B **77**, 205418 (205411-205410). (2008).
105. A. Genest, S. Krüger and N. Rösch, Zeitschrift für Naturforschung B **64** (11-12), 1246-1258 (2009).
106. V. R. Stamenkovic, B. Fowler, B. S. Mun, G. Wang, P. N. Ross, C. A. Lucas and N. M. Marković, Science **315** (5811), 493 (2007).
107. F. Tao, M. E. Grass, Y. Zhang, D. R. Butcher, J. R. Renzas, Z. Liu, J. Y. Chung, B. S. Mun, M. Salmeron and G. A. Somorjai, Science **322** (5903), 932 (2008).
108. B. Lim, M. Jiang, P. H. C. Camargo, E. C. Cho, J. Tao, X. Lu, Y. Zhu and Y. Xia, Science **324** (5932), 1302 (2009).
109. T. Omori, K. Ando, M. Okano, X. Xu, Y. Tanaka, I. Ohnuma, R. Kainuma and K. Ishida, Science **333** (6038), 68 (2011).
110. E. González, J. Arbiol and V. F. Puntes, Science **334** (6061), 1377 (2011).
111. N. Toshima and T. Yonezawa, New Journal of Chemistry **22** (11), 1179-1201 (1998).
112. N. Toshima, K. Kushihashi, T. Yonezawa and H. Hirai, Chemistry Letters **18** (10), 1769-1772 (1989).
113. H. Zhang, J. Okuni and N. Toshima, J Colloid Interface Sci **354** (1), 131-138 (2011).
114. H. Zhang, M. Okumura and N. Toshima, The Journal of Physical Chemistry C **115** (30), 14883-14891 (2011).
115. H. Zhang, T. Watanabe, M. Okumura, M. Haruta and N. Toshima, Nature Materials **11**, 49 (2011).
116. H. Lang, S. Maldonado, K. J. Stevenson and B. D. Chandler, Journal of the American Chemical Society **126** (40), 12949-12956 (2004).
117. H. Ataee-Esfahani, L. Wang, Y. Nemoto and Y. Yamauchi, Chemistry of Materials **22** (23), 6310-6318 (2010).

118. H. Zhang and N. Toshima, J Colloid Interface Sci **394**, 166-176 (2013).
119. A. I. Frenkel, Chemical Society Reviews **41** (24), 8163-8178 (2012).
120. X. Liu, D. Wang and Y. Li, Nano Today **7** (5), 448-466 (2012).
121. M. Sankar, N. Dimitratos, P. J. Miedziak, P. P. Wells, C. J. Kiely and G. J. Hutchings, Chemical Society Reviews **41** (24), 8099-8139 (2012).
122. C.-H. Chen, L. S. Sarma, J.-M. Chen, S.-C. Shih, G.-R. Wang, D.-G. Liu, M.-T. Tang, J.-F. Lee and B.-J. Hwang, ACS Nano **1** (2), 114-125 (2007).
123. H. Ataee-Esfahani, L. Wang and Y. Yamauchi, Chemical Communications **46** (21), 3684-3686 (2010).
124. H. M. Chen, H. C. Peng, R. S. Liu, S. F. Hu and L. Y. Jang, Chemical Physics Letters **420** (4), 484-488 (2006).
125. T. Yao, Z. Sun, Y. Li, Z. Pan, H. Wei, Y. Xie, M. Nomura, Y. Niwa, W. Yan, Z. Wu, Y. Jiang, Q. Liu and S. Wei, Journal of the American Chemical Society **132** (22), 7696-7701 (2010).
126. A. I. Frenkel, Q. Wang, S. I. Sanchez, M. W. Small and R. G. Nuzzo, The Journal of Chemical Physics **138** (6), 064202 (2013).
127. I. Banerjee, V. Kumaran and V. Santhanam, The Journal of Physical Chemistry C **119** (11), 5982-5987 (2015).
128. M. Khalid, N. Wasio, T. Chase and K. Bandyopadhyay, Nanoscale Research Letters **5** (1), 61 (2009).
129. L. Qian, Y. Sha and X. Yang, Thin Solid Films **515** (4), 1349-1353 (2006).
130. D. I. Garcia-Gutierrez, C. E. Gutierrez-Wing, L. Giovanetti, J. M. Ramallo-López, F. G. Requejo and M. Jose-Yacaman, The Journal of Physical Chemistry B **109** (9), 3813-3821 (2005).
131. H.-J. Jang, S. Hong, S. Ham, K. L. Shuford and S. Park, Nanoscale **6** (13), 7339-7345 (2014).
132. T. Bian, H. Zhang, Y. Jiang, C. Jin, J. Wu, H. Yang and D. Yang, Nano Letters **15** (12), 7808-7815 (2015).
133. Y. Li, W. Ding, M. Li, H. Xia, D. Wang and X. Tao, Journal of Materials Chemistry A **3** (1), 368-376 (2015).
134. J. Zeng, J. Yang, J. Y. Lee and W. Zhou, The Journal of Physical Chemistry B **110** (48), 24606-24611 (2006).
135. X. Meng, A. Baride and C. Jiang, Langmuir **32** (26), 6674-6681 (2016).
136. K. L. Kelly, E. Coronado, L. L. Zhao and G. C. Schatz, The Journal of Physical Chemistry B **107** (3), 668-677 (2003).
137. S. Tomita, M. Hikita, M. Fujii, S. Hayashi and K. Yamamoto, Chemical Physics Letters **316** (5), 361-364 (2000).
138. R. Narayanan and M. A. El-Sayed, The Journal of Physical Chemistry B **109** (26), 12663-12676 (2005).
139. D. L. Fedlheim and C. A. Foss, *Metal nanoparticles: synthesis, characterization, and applications*. (CRC press, 2001).
140. M. B. Gawande, A. Goswami, F.-X. Felpin, T. Asefa, X. Huang, R. Silva, X. Zou, R. Zboril and R. S. Varma, Chemical Reviews **116** (6), 3722-3811 (2016).
141. F. Zaera, Chemical Society Reviews **42** (7), 2746-2762 (2013).
142. G. Evano, N. Blanchard and M. Toumi, Chemical Reviews **108** (8), 3054-3131 (2008).

143. G. A. Somorjai and J. Y. Park, Angewandte Chemie International Edition **47** (48), 9212-9228 (2008).
144. M. A. Ben Aissa, B. Tremblay, A. Andrieux-Ledier, E. Maisonhaute, N. Raouafi and A. Courty, Nanoscale **7** (7), 3189-3195 (2015).
145. S. Nishimura, A. Takagaki, S. Maenosono and K. Ebitani, Langmuir **26** (6), 4473-4479 (2010).
146. W. H. Cassinelli, L. Martins, M. Magnani, S. H. Pulcinelli, V. Briois and C. V. Santilli, RSC Advances **6** (25), 20453-20457 (2016).
147. W. H. Cassinelli, L. Martins, A. R. Passos, S. H. Pulcinelli, A. Rochet, V. Briois and C. V. Santilli, ChemCatChem **7** (11), 1668-1677 (2015).
148. H. R. Oswald, A. Reller, H. W. Schmalle and E. Dubler, Acta Crystallographica Section C **46** (12), 2279-2284 (1990).
149. S. Basu, D. Y. Inamdar, S. Mahamuni, A. Chakrabarti, C. Kamal, G. R. Kumar, S. N. Jha and D. Bhattacharyya, The Journal of Physical Chemistry C **118** (17), 9154-9164 (2014).
150. S. Kumari, A. Shekhar and D. D. Pathak, RSC Advances **6** (19), 15340-15344 (2016).
151. A. Kirfel and K. Eichhorn, Acta Crystallographica Section A **46** (4), 271-284 (1990).
152. P. Conti, S. Zamponi, M. Giorgetti, M. Berrettoni and W. H. Smyrl, Analytical Chemistry **82** (9), 3629-3635 (2010).
153. S. Muthukumaran and R. Gopalakrishnan, Physica B: Condensed Matter **407** (17), 3448-3456 (2012).
154. J. Majeed, C. Nayak, S. N. Jha, K. Bhattacharyya, D. Bhattacharyya and A. K. Tripathi, RSC Advances **5** (110), 90932-90940 (2015).
155. T. Čižmar, U. L. Štangar and I. Arčon, Catalysis Today **287**, 155-160 (2017).
156. L. van Haandel, G. M. Bremmer, E. J. M. Hensen and T. Weber, Journal of Catalysis **351**, 95-106 (2017).
157. A. J. Dent, Topics in Catalysis **18** (1-2), 27-35 (2002).
158. J.-D. Grunwaldt and B. S. Clausen, Topics in Catalysis **18** (1-2), 37-43 (2002).
159. A. Rochet, V. Moizan, F. Diehl, C. Pichon and V. Briois, Catalysis Today **205**, 94-100 (2013).
160. D. Yuming, H. Kun, Y. Lin and Z. Aimin, Nanotechnology **18** (43), 435602 (2007).
161. A. Y. Khodakov, Catalysis Today **144** (3), 251-257 (2009).
162. G. Jacobs, J. A. Chaney, P. M. Patterson, T. K. Das and B. H. Davis, Applied Catalysis A: General **264** (2), 203-212 (2004).
163. K. Jalama, N. J. Coville, D. Hildebrandt, D. Glasser, L. L. Jewell, J. A. Anderson, S. Taylor, D. Enache and G. J. Hutchings, Topics in Catalysis **44** (1-2), 129-136 (2007).
164. A. R. Passos, L. Martins, S. H. Pulcinelli, C. V. Santilli and V. Briois, ChemCatChem **9** (20), 3918-3929 (2017).
165. A. T. DeLaRiva, T. W. Hansen, S. R. Challa and A. K. Datye, Journal of Catalysis **308**, 291-305 (2013).
166. A. R. Passos, L. Martins, S. H. Pulcinelli, C. V. Santilli and V. Briois, Catalysis Today **229**, 88-94 (2014).
167. D. J. Moodley, J. van de Loosdrecht, A. M. Saib, M. J. Overett, A. K. Datye and J. W. Niemantsverdriet, Applied Catalysis A: General **354** (1), 102-110 (2009).
168. O. Ola and M. M. Maroto-Valer, Journal of Photochemistry and Photobiology C: Photochemistry Reviews **24**, 16-42 (2015).

169. O. K. Varghese, M. Paulose, T. J. LaTempa and C. A. Grimes, Nano Letters **9** (2), 731-737 (2009).
170. E. Karamian and S. Sharifnia, Journal of CO2 Utilization **16**, 194-203 (2016).
171. S. S. Tan, L. Zou and E. Hu, Catalysis Today **115** (1), 269-273 (2006).
172. L. Liu and Y. Li, Aerosol and Air Quality Research **14** (2), 453-469 (2014).
173. R. Camarillo, S. Tostón, F. Martínez, C. Jiménez and J. Rincón, Journal of Chemical Technology & Biotechnology **93** (5), 1237-1248 (2017).
174. Y. Li, W.-N. Wang, Z. Zhan, M.-H. Woo, C.-Y. Wu and P. Biswas, Applied Catalysis B: Environmental **100** (1), 386-392 (2010).
175. M. Horn, C. F. Schwerdtfeger and E. P. Meagher, Zeitschrift fur Kristallographie **136**, 273-281 (1972).
176. P. C. Angelomé, L. Andrini, M. E. Calvo, F. G. Requejo, S. A. Bilmes and G. J. A. A. Soler-Illia, The Journal of Physical Chemistry C **111** (29), 10886-10893 (2007).
177. U. Lafont, D. Carta, G. Mountjoy, A. V. Chadwick and E. M. Kelder, The Journal of Physical Chemistry C **114** (2), 1372-1378 (2010).
178. K. Huang, K. Sasaki, R. R. Adzic and Y. Xing, Journal of Materials Chemistry **22** (33), 16824-16832 (2012).
179. L. Liu, F. Gao, H. Zhao and Y. Li, Applied Catalysis B: Environmental **134**, 349-358 (2013).
180. L. Liu, C. Zhao and Y. Li, The Journal of Physical Chemistry C **116** (14), 7904-7912 (2012).
181. H. Irie, K. Kamiya, T. Shibanuma, S. Miura, D. A. Tryk, T. Yokoyama and K. Hashimoto, The Journal of Physical Chemistry C **113** (24), 10761-10766 (2009).
182. Ş. Neaţu, J. A. Maciá-Agulló, P. Concepción and H. Garcia, Journal of the American Chemical Society **136** (45), 15969-15976 (2014).
183. Slamet, H. W. Nasution, E. Purnama, S. Kosela and J. Gunlazuardi, Catalysis Communications **6** (5), 313-319 (2005).